

ANALYSIS AND MEASUREMENT OF STRESSES IN PLANAR SOIL REINFORCEMENTS

by

MAURICIO ABRAMENTO

B.S. Civil Engineering, Escola Politécnica da Universidade de São Paulo, 1984

M.S. Civil Engineering, Escola Politécnica da Universidade de São Paulo, 1988

SUBMITTED TO THE DEPARTMENT OF
CIVIL AND ENVIRONMENTAL ENGINEERING
IN PARTIAL FULFILLMENT OF THE REQUIREMENTS FOR THE DEGREE OF
DOCTOR OF PHILOSOPHY IN CIVIL ENGINEERING

at the

MASSACHUSETTS INSTITUTE OF TECHNOLOGY

MAY 1993

© 1993 Massachusetts Institute of Technology

All Rights Reserved

Signature of Author _____
Department of Civil and Environmental Engineering

Certified by _____
Prof. Andrew J. Whittle
Thesis Supervisor

Accepted by _____
Prof. Eduardo Kausel
Chairman, Departmental Committee on Graduate Studies

ARCHIVES
MASSACHUSETTS INSTITUTE
OF TECHNOLOGY

[JUN 08 1993

Analysis and Measurement of Stresses in Planar Soil Reinforcements

by: **Mauricio Abramento**

Submitted to the Department of Civil and Environmental Engineering on May 7, 1993, in partial fulfillment of the requirements for the degree of
Doctor of Philosophy in Civil Engineering

ABSTRACT

This thesis describes the development of analytical solutions for estimating the tensile stresses in planar soil reinforcements in three fundamental modes of interaction. The formulation adapts techniques of 'shear-lag' analysis, and relates the complete stress field in the reinforcement and soil matrix as closed-form functions of the external stresses, overall geometry, elastic properties of the constituent materials and interface friction. The analyses assume that the soil and reinforcement are linear, isotropic and elastic materials, linked through a frictional interface. The analytical solutions are evaluated through comparisons with experimental data in well controlled laboratory experiments in the Automated Plane Strain Reinforcement (APSR) cell.

The first analysis considers a 'base case geometry' in which tensile stresses develop in the reinforcement due to plane strain compression shearing of the surrounding soil matrix, with inclusion oriented parallel to the minor, external principal stress. The solutions show that the major factors affecting load transfer are the inclusion length, relative soil-reinforcement stiffness, inclusion spacing and shear stress condition in the soil matrix, while interface slippage is of secondary importance. The accuracy of the proposed shear-lag solutions is confirmed through comparisons with numerical finite element analyses for a wide range of geometries and constituent material properties. The analyses show very good agreement with APSR cell measurements of tensile stress distributions for steel sheet reinforcements of various lengths, embedded in dense and loose specimens of dry Ticino sand.

The second analysis extends the previous solution for general orientations of the reinforcement and external principal stress directions in the soil matrix. The analysis assumes small deformations and negligible bending resistance of the reinforcements. Preliminary comparisons show good agreement with small strain measurements in direct shear box and direct simple shear experiments reported in the literature. Modifications of the analysis which incorporate soil dilation are necessary in order to evaluate the effects of the inclusion on the shear strength of the composite reinforced soil.

The third application of shear-lag analysis is for predicting and interpreting stress distributions and load-elongation response in pullout tests on frictional planar soil reinforcements. The analyses describe the initiation and development of sliding fronts which are characterized by local concentrations of the interface tractions. The results show that the peak pullout resistance can be significantly larger than that estimated from conventional limit equilibrium calculations. Principal parameters affecting the non-linear load-elongation behavior are the inclusion length, relative soil-reinforcement stiffness and interface friction. The analysis describe a characteristic snap-through mechanism which is particularly pronounced for more extensible reinforcements.

A special series of pullout tests were performed in the APSR cell using instrumented steel and nylon 6/6 inclusions. These materials have elastic properties, low interface friction and represent the extreme ranges of axial stiffness for practical soil reinforcements. Tensile stresses in the steel sheet are distributed linearly along the inclusion during pullout and closely resemble the ideal inextensible reinforcement. In contrast, stress distributions are highly non-linear for the nylon 6/6 and exhibit a brittle post-peak reduction in pullout resistance. These results are in excellent agreement with predictions from the proposed shear-lag analysis.

Thesis Supervisor: **Dr. Andrew J. Whittle**
Title: Associate Professor of Civil Engineering

Acknowledgements

This thesis is the product of support from a number of people who have helped me in studies and research. In particular, I would like to express my appreciation to the following people and institutions:

Professor Andrew Whittle, thesis supervisor, for his guidance and technical insights during all the research, and also for his meticulous review of this thesis. It has been a most rewarding experience working with him.

Professors Herbert H. Einstein, Frederick J. McGarry and Christopher K. Y. Leung for serving on my thesis committee.

"Conselho Nacional de Desenvolvimento Científico e Tecnológico" and "Instituto de Pesquisas Tecnológicas do Estado de São Paulo", for their financial support.

The APSR group, including Samir Chauhan and Doug Larson, for the lengthy discussions we had and for their help with the pullout tests in the APSR cell. Juan Pestana and Dante Legaspi, my officemates, for the friendship along the years and the moral support. Antonio Bobet for reviewing the calculations of Chapter 4. Marika, Doug Cauble, Ajay and all the other geotechnical students, who provided a much lighter working atmosphere at MIT.

Eduardo and Lin, for their invaluable friendship.

My parents, Geni and Isaac, who provided me with encouragement throughout the studies. Without their help I would not have come so far.

Adriana, for her patience, encouragement and support during all this long process. I would like to express my sincere gratitude dedicating this thesis to her.

Table of Contents

Abstract	2
Acknowledgements	3
Table of Contents	4
List of Tables	8
List of Figures	9
Chapter 1: Introduction	14
Appendix 1.A: References	18
Chapter 2: Shear Lag Analysis of a Planar Soil Reinforcement in Plane Strain Compression	19
2.1. Introduction	19
2.2. Shear Lag Formulation	22
2.3. Comparison with Finite Element Solutions	26
2.4. Results	27
2.4.1. Stresses Along Inclusion	27
2.4.2. "Pickup" Curves	28
2.4.3. Definition of Short Reinforcements	29
2.4.4. Stress Distribution due to Shearing of Soil Mass	29
2.4.5. Maximum Tensile Stresses in Long Inclusions	30
2.4.6. The Reinforcing Effect	31
2.5 Extension of Solution for Slipping Frictional Interface	32
2.5.1. Frictional Sliding along Interface	32
2.5.2. Modified Formulation for Slipping Interface	33
2.5.3. Effects of Frictional Sliding on Load Transfer	34
2.6 Conclusions	35
Appendix 2.A: Stress Averaging in the Decoupled Model	49
Appendix 2.B: References	50
Appendix 2.C: Notation	53
Chapter 3: Interpretation of APSR Cell Test Results using the Shear-Lag Analysis	55
3.1. Introduction	55
3.2. Overview of the APSR Cell	55
3.2.1. Conceptual Design	55

3.2.2. Geometry	56
3.2.3. Boundary Traction	57
3.2.4. Instrumentation	58
3.2.5. Hardware	59
3.2.6. Sand Deposition	60
3.2.7. Instrumentation for Steel Sheet Reinforcements	61
3.2.8. Proof Tests	61
3.3. APSR Measurements	62
3.3.1. Shear Behavior of Ticino Sand	62
3.3.2. Tensile Stress in Steel Reinforcement	63
3.4. Comparison of APSR Test Results and Shear Lag Predictions	64
3.4.1. Selection of Input Parameters	64
3.4.2. Inclusion Loads - Dense Sand	66
3.4.3. Inclusion Loads - Loose Sand	66
3.4.4. Influence of Inclusion Length on Centerline Loads	67
3.4. Conclusions	68
Appendix 3.A: References	87
Appendix 3.B: Notation	89
Chapter 4: Effects of Inclusion Orientation	90
4.1. Introduction	90
4.2. Formulation	92
4.2.1. Generalization for Arbitrary θ	97
4.3. Results	98
4.3.1. Plane Strain Compression of Soil Specimen	98
4.3.2. Direct Shear	100
4.3.3. Direct Simple Shear Tests	101
4.3.4. Behavior of Long Inclusions	102
4.3.5. Comparison with Finite Element Results	103
4.4. Interpretation of Tests Results Available in the Literature	104
4.4.1. Plane Strain Tests	104
4.4.2. Direct Shear Box Tests	109
4.5 Conclusions	113
Appendix 4.A: Complete Expressions for the Interface Traction	145
Appendix 4.B: References	146
Appendix 4.C: Notation	148

Chapter 5: Analysis of Pullout Tests for Planar Soil Reinforcement	151
5.1. Introduction	151
5.2. Shear-Lag Formulation	156
5.2.1. Governing Equations	156
5.2.2. Particular Solutions	159
5.2.2.1 No Slippage	160
5.2.2.2 One-Way Debonding	161
5.2.2.3. Two-Way Debonding	163
5.2.2.4. Representation of Pullout Response	166
5.3. Interpretation of Pullout Behavior	166
5.3.1. Typical Results	166
5.3.1.1. Effect of Reinforcement-Soil Stiffness Ratio	168
5.3.1.2. Effect of Residual Stresses	169
5.3.1.3. Pullout-Elongation Response	170
5.3.2. Yield, Peak and Residual Pullout Stresses	171
5.3.2.1. Factors Affecting Pullout Response	171
5.3.2.2. Initial Yield	172
5.3.2.3. Comparison with Limit Equilibrium Solutions	173
5.3.2.4. Residual Pullout Stress	174
5.3.3. Soil Failure	174
5.4 Conclusions	176
Appendix 5.A: Complete Expressions for Pullout Curves	198
Appendix 5.B: References	200
Appendix 5.C: Notation	204
Chapter 6: Pullout Tests of Planar Inclusions in the APSR Cell	207
6.1. Introduction	207
6.2. Experimental Program	208
6.3. Test Procedure	209
6.3.1. Preparation of Instrumented Inclusions	210
6.3.1.1. Steel Sheet	212
6.3.1.2. Nylon 6/6 Sheet	212
6.3.2. APSR Cell and Specimen Preparation	213
6.3.3. Consolidation and Pullout Test Procedures	214
6.4. Results	215

6.4.1. Steel Sheet Inclusion	215
6.4.2. Nylon 6/6 Sheet Inclusions	218
6.5 Comparison with Analytical Predictions	221
6.5.1. Steel Inclusions	222
6.5.2. Nylon 6/6 Inclusions	223
6.6 Conclusions	224
Appendix 6.A: References	257
Appendix 6.B: Notation	259
Chapter 7: Summary, Conclusions and Recommendations	261
7.1. Planar Soil Reinforcement in Plane Strain Compression	261
7.2. Effects of Inclusion Orientation	263
7.3. Pullout Tests on Planar Inclusions	265
7.4. Recommendations	266
7.4.1. Evaluation of Shear-Lag Analyses	267
7.4.2. Extension of Shear-Lag Analyses	268
7.4.3. Other Applications	269
7.4.3.1. Stresses in a Reinforced Earth Wall	269
7.4.3.2. Tension Tests for Piles	270
Appendix 7.A: References	273

List of Tables

1.1	Thesis Outline	17
2.1	Comparison of Maximum Inclusion Stress σ_{\max}^f/σ_1 from Shear-Lag and Finite Element Methods	37
2.2	Reinforcement Effectiveness of Long Inclusions at $\sigma_1/\sigma_3=6$	38
3.1	Performance Characteristics of the APSR Cell.(after Larson, 1992)	70
3.2	Summary of APSR Tests with Steel Sheet Reinforcements	71
3.3	Input Parameters for Shear Lag Predictions of Load Pickup in Dense Ticino Sand	72
3.4	Input Parameters for Shear Lag Predictions of Load Pickup in Loose Ticino Sand	72
4.1	Laboratory Measurements for Reinforced Soils with Inclined Inclusions and Principal Stress Rotations	115
4.2	Parameters for Proposed Shear-Lag Analysis	116
4.3	Input Parameters for Shear-lag Analysis of Plane Strain Unit Cell Tests Reported by McGown et al. (1978)	137
6.1	Pullout Tests Performed in the APSR cell	226
6.2	Input Parameters for Shear-Lag Analysis of Pullout Tests in the APSR cell	227

List of Figures

2.1	Plane Strain Geometry for an Element of Reinforced Soil	39
2.2	Decoupling of Stresses and Displacements in Shear-Lag Model	40
2.3	Effect of Inclusion Length on Axial Stresses and Interface Traction	41
2.4	Effect of Inclusion Length and Stiffness on the Maximum Load Transfer Ratio	42
2.5	Definition of Short Reinforcements	43
2.6	Development of Reinforcement Stress due to Shearing of the Soil	44
2.7	Load Transfer for Long Inclusions	45
2.8	Minimum Interface Friction Required to Prevent Slippage for a Long Rigid Inclusion	46
2.9	Effect of Interface Slippage on the Predicted Load Transfer	47
2.10	Effect of Interface Slippage on the Maximum Load Transfer Ratio	48
3.1	Geometry of the APSR Ideal Plane Strain Reinforced Soil Element	73
3.2	Conceptual Design of the APSR Cell (after Whittle et al., 1991)	73
3.3	Cross Section Through the APSR cell (after Larson, 1992)	74
3.4	APSR Cell Instrumentation (after Larson, 1992)	75
3.5	The APSR Cell Raining Apparatus.(after Larson, 1992)	76
3.6	Repeatability of Externally Measured Shear Behavior (after Larson, 1992)	77
3.7	Comparison of External and Corrected Internal Measurements for Dense Ticino Sand (after Larson, 1992)	78
3.8	Estimated Plane Strain Shear Behavior of Ticino Sand.(after Larson, 1992)	79
3.9	Comparison of Load Pickup Measurements for Base-Case Tests in Dense Ticino Sand (after Larson, 1992)	80
3.10	Elastic Approximations to Plane Strain Behavior of Dense Ticino Sand	81
3.11	Elastic Approximations to Plane Strain Behavior of Loose Ticino Sand	82
3.12	Comparison of Shear-Lag Predictions of Inclusion Tensile Loads to Measured Data for a Base-Case Test	83
3.13	Comparison of Shear Lag Predictions of Inclusion Tensile Loads to Measured Data for Loose Sand	84
3.14	Shear Lag Predictions vs. Measured Inclusion Tensile Loads for Inclusions of Different Lengths	85
3.15	Predicted vs. Measured Maximum Tensile Force in Inclusion at $R = 6.0$	86

4.1	Effects of Inclusion Orientation on Reinforced Direct Shear Tests	117
4.2	Plane Strain Geometry for Composite Reinforced Soil Element with General Inclusion Orientation and Principal Stress Directions	118
4.3	Soil Stress Conditions Assumed in Proposed Analysis	119
4.4	Effect of Inclusion Orientation on Shear-Lag Approximations	120
4.5	Influence of Geometric Parameters on Shear Spring Layer	121
4.6	Effects of Inclusion Orientation on Tensile Inclusion Stresses and Interface Traction	122
4.7	Factors Affecting Maximum Load Transfer in Plane Strain Compression	123
4.8	Effect of Inclusion Orientation on Load Transfer in Direct Shear	125
4.9	Factors Affecting Maximum Load Transfer in Direct Shear	126
4.10	Inclusion Tensile Stresses and Interface Traction during Simple Shear Tests	127
4.11	Effect of Inclusion Orientation on Maximum Load Transfer in Simple Shear Tests	128
4.12	Maximum Stresses Carried by Long Inclusions	129
4.13	Effect of Inclusion Length, Orientation and Stiffness on the Maximum Load Transfer Ratio	130
4.14	Typical Finite Element Model for Computing Axial Stress in a Thin Inclined Reinforcement	131
4.15	Reduction in Maximum Axial Inclusion Stress at Centerline	132
4.16	Influence of Inclusion Orientation on Maximum Stress at Inclusion Centerline and Comparison with Finite Element Results	133
4.17	Unit Cell for Plane Strain Tests on Leighton Buzzard Sand (McGown et al., 1978)	134
4.18	Contours of Volumetric and Shear Strains for Plane Strain Shear with a Horizontal Reinforcement (McGown et al., 1978)	134
4.19	Effect of Reinforcements on External Stress-Strain Behavior Measured in Plane Strain Shear Tests (McGown et al., 1978)	135
4.20	Constituent Material Properties for Unit Cell Tests	136
4.21	Comparison of Shear-Lag Predictions and Measured Peak Stress Ratio for Unit Cell Tests	138
4.22	Stresses Predicted for Reinforcements in Dense Sand at Peak Strength Conditions in Unit Cell Tests	139
4.23	Typical Results of Direct Shear Tests on Leighton Buzzard Sand Reinforced by a Single Steel Grid at Different Orientations (Jewell, 1980)	140

4.24	Limit Equilibrium Interpretation of Direct Shear Tests	141
4.25	Proposed Interpretation of Direct Shear Box Tests on Unreinforced Dense Leighton Buzzard Sand	142
4.26	Comparison of Shear-Lag Analysis and Results of Direct Shear Tests in Reinforced Leighton Buzzard Sand (Jewell and Wroth, 1987)	143
4.27	Link Between Reinforcing Effect and Soil Dilatation in Large Direct Shear Box Test at $\theta=90^\circ$ (after Palmeira, 1987)	144
5.1	Boundary Conditions in Laboratory Pullout Tests	178
5.2	Stresses around a Rough Sheet and a Grid in a Pullout Test (after Dyer, 1985 and Palmeira, 1987)	179
5.3	Geometry and Boundary Conditions used in Analysis of Pullout Tests for Planar Soil Reinforcements	180
5.4	Schematic Sequence of Events during Pullout of Planar Inclusions	181
5.5	Axial Inclusion Stress and Interface Traction During Pullout Test: Base Case Analysis	182
5.6	Tensile Stress and Interface Traction During Pullout Tests: Extensible Inclusion under K_0 Compression	183
5.7	Effects of Residual Stresses on Tensile Stress and Interface Traction During Pullout Tests	184
5.8	Effects of Stiffness Ratio E_f/G_m and Residual Stresses (σ_1/σ_3) on Pullout Response	185
5.9	Effects of Geometry on Load-Elongation Response	186
5.10	Effects of Inclusion Length on Axial Inclusion Stress and Interface Traction	187
5.11	Effect of Material and Interface Properties on Load-Elongation Response	188
5.12	Limiting Friction for Sliding at Soil-Reinforcement Interface	189
5.13	Limit Values of Yield Stresses for Inextensible Reinforcements	190
5.14a	Contours of Shear Stresses in the Soil Matrix During Pullout Test for Reference Properties	191
5.14b	Contours of Normal Stresses in the Soil Matrix During Pullout Test for Reference Properties	192
5.14c	Contours of Mobilized Pseudo-Friction Angle in the Soil Matrix During Pullout Test for Reference Properties	193
5.15a	Contours of Shear Stresses in the Soil Matrix During Pullout Test in Extensible Inclusion	194
5.15b	Contours of Normal Stresses in the Soil Matrix During Pullout Test in	

	Extensible Inclusion	195
5.15c	Contours of Mobilized Pseudo-Friction Angle in the Soil Matrix During Pullout Test in Extensible Inclusion	196
5.16	Evaluation of Conditions for Soil Failure in Pullout Tests	197
6.1	Comparison of Boundary Conditions used in the APSR Cell	228
6.2	Schematic of the Instrumented Inclusion for Pullout Tests	229
6.3	In-isolation Test Setup in Instron Machine	229
6.4	Typical Stress-Strain Results for In-Isolation Tension Tests on Nylon 6/6	230
6.5	Specimen Membrane Preparation.(after Larson, 1992)	231
6.6	APSR Specimen Membrane Installation (after Larson, 1992)	232
6.7	Inclusion Assembly to External Arch Piston and Monitoring Mechanism of Active End in Pullout Tests	233
6.8	Measured Pullout Load-Displacement Response for Steel Sheet Reinforcements	234
6.9	Coefficient of Interface Friction Between Steel and Sand (after Kishida and Uesugi, 1987)	235
6.10	Dimensionless Pullout Response for Tests on Steel Sheet Inclusions	236
6.11	Pullout Measurements in Test APSR 50-1	237
6.12	Pullout Measurements in Test APSR 50-2	238
6.13	Pullout Measurements in Test APSR 50-3	239
6.14	Pullout Measurements in Test APSR 50-4	240
6.15	Tensile Stress Distribution in Pullout Tests on Steel Sheet Inclusion	241
6.16	Interpreted Load-Elongation Behavior for Pullout Tests on Steel Sheet Inclusions	242
6.17	Measured Pullout Load-Displacement Response for Nylon 6/6 Reinforcements	243
6.18	Pullout Measurements from Test APSR 51	244
6.19	Pullout Measurements from Test APSR 57	245
6.20a	Pullout Measurements from Test APSR 59	246
6.20b	Pullout Measurements from Test APSR 59	247
6.20c	Stability of Residual Pullout Behavior	248
6.20d	Detail of Stick-Slip Behavior in Pullout Test APSR 59	249
6.21	Tensile Stress Distribution in Pullout Tests on Nylon 6/6 Inclusions	249
6.22	Interpreted Load-Elongation Behavior for Pullout Tests on Nylon 6/6 Inclusions	250

6.23	Measurements of Sand-MDPE Interface Friction. (after O'Rourke et al., 1990)	251
6.24	Comparison of Predicted and Measured Load-Elongation Response for Steel Sheet Inclusions	252
6.25	Comparison of Predicted and Measured Tensile Stress Distribution for Pullout Tests on Steel Sheet Inclusions	253
6.26	Comparison of Predicted and Measured Load-Elongation Response for Nylon 6/6 Inclusions	254
6.27	Comparison of Predicted and Measured Tensile Stress Distribution for Pullout Tests on Steel Sheet Inclusions	255
6.28	Evaluation of Soil Failure Conditions for Pullout Tests in Dense Ticino Sand	256
7.1	Approach for the Solution of Reinforced Wall Using the Shear-Lag Analysis	272

Chapter 1: Introduction

Techniques of earth reinforcement have been used since as early as 3000 BC, in ancient oriental regions. Typical reinforcing materials used at that time included plaited reeds treated with bitumen (Middle East countries) and bamboo (India and Japan), with the purpose of reinforcing embankments and retaining walls. Modern soil reinforcement was introduced in 1966, when Vidal patented a system of retaining wall construction known as "terre armée" (reinforced earth). The original method uses flat steel strips laid in the soil backfill to produce a composite material which reduces the lateral pressure against the wall face. In current practice, planar inclusions such as steel strips, arrays of fibers and geosynthetics (ranging from woven and non-woven fabrics to high strength polymer grids) are widely used to reinforce soil masses in the construction of retaining walls, embankments, foundations and pavements. The performance of these composite soil structures depends, in large part, on the interaction between the soil matrix and reinforcing inclusions, which determine the magnitude of loads carried by the reinforcements. The mechanisms of interaction are particularly complex for inclusions with non-planar geometry such as grids, and for materials such as geosynthetics, which exhibit non-linear and time dependent behavior. Lee (1978) states that soil-reinforcement interaction is 'one of the most fundamentally important but least understood aspects of soil reinforcement'.

This thesis describes the formulation and evaluation of approximate closed-form solutions for estimating the load-transfer between soil and planar reinforcements in three fundamental modes of interaction (Table 1.1): 1) plane strain compression, with reinforcement parallel to minor principal stress direction; 2) effects of inclusion orientation

and principal stress directions in the soil; and 3) pullout of a planar extensible reinforcement.

Chapter 2 introduces an approximate analytical method for estimating the tensile stresses in a single planar reinforcement due to shearing of the surrounding soil matrix. The analysis expresses reinforcement stresses as closed form functions of the inclusion geometry, elastic properties of the constituent materials (i.e., soil matrix and reinforcement) and interface friction. The proposed formulation adapts the techniques of shear-lag analysis, introduced by Cox (1952) and commonly used in the mechanics of fiber reinforced composites. The essence of shear-lag analyses is to assume a simplified deformation field within the matrix, such that tensile stresses in the inclusion can be solved from equilibrium considerations. Comparisons with numerical finite element calculations demonstrate the accuracy of the analytical solutions for a wide range of practical geometric and material properties. The proposed formulation provides a simple and direct method for estimating the stress distribution within reinforced soil masses at working load conditions.

Chapter 3 describes the application of the proposed shear-lag analysis for interpreting measurements of tensile stresses in steel sheet reinforcements obtained by Larson (1992). The measurements were made in a new laboratory device referred to as the Automated Plane Strain Reinforcement (APSR) cell, which is capable of measuring the tensile force transferred to a planar reinforcing inclusion due to plane strain shearing of the surrounding soil matrix. Larson (1992) reports measurements for steel sheet reinforcements of various length embedded in specimens of dense and loose Ticino sand. Input parameters for the shear-lag analysis are based on measurements for the unreinforced sand. The proposed analysis provides a useful framework for extrapolating the results of small scale laboratory tests to dimensions which are typical of field situations.

Chapter 4 presents generalizations of the basic shear-lag analysis in order to describe the load transfer for planar reinforcements sheared within a soil element at

arbitrary orientation and principal stress directions. The analyses show clearly the range of orientations and stress directions for which the inclusion carry tensile loads and, hence, develop effective reinforcement of the soil. The analyses are used to interpret measurements of soil-reinforcement interaction in laboratory plane strain compression and direct shear box tests reported in the literature.

In contrast to these basic studies of soil-reinforcement interaction, pullout tests are widely used in practice for estimating the bond capacity in design calculations based on limit equilibrium analyses. For planar reinforcements, the 'bond' is controlled by interface friction; however, none of the existing interpretations have clarified the important role of inclusion extensibility on pullout performance. Chapter 5 describes a new shear-lag analysis which describes the complete load-transfer mechanisms for an elastic reinforcement linked through a frictional interface to an elastic soil matrix. The analyses show that non-uniformities in the shear resistance can be related to stress concentrations in the soil. These results show important limitations in applying limit equilibrium calculations for interpreting pullout measurements on extensible reinforcements.

Chapter 6 describes results of an experimental program of pullout tests performed on instrumented inclusions in the APSR cell. Measurements of tensile stress distribution were obtained for two elastic materials of widely different stiffness (steel and nylon 6/6) in order to evaluate the shear-lag predictions described in Chapter 5. Detailed comparisons between the predictions and measurements show the capability of the proposed shear-lag analysis.

Chapter 7 summarizes the main results of the thesis and proposes further applications of shear-lag analysis for other geotechnical problems.

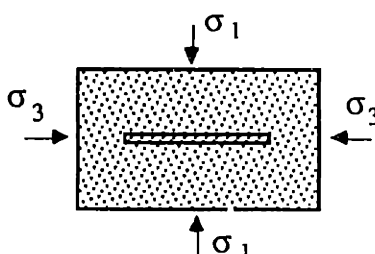
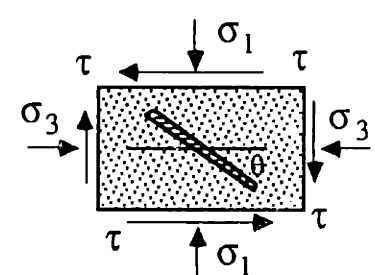
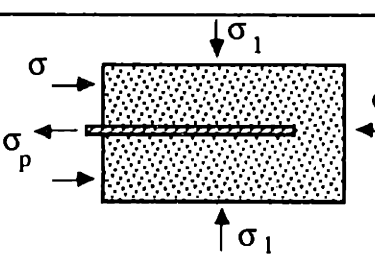
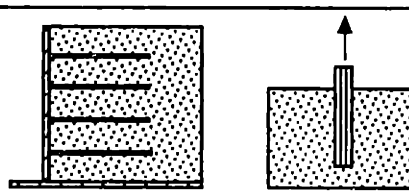
Model	Chapter	Subject
	1	• Introduction
	2	<ul style="list-style-type: none"> • Shear-Lag Analysis of a Planar Soil Composite in Plane Strain Compression • Numerical Verification
	3	• Interpretation of APSR Tests Results Using the Shear-Lag Analysis
	4a	<ul style="list-style-type: none"> • Effects of Inclusion Orientation and External Stresses on the Behavior of a Planar Soil Composite • Numerical Verification
	4b	• Interpretation of Reinforced Plane Strain and Direct Shear Test Results Available in the Literature
	5	• Shear-Lag Analysis of Pullout Tests of Planar Inclusions
	6	• Experimental Verification: Pullout Tests on Planar Inclusions in the APSR Cell
 <p>Walls Pile</p>	7	<ul style="list-style-type: none"> • Application of Shear-Lag Solutions for: <ul style="list-style-type: none"> a) Analysis of Reinforced Walls b) Pullout Behavior of Piles

Table 1.1: Thesis Outline.

Appendix 1.A: References

- Cox, H. L. (1952) "The Elasticity and Strength of Paper and Other Fibrous Materials", *British Journal of Applied Physics*, 3, 72-79.
- Larson, D. G. (1992) " A Laboratory Investigation of Load Transfer in Reinforced Soil", PhD Thesis, MIT, Cambridge, MA.
- Lee, K.L. (1978) "Mechanisms, Analysis, and Design of Reinforced Earth: State-of-the-Art Report", *Proc. Symposium on Earth Reinforcement*, ASCE, Pittsburgh, 62-76.
- Vidal, H. (1966) "La Terre Armée", *Annales de l'Institut Techniques des Bâtiments et des Travaux Publiques*, Paris, 888-938.

Chapter 2: Shear-Lag Analysis of a Planar Soil Reinforcement in Plane Strain Compression

2.1. Introduction

Planar inclusions, such as steel strips, arrays of fibers, geosynthetic fabrics and grids, are widely used to reinforce soil masses in the construction of retaining walls, embankments, foundations and pavements (Jones, 1988). The performance of these composite soil structures depends, in large part, on the interaction between the soil matrix and reinforcing inclusions, which determine the magnitude of loads carried by the reinforcements. The analysis of these load transfer mechanisms must address many complex factors such as: a) non-linear, inelastic constitutive behavior of soils (especially compacted earthfill); b) time dependent behavior of geosynthetic reinforcing materials (e.g. Allen, 1991); and c) non-linear and frictional properties of the reinforcement-soil interface.

There are three basic approaches used in existing studies of soil-reinforcement interaction 1) homogenization methods, 2) limit equilibrium calculations, and 3) explicit modelling of the soil matrix and reinforcing inclusions. Homogenization methods typically assume that the soil is reinforced with closely spaced inclusions (periodically heterogeneous) and behaves, at the 'macroscopic level', as a homogeneous, anisotropic composite material. For example, Harrison & Gerrard (1972) derive equivalent elastic moduli for a linear, isotropic soil, reinforced with thin, stiff, elastic layers; while DeBuhan et al. (1989) perform collapse calculations using an anisotropic shear strength criterion, mobilizing the frictional failure of sand together with tensile yield of the reinforcements. Homogenization has also been used to estimate reinforcement stresses by equating tensile

strains in the reinforcement with soil strains acting in the same direction. This 'strain compatibility' approach has been used in finite element simulations of reinforced earth as a composite material (Romstad et al., 1976), and in the formulation of non-linear, constitutive models (Juran et al., 1988). Although homogenization greatly simplifies the representation of soil-reinforcement interaction, the importance of inclusion spacing and strain approximations require further evaluation.

Current design methods for reinforced soil masses are based primarily on limit equilibrium analyses (e.g., Jarrett & McGown, 1987; Leshchinsky & Boedeker, 1989; Jewell, 1990). These calculations consider the reaction of the inclusions to postulated failure mechanisms within the reinforced soil. Stability of the structure is maintained either: a) through sliding resistance along the soil-reinforcement interface; or b) through tensile (and bending) stresses generated in the reinforcement, which are resisted by a bond or anchor length embedded in the stable soil mass (i.e., pullout mode). Limit equilibrium calculations are not reliable for estimating the magnitude and distribution of reinforcement stresses at working load conditions.

In principle, comprehensive stress analyses for reinforced soil masses can be achieved using non-linear finite element (or boundary element) methods which model explicitly the constitutive properties of the soil, reinforcement and interfaces. These analyses offer great flexibility for simulating complex problem geometries, construction histories, etc. However, it is difficult to interpret the underlying mechanisms controlling soil-reinforcement interaction from complex numerical analyses.

This chapter describes an approximate analytical method for estimating the tensile stresses in a single planar reinforcement due to shearing of the surrounding soil matrix (Abramanto & Whittle, 1993). The analysis expresses reinforcement stresses as closed form functions of the inclusion geometry, elastic properties of the constituent materials

(i.e., soil matrix and reinforcement) and interface friction, and hence provides physical insight into the mechanism of load-transfer in reinforced soils.

The proposed formulation adapts the techniques of shear-lag analysis (Cox, 1952; Kuhn, 1956) which are commonly used in the mechanics of fiber reinforced composites (e.g., Tyson & Davies, 1965; Amirbayat & Hearle, 1969; Aveston & Kelly, 1973; Piggott, 1980; Budiansky et al., 1986). The essence of shear lag analyses is to assume a simplified deformation field within the matrix, such that tensile stresses in the inclusion σ_{xx}^f can be solved from equilibrium considerations:

$$\frac{d\sigma_{xx}^f}{dx} = \frac{2}{f} \sigma_{xy}^i = \alpha (u - v) \quad (2.1)$$

where f is the thickness of the fiber/inclusion (planar geometry). The coefficient of proportionality α relates the shear stresses at the interface, σ_{xy}^i , to the axial displacements at the same location, for situations with and without the inclusion (u , v , respectively). There are several different definitions of u , v and α reported in the literature; the derivation presented in this paper follows the assumptions used by Budiansky et al (1986). Existing shear-lag formulations consider axisymmetric geometries (fiber embedded in a cylindrical matrix) under uniaxial tension. In contrast, the proposed formulation considers a plane strain geometry and represents the first adaptation of shear-lag analyses for compressive stresses in the (soil) matrix.

The analyses assume that the soil and reinforcement behave as linear, isotropic and elastic materials, linked through a frictional interface. Closed form solutions are presented for the axial reinforcement stress and interface tractions as functions of the material properties and inclusion geometry. Comparisons with numerical finite element calculations demonstrate the accuracy of the analytical solutions for a wide range of practical geometric and material properties. The proposed formulation provides a simple and direct method for estimating the stress distribution within reinforced soil masses at working load conditions.

2.2. Shear-Lag Formulation

Figure 2.1 shows the idealized geometry for a composite plane strain element of reinforced soil considered in the proposed analysis. The element comprises a planar inclusion of thickness, f , and length, L , embedded in a soil matrix of overall height, $m+f$ (corresponding to the typical inclusion spacing). The orientation of the inclusion is parallel to the minor, external, principal stress acting on the soil matrix, σ_3 . The soil is sheared in a plane strain compression mode by increasing the major principal stress, σ_1 , at the boundary of the element (with σ_3 constant). For these loading conditions, the inclusion reduces the lateral tensile strains which would otherwise develop in the soil, and hence represents the optimal orientation for a planar tensile reinforcement.

Even for this simple geometry, complete analytical solutions are difficult to achieve. The following stresses must be determined: a) axial stresses in the inclusion (σ_{xx}^f); b) shear (σ_{xy}^i) and normal (σ_{yy}^i) stresses along the inclusion-matrix interface; and c) axial (σ_{xx}^m), normal (σ_{yy}^m) and shear (σ_{xy}^m) stresses within the soil matrix. The proposed analysis assumes the following:

1. The soil matrix and reinforcement behave as linear, isotropic and elastic materials (with properties G_m , ν_m and E_f , ν_f , respectively, Fig. 2.1).
2. The soil matrix and reinforcing inclusion are linked through a frictional interface (δ ; Fig. 2.1). The effects of interface slippage are considered in a subsequent section.
3. There is no axial stress acting at the ends of the inclusion, (i.e. $\sigma_{xx}^f=0$ at $x=0, L$) as the inclusion is thin and is not physically bonded to the soil matrix.
4. The axial stresses in the soil matrix and in the inclusion are functions of x only, i.e., $\sigma_{xx}^m(x)$, $\sigma_{xx}^f(x)$. This implies that σ_{xx}^m is the average stress acting in the soil matrix (for $|y-f/2| \leq m/2$). Thus, the horizontal stresses in the inclusion and the soil can be related by:

$$\bar{\sigma}_{xx}^m = \sigma_{xx}^m = a \sigma_{xx}^f + \sigma_3 (1 + a) \quad (2.2)$$

and hence,

$$\frac{d\sigma_{xx}^m}{dx} = a \frac{d\sigma_{xx}^f}{dx} \quad (2.2a)$$

where $a=f/m$ is the 'inclusion ratio'. The sign convention (Fig. 2.1) assumes that compressive stresses are positive in the soil matrix; while the inclusion stress, σ_{xx}^f , is positive in tension.

Neglecting body forces, the equilibrium equations in the soil matrix and inclusion can be written:

$$\frac{\partial \sigma_{xx}^m}{\partial x} + \frac{\partial \sigma_{xy}^m}{\partial y} = 0 \quad (2.3a)$$

$$\frac{\partial \sigma_{xy}^m}{\partial x} + \frac{\partial \sigma_{yy}^m}{\partial y} = 0 \quad (2.3b)$$

$$\frac{d\sigma_{xx}^f}{dx} - \frac{2}{f} \sigma_{xy}^i = 0 \quad (2.3c)$$

with boundary conditions:

$$\begin{aligned} x = 0, L ; \quad \left| y - \frac{f}{2} \right| \leq \frac{m}{2} & : \quad \sigma_{xx}^m = \sigma_3 \\ 0 \leq x \leq L ; \quad \left| y - \frac{f}{2} \right| = 0 & : \quad \sigma_{xy}^m = \sigma_{xy}^i \text{ and } \sigma_{yy}^m = \sigma_{yy}^i \\ 0 \leq x \leq L ; \quad \left| y - \frac{f}{2} \right| = \frac{m}{2} & : \quad \sigma_{xy}^m = 0 \text{ and } \sigma_{yy}^m = \sigma_1 \end{aligned} \quad (2.4)$$

Equations 2.2, 2.3 and 2.4 can be used to determine distributions of the shear and normal stress components in the soil matrix as functions of the boundary tractions:

$$\sigma_{xy}^m = \sigma_{xy}^i \left[1 - a \left(\frac{2y}{f} - 1 \right) \right] \quad (2.5a)$$

$$\sigma_{yy}^m = \sigma_{yy}^i + \frac{4}{m} (\sigma_1 - \sigma_{yy}^i) \left[y^2 \left(-\frac{1}{m} \right) + y (1 + a) \cdot \frac{f}{2} \left(1 + \frac{a}{2} \right) \right] \quad (2.5b)$$

In these expressions, σ_{xy}^m is a linear function of y , while σ_{yy}^m varies parabolically.

Equilibrium conditions (eqns. 2.2, 2.3 and 2.4) also impose the following conditions which relate the interface tractions to the axial stress in the inclusion:

$$\sigma_{yy}^i = \sigma_1 + \frac{m}{4} \frac{d\sigma_{xy}^i}{dx} = \sigma_1 + \frac{mf}{8} \frac{d^2\sigma_{xx}^f}{dx^2} \quad (2.6)$$

In order to apply the shear lag formulation, it is necessary to relate stresses and strains in the direction of the inclusion. This can be accomplished by decoupling the normal and shear stresses acting in the soil matrix (similar to the 'substitute single stringer' method used by Kuhn, 1956). Decoupling subdivides the soil matrix into two zones (Fig. 2.2): 1) an inner 'shear spring' layer of lateral dimension \bar{m} , adjacent to the inclusion, in which only shear stresses occur; and 2) an outer layer, having the same lateral dimension as the physical model (i.e., m), with normal stresses acting in the x and y directions. The following assumptions are used to obtain average stresses in the inner and outer zones:

1. For the inner layer, the shear stresses are equated with the interface shear tractions (i.e., $\bar{\sigma}_{xy}^m = \sigma_{xy}^i$). The lateral dimension of the shear spring layer, \bar{m} , is then determined by equating the elastic shear strain energy in the physical (real) and decoupled models (after Budiansky et al., 1986). For the plane strain geometry, Appendix 1.A shows that $\bar{m} = m/3$.
2. In the outer layer, the axial stress, $\bar{\sigma}_{xx}^m$, is the same for both real and decoupled geometries (eqn. 2.2); while the average normal stress $\bar{\sigma}_{yy}^m$ is obtained by considering statically equivalent forces in the two systems (Appendix 1.A):

$$\bar{\sigma}_{yy}^m = \frac{2}{3} \sigma_1 + \frac{1}{3} \sigma_{yy}^i \quad (2.7)$$

Shear stresses in the inner layer relate the interface tractions to axial displacements in the soil matrix, u_x , as follows:

$$\sigma_{xy}^i = \bar{\sigma}_{xy}^m = G_m \frac{du_x}{dy} = -G_m \frac{2}{\bar{m}} (u_x^{\bar{m}} - u_x^i) \quad (2.8)$$

where u_x^i , u_x^m are the axial displacements at the inclusion-soil and inner-outer zone interfaces, respectively (Fig. 2.2). Equation 2.8 expresses the shear lag approximation for the proposed analysis (cf. eqn. 2.1). The axial strains at the same two locations can be estimated directly from the assumed elastic properties of the soil and reinforcement:

$$\epsilon_{xx}^m = \frac{du_x^m}{dx} = \frac{1 + \nu_m}{E_m} [(1 - \nu_m) \sigma_{xx}^m - \nu_m \sigma_{yy}^m] \quad (2.9a)$$

$$\epsilon_{xx}^i = \frac{du_x^i}{dx} = \frac{1 + \nu_f}{E_f} [-(1 - \nu_f) \sigma_{xx}^f - \nu_f \sigma_{yy}^i] \quad (2.9b)$$

By combining equations 2.2, 2.6, 2.7 and 2.9, the axial stress in the inclusion can be expressed by the following ordinary differential equation:

$$\frac{d^2 \sigma_{xx}^f}{dx^2} - K_1 \sigma_{xx}^f + K_2 \sigma = 0 \quad (2.10)$$

where:

$$K_2 \sigma = K_2^1 \sigma_1 + K_2^3 \sigma_3 \quad (2.10a)$$

and K_1 , K_2^1 , K_2^3 are constants defined in terms of the material properties and geometry:

$$K_1 = \frac{6}{mf} \frac{\left[(1 - \nu_m) a + 2 \frac{G_m}{E_f} (1 + \nu_f) (1 - \nu_f) \right]}{\left[1 + \frac{1}{4} \nu_m - \frac{3}{2} \frac{G_m}{E_f} (1 + \nu_f) \nu_f \right]} \quad (2.11a)$$

$$K_2^1 = \frac{6}{mf} \frac{\left[\nu_m - 2 \frac{G_m}{E_f} (1 + \nu_f) \nu_f \right]}{\left[1 + \frac{1}{4} \nu_m - \frac{3}{2} \frac{G_m}{E_f} (1 + \nu_f) \nu_f \right]} \quad (2.11b)$$

$$K_2^3 = -\frac{6}{mf} \frac{(1 - \nu_m) (1 + a)}{\left[1 + \frac{1}{4} \nu_m - \frac{3}{2} \frac{G_m}{E_f} (1 + \nu_f) \nu_f \right]} \quad (2.11c)$$

The axial stress reaches a maximum value at the center of the inclusion, due to symmetry, and hence the boundary conditions can be written:

$$\begin{aligned}
x = 0, L & \quad ; \quad \sigma_{xx}^f = 0 \\
x = L/2 & \quad ; \quad \frac{d\sigma_{xx}^f}{dx} = 0
\end{aligned}
\tag{2.12}$$

Hence, the general solution for the axial stress in the reinforcement can be obtained directly from equations 2.10 and 2.12:

$$\sigma_{xx}^f = \frac{K_2 \sigma}{K_1} \left[1 - \frac{\cosh \sqrt{K_1} \left(\frac{L}{2} - x \right)}{\cosh \sqrt{K_1} \frac{L}{2}} \right]
\tag{2.13}$$

The maximum axial stress at the center of the inclusion is then:

$$\sigma_{xx}^f (L/2) = \sigma_{\max}^f = \frac{K_2 \sigma}{K_1} \left[1 - \operatorname{sech} \sqrt{K_1} \frac{L}{2} \right]
\tag{2.13a}$$

for a very long inclusion ($L \rightarrow \infty$) this becomes:

$$\sigma_{xx}^f (\infty) = \sigma_{\infty}^f = \frac{K_2 \sigma}{K_1}
\tag{2.13b}$$

Similar expressions can then be derived for the interface tractions (eqn. 2.6):

$$\sigma_{xy}^i = \frac{f}{2} \frac{K_2 \sigma}{K_1} \sqrt{K_1} \left[\frac{\sinh \sqrt{K_1} \left(\frac{L}{2} - x \right)}{\cosh \sqrt{K_1} \frac{L}{2}} \right]
\tag{2.14a}$$

$$\sigma_{yy}^i = \sigma_1 - \frac{mf}{8} K_2 \sigma \left[\frac{\cosh \sqrt{K_1} \left(\frac{L}{2} - x \right)}{\cosh \sqrt{K_1} \frac{L}{2}} \right]
\tag{2.14b}$$

2.3 Comparison with Finite Element Solutions

One method for evaluating the proposed analysis is to compare the closed form expressions for axial inclusion stresses (eqn. 2.13) with numerical results from finite element analyses. Finite element calculations have been performed (using the ABAQUS code) assuming that the inclusion is fully bonded to the soil matrix. In this case, differences between the analytical and the numerical solutions should only be significant in the

vicinity of the tip of the inclusion (i.e., $x \rightarrow 0$). In the shear lag analysis, the tip of the inclusion is not physically attached to the matrix and hence, the axial stress is always zero at this point. This boundary condition represents realistically the behavior for a thin planar reinforcement. In contrast, the tip stress is always non-zero in elastic finite element calculations as the inclusion is completely bonded to the matrix. Separation at the tip of the inclusion can be achieved using special interface or gap elements. However, these elements introduce non-linearities in the finite element solution, and hence generate additional uncertainties in comparing results at the tip of the inclusion.

Table 2.1 compares predictions of the maximum axial stress at the center of the inclusion, $\sigma_{\max}^f (= \sigma_{xx}^f(L/2)$; eqn. 2.13a) with values computed from finite element analyses. The results show that, for a wide range of material properties, geometry and external stresses, the proposed shear lag analyses match the finite element solutions within 5%. These results support the use of the shear lag analysis as a method of estimating load transfer for the simple problem geometry described above (Fig. 2.1). Chapter 3 presents results of experimental verification through comparisons with well controlled laboratory tests (APSR cell).

2.4. Results

2.4.1. Stresses Along Inclusion

The proposed shear lag analysis derives the axial inclusion stress (σ_{xx}^f) and interface tractions (σ_{xy}^i , σ_{yy}^i) as linear functions of the exterior soil stresses (σ_1 , σ_3). The load-transfer is affected by both material properties (E_f/G_m , ν_f , ν_m) and geometry (f , m , L). Figure 2.3 presents distributions of σ_{xx}^f , σ_{xy}^i , and σ_{yy}^i (normalized by the major principal stress, σ_1), for inclusions with half lengths, $L/2=0.25$, 0.5 and 1.5 m, at an external stress ratio, $\sigma_1/\sigma_3=6$. The calculations assume typical/representative values for the material

properties, spacing and thickness of reinforcement (Fig. 2.3). The results show the following:

1. There are two distinct regions which characterize the soil-reinforcement interaction: I) the zone close to the tip of the inclusion, in which the axial stress (σ_{xx}^f) accumulates ('builds up'), due to the development of interface shear stresses (σ_{xy}^i); and II) the zone of constant axial inclusion stress (i.e., $\sigma_{xx}^f \rightarrow \sigma_{xx}^f$) where there are no shear tractions at the soil-reinforcement interface. These two regions are fully developed for 'long' inclusions (e.g., $L/2=1.5\text{m}$; Fig. 2.3). However, for short inclusions ($L/2=0.25, 0.5\text{m}$; Fig. 2.3), maximum load transfer is not achieved, and there are gradients of the interface shear tractions occurring at the center of the inclusion (i.e., $d\sigma_{xy}^i/dx < 0$ at $2x/L=1$).
2. The shear lag parameter, K_1 (eqn. 2.11a) controls the distribution of axial stress in the inclusion (Fig. 2.3a) in zone I, while the ratio, $K_2\sigma/K_1$ determines the maximum load transfer in zone II (eqn. 2.13b).
3. Maximum interface shear tractions occur at the tip of the inclusion (Fig. 2.3b), while $\sigma_{xy}^i=0$ at $2x/L=1$ due to symmetry. The proposed analysis also relates the normal traction, σ_{yy}^i , to the gradient of interface shear stress (eqn. 2.6). Figure 2.3c shows that $\sigma_{yy}^i/\sigma_1 < 1$ throughout zone I and reaches a minimum value at the tip of the inclusion. The ratio $\sigma_{xy}^i/\sigma_{yy}^i$ corresponds to the mobilized friction and is discussed in more length in the next section. In zone II, $\sigma_{xy}^i=0$ and $\sigma_{yy}^i = \sigma_1$, hence no rotations of principal stresses take place in the surrounding soil matrix.

2.4.2. "Pickup" Curves

The 'maximum load transfer ratio', $\sigma_{\max}^f/\sigma_{\infty}^f$ (eqns. 2.13a, b) is a convenient parameter for characterizing the length of reinforcement which mobilizes maximum axial stresses in the inclusion L_1 (i.e., the length of zone I). The principal factors affecting

$\sigma_{\max}^f/\sigma_{\infty}^f$ are the stiffness ratio, E_f/G_m , spacing and thickness of reinforcement (m, f). Figure 2.4 shows the maximum load transfer ratio as a function of the inclusion length and stiffness ratio of typical soil reinforcements, $10^2 \leq E_f/G_m \leq 10^5$. The pickup length ranges from $L_I = 0.8\text{m}$ for a soft inclusion ($E_f/G_m=10^2$) up to 3.2m for stiff reinforcements. The stiffness ratio also affects significantly the load transfer for short inclusions ($L < L_I$, zone I behavior only). These results have important practical implications for the design and interpretation of small scale laboratory tests on reinforced soils (e.g., Whittle et al., 1992).

2.4.3. Definition of Short Reinforcements

Figures 2.5a,b summarizes reference values of L_I , defined at $\sigma_{\max}^f/\sigma_{\infty}^f=0.95$, for combinations of material properties and geometry. The pick-up length increases with stiffness ratio, E_f/G_m , Poisson's ratio in the soil, ν_m , inclusion thickness, f , and spacing, m . For closely spaced reinforcements ($m=0.2\text{m}$; Fig. 2.5a), full load transfer can develop for $L_I \leq 0.6\text{m}$, while widely spaced, stiff reinforcements ($m=2.0\text{m}$, $E_f/G_m > 10^4$; Fig. 2.5b) accumulate axial stress for lengths, $L_I > 6\text{m}$. The inclusion thickness affects load transfer mainly for low stiffness ratios ($E_f/G_m \leq 10^3$), while ν_m is only significant for stiff reinforcements ($E_f/G_m \geq 10^4$).

2.4.4. Stress Distribution due to Shearing of Soil Mass

Figure 2.6 shows the development of axial inclusion stress and interface tractions due to shearing of the soil matrix, for a short inclusion with $L=1.0\text{m}$. The external stress ratio, σ_1/σ_3 , represents the level of shear stress existing in the soil matrix. For a soil matrix with linear, isotropic properties, the ratio $\sigma_1/\sigma_3 = (1-\nu_m)/\nu_m = 1/K_0 = 2.33$ corresponds to one-dimensional deformation of the unreinforced soil matrix (i.e., $\epsilon_{xx} = 0$). In this case, there is no load transfer to the reinforcement and hence, $\sigma_{xx}^f = \sigma_{xy}^f = 0$, $\sigma_{yy}^f = \sigma_1$. For external stress ratios, $\sigma_1/\sigma_3 < 1/K_0$, lateral compression of the soil matrix generates compressive stresses in the inclusion, which are not of practical interest for thin planar reinforcements.

However, as the level of external shear stress increases (either due to an increase in the vertical stress σ_1 or a reduction in the lateral stress σ_3), significant tensile stresses develop in the reinforcement (cf., Fig. 2.3). There are two important limitations on the interpretation of results in figure 2.6:

1. For drained shearing of cohesionless soils (e.g. good quality granular fills), the shear strength is most commonly described by a Mohr-Coulomb failure criterion with friction angle $\sin\phi = (\sigma_1 - \sigma_3) / (\sigma_1 + \sigma_3)$. Ladd et al. (1977) report $35^\circ \leq \phi \leq 57^\circ$ (i.e., $3.7 \leq \sigma_1/\sigma_3 \leq 11.7$) for typical sands sheared in plane strain compression. Thus, local failure will initiate in the matrix (at locations close to the tip of the inclusion) when the stress ratio mobilizes the frictional strength of the soil.
2. The linear, isotropic model of soil behavior does not describe accurately the volumetric response of cohesionless soils in drained shearing. Extensive observations show that sands dilate when the mobilized friction exceeds a threshold value, $\phi_{cv} = 35^\circ$ to 45° ($\sigma_1/\sigma_3 = 3.7$ to 5.8) (Bolton, 1986; Larson, 1992). The practical implication of this behavior is that the proposed analysis will tend to underestimate both the lateral strains occurring in the soil matrix (especially for $\sigma_1/\sigma_3 \geq 6$) and the tensile stresses in the reinforcement at a given stress ratio σ_1/σ_3 .

2.4.5. Maximum Tensile Stresses in Long Inclusions

These aspects of soil behavior do not affect significantly the interpretation of load transfer for long inclusions (zone II behavior). Figure 2.7 summarizes maximum tensile stresses, σ_f^t/σ_3 , as a function of the external stress ratio for ranges of material properties E_f/G_m , v_m , and the reinforcement volume ratio, f/m . The results show the following:

1. The reinforcement stress increases significantly with the stiffness ratio, E_f/G_m . However, close spacing of reinforcing layers (high f/m ; Fig. 2.7b) reduces the benefits

of high stiffness ratios. For example, calculations for a volume ratio, $a=0.02$ (Fig. 2.7b), show similar load transfer behavior for reinforcements with $E_f/G_m=10^3, 10^4$.

2. As v_m increases from 0.3 to 0.5 (constant volume shearing), the reinforcement stress increases by a factor of 2 to 3 (Fig. 2.7a). This behavior confirms the underlying mechanism whereby tensile stresses in the reinforcement counteract lateral straining of the soil matrix.

2.4.6. The Reinforcing Effect

The results in figure 2.7 also provide a basis for quantifying the reinforcing effect of the inclusion on the soil matrix. Equation 2.2 relates the average lateral stress, $\bar{\sigma}_{xx}^m$, in the soil matrix, to the external lateral stress, σ_3 , and the reinforcement stress, $\sigma_{xx}^f \rightarrow \sigma_\infty^f$. Thus, the mobilized stress ratio within the reinforced soil matrix, $\sigma_1/\bar{\sigma}_{xx}^m$, can be written:

$$\frac{\sigma_1}{\bar{\sigma}_{xx}^m} = \left(\frac{\sigma_1}{\sigma_3} \right) \left[1 + a \left(1 + \frac{\sigma_\infty^f}{\sigma_3} \right) \right]^{-1} \quad (2.15)$$

where values of σ_∞^f/σ_3 are given in figure 2.7, and $a=f/m$.

Table 2.2 compares the effectiveness of the reinforcement for five examples at an external stress ratio, $\sigma_1/\sigma_3=6$ (Fig. 2.7):

1. In all cases, the reinforcement reduces the mobilized stress ratio in the soil (i.e., $\sigma_1/\bar{\sigma}_{xx}^m < 6$); and is highly effective in three cases (2, 3, 4; Fig. 2.7) for which $\sigma_1/\bar{\sigma}_{xx}^m \rightarrow 1/K_0$.
2. A comparison of the results in Table 2.2 shows that reinforcement effectiveness: a) increases with the stiffness ratio, E_f/G_m ; b) is unaffected by v_m ; and c) increases with the volume ratio of the reinforcement, f/m .

2.5 Extension of Solution for Slipping Frictional Interface

2.5.1. Frictional Sliding along Interface

The preceding shear lag analysis assumes that there is no slip between the soil matrix and the reinforcing inclusion. However, the results (e.g., Figs. 2.4, 2.6) indicate that frictional sliding is possible at locations close to the tip where maximum values of $\sigma_{xy}^i/\sigma_{yy}^i$ occur. The analysis can be readily modified to account for interface sliding by imposing the following constraint:

$$\frac{\sigma_{xy}^i}{\sigma_{yy}^i} \leq \mu = \tan \delta \quad (2.16a)$$

where μ is the interface friction coefficient, and δ is the angle of interface friction. Extensive experimental data for interface friction between sands and various construction materials in direct shear box (e.g., Potyondy, 1961) and simple shear tests (e.g., Uesugi & Kishida, 1986) show typical values, $\mu=0.2$ to 0.7 ($\delta=10^\circ$ to 35°).

The minimum friction coefficient, μ_{crit} , necessary to prevent slippage at the interface can be determined imposing $\sigma_{xy}^i/\sigma_{yy}^i=\mu_{crit}$ at $x=0$. From equations 2.14a, b:

$$\mu_{crit} = \frac{\tanh \sqrt{K_1} L/2}{\sqrt{K_1} \left(\frac{2}{f} \frac{\sigma_1}{K_2 \sigma} - \frac{m}{4} \right)} \quad (2.16b)$$

For combinations of soil and reinforcement with $\mu \geq \mu_{crit}$, interface friction has no effect on the load-transfer analysis described above. Maximum values of μ_{crit} arise for long, stiff inclusions ($L/2 \rightarrow \infty$, $E_f/G_m \rightarrow \infty$) for which equation 2.16b can be simplified to:

$$\mu_{crit} = \left[\frac{(4 + \nu_m)}{24(1 - \nu_m)} \right]^{1/2} \left[\frac{(4 + \nu_m)}{12} \frac{1}{\nu_m - (1 - \nu_m)(1 + a) \frac{\sigma_3}{\sigma_1}} - \frac{1}{4} \right]^{-1} \quad (2.16c)$$

Figure 2.8 shows that magnitudes of μ_{crit} for long, stiff inclusions depend primarily on the Poisson's ratio, ν_m , and on the external stress ratio, σ_1/σ_3 (i.e., μ_{crit} depends on lateral strains in the soil matrix). The results suggest that for many practical situations of interest ($\nu_m > 0.3$, $\sigma_1/\sigma_3 \geq 5$), μ_{crit} will exceed the frictional resistance which can be mobilized at the soil-reinforcement interface. In this case, interface sliding must be included in the shear lag analysis.

2.5.2. Modified Formulation for Slipping Interface

Interface sliding occurs when $\sigma_{xy}^i/\sigma_{yy}^i = \mu$. In this case, the equilibrium conditions (eqns. 2.3c, 2.6) can be combined directly to estimate the axial stress in the inclusion:

$$\frac{d^2\sigma_{xx}^{fd}}{dx^2} - \frac{4}{\mu m} \frac{d\sigma_{xx}^{fd}}{dx} + \frac{8}{m f} \sigma_1 = 0 \quad (2.17)$$

where σ_{xx}^{fd} is the axial stress in the 'debonded' region. Equation 2.17 can be solved directly by defining the debonded length, x_d (where $0 \leq x_d \leq L/2$), at which the 'transition' axial stress is σ_t (i.e., at $x=x_d$). The axial stress and interface tractions in the debonded region ($0 \leq x \leq x_d$) are:

$$\sigma_{xx}^{fd} = \frac{2\mu\sigma_1}{f} x + \left[\frac{\sigma_t - \frac{2\mu\sigma_1}{f} x_d}{\exp\left(\frac{4}{m\mu} x_d\right) - 1} \right] \left[\exp\left(\frac{4}{m\mu} x\right) - 1 \right] \quad (2.18a)$$

$$\sigma_{xy}^{id} = \mu \sigma_1 + \left[\frac{\sigma_t - \frac{2\mu\sigma_1}{f} x_d}{\exp\left(\frac{4}{m\mu} x_d\right) - 1} \right] \frac{2}{a \mu} \exp\left(\frac{4}{m\mu} x\right) \quad (2.18b)$$

$$\sigma_{yy}^{id} = \frac{\sigma_{xy}^{id}}{\mu} \quad (2.18c)$$

Modified solutions for the axial stress and interface tractions in the bonded (no slip) region, $x_d \leq x \leq L/2$, are obtained by re-solving equation 2.10, with boundary conditions $\sigma_{xx}^f = \sigma_t$ at $x = x_d$ and $d\sigma_{xx}^f/dx = 0$ at $x = L/2$:

$$\sigma_{xx}^f = \left(\sigma_t - \frac{K_2 \sigma}{K_1} \right) \left[\frac{\cosh \sqrt{K_1} \left(\frac{L}{2} - x \right)}{\cosh \sqrt{K_1} \left(\frac{L}{2} - x_d \right)} \right] + \frac{K_2 \sigma}{K_1} \quad (2.19a)$$

$$\sigma_{xy}^i = -\frac{f}{2} \left(\sigma_t - \frac{K_2 \sigma}{K_1} \right) \sqrt{K_1} \left[\frac{\sinh \sqrt{K_1} \left(\frac{L}{2} - x \right)}{\cosh \sqrt{K_1} \left(\frac{L}{2} - x_d \right)} \right] \quad (2.19b)$$

$$\sigma_{yy}^i = \sigma_1 + \frac{mf}{8} \left(\sigma_t - \frac{K_2 \sigma}{K_1} \right) K_1 \left[\frac{\cosh \sqrt{K_1} \left(\frac{L}{2} - x \right)}{\cosh \sqrt{K_1} \left(\frac{L}{2} - x_d \right)} \right] \quad (2.19c)$$

Finally, the transition stress, σ_t , and debonded length, x_d , must be computed by matching the axial stresses and interface tractions at $x = x_d$ (i.e., $\sigma_{xx}^f = \sigma_{xx}^{fd} = \sigma_t$; $\sigma_{xy}^i = \sigma_{xy}^{id}$; $\sigma_{yy}^i = \sigma_{yy}^{id}$). The transition stress is given by:

$$\sigma_t = \frac{K_2 \sigma}{K_1} - \frac{\sigma_1}{\frac{mf}{8} K_1 + \frac{f}{2\mu} \sqrt{K_1} \tanh \sqrt{K_1} \left(\frac{L}{2} - x_d \right)} \quad (2.20)$$

while x_d is obtained numerically (by Newton's method) from the following non-linear equation:

$$\frac{\left(\frac{K_2 \sigma}{K_1} - \frac{2\mu \sigma_1}{f} x_d \right) \left(\frac{16}{m^2 \mu^2 K_1} \right) \exp \left(\frac{4}{m\mu} x_d \right)}{\left[\left(1 - \frac{16}{m^2 \mu^2 K_1} \right) \exp \left(\frac{4}{m\mu} x_d \right) \right] - 1} \left[\frac{m\mu \sqrt{K_1}}{4} + \tanh \sqrt{K_1} (L/2 - x_d) \right] + \frac{2\mu \sigma_1}{f \sqrt{K_1}} = 0 \quad (2.21)$$

2.5.3. Effects of Frictional Sliding on Load Transfer

Figure 2.9 illustrates the effects of interface slippage on the axial stress and interface tractions for the case of an inclusion with $L = 1.0\text{m}$, at an external stress, $\sigma_1/\sigma_3 = 6$:

1. Although $\mu_{crit}=0.55$ for the selected material properties and geometry (eqn. 2.16b), interface slippage has very little influence on axial stress in the reinforcement for $\mu \geq 0.3$ ($\delta \geq 17^\circ$). There are significant reductions in load transfer when the friction ratio is artificially low ($\mu=0.1$, $\delta=7^\circ$), and in the limiting condition, $\sigma_{xx}^f \rightarrow 0$ for $\mu \rightarrow 0$.
2. At the boundary of the zone of slippage (x_d ; Fig. 2.9), the proposed analysis describes continuous variations in σ_{xx}^f , σ_{xy}^i and also in the gradients of these stresses $d\sigma_{xx}^f/dx$, $d\sigma_{xy}^i/dx$. However, the normal interface traction achieves a minimum value at x_d , and the stress gradient is discontinuous at this location.
3. Throughout the slip zone ($x \leq x_d$), $\sigma_{xy}^i/\sigma_{yy}^i = \mu$. The slip zone is 'fully developed' for low friction coefficients ($\mu \leq 0.2$; Fig. 2.9b,c), when $\sigma_{yy}^i/\sigma_1 = 1$ and $\sigma_{xy}^i/\sigma_1 = \mu$. In contrast, for $\mu \geq 0.3$, the normal interface traction, $\sigma_{yy}^i/\sigma_1 < 1$ at the tip of the inclusion.

Figure 2.10 illustrates the effects of slippage on the maximum load transfer as a function of the inclusion length for a smooth interface ($\delta=10^\circ$). For short reinforcements, interface slippage causes a reduction of up to 10% in the maximum stress in the reinforcement, but has little influence on the inclusion length required to achieve full load transfer.

Overall, figures 2.8, 2.9 and 2.10 show that slippage has relatively little effect on analytical predictions of load transfer for plane strain compression of the reinforced soil composite.

2.6 Conclusions

The underlying mechanism of soil reinforcement, using planar inclusions, relies on the development of tensile stresses within the reinforcing material. This chapter considers the load transfer for a single reinforcement, due to plane strain compression shearing of the surrounding soil matrix. Closed form expressions for the reinforcement stresses are then

derived using shear lag approximations and assuming elastic properties for the soil matrix and reinforcing material. Comparisons with finite element analyses show that these solutions are accurate for a wide range of geometric and material properties.

The shear lag solutions relate the accumulation and magnitude of axial stresses in the reinforcement to a) the length of the inclusion, b) the relative stiffness of the reinforcement and soil, c) reinforcement spacing, d) volume changes in the soil and e) the external level of shear stress in the soil matrix. Modifications of the analysis have also shown that frictional sliding at the soil-reinforcement interface can reduce the load transfer. However, for practical ranges of the input parameters these effects are not expected to be significant. The results enable comparisons of the effectiveness of different reinforcements and provide important practical guidance for the design and interpretation of small scale experiments on reinforced soil (e.g., Whittle et al., 1992, 1993; Larson, 1992), as described in Chapter 3. Chapter 4 describes generalizations of the shear-lag solutions which account for inclusion orientation and rotation of external principal stress directions in the soil matrix.

Property	Symbol	Reference Value
Matrix height	m	0.57m
Inclusion thickness	f	1.0mm
Inclusion length	L	1.0m
Soil Poisson's ratio	ν_m	0.3
Inclusion Poisson's ratio	ν_f	0.2
Young's modulus of soil	E_m	10^4 kPa
Stiffness ratio	E_f/G_m	10^3
External stress ratio	σ_1/σ_3	10

a) Reference Properties.

E_f/G_m	$L/2=0.5m$				$L/2 \rightarrow \infty$			
	$\nu_m=0.3$		$\nu_m=0.5$		$\nu_m=0.3$		$\nu_m=0.5$	
	F. E.	Shear Lag	F. E.	Shear Lag	F. E.	Shear Lag	F. E.	Shear Lag
10	0.93	0.94	2.07	2.08	0.93	0.94	2.07	2.08
10^2	10.9	11.0	21.8	22.2	10.9	11.0	21.8	22.2
10^3	63.6	64.0	135	136	74.4	73.4	163	161
10^4	115	109	264	255	168	165	438	427

b) Effect of $L/2$, ν_m and E_f/G_m .

Analysis	σ_1/σ_3			f (mm)		ν_f		
	2.33	5	10	5	1	0	0.2	0.5
F. E.	0	44.1	63.6	21.1	63.6	62.4	63.6	71.2
Shear Lag	0	44.4	64.0	21.1	64.0	62.8	64.0	71.3

c) Effect of σ_1/σ_3 , f, and ν_f .

Table 2.1: Comparison of Maximum Inclusion Stress σ_{max}^f/σ_1 from Shear Lag and Finite Element Methods.

Case	Stiffness Ratio E_f/G_m	Soil Matrix Property		Volume Ratio $a=f/m$	$\sigma_1/\bar{\sigma}_{xx}^m$
		ν_m	$1/K_0$		
1	10^2	0.3	2.33	0.002	5.4
2	10^4	0.3	2.33	0.002	2.5
3	10^4	0.5	1.0	0.002	1.1
4	10^4	0.3	2.33	0.02	2.3
5	10^4	0.3	2.33	0.0001	4.0

Table 2.2: Reinforcement Effectiveness of Long Inclusions at $\sigma_1/\sigma_3=6$.

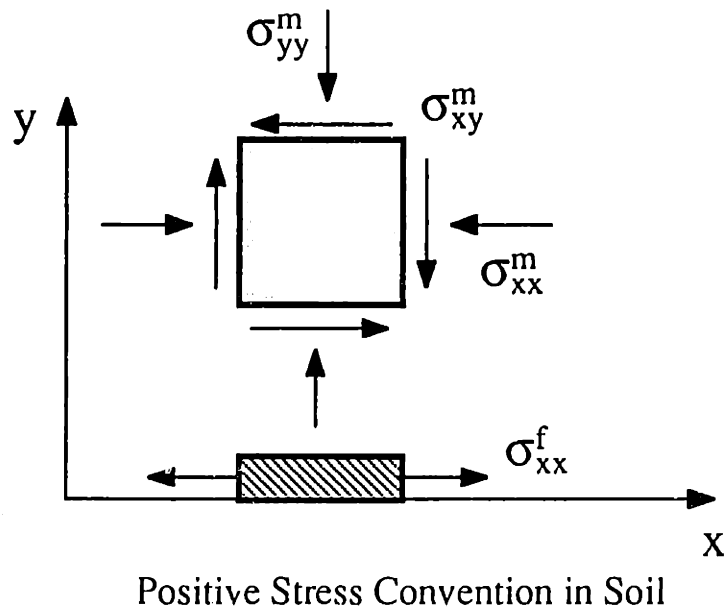
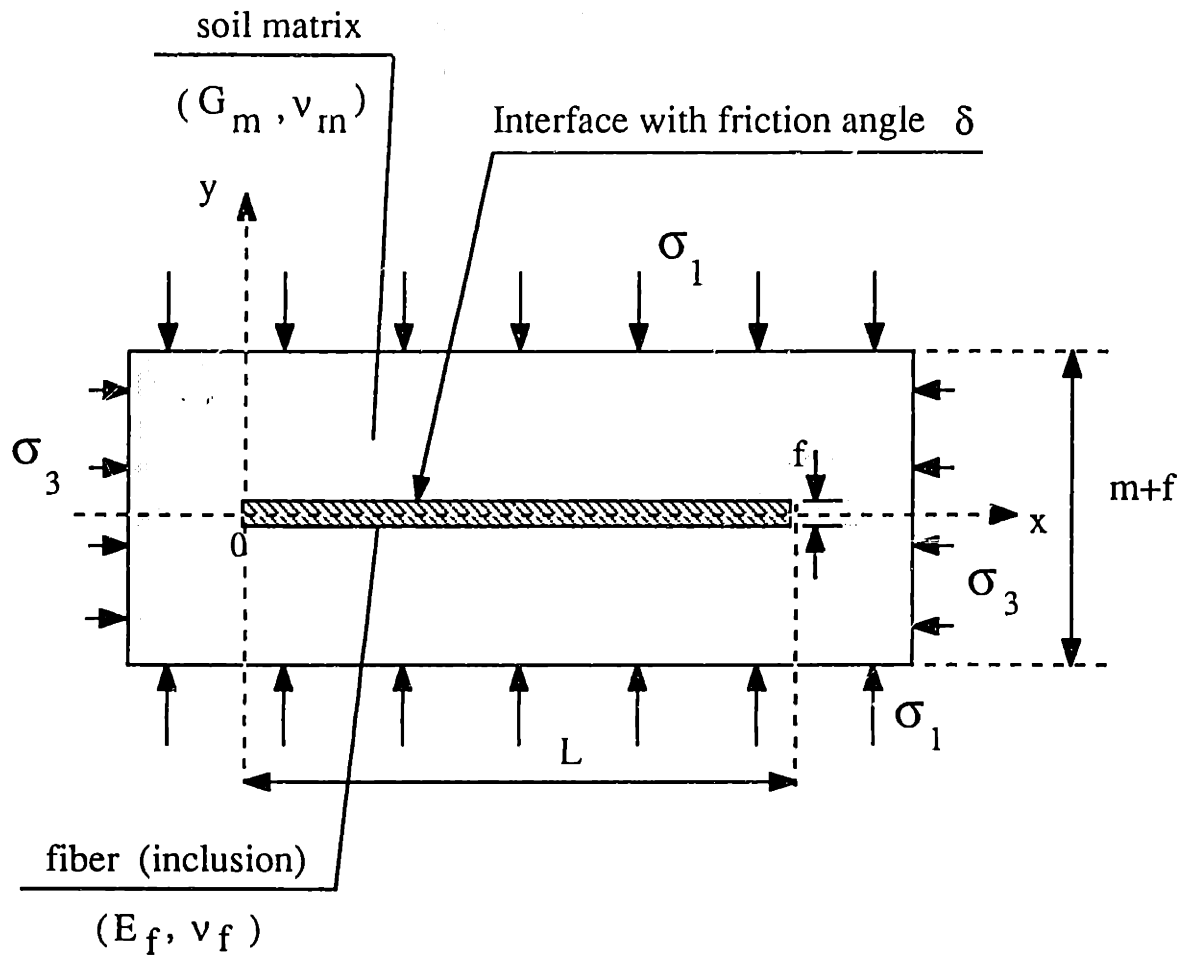


Figure 2.1: Plane Strain Geometry for an Element of Reinforced Soil.

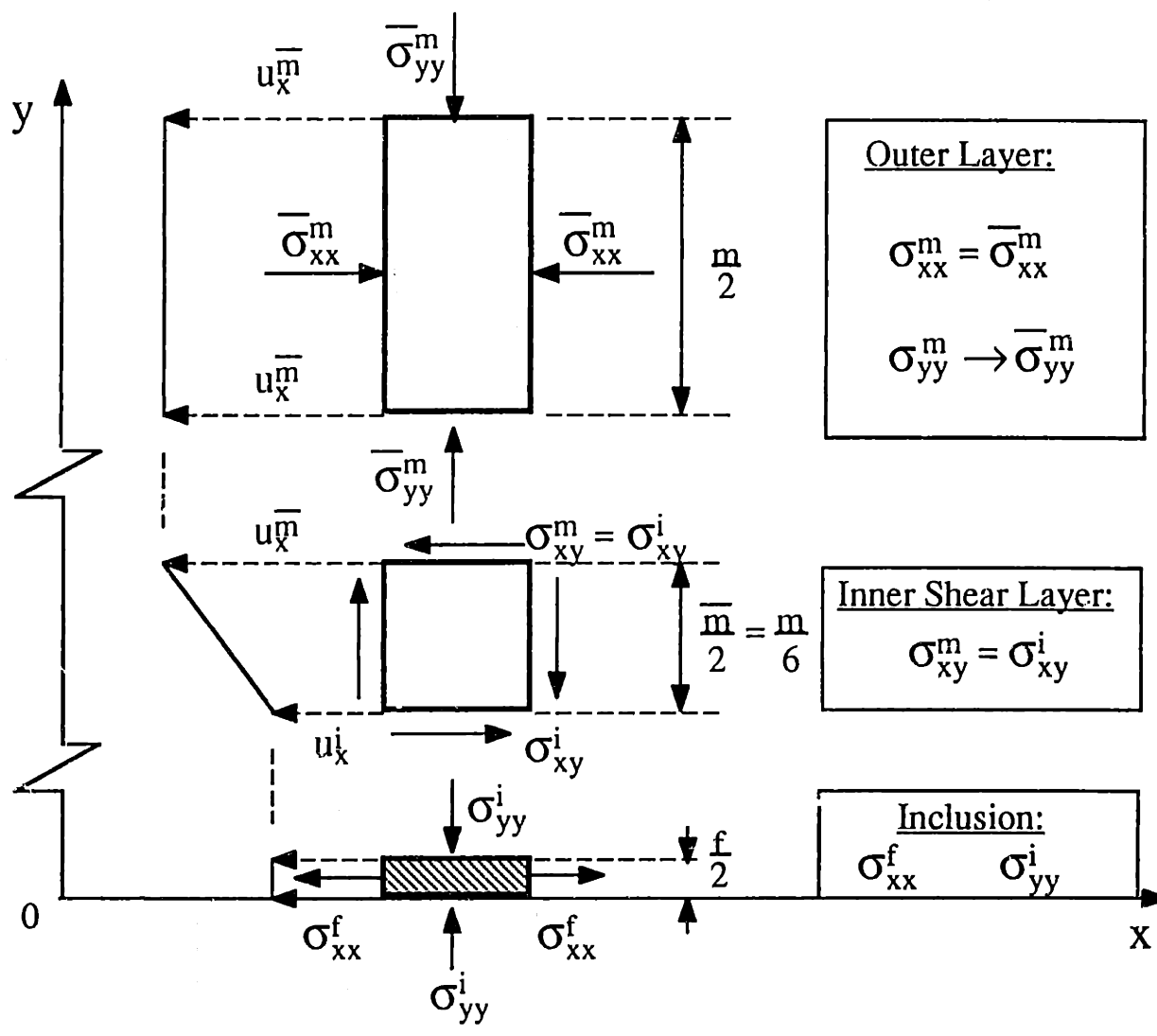


Figure 2.2: Decoupling of Stresses and Displacements in Shear-Lag Model.

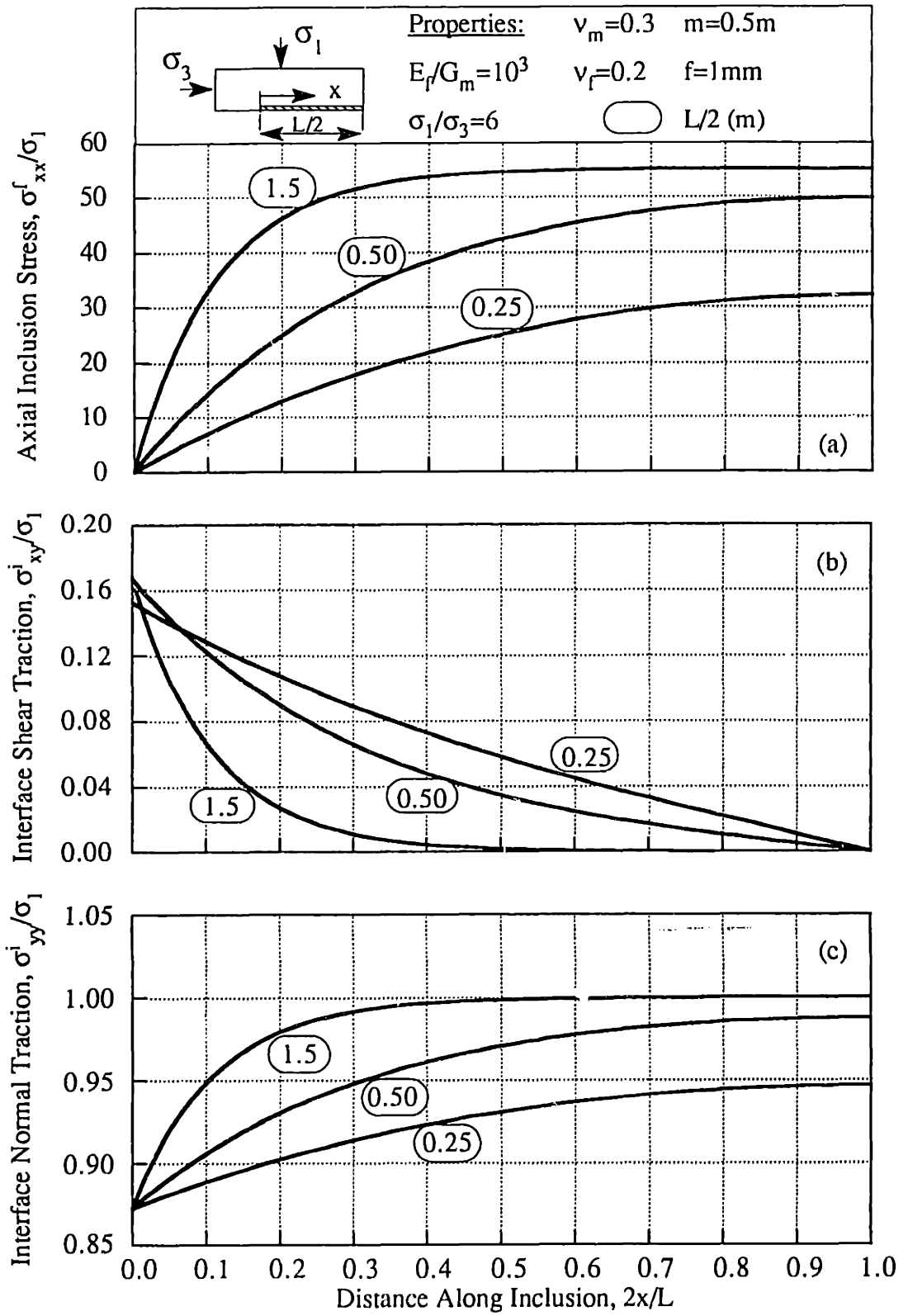


Figure 2.3: Effect of Inclusion Length on Axial Stresses and Interface Traction.

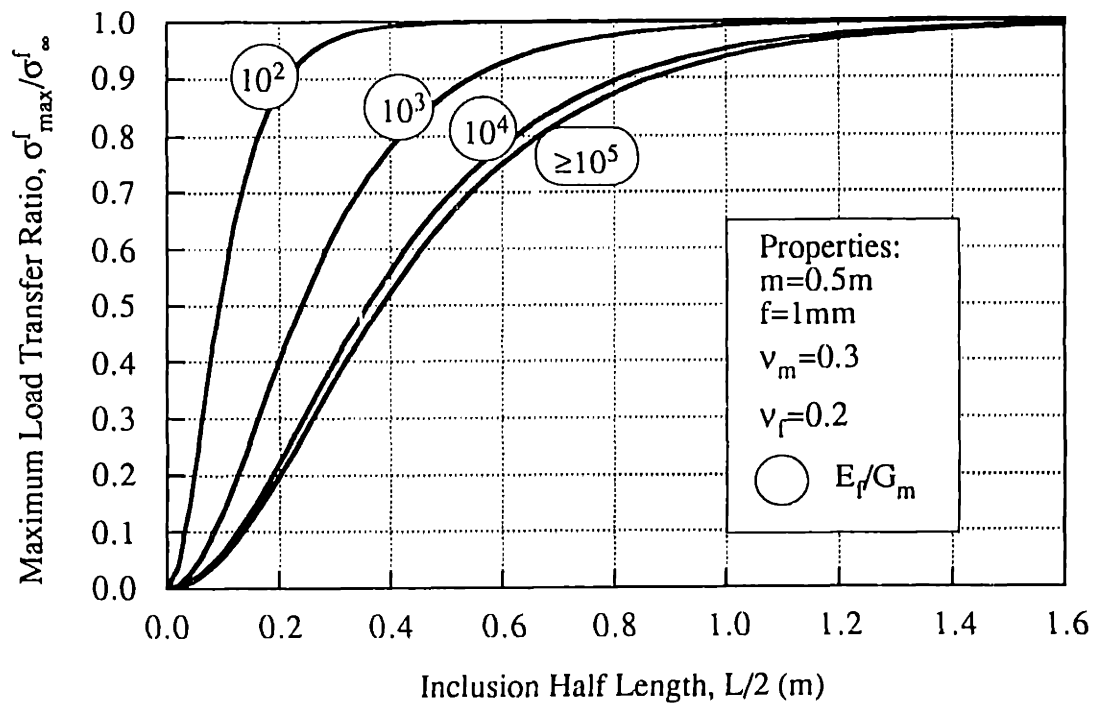
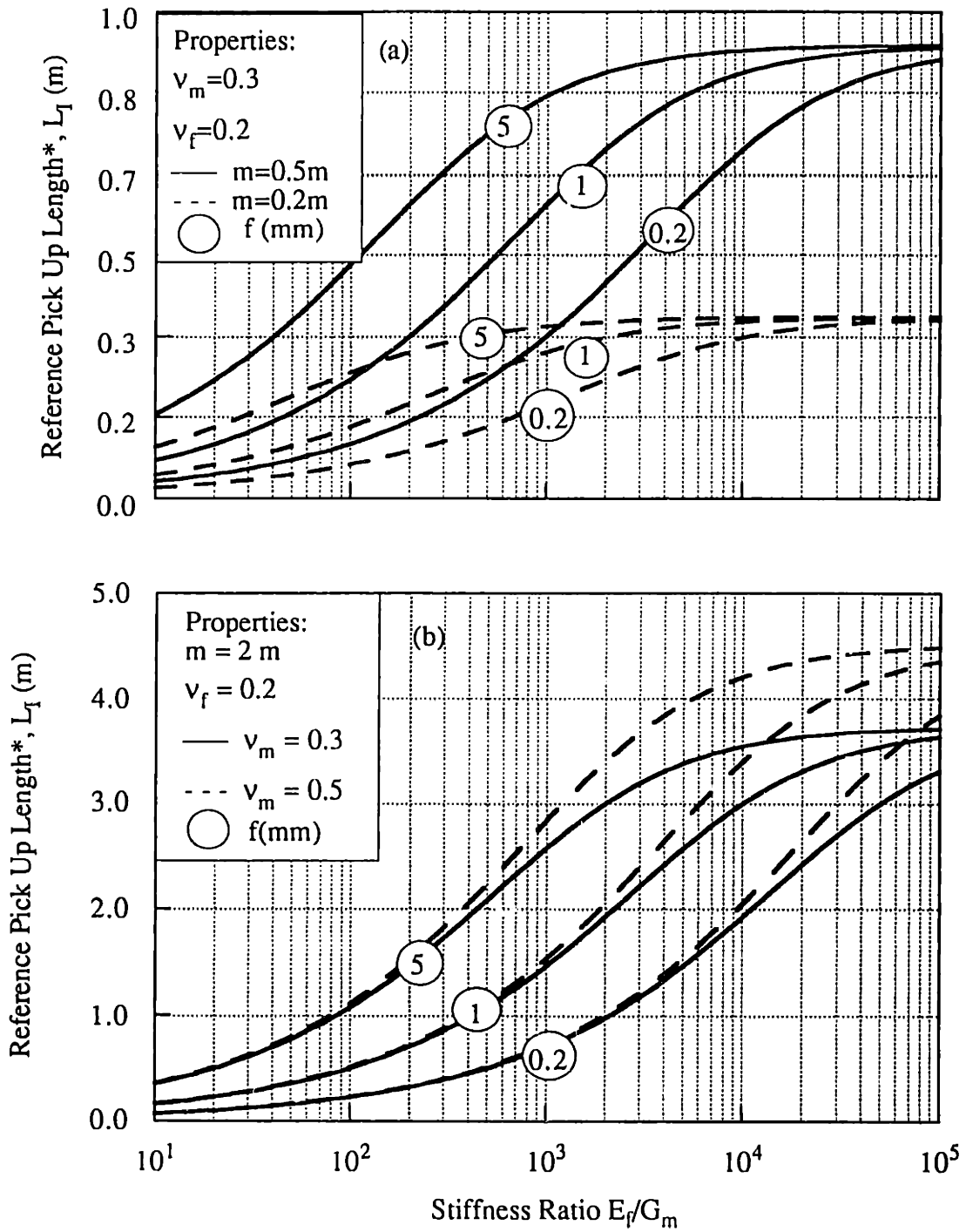


Figure 2.4: Effect of Inclusion Length and Stiffness on the Maximum Load Transfer Ratio.



* Defined at $\sigma_{\max}^f / \sigma_{\infty}^f = 0.95$

Figure 2.5: Definition of Short Reinforcements.

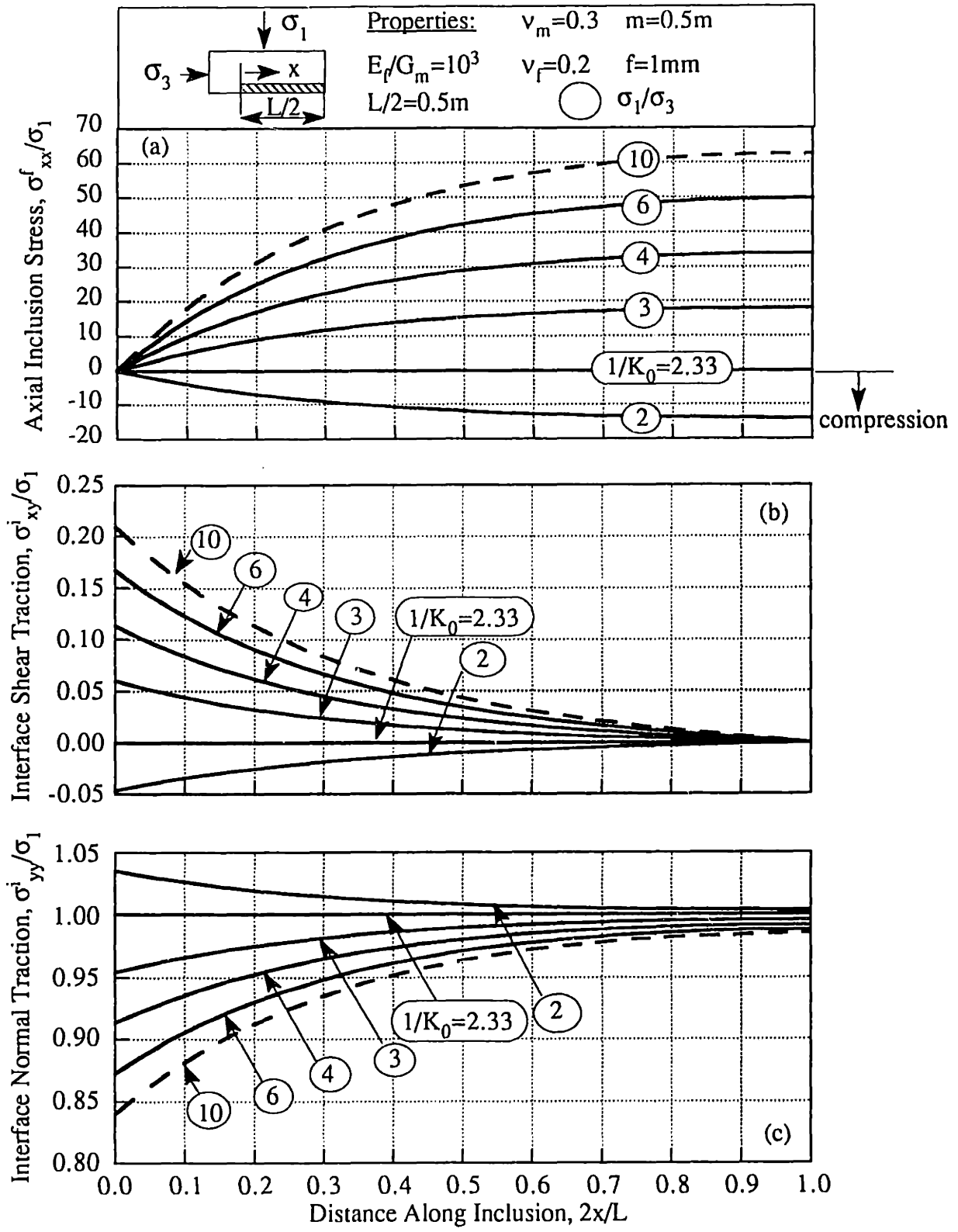


Figure 2.6: Development of Reinforcement Stress due to Shearing of the Soil.

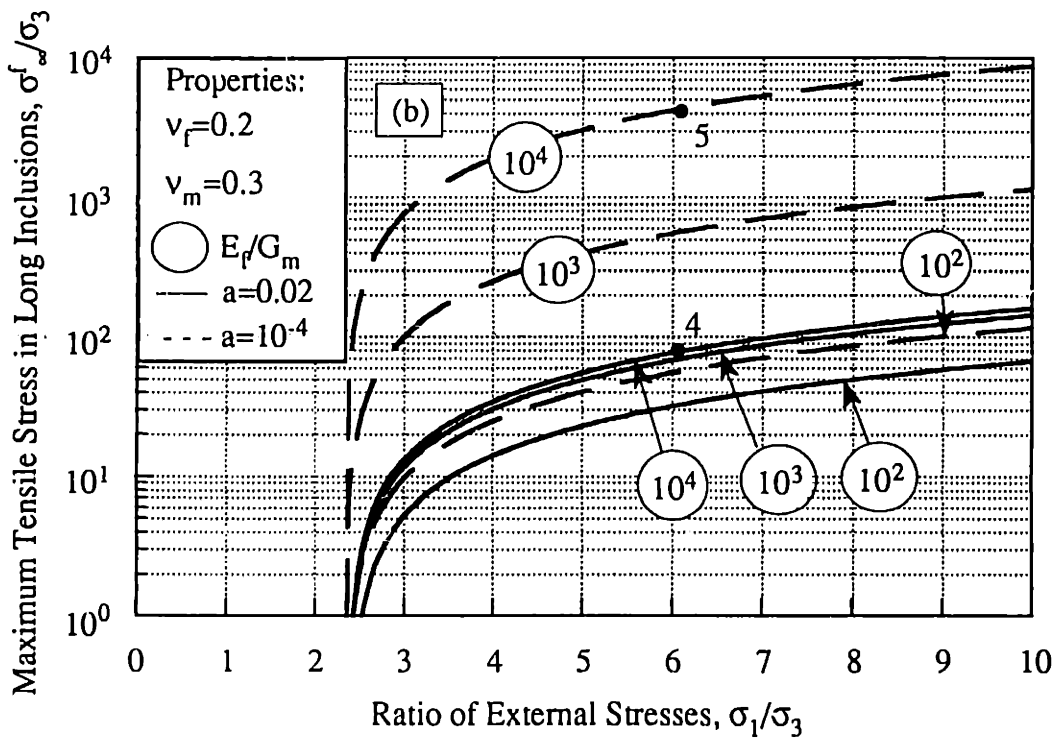
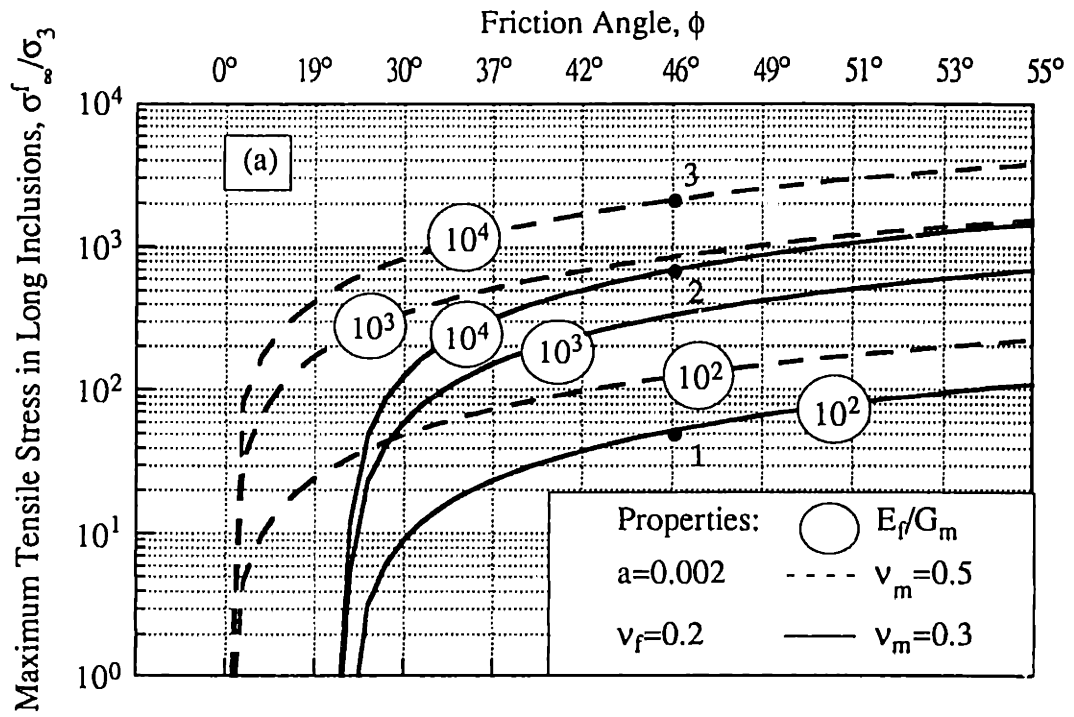


Figure 2.7: Load Transfer for Long Inclusions.

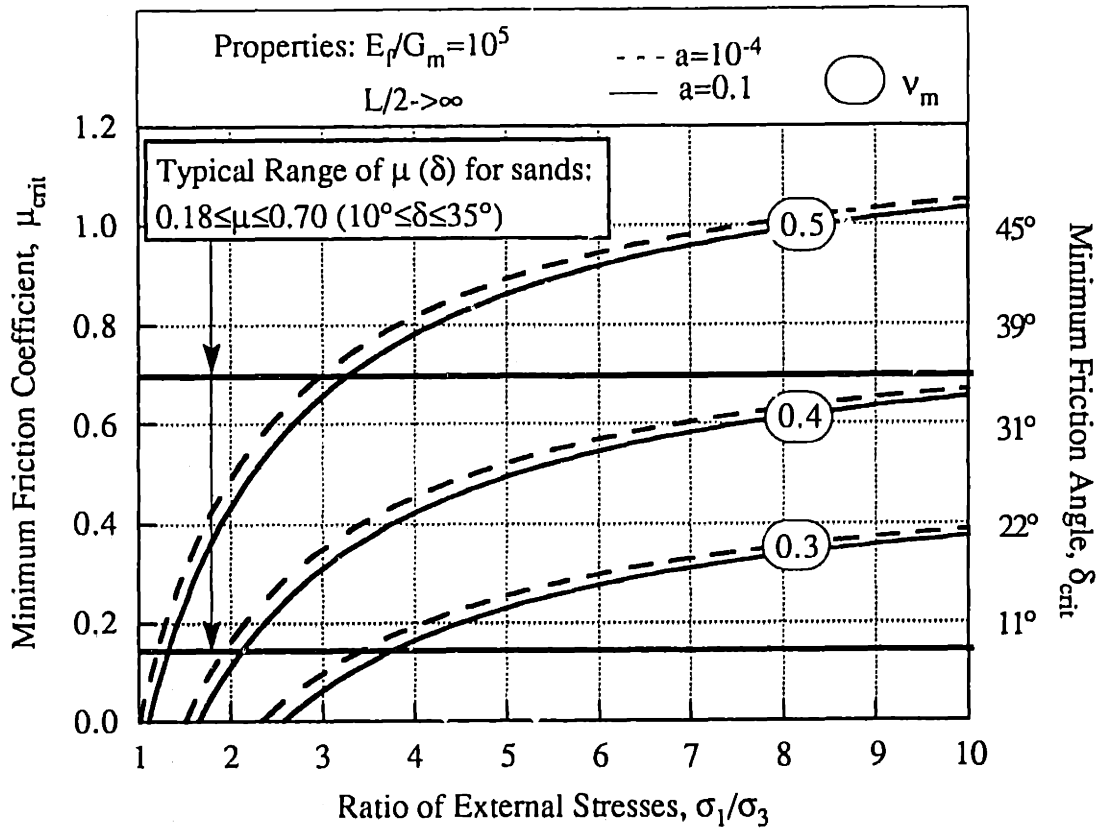


Figure 2.8: Minimum Interface Friction Required to Prevent Slippage for a Long Rigid Inclusion.

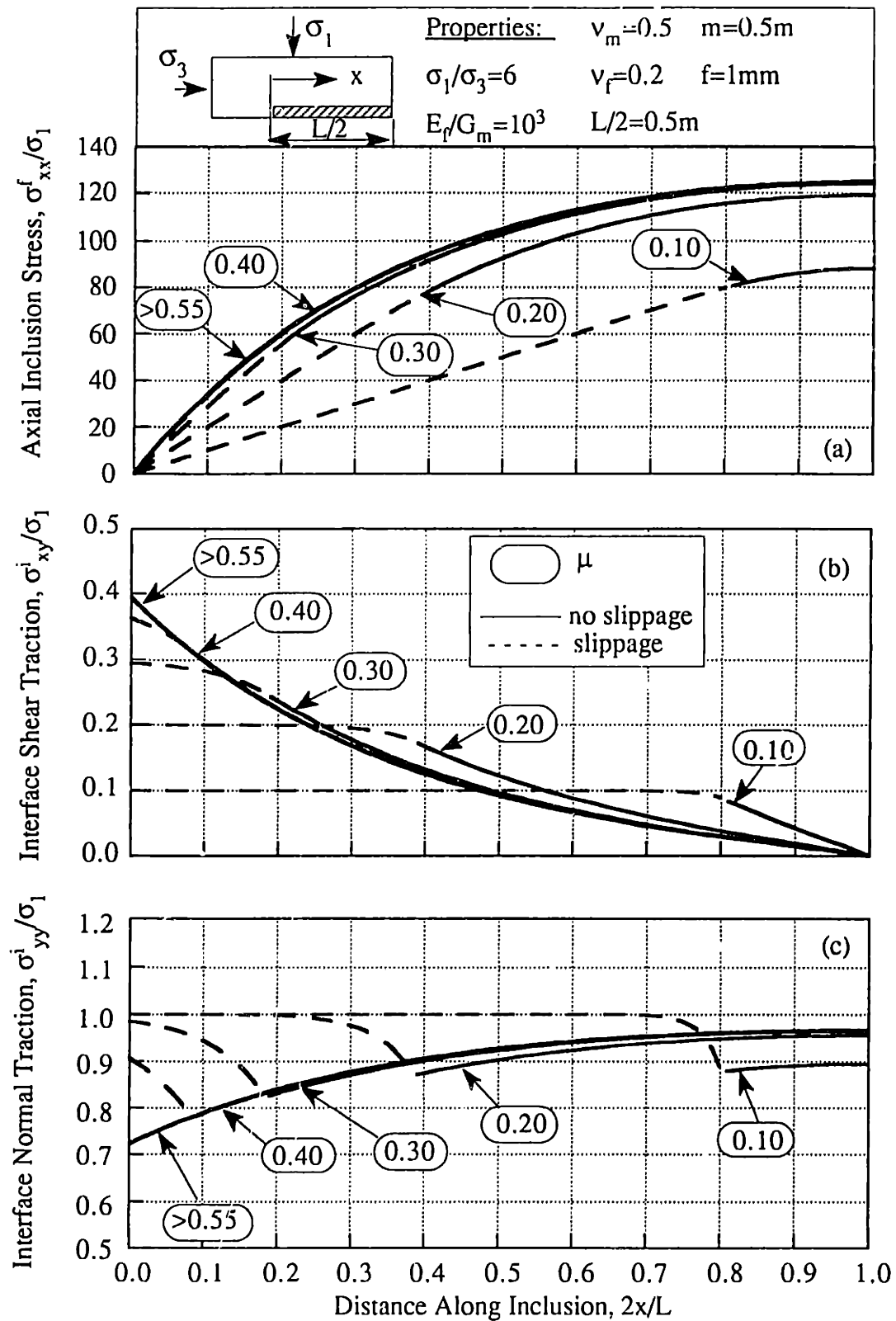


Figure 2.9: Effect of Interface Slippage on the Predicted Load Transfer.

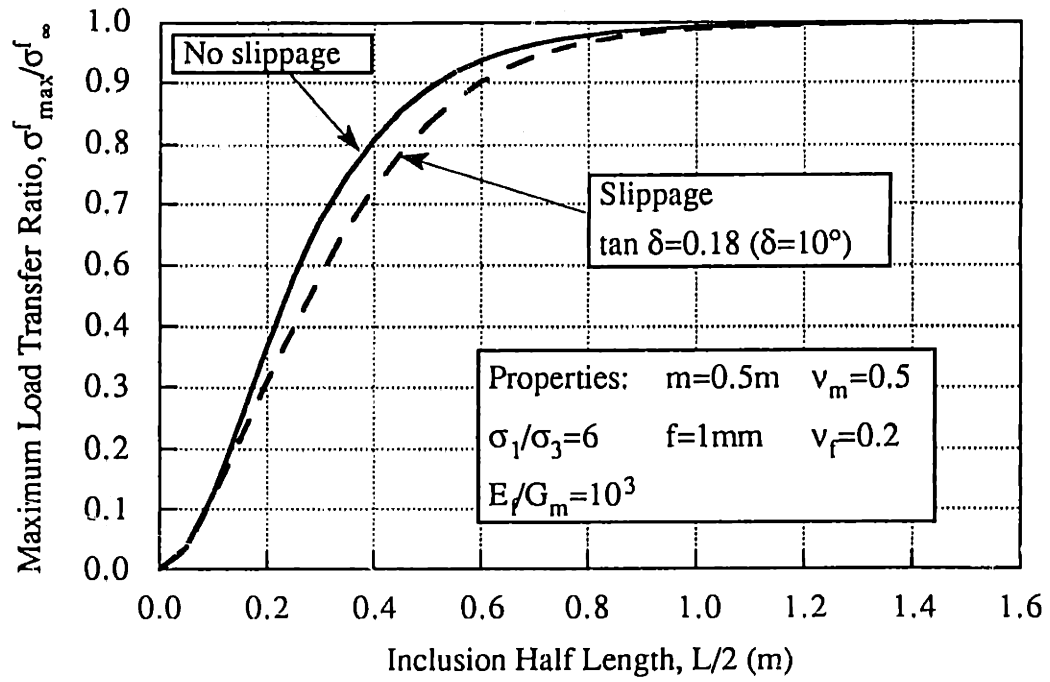


Figure 2.10: Effect of Interface Slippage on the Maximum Load Transfer Ratio.

Appendix 2.A: Stress Averaging in the Decoupled Model

In the 'substitute single stringer' approach proposed by Kuhn (1956), the matrix stresses in the real/physical model (Fig. 2.1; eqns. 2.2, 2.5a, 2.5b) can be decoupled into two zones (Fig. 2.2): 1) an inner zone of lateral dimension, $\bar{m}/2$, carrying shear stresses only; and 2) an outer zone, of dimension $m/2$, which deforms under normal and axial stresses. For the inner zone, equilibrium conditions impose constant shear stresses, $\sigma_{xy}^m = \sigma_{xy}^i$. Following Budiansky et al (1986), the dimension \bar{m} can be estimated by equating the elastic shear strain energy per unit length, E , in the real and decoupled models:

$$E = \frac{1}{G_m} \int_A (\sigma_{xy}^m)^2 dA = \frac{1}{G_m} \int_{\frac{f}{2}}^{\frac{\bar{m}}{2} + \frac{f}{2}} \left\{ \sigma_{xy}^i \left[1 - a \left(\frac{2y}{f} - 1 \right) \right] \right\}^2 dy = \frac{1}{G_m} \int_{\frac{f}{2}}^{\frac{\bar{m}}{2} + \frac{f}{2}} (\sigma_{xy}^i)^2 dy \quad (A.1)$$

Solving equation A.1, $\bar{m} = m/3$, independent of material properties and geometry.

In comparison, Budiansky et al (1986) present solutions for a cylindrical (axisymmetric) geometry in which $0.33 \leq (\bar{R}-a)/(R-a) \leq 0.47$, where a is the fiber radius, R , \bar{R} are the radius of the surrounding matrix and radial shear spring layer, respectively. For the axisymmetric geometry, the ratio $(\bar{R}-a)/(R-a)$ is a function of the volume fractions of the composite.

For the outer layer, average axial stresses $\bar{\sigma}_{xx}^m$ are given by equation 2.2, while statically equivalent average stresses in the y -direction, $\bar{\sigma}_{yy}^m$, can be obtained as follows:

$$\bar{\sigma}_{yy}^m = \frac{2}{m} \int_{\frac{f}{2}}^{\frac{\bar{m}}{2} + \frac{f}{2}} \left\{ \sigma_{yy}^i + \frac{4}{m} (\sigma_1 - \sigma_{yy}^i) \left[y^2 \left(-\frac{1}{m} \right) + y(1+a) - \frac{f}{2} \left(1 + \frac{a}{2} \right) \right] \right\} dy = \frac{2}{3} \sigma_1 + \frac{1}{3} \sigma_{yy}^i \quad (A.2)$$

Appendix 2.B: References

- Abramanto, M. and Whittle, A. J. (1993) "Shear-Lag Analysis of a Planar Soil Reinforcement in Plane Strain Compression", *ASCE Journal of Engineering Mechanics*, 119(2), 270-291.
- Allen, T. M. (1991) "Determination of Long-Term Tensile Strength of Geosynthetics: A State-of-the Art Review", *Proc. Geosynthetics '91*, Atlanta, GA, 1,351-381.
- Amirbayat, J. and Hearle, W. S. (1969) "Properties of Unit Composites as Determined by the Properties of the Interface. Part I: Mechanism of Matrix-Fibre Load Transfer", *Fibre Science and Technology*, 2, 123-141.
- Aveston, J. and Kelly, A. (1973) "Theory of Multiple Fracture of Fibrous Composites", *Journal of Materials Science*, 8, 352-362.
- Bolton, M. D. (1986) "The Strength and Dilatancy of Sands", *Géotechnique*, 36(1), 65-79.
- Budiansky, B., Hutchinson, J. W. and Evans, A. G. (1986) "Matrix Fracture in Fiber-Reinforced Ceramics", *Journal of the Mechanics and Physics of Solids*, 34(2), 167-189.
- Cox, H. L. (1952) "The Elasticity and Strength of Paper and Other Fibrous Materials", *British Journal of Applied Physics*, 3, 72-79.
- De Buhan, P., Mangiavacchi, R., Nova, R., Pellegrini, G. and Salençon, J. (1989) "Yield Design of Reinforced Earth Walls by a Homogenization Method", *Géotechnique*, 39(2), 189-203.

- Harrison, W. J. and Gerrard, C. M. (1972) "Elastic Theory Applied to Reinforced Earth", *ASCE Journal of the Soil Mechanics and Foundation Engineering Division*, 98(12), 1325-1344.
- Jarrett, P. M. and McGown, A. , eds. (1987) *The Application of Polymeric Reinforcement in Soil Retaining Structures*, Kingston, Ontario. NATO ASI Series, Series E: Applied Sciences, 147, Kluwer Academic Publishers, Boston.
- Jewell, R. A. (1990) "Strength and Deformation in Reinforced Soil Design", *Proc. 4th Intl. Conf. on Geotextiles, Geomembranes and Related Products*, The Hague, 79 pp.
- Jones, C.J.F.P. (1988) *Earth Reinforcement and Soil Structures*, Butterworths, London.
- Juran, I., Guermazi, A., Chen, C. L. and Idler, M. H. (1988) "Modelling and Simulation of Load Transfer in Reinforced Soils: Part 1", *International Journal for Numerical and Analytical Methods in Geomechanics*, 12, 141-158.
- Kuhn, P. (1956) *Stresses in Aircraft and Shell Structures*, McGraw-Hill, 435 pp.
- Ladd, C. C., Foott, R., Ishihara, K., Schlosser, F. & Poulos, H. G. (1977) "Stress-Deformation and Strength Characteristics", *Proc. 9th Intl. Conf. on Soil Mechanics and Foundation Engineering*, Tokyo, 2, 421-494.
- Larson, D. G. (1992) " A Laboratory Investigation of Load Transfer in Reinforced Soil", PhD Thesis, MIT, Cambridge, MA.
- Leshchinsky, D. and Boedeker, R. H. (1989) "Geosynthetic Reinforced Soil Structures", *ASCE Journal of Geotechnical Engineering*, 115(10), 1459-1478.
- Piggott, M. R. (1980) *Load-Bearing Fibers Composites*, Pergamon Press, Oxford.

- Potyondy, J. G. (1961) "Skin Friction Between Cohesive Granular Soils and Construction Materials", *Géotechnique*, 11(4), 339-353.
- Romstad, K. M.; Herrmann, L. R. and Shen, C. K.(1976) "Integrated Study of Reinforced Earth-I: Theoretical Formulation", *ASCE Journal of Geotechnical Engineering*, 102(5).
- Tyson, W. R. and Davies, G. J. (1965) "A Photoelastic Study of the Shear Stresses Associated with the Transfer of Stress During Fibre Reinforcement", *British Journal of Applied Physics*, 16, 199-205.
- Uesugi, M. and Kishida, H. (1986) "Influential Factors of Friction between Steel and Dry Sands," *Soils and Foundations*, 26(2), 33-46.
- Whittle, A. J.; Germaine, J. T.; Larson, D. G. and Abramento, M. (1992) "Measurement and Interpretation of Reinforcement Stresses in the APSR Cell", *Proceedings International Symposium on Earth Reinforcement Practice*, Fukuoka, Japan, November.
- Whittle, A. J.; Larson, D. G.; Germaine, J. T. and Abramento, M. (1993) "A New Device for Evaluating Load-Transfer in Geosynthetic Reinforced Soils", *Geosynthetic Soil Reinforcement Testing Procedures*, ASTM STP 1190, S. C. Jonathan Cheng, Ed., American Society for Testing and Materials, Philadelphia.

Appendix 2.C: Notation

The following symbols are used in Chapter 1:

a	=	inclusion ratio (f/m)
E	=	elastic shear strain energy per unit length
E_f	=	inclusion elastic modulus
E_m	=	soil matrix elastic modulus
f	=	inclusion thickness
G_m	=	soil matrix shear modulus
K_0	=	coefficient of lateral stress at rest
K_1	=	shear lag parameter
$K_2\sigma$	=	expression defined by eqn. 2.11b, c
L	=	inclusion length
L_1	=	length of zone I
m	=	soil matrix height
\bar{m}	=	shear spring layer height
u, v	=	displacements with and without reinforcement in shear-lag equation 2.1
u	=	displacement in x direction
u_x^i	=	interface displacement in x direction
$u_x^{\bar{m}}$	=	far field (outer layer) displacement in x direction
x	=	distance along inclusion
x_d	=	debonded length
y	=	distance along soil matrix
α	=	coefficient in shear-lag equation 2.1
δ	=	interface friction angle

δ_{crit}	=	minimum friction angle to prevent slippage
ϵ_{xx}	=	strain in x direction
ϵ_{xx}^i	=	interface strain
$\bar{\epsilon}_{xx}^m$	=	far field (outer layer) strain
ϕ	=	mobilized soil friction angle
ϕ_{cv}	=	threshold soil friction angle
μ	=	interface friction coefficient
μ_{crit}	=	minimum friction coefficient to prevent slippage
ν_f	=	inclusion Poisson's ratio
ν_m	=	soil matrix Poisson's ratio
σ_1, σ_3	=	major and minor external principal stresses
σ_t	=	transition stress bonded-debonded region in inclusion
σ_{∞}^f	=	maximum axial stress carried by long inclusions
σ_{max}^f	=	maximum axial stress at inclusion centerline
σ_{yy}^{eq}	=	equivalent normal stress for outer layer
σ_{xx}^f	=	axial stress along inclusion (positive in tension)
$\sigma_{xy}^i, \sigma_{yy}^i$	=	interface shear and normal stresses
$\sigma_{xx}^m, \sigma_{xy}^m, \sigma_{yy}^m$	=	soil matrix axial, shear and normal stresses
$\bar{\sigma}_{xx}^m, \bar{\sigma}_{xy}^m, \bar{\sigma}_{yy}^m$	=	average soil matrix axial, shear and normal stresses
$\sigma_{xx}^{fd}, \sigma_{xy}^{id}, \sigma_{yy}^{id}$	=	axial, shear and normal stresses at interface under debonding conditions

Chapter 3: Interpretation of APSR Cell Test Results using the Shear-Lag Analysis

3.1. Introduction

Larson (1992) has developed a new laboratory device, referred to as the Automated Plane Strain Reinforcement (APSR) cell, which is capable of measuring directly the tensile force transferred to a planar reinforcing inclusion due to plane strain shearing of the surrounding soil matrix. The initial test program in the APSR cell (Larson, 1992) has focused on measurements of load transfer for elastic, steel sheet inclusions of various lengths, embedded in dry sand at two relative densities. These unique data provide the first reliable experimental results for evaluating the proposed shear-lag analysis of load-transfer described in Chapter 2.

This chapter summarizes the principal features of the APSR cell, test procedures and measurements for the steel sheet reinforcement. Constituent elastic material properties for the shear-lag analysis are selected from plane strain shear tests on the unreinforced sand and in-isolation, uniaxial tests on the steel sheet reinforcement. Shear-lag predictions are then compared directly with APSR measurements of the development and distribution of tensile stresses in the steel sheet reinforcements.

3.2. Overview of the APSR Cell

3.2.1. Conceptual Design

Figure 3.1 shows the idealized geometry for a composite plane strain element of soil reinforced by a planar inclusion of length L , which is oriented parallel to the direction

of the external minor principal stress, σ_3 . As the soil is sheared in a plane strain compression mode (by increasing the major principal stress, σ_1), tensile stresses are transferred to the inclusion. The plane of symmetry, $x=0$ (Fig. 3.1) has well defined, mixed boundary conditions specified by: 1) no lateral displacement, $u_x=0$, and 2) no shear stress acting along the plane, $\sigma_{xy}=0$. These conditions are simulated in the design of the APSR cell, which corresponds to one-half of the unit element containing an inclusion of length $L/2$, as shown in Figure 3.2. The rear wall of the cell ($x=0$ plane) is rigid and lubricated to minimize friction. The key design feature of the APSR cell is that the inclusion is clamped externally to a load cell which measures the force in the reinforcement at a location equivalent to the centerline of an inclusion with length L . Symmetry along the rear wall is maintained by a hydraulic piston, which uses a feedback control to ensure that there is no displacement of the inclusion at the reference entry point (X in Fig. 3.2).

3.2.2. Geometry

Figure 3.3 shows the actual cross section through the APSR cell. It contains a soil specimen measuring 570mm high by 450mm wide by 152mm deep (plane strain direction) enclosed in a thin rubber membrane. The inclusion passes through a slot in the rear wall of the cell and is supported by jacking against an external support arch.

The principal factors affecting the overall cell dimensions were as follows:

- a) Characteristic dimensions for typical reinforcing materials used in practice (polymer grids, woven and non-woven fabrics): non-planar inclusions such as grids are of particular concern, since the grid aperture is a characteristic dimension affecting the load transfer. Ideally the inclusion specimen used in the APSR cell should have enough grid 'cells' to approximate the behavior of an infinite sheet. McGown et al. (1985) performed a set of uniaxial tensile tests on uniaxially and biaxially drawn Tensar geogrids, at constant rate of strain, to determine the necessary specimen size which approximates an

infinite sheet. For the biaxial specimen (Tensar SS2, representative of many geogrids commonly used in reinforced earth construction), the critical dimensions were 11cm wide by 18cm long. The width of the APSR cell (in the plane strain direction), $z=15.2\text{cm}$ was based on these findings.

- b) Inclusion length necessary to achieve full load transfer: prior to the development of the shear-lag analysis in Chapter 2, preliminary estimates of the inclusion length required to achieve load transfer in the APSR cell were based on the original formulation (Cox, 1952) for a cylindrical fiber (axisymmetric case). The results showed that relatively large dimensions ($L/2 > 1\text{m}$) were required to achieve the full load transfer expected at the prototype scale¹.
- c) Stress levels comparable to field situations: the structural design of the APSR cell was a compromise between the requirements of applying stresses representative of in situ conditions and having the strong box dimensions necessary to support the resulting forces. The final design of the APSR cell assumes a maximum confining stress, $\sigma_3 \leq 50\text{kPa}$, which is roughly equivalent to 3m of overburden pressure.

3.2.3. Boundary Traction

The cell applies air pressure to the outside of the specimen to control the confining stress ($\sigma_3 \leq 50\text{kPa}$), while the major principal stress is imposed by moving two end platforms into the specimen (Fig. 3.3). Waterbags on top of these platforms provide uniform boundary pressures ($\sigma_1 \leq 400\text{kPa}$). All of the water pressures in the APSR cell are applied by custom-designed pressure-volume actuators, in which an electric motor controls

¹The proposed shear-lag analysis is affected by the relative soil-reinforcement stiffness ratio E_f/G_m (Fig. 2.4). For very stiff reinforcements such as steel sheet, the pickup length for full load transfer is $L/2=1.5\text{m}$ (for $f=1\text{mm}$).

the movement of a ball screw jack which drives the piston. The specimen can deform freely in the lateral direction into the air void at the front face of the cell. The cell imposes axial strains up to 10% on the specimen, necessary for investigating load transfer using relatively extensible reinforcing materials (e.g., Palmeira and Milligan, 1989).

There are many plane strain laboratory devices described elsewhere in the literature (Seah, 1990; Tatsuoka et al., 1986; McGown and Andrawes, 1977; Green and Reades, 1975). All of these devices rely on the high bending stiffness of the side platens to approximate plane strain conditions. The large surface area of the APSR cell ($A_s=0.26\text{m}^2$) and range of design pressures ($\sigma_{zz}\leq 215\text{ kPa}$; Fig. 3.2) impose a serious constraint on the size of the sidewalls. This is a particular limitation for using radiographic measurements to compute deformations within the soil specimen. Therefore, the plane strain walls of the APSR cell have a unique active control system which ensures that $\epsilon_{zz}\leq 0.02\%$ (plane strain conditions) throughout the test. The design uses a three layer side wall, with a pressurized water diaphragm sandwiched between two metal plates. Movements of the inner membrane (in contact with the soil) are prevented by adjusting the pressure of the water diaphragm through a feedback control, while the outer structural panel transfers the reaction forces.

3.2.4. Instrumentation

Figure 3.4 shows the external instrumentation used in the APSR cell:

- 1) Boundary Displacements: The APSR cell has eleven LVDTs (Linear Voltage Displacement Transducers) to measure specimen boundary displacements. These include the axial displacement of the specimen imposed by the waterbags (D8, D9), the lateral deformation of the specimen against the confining air pressure (D5, D6, D7), and the out-of-plane deformation in the plane strain sidewalls (D10, D11). Four LVDTs (D1, D2, D3, D4) measure the displacements of the two load platforms.

2) Boundary Stresses: Five pressure transducers measure the boundary stresses in the APSR cell. They consist of a sealed chamber with a stainless steel diaphragm that deforms under an external pressure. Two transducers measure the axial stress σ_{yy} on the soil specimen through the two waterbags (P1, P2).

3) Inclusion Load: A load cell mounted on top of the arch piston measures the force applied by the piston on the inclusion. This force corresponds to the maximum force in the reinforcement providing that the reference point (X; Fig. 3.2) does not displace during the test. The reference point is marked by a metal flag attached directly to the reinforcing inclusion and is monitored by a proximity sensor (D12; Fig. 3.4). Feedback control is then used to fix the reference point by adjusting the hydraulic pressure in the arch piston.

Internal soil deformations in the APSR cell can be measured using radiography. During a typical test, five X-rays are taken to record successive displacements of a grid of tungsten carbide markers located at the midplane of the specimen.

3.2.5. Hardware

Overall, the APSR control hardware includes: 1) seven pressure actuators with seven corresponding motor control panels, feeding the four platform jacks, the arch piston, and the two plane strain walls; 2) one voltage-pneumatic air pressure regulator; 3) a personal microcomputer to control the feedback loops and reduce the test data; 4) three junction boxes to send power to and read the signals from all of the transducers; and 5) a set of power supplies and voltmeters.

The APSR cell is fully automated with eight closed feedback control loops for the displacements of the platform and arch jacks, the positions of the plane strain walls, and the confining air pressure. These are controlled by the microcomputer (containing two analog-to-digital (A/D) converter cards that enable it to read transducer signals coming from the APSR cell), and three custom-built analog feedback circuits.

3.2.6. Sand Deposition

Uniform specimens of dry sand are prepared using a custom-built raining apparatus. The sand can be deposited along either the z or y axes (Fig. 3.2). Sand specimens deposited in the z direction initially exhibit isotropic properties for plane strain shearing in the x-y plane, while those formed in the y-direction will have cross-anisotropic properties (Arthur and Menzies, 1972). Deposition in the z-direction permits load-transfer behavior to be examined independent of the effects of soil anisotropy.

Specimens are prepared in the APSR cell by means of multiple sieve dry pluviation, a method in which the sand is dropped from a controlled height through a set of sieves configured to achieve a desired density (Miura and Toki, 1983; Rad and Tumay, 1987). Figure 3.5 shows the raining configuration for preparing dense APSR specimens. It consists of a sand hopper (with a perforated floor, and shutter porosity of 6.7%) perched on top of a 1.4m high chimney. A sliding plate covers the holes in the floor so the hopper can be filled with sand. Inside the chimney are two wire mesh screens with 6.3mm square openings, mounted on a frame which can be removed as a unit. The two sieve patterns are rotated at 45° with respect to each other at a distance 200mm apart. The lowest sieve is 430mm above the floor of the cell such that the fall height of the sand varies from 430mm to 280mm as the specimen forms. The raining configuration for depositing a loose specimen involves removing the diffuser screens from the chimney, so that the specimen is deposited at a higher velocity with a reasonable uniformity (Larson, 1992).

The tests are all performed using dry Ticino sand as the reference soil. Ticino is a clean (less than 0.3% fines content), relatively uniform, medium grained sand ($G_s=2.67$; $d_{50}=0.5\text{mm}$; $C_u=1.5$) with maximum and minimum dry densities $\gamma_d=1.70\text{g/cm}^3$ and 1.38g/cm^3 , respectively. The engineering properties of Ticino sand are typical of many natural sands and have been extensively documented in the literature (e.g. Baldi et al.,

1985). Test data reported by Larson (1992) show that the APSR raining apparatus provides uniform dense specimens of Ticino sand with dry density $\gamma_d=1.62\pm 0.01\text{g/cm}^3$ (corresponding to $D_r=79\pm 3\%$) and loose specimens with $\gamma_d=1.47\pm 0.04\text{g/cm}^3$ ($D_r=36\pm 10\%$).

Further details of specimen preparation are presented in Chapter 6 in conjunction with pullout tests performed by the author.

3.2.7. Instrumentation for Steel Sheet Reinforcements

The primary method for characterizing load-transfer in the APSR cell is through the measurements of tensile stress at the reference point X (Fig. 3.2), corresponding to the maximum stress at the center of an inclusion of length L (cf. Fig. 3.1). For the steel sheet reinforcements, additional instrumentation is used to measure the distribution of strains within the inclusion. The instrumented reinforcements comprise two sheets, made from 0.127mm thick steel shim stock, which are bonded together using flexible adhesive. Strain gauges are mounted on the inside face of one of the sheets, such that the gauges and electrical leads are protected from abrasion by the surrounding sand.

3.2.8. Proof Tests

The APSR cell represents a major departure from pre-existing laboratory equipment used in evaluating soil-reinforcement interactions. Thus, proof testing of the new device was an essential component of the development process in order to: a) evaluate the control and data acquisition systems; b) establish if the design parameters can be achieved in practice; and c) compare measured data for unreinforced sand with behavior reported previously from other shear devices, to determine the reliability of material properties measured in the APSR cell. Table 3.1 summarizes the performance characteristics of the APSR cell established from the extensive program of proof tests performed by Larson (1992).

3.3. APSR Measurements

3.3.1. Shear Behavior of Ticino Sand

A series of five plane strain shear tests (Table 3.2) were performed on unreinforced specimens of Ticino sand at a constant confining pressure, $\sigma_3=31$ kPa. Figure 3.6 compares the stress-strain behavior of three tests (APSR 36, 38 and 45) on dense Ticino sand ($D_r=79\%$) interpreted from external (i.e. boundary) measurements of displacements and tractions. These results demonstrate capabilities of the APSR for obtaining repeatable measurements of soil properties. In all three cases, the peak shear strength, $R=8.2$ to 9.1 (corresponding to $\phi'=52^\circ$ to 53°) is mobilized at axial strains $\epsilon_f=1.7$ to 1.9% . Larson (1992) has made careful comparisons between soil strains interpreted from boundary deformations and those obtained from radiographic measurements locally within the soil specimen. Figure 3.7 summarizes the comparisons for test APSR 45 which show that: a) the shear stress-axial strain response (R vs. ϵ_{yy}) can be estimated reliably from the external boundary measurements; b) there are large differences between lateral strains interpreted from external and internal deformation measurements; and c) radiographic measurements of deformations within the soil specimen are essential for estimating the 'true' volumetric response ($\epsilon_{yy}-\epsilon_{vol}$) of the material.

Figure 3.8 summarizes the plane strain shear behavior for dense and loose ($D_r=42\%$) specimens of Ticino sand measured in the APSR cell. The loose specimen is characterized by a peak shear strength $R=5.6$ ($\phi'=44^\circ$) which is mobilized at an axial strain $\epsilon_f=3.5\%$. There is negligible net volume change measured at the peak shear resistance for both dense and loose specimens ($\epsilon_{vol}=-0.5\%$).

3.3.2. Tensile Stress in Steel Reinforcement

Table 3.2 summarizes the program of APSR tests performed by Larson (1992) to measure load transfer for steel sheet reinforcements. The most comprehensive measurements were obtained for a 'base case geometry' with an inclusion half length $L/2=36\text{cm}$, sheared in dense Ticino sand, instrumented with 4 strain gauges to measure the tensile stress distribution. The subsequent test program focuses on the effects of inclusion length ($L/2=9, 18, 27, 36\text{cm}$) and formation density (loose/dense $D_r \cong 36$ and 79%) for specimens sheared at constant confining pressure $\sigma_3=31\text{kPa}$.

Figure 3.9 shows the measurements of 'centerline' tensile load and load distribution for the base case tests (APSR 35, 41, 60), as functions of the external stress ratio, $R=\sigma_1/\sigma_3$ (Fig. 3.1). The results are generally very consistent² and show the following: 1) during the initial phase of the test ($R \leq 1.4$; Fig. 3.9a) the inclusion is in compression; and 2) for intermediate levels of shearing ($1.4 \leq R \leq 8$), significant tensile stresses are measured throughout the inclusion; changes in the centerline loads are approximately proportional to changes in external stress ratio ΔR .

Tensile stresses interpreted from strain gauge measurements in two tests (APSR 35, 41; Fig. 3.9b) differ by less than 15% and show a smooth distribution of load within the inclusion, with maximum values measured by the centerline (by the external load cell). Further details of load-transfer measurements are described in the next section through comparisons with predictions of the proposed shear-lag analysis.

²Larson (1992) describes the refinement of control systems used to achieve reliable measurements of centerline loads. Subsequent developments by Chauhan (1993) have greatly improved the robustness of these original systems.

3.4. Comparison of APSR Test Results and Shear Lag Predictions

3.4.1. Selection of Input Parameters

Input parameters for shear-lag analyses of the APSR tests include the elastic properties of the constituent materials (soil and reinforcement) and specified geometry (L , f , m). The interface friction δ was shown to have very little effect on predictions of load-transfer when the inclusion is oriented parallel to the direction of σ_3 (Chapter 2). The steel sheet reinforcement is well characterized as an elastic material with properties $E_f=2.07 \times 10^8 \text{ kPa}$ and $\nu_f=0.2$, determined from in-isolation, uniaxial tensile tests (Larson, 1992). However, the selection of elastic properties (G_m, ν_m) for representing sand behavior is only approximate and requires careful documentation.

Figure 3.10 illustrates the elastic approximations for the unreinforced dense Ticino sand ($D_r=79\%$) sheared at a confining stress $\sigma_3=31 \text{ kPa}$. The parameters α and β in the figure were derived from the elastic stress-strain relations in plane strain compression:

$$\epsilon_{xx} = \frac{1 + \nu_m}{E_m} [(1 - \nu_m) \sigma_{xx} - \nu_m \sigma_{yy}] \quad (3.1a)$$

$$\epsilon_{yy} = \frac{1 + \nu_m}{E_m} [(1 - \nu_m) \sigma_{yy} - \nu_m \sigma_{xx}] \quad (3.1b)$$

From equation 3.1a, the axial stress σ_{yy} is a linear function of ϵ_{yy} for a constant confining stress ($\sigma_{xx}=\sigma_3$):

$$\sigma_{yy} = \frac{E_m \epsilon_{yy}}{(1 - \nu_m^2)} + \frac{\nu_m \sigma_{xx}}{(1 - \nu_m)} \quad (3.2)$$

The secant slope of the stress-strain response at 50% of the failure stress (Fig. 3.10a) can then be obtained as:

$$\alpha = \frac{\Delta(\sigma_{yy} - \sigma_{xx})}{\Delta \epsilon_{yy}} = 2 \frac{G_m}{(1 - \nu_m)} = 19.2 \text{ MPa} \quad (3.3)$$

where G_m is the elastic shear modulus.

For an elastic material in plane strain compression, the lateral strain ϵ_{xx} is a linear function of ϵ_{yy} . The slope of the idealized relationship between ϵ_{xx} and ϵ_{yy} is the derivative of equation 3.1a with respect to ϵ_{yy} :

$$\beta = \frac{\Delta \epsilon_{xx}}{\Delta \epsilon_{yy}} = \frac{-\nu_m}{1 - \nu_m} \quad (3.4)$$

Predictions of load transfer are sensitive to the value of ν_m , and hence two values are used to make predictions of the APSR tests: a) the initial slope of the lateral strain curve; and b) the value based on a line passing from the origin through the point of zero dilation rate on the lateral strain curve. For the data in figure 3.10, the corresponding values are $\beta = -0.486$ and -0.729 (Fig. 3.10b), which lead to estimated Poisson's ratios $\nu_m = 0.33$ and 0.42 , respectively. Substituting in equation 3.3, $G_m = 5600$ to 6400 kPa. Small variations in the soil modulus have little effect on the predictions of load transfer, especially for a relatively stiff reinforcement ($E_f/G_m \approx 3.5 \times 10^4$ for the steel sheet; cf. Fig. 2.4). Therefore, the following comparisons assume $G_m = 6000$ kPa. Table 3.3 summarizes the input parameters and APSR test geometry used in the shear-lag analysis.

Figures 3.11 and Table 3.4 show similar procedures for estimating elastic properties of unreinforced loose Ticino sand ($D_r = 36\%$; APSR 37). The selection of ν_m from this test involves greater uncertainty due to the larger variation in β , between the initial and zero dilation rate conditions. Equation 3.4 gives corresponding Poisson's ratios ranging from $\nu_m = 0.16$ to 0.37 (for initial and zero dilation rates, respectively). The straight line through the stress-strain curve at the point halfway to failure has slope $\alpha = 8334$ kPa and hence $G_m = 2600$ to 3500 kPa. The shear-lag analyses for loose sand assume $G_m = 3000$ kPa ($E_f/G_m = 69000$; Table 3.4).

3.4.2. Inclusion Loads - Dense Sand

Figure 3.12a compares shear lag predictions with the centerline tensile loads measured for the base case geometry ($L/2=36\text{cm}$, $f=0.25\text{mm}$) as a function of the external stress ratio R . The plot shows that the parameter ν_m has two important effects on the shear-lag predictions: 1) the offset stress ratio R_0 (i.e., $1/K_0$) increases as ν_m decreases; and 2) the load transfer rate ($\Delta F_R/\Delta R$) increases with ν_m . The value $\nu_m=0.42$ (based on the zero dilation condition) substantially overpredicts the tensile force at the centerline of the inclusion at all R values. The measured centerline stresses are in excellent agreement with shear-lag predictions using $\nu_m=0.32\text{-}0.35^3$ for stress ratios $R \leq 8$ ($\phi' \leq 51^\circ$).

Figure 3.12b shows that there is very good agreement between the predicted tensile force distribution along the length of the inclusion and the measured loads from APSR 35 at two stress ratios, $R=3$ and 6 , using the best estimate, $\nu_m=0.35$. The predictions and measurements agree within 10% for most gauges, with a maximum difference of 18% for gauge 3 at $R=3$.

3.4.3. Inclusion Loads - Loose Sand

Figure 3.13 compares the predicted and measured centerline loads in a inclusion with $L/2=36\text{cm}$ (base case geometry) sheared in loose Ticino sand. In this case, shear-lag predictions using the initial value of ν_m ($=0.16$) greatly underestimate the measured centerline load, while very good agreement is obtained for an average value, $\nu_m=0.32$. This result implies that it is more reliable to estimate ν_m indirectly from estimates of K_0^3 than to use the lateral strains during shearing of the unreinforced soil. For $\nu_m=0.32$, the predicted offset stress ratio R_0 is slightly higher than the observed value ($R_0=1.8$), while the load

³Note that for an elastic soil, $K_0 = \frac{\nu_m}{1 - \nu_m}$. Thus, for $\nu_m=0.32$ to 0.35 , $K_0 = 0.47$ to 0.54 .

transfer rate is in good overall agreement with the measured behavior. The plot of predicted vs. measured inclusion load distribution in Figure 3.13b again demonstrates that shear-lag analysis predicts accurately the form of the distribution. The largest discrepancy occurs at $R=5.5$ for the centerline load. Larson (1992) suggests that further refinements of the reinforcement positioning mechanism at the exit point (X, Fig. 3.2) are necessary in order to improve the reliability of the centerline loads. Therefore, the results in Figures 3.12 and 3.13 should be viewed as preliminary.

3.4.4. Influence of Inclusion Length on Centerline Loads

Figure 3.14 compares the shear-lag predictions with APSR measurements of centerline stresses for inclusions with half-lengths, $L/2=9$ to 36cm. The predictions assume the elastic parameters listed in Tables 3.3 and 3.4 for dense and loose sand, respectively. The results for dense sand (Fig. 3.14a) show that the shear-lag analysis is in better agreement with the data for long inclusions ($L/2=36$ cm); however, the overall framework is in reasonable agreement with the APSR data. The most significant discrepancy is the non-linearity measured in short inclusions for $R \leq 4$ (particularly in the test with $L/2=18$ cm). There is generally better agreement between the predicted and measured inclusion loads at $R=8$ than at $R=4$. Differences between the predicted and measured results may be due to several factors, including the following: a) soil behavior is not well represented as a linear elastic material; b) soil stresses are not perfectly uniform within the APSR specimen due to boundary friction.

There is a better correlation between the predicted and measured load transfer for the loose sand than for the dense sand. For the two tests shown in Figure 3.14b, the shear-lag analysis is in good agreement with measured loads at all R values. The analysis describes accurately the effect of inclusion length on the load transfer measured in the loose Ticino sand.

Figure 3.15 replots the comparison of predicted and measured centerline tensile loads at a stress ratio $R=6$, as a function of the inclusion length. These results demonstrate the role of the shear lag analysis for predicting loads in a very long inclusion (i.e. field scale situation) based on APSR test data. Measurements of load transfer in the APSR cell provide essential data for evaluating the predictive capabilities and limitations of the proposed shear-lag analysis. Shear-lag predictions for long reinforcements can then be obtained by extrapolation of the load pickup curve (Fig. 3.15). For the relatively inextensible elastic steel sheet reinforcements described in this thesis, the shear lag analysis shows that the tensile load measured in the APSR cell ($L/2=36\text{cm}$) corresponds to approximately 50% of the load that would occur in a long inclusion in the field. Full load transfer occurs for inclusions of half-length $L/2 \geq 1.50\text{m}$ for both loose and dense Ticino sand at $\sigma_3 = 31 \text{ kPa}$.

3.4. Conclusions

This chapter describes the interpretation of tests results performed on steel-reinforced Ticino sand using a new laboratory device, referred to as the Automated Plane Strain Reinforcement (APSR) cell (Larson, 1992). Elastic input properties (G_m, ν_m) were obtained for dense and loose Ticino sand from unreinforced tests in the APSR cell. Using these properties and known elastic constants for the steel sheet reinforcement, shear-lag predictions were made of the inclusion loads measured in the APSR tests.

Predictions made for tests with a 36cm steel inclusion show that the analysis is sensitive to the value of Poisson's ratio of the soil, ν_m . For dense sand, predictions of the maximum inclusion load made using $E_f/G_m=35,000$ and $\nu_m=0.35$ match closely the externally measured inclusion loads in the APSR cell at all R -values. For loose sand, the measured relationship between the inclusion tensile load and external stress ratio is closely approximated by the shear lag analysis with $E_f/G_m=69,000$ and $\nu_m=0.32$. The analysis also

predicts accurately the measured load distribution along the length of the inclusion for both dense and loose sands.

The centerline tensile loads for short inclusions in dense sand (i.e., for $L/2 < 36\text{cm}$) are slightly higher than those predicted by the shear-lag analysis. However, there is better agreement between the predicted and measured load transfer for tests in loose sand. The shear-lag analysis predicts reliably the gradient of the linear load transfer function for both the 18 and 36cm steel inclusions in loose sand.

The shear-lag analysis shows that the tensile force measured in APSR tests with $L/2 = 36\text{cm}$ steel sheet reinforcements represents approximately half the load transferred to a long inclusion ($L/2 \geq 1.5\text{m}$) for both dense and loose Ticino sand.

The comparisons described in this chapter demonstrate the use of shear-lag analysis for predicting and interpreting load transfer in the APSR tests. The analysis provides physical insight into the constituent properties controlling load transfer, and gives good agreement with measured data for elastic steel sheet inclusions.

Design Parameter	Tolerance/Response*
Confining air pressure, σ_3	± 0.15 kPa
Position of loading platforms	± 0.005 mm
Major principal stress, σ_1	± 1 kPa
Plane strain control, ϵ_2	$\pm 0.02\%$
Boundary friction* (due to grease cohesion, C_g)	$C_g=1.4$ kPa

* Measured by translation test.

Table 3.1: Performance Characteristics of the APSR Cell.
(after Larson, 1992)

Test No.	Relative Density (%)		Inclusion Length ¹ (cm)				# Strain Gauges ²	Comments
	Dense	Loose	Full	3/4	1/2	1/4		
APSR 36	79		unreinforced				-	Selection of soil properties
APSR 38	79							
APSR 45	79							
APSR 34		33						
APSR 37		42						
APSR 35	79		36				4	-
APSR 39	78		36				4	Test repeatability
APSR 41	79		36				3	
APSR 60	79		36				-	-
APSR 62	79			27			-	-
APSR 43	78				18		-	Test repeatab.
APSR 64	79				18		-	-
APSR 44		42			18		-	-
APSR 46		33	35				2	-
APSR 47		32				9	-	Not reliable
APSR 65	79					9	-	-
APSR 48	78					10	-	Not reliable

Note: ¹All inclusions were 0.25mm thick steel sheet, 13.3cm wide.

²Bonded resistance strain gauges (BLH SR-4) of length 12.7mm with nominal resistance of 350Ω.

Table 3.2: Summary of APSR Tests with Steel Sheet Reinforcements.

(after Larson, 1992)

Elastic Properties for the Sand and Reinforcement			
Property	Sand		Reinforcement
Modulus	$G_m = 6000 \text{ kPa}$		$E_f = 2.07 \times 10^8 \text{ kPa}$
Poisson's ratio	$\nu_m = 0.33 \text{ to } 0.42$		$\nu_f = 0.2$
Lateral dimension	$m = 0.57 \text{ m}$		$f = 2.54 \times 10^{-4} \text{ m}$
Length			$L/2 = 0.36 \text{ m}$
Resulting Shear Lag Parameters			
	$\nu_m = 0.33$	$\nu_m = 0.35$	$\nu_m = 0.42$
K_1	13.561	13.159	11.781
K_2^1	12,633	13,337	15,751
K_2^3	-25,662	-24,781	-21,762

Table 3.3: Input Parameters for Shear Lag Predictions of Load Pickup in Dense Ticino Sand.

Elastic Properties for the Sand and Reinforcement			
Property	Sand		Reinforcement
Modulus	$G_m = 3000 \text{ kPa}$		$E_f = 2.07 \times 10^8 \text{ kPa}$
Poisson's ratio	$\nu_m = 0.16 \text{ to } 0.37$		$\nu_f = 0.2$
Lateral dimension	$m = 0.57 \text{ m}$		$f = 2.54 \times 10^{-4} \text{ m}$
Length			$L/2 = 0.35 \text{ m}$
Resulting Shear Lag Parameters			
	$\nu_m = 0.16$	$\nu_m = 0.32$	$\nu_m = 0.37$
K_1	16.025	12.695	11.705
K_2^1	6375.5	12,279	14,035
K_2^3	-33,488	-26,105	-23,909

Table 3.4: Input Parameters for Shear Lag Predictions of Load Pickup in Loose Ticino Sand.

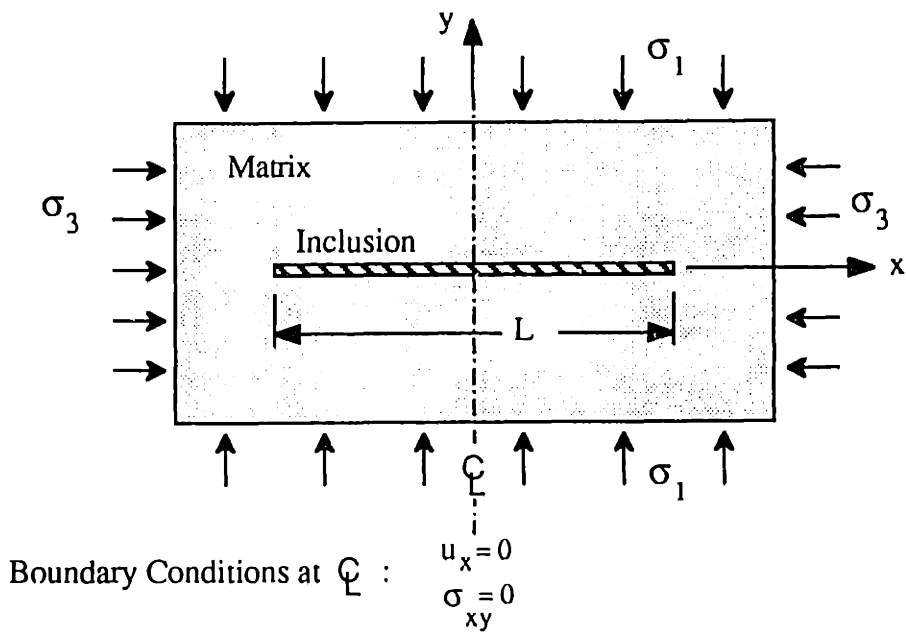


Figure 3.1: Geometry of the APSR Ideal Plane Strain Reinforced Soil Element.

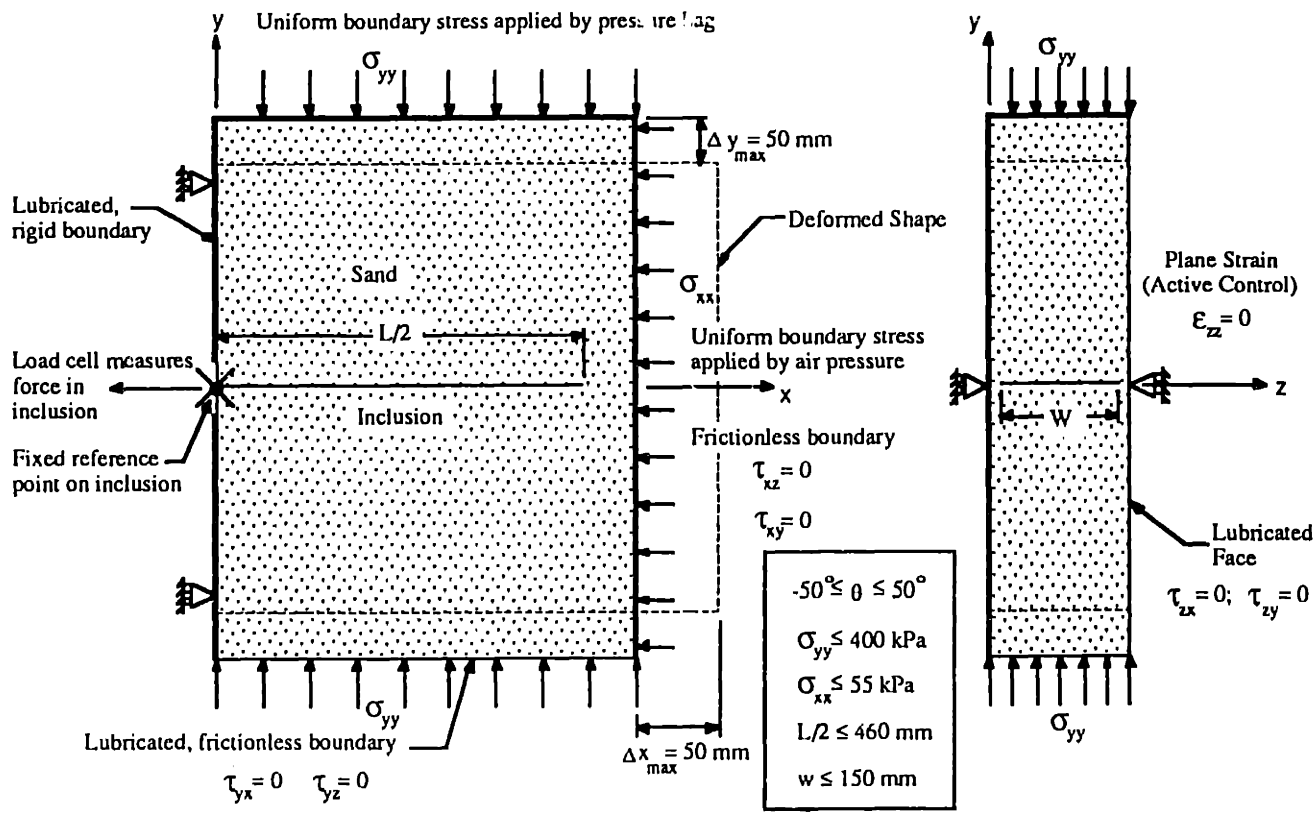
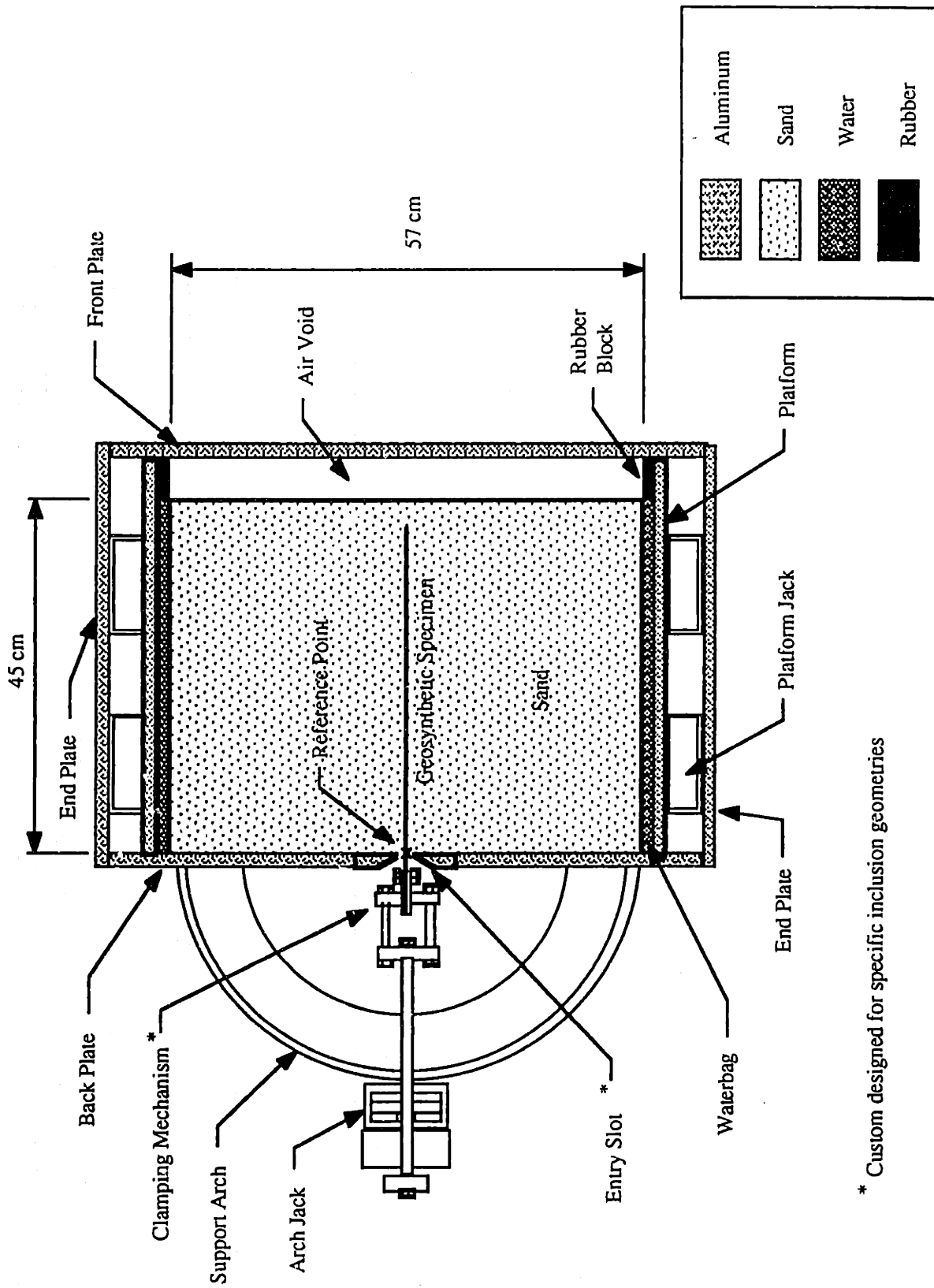


Figure 3.2: Conceptual Design of the APSR Cell (after Whittle et al., 1991).



* Custom designed for specific inclusion geometries

Figure 3.3: Cross Section Through the APSR Cell.
(Larson, 1992)

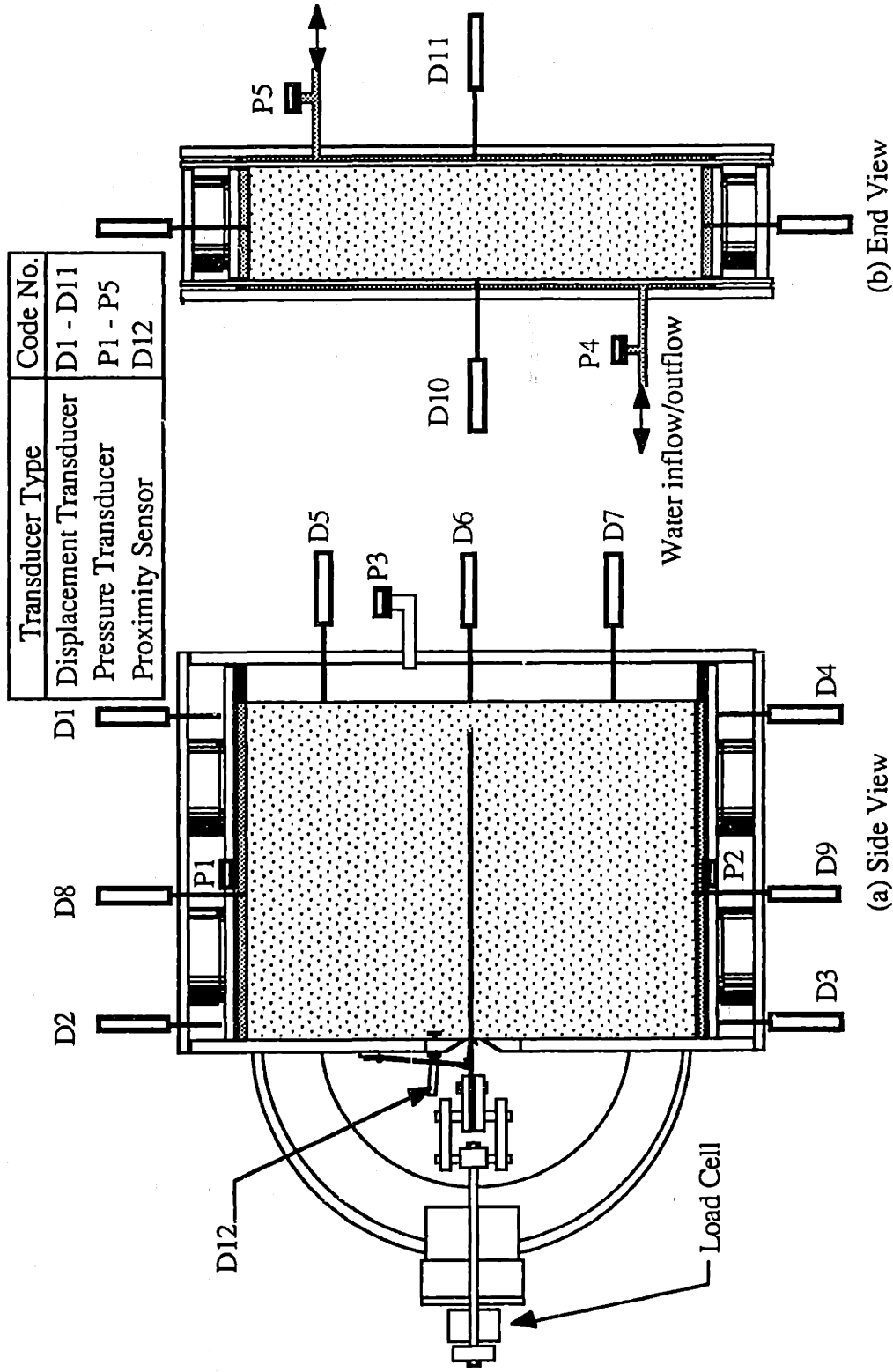


Figure 3.4: APSR Cell Instrumentation.
(after Larson, 1992)

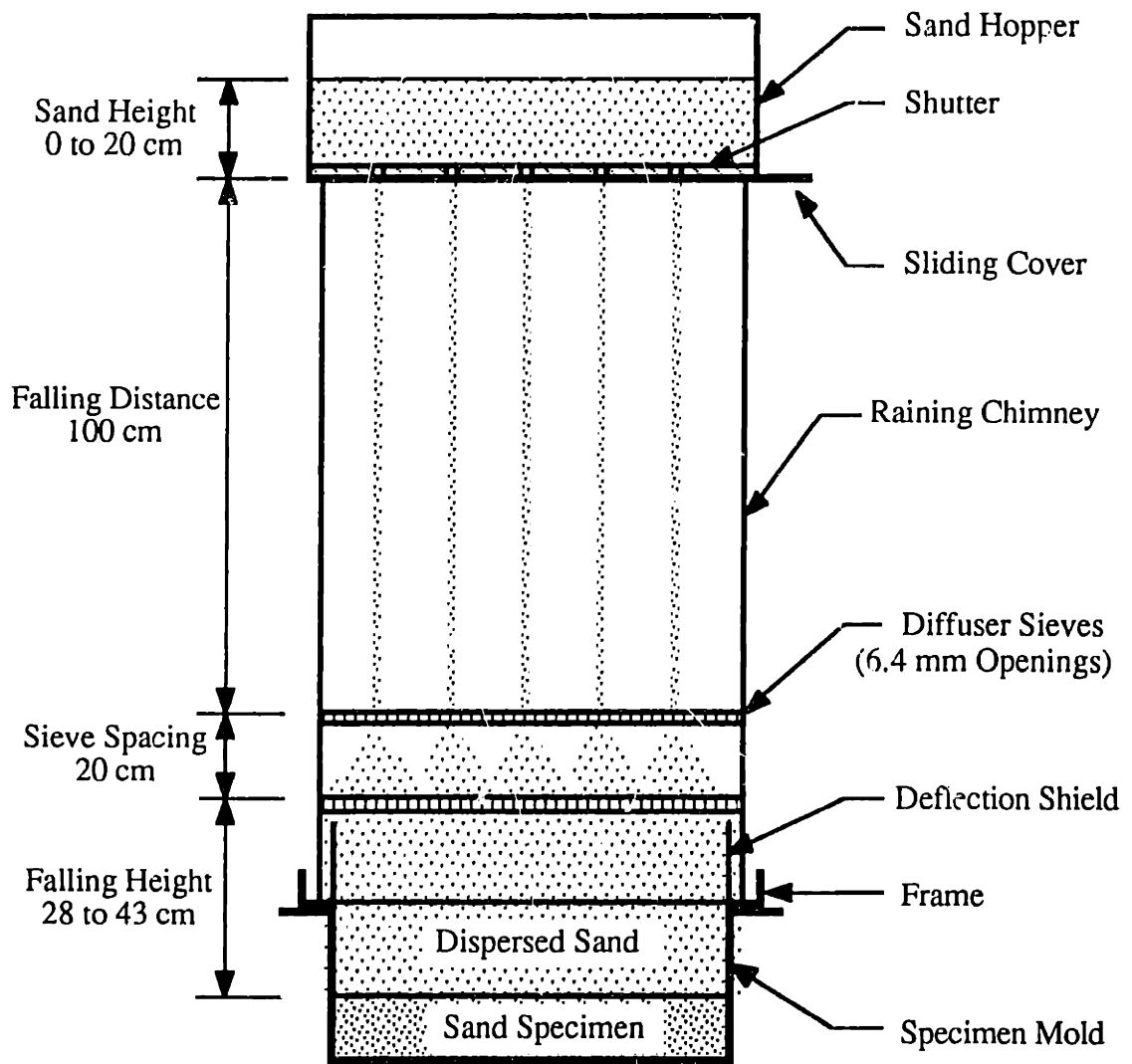
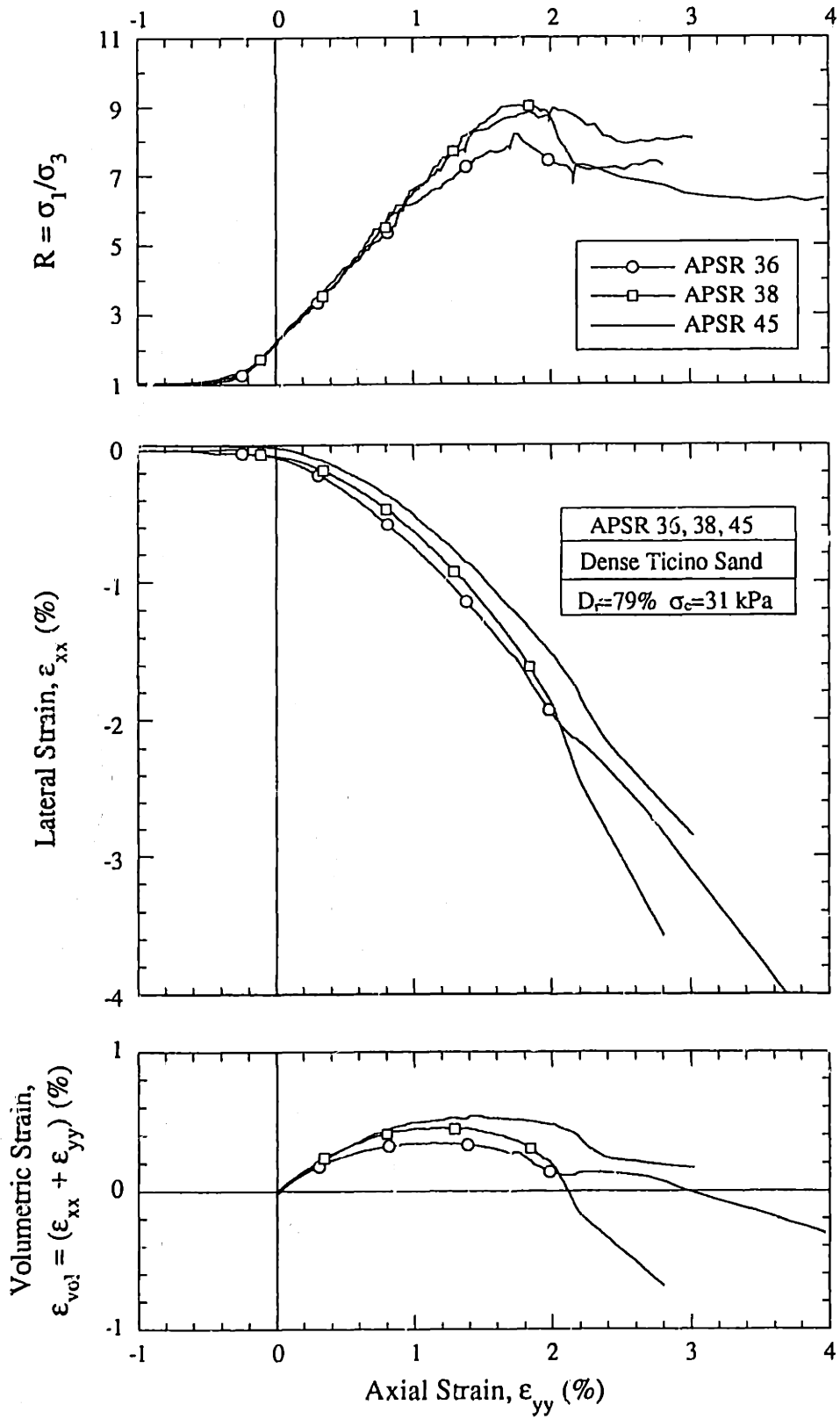


Figure 3.5: The APSR Cell Raining Apparatus.
(after Larson, 1992)



Note: Lateral strains: measured at centerline of specimens by transducer D6 (Fig. 3.4).

Figure 3.6: Repeatability of Externally Measured Shear Behavior (after Larson, 1992).

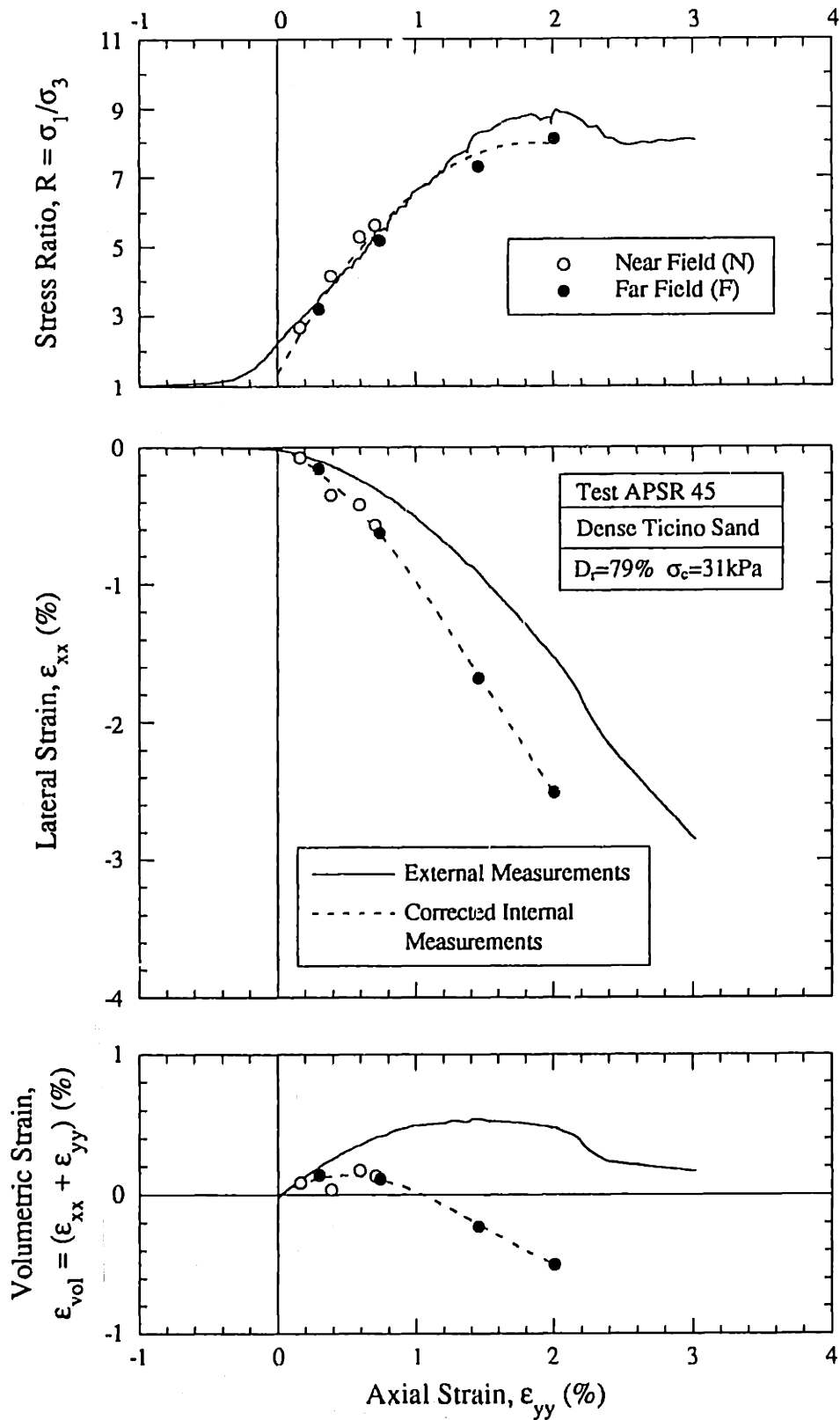


Figure 3.7: Comparison of External and Corrected Internal Measurements for Dense Ticino Sand (after Larson, 1992).

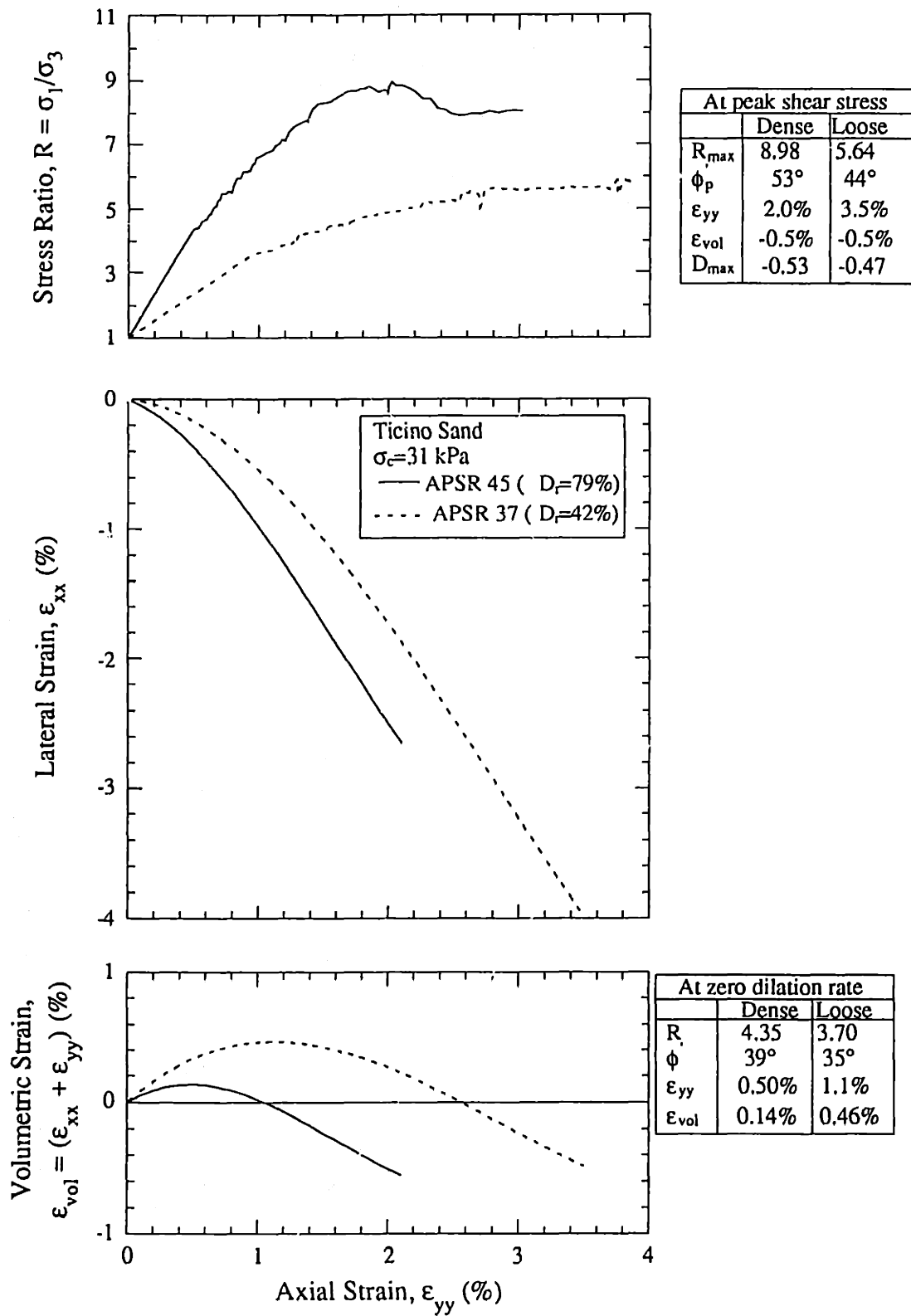
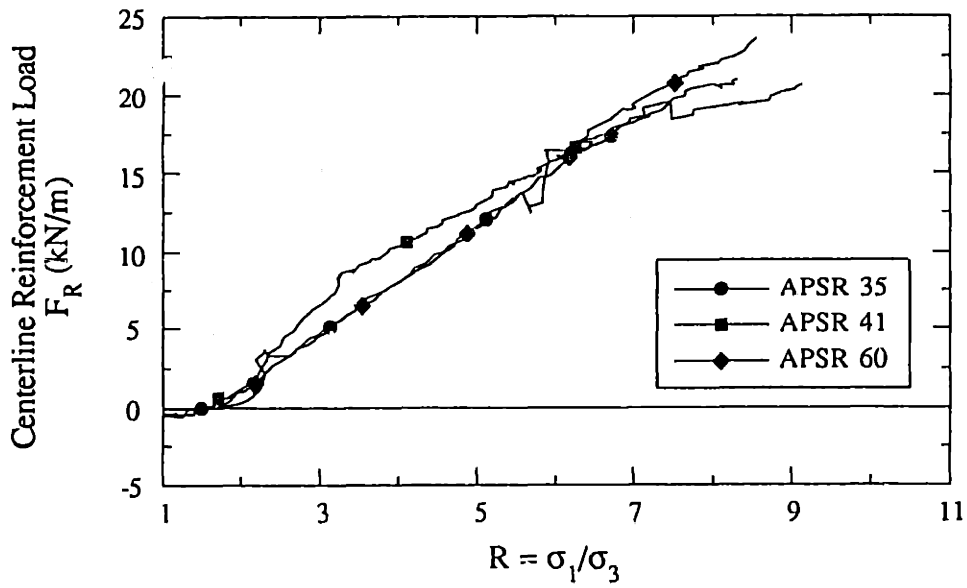
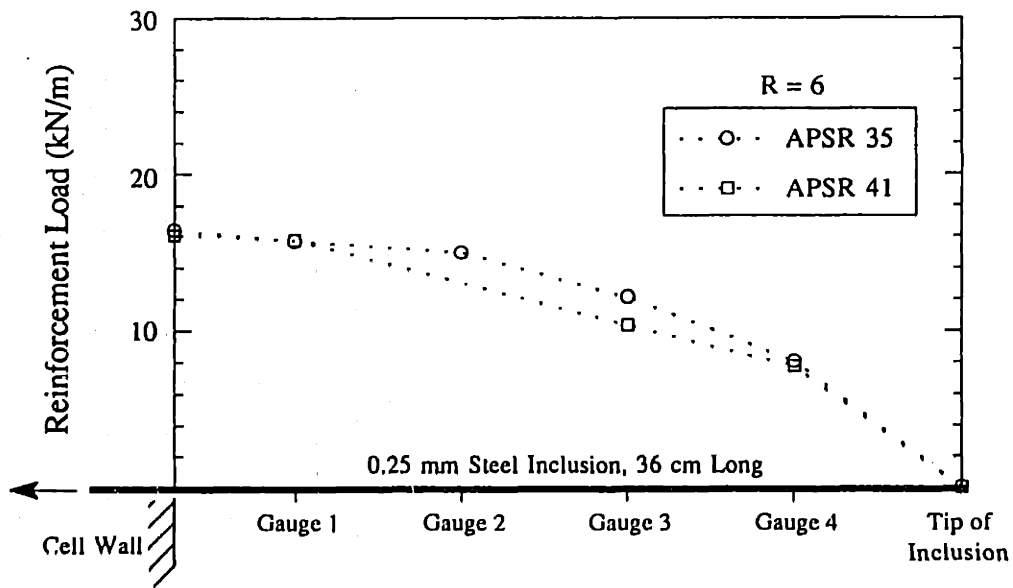


Figure 3.8: Estimated Plane Strain Shear Behavior of Ticino Sand.
 (after Larson, 1992)



(a) Centerline loads (external load cell)



(b) Load distribution (external load cell and strain gauges)

Figure 3.9: Comparison of Load Pickup Measurements for Base-Case Tests in Dense Ticino Sand (after Larson, 1992).

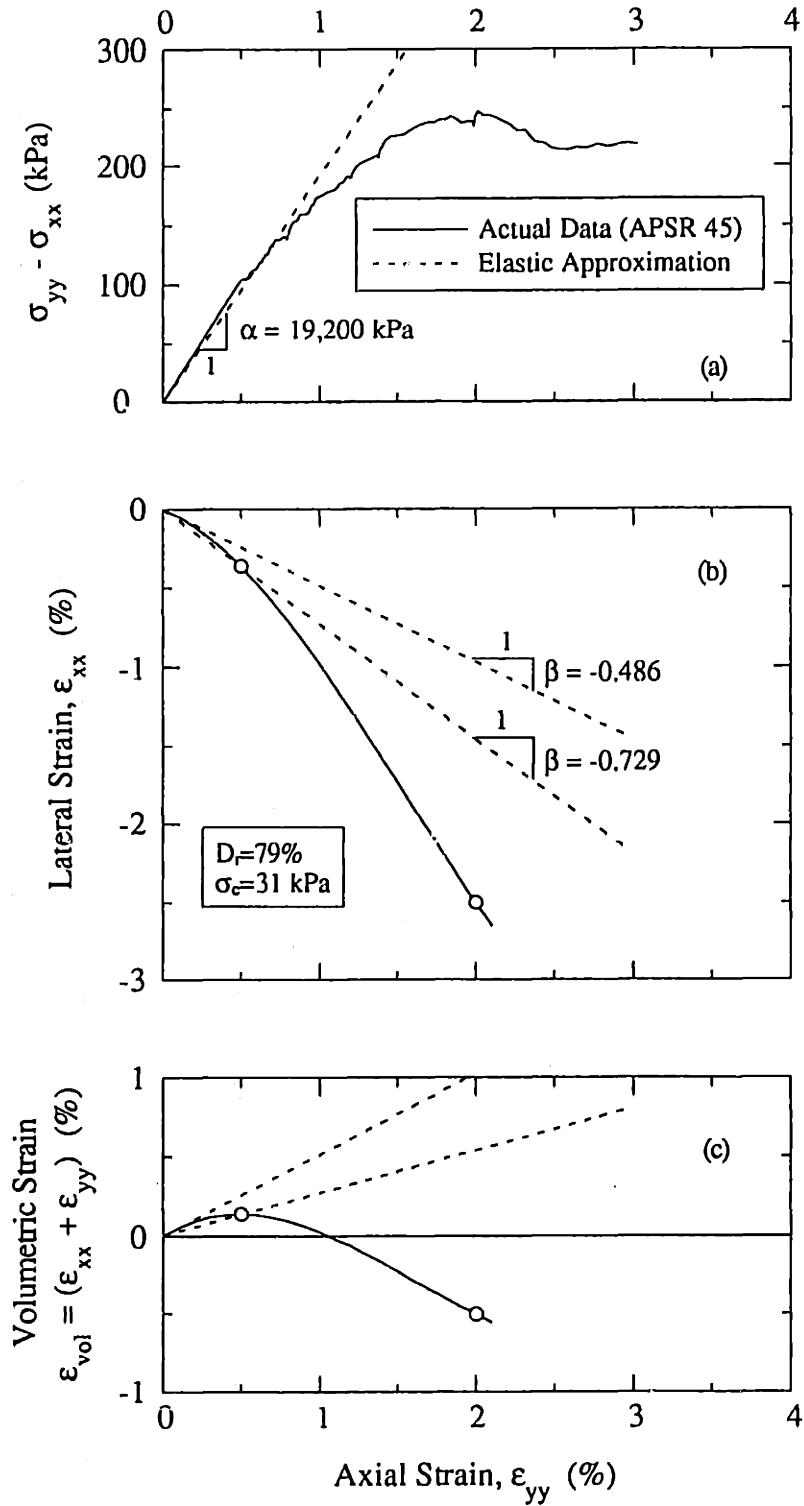


Figure 3.10: Elastic Approximations to Plane Strain Behavior of Dense Ticino Sand.

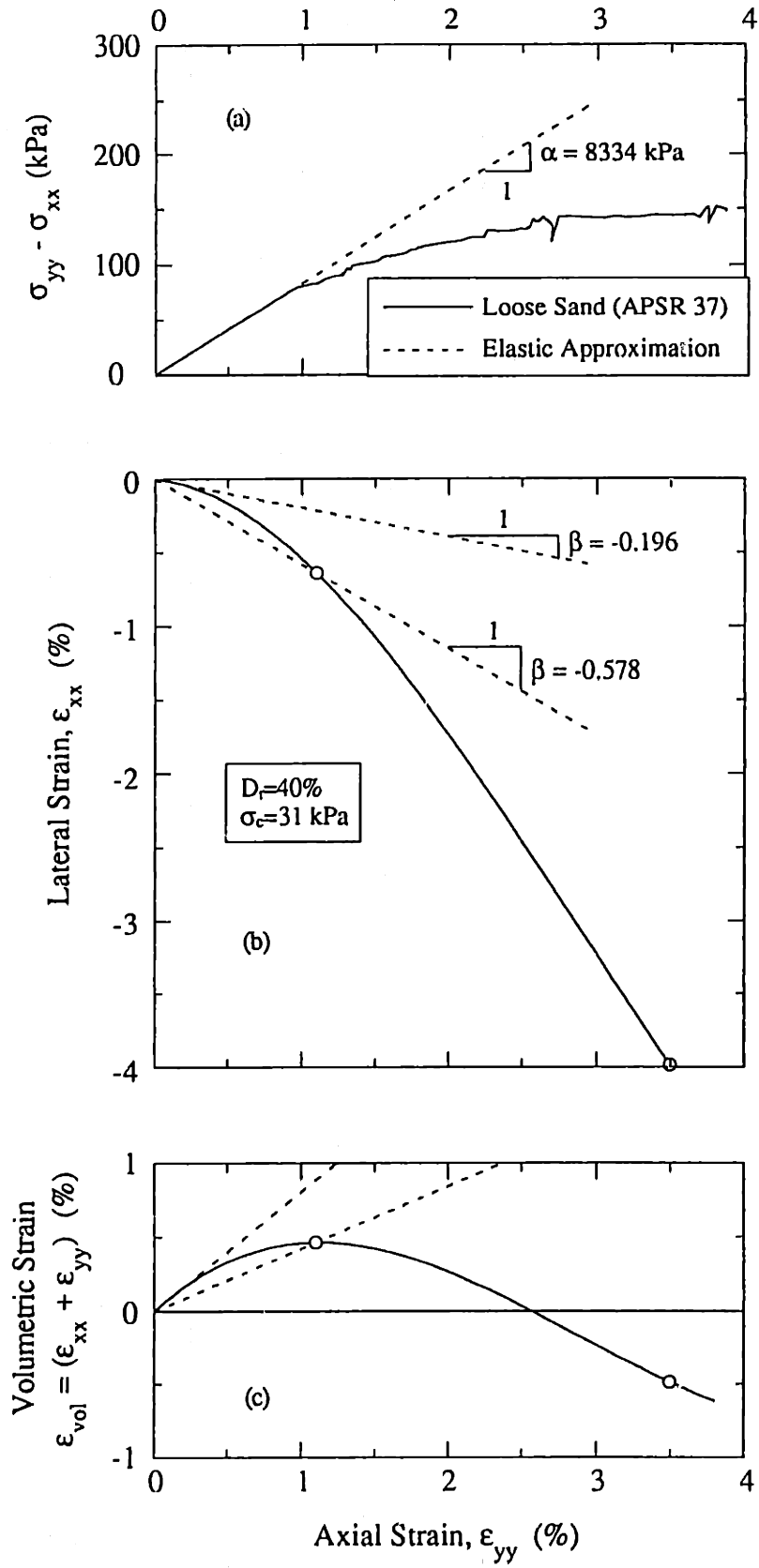
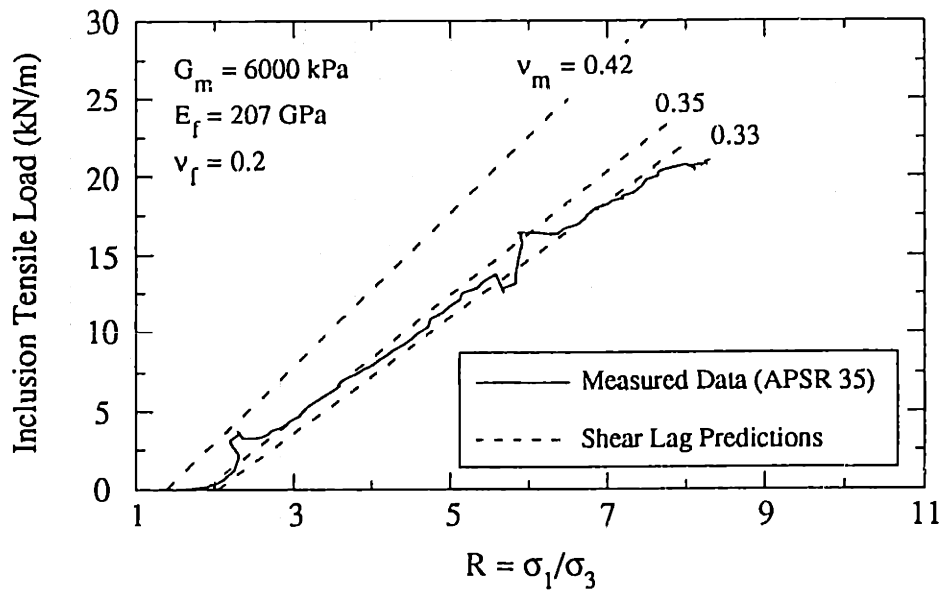
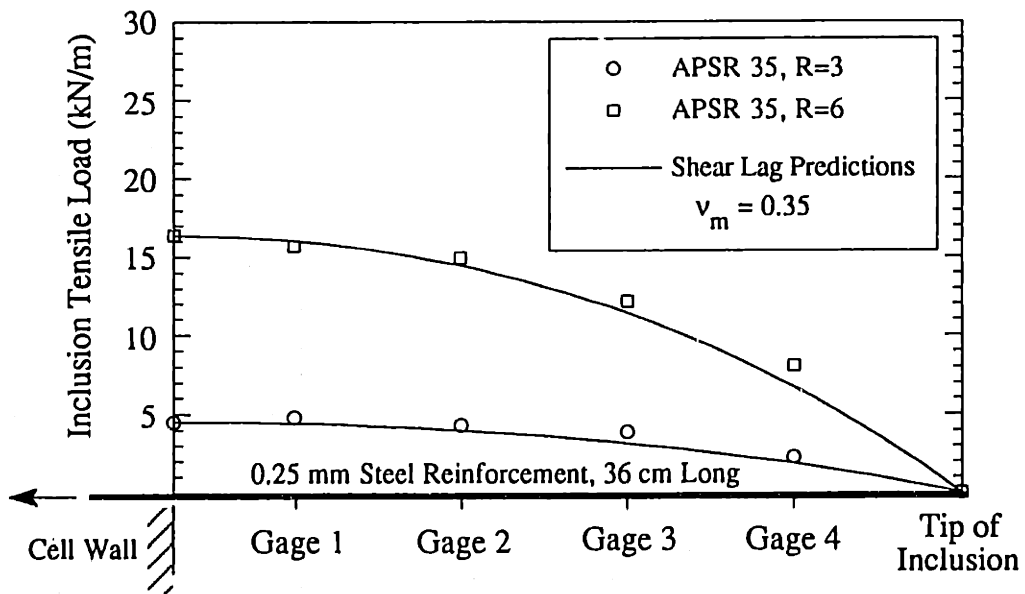


Figure 3.11: Elastic Approximations to Plane Strain Behavior of Loose Ticino Sand.

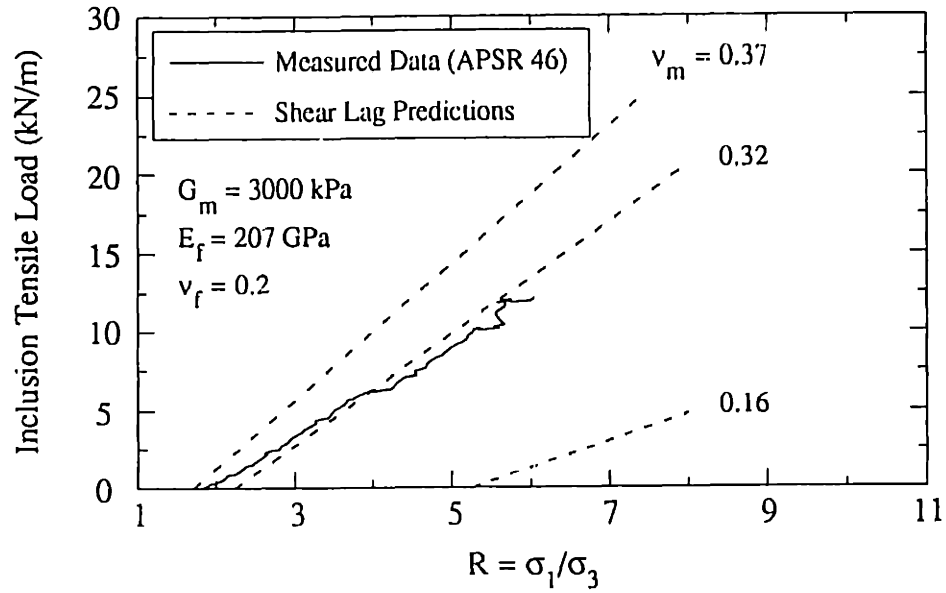


(a) Predicted vs. measured tensile load at inclusion centerline

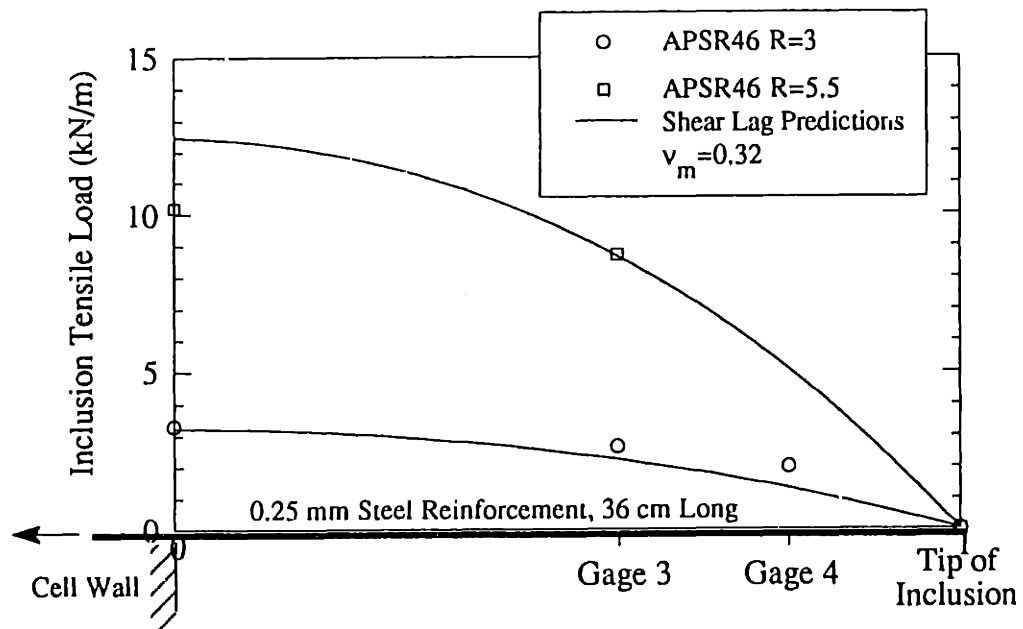


(b) Predicted vs. measured inclusion load distribution

Figure 3.12: Comparison of Shear-Lag Predictions of Inclusion Tensile Loads to Measured Data for a Base-Case Test.

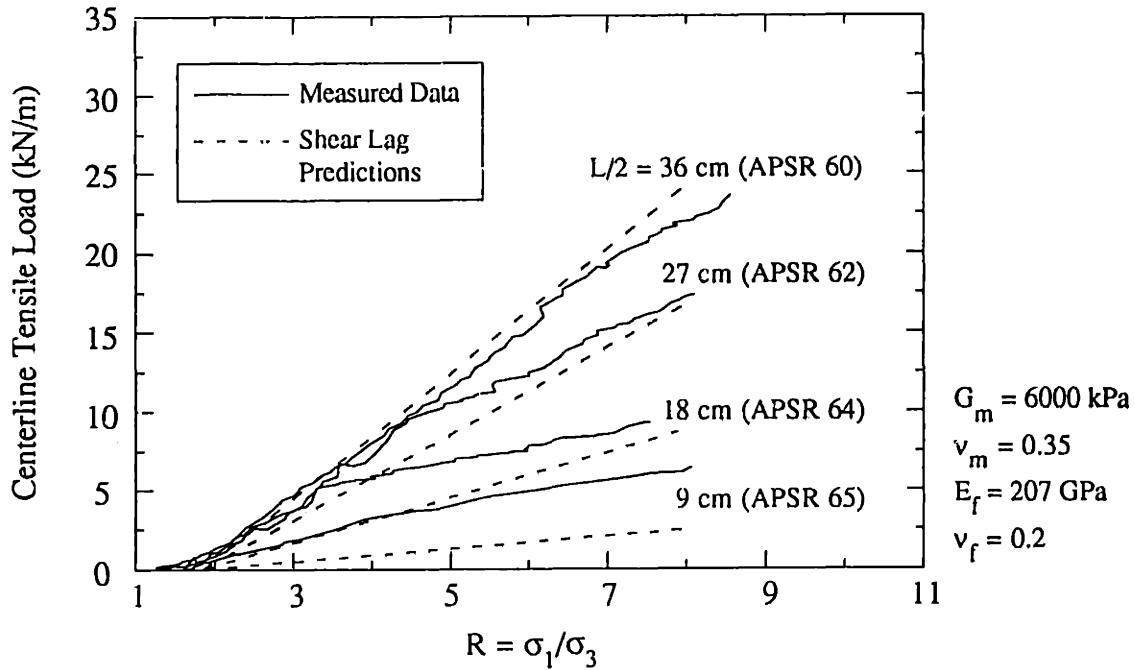


(a) Predicted vs. measured tensile load at inclusion centerline

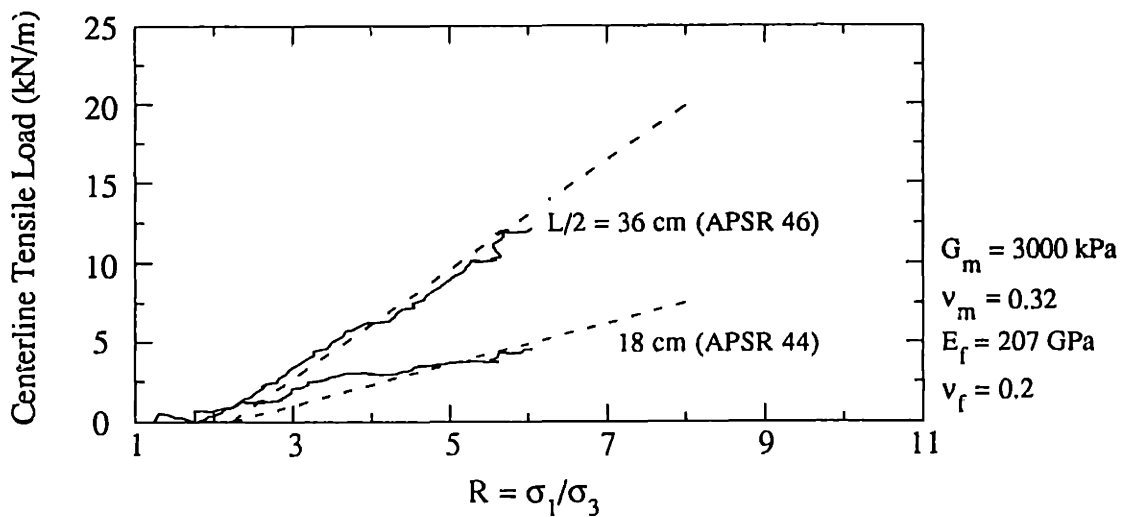


(b) Predicted vs. measured inclusion load distribution

Figure 3.13: Comparison of Shear Lag Predictions of Inclusion Tensile Loads to Measured Data for Loose Sand.



(a) Predicted vs. measured tensile load at inclusion centerline for dense sand



(b) Predicted vs. measured tensile load at inclusion centerline for loose sand

Figure 3.14: Shear Lag Predictions vs. Measured Inclusion Tensile Loads for Inclusions of Different Lengths.

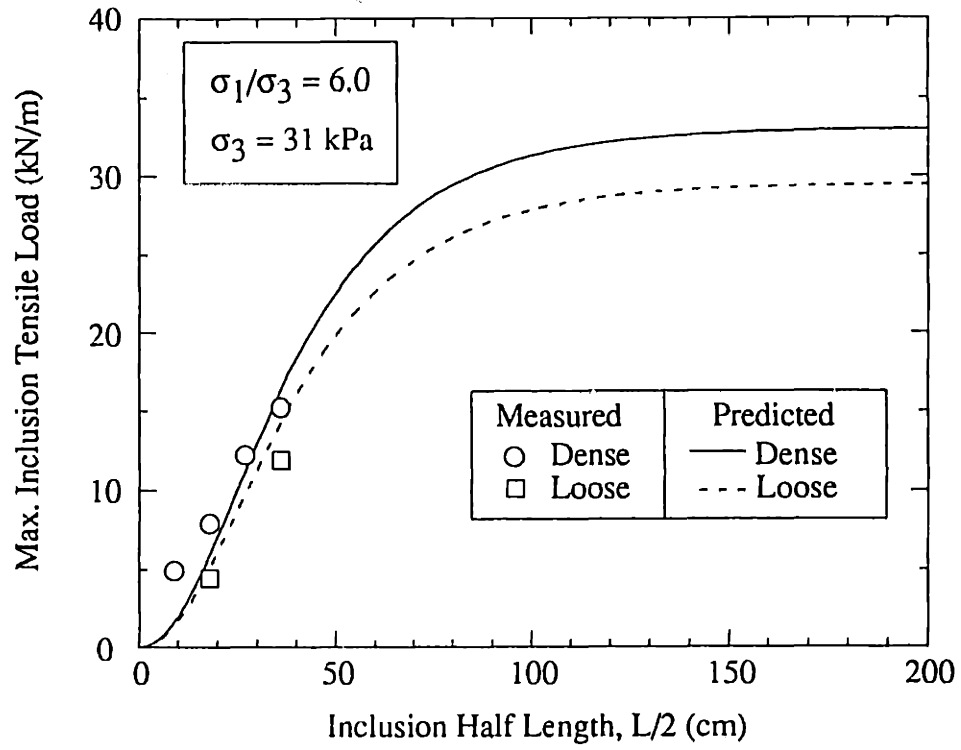


Figure 3.15: Predicted vs. Measured Maximum Tensile Force in Inclusion at R = 6.0.

Appendix 3.A: References

- Abramento, M. and Whittle, A. J. (1993) "Shear-Lag Analysis of a Planar Soil Reinforcement in Plane Strain Compression", *ASCE Journal of Engineering Mechanics*, 119(2), 270-291.
- Arthur, J.R.F., and Menzies, B.K. (1972) "Inherent Anisotropy in a Sand", *Géotechnique*, 22(1), 115-128.
- Baldi, G., et al. (1985) "Laboratory Validation of In-Situ Tests", *AGI Jubilee Volume, Proc. 11th International Conference on Soil Mechanics and Foundation Engineering*, San Francisco, CA.
- Chauhan, S. (1993) PhD Thesis in progress, MIT.
- Cox, H.L. (1952) "The Elasticity and Strength of Paper and Other Fibrous Materials", *British Journal of Applied Physics*, 3, 72-79.
- Green, G.E., and Reades, D.W. (1975) "Boundary Conditions, Anisotropy and Sample Shape Effects on the Stress-Strain Behaviour of Sand in Triaxial Compression and Plane Strain", *Géotechnique*, 25(2), 333-356.
- Larson, D.G. (1992) "A Laboratory Investigation of Load-Transfer in Reinforced Soil", Ph.D. Thesis, Massachusetts Institute of Technology, Cambridge, MA.
- McGown, A., and Andrawes, K.Z. (1977) "The Influences of Non-Woven Fabric Inclusions on the Stress-Strain Behaviour of a Soil Mass", *C. R. Coll. Int. Sols Textiles*, Paris, 161-165.

- McGown, A., Andrawes, K.Z., and Yeo, K.C. (1985) "The Load-Strain-Time Behaviour of Tensar Geogrids", *Polymer Grid Reinforcement*, Thomas Telford Ltd., London, 11-17.
- Miura, S., and Toki, S. (1983) "A Sample Preparation Method and Its Effect on Static and Cyclic Deformation-Strength Properties of Sand", *Soils and Foundations*, 22(1), 61-77.
- Palmeira, E.M., and Milligan, G.W.E. (1989) "Scale and Other Factors Affecting the Results of Pullout Tests of Grids Buried in Sand", *Géotechnique*, 39(3), 511-524.
- Rad, N.S. and Tumay, M.T. (1987) "Factors Affecting Sand Specimen Preparation by Raining", *ASTM Geotechnical Testing Journal*, 10(1), 31-37.
- Seah, T.H. (1990) "*Anisotropy of Resedimented Boston Blue Clay*", Ph.D. Thesis, Massachusetts Institute of Technology, Cambridge, MA.
- Tatsuoka, F., Sakamoto, M., Kawamura, T., and Fukushima, S. (1986) "Strength and Deformation Characteristics of Sand in Plane Strain Compression at Extremely Low Pressures", *Soils and Foundations*, 26(1), 65-84.
- Whittle, A.J., Larson, D.G., and Abramento, M. (1991) "Annual Technical Report on Geosynthetic Reinforcement of Soil Masses", *Research Report, Department of Civil Engineering, Massachusetts Institute of Technology*.

Appendix 3.B: Notation

The following symbols are used in Chapter 3:

D_r	=	relative density
E_f	=	inclusion elastic modulus
E_m	=	soil matrix elastic modulus
f	=	inclusion thickness
F_R	=	force at reinforcement centerline
G_m	=	soil matrix shear modulus
K_0	=	coefficient of lateral stress at rest
L	=	inclusion length
m	=	soil matrix height
R	=	ratio σ_1/σ_3
R_0	=	offset stress ratio
x	=	distance along inclusion
y	=	distance along soil matrix
α, β	=	parameter described by 3.3, 3.4
$\epsilon_{xx}, \epsilon_{yy}, \epsilon_{zz}$	=	strains in x, y and z directions
ϵ_{vol}	=	volumetric strain
ϵ_f	=	mobilized axial strain at peak stress ratio R
ϕ'	=	mobilized friction
γ_d	=	dry density
ν_f	=	inclusion Poisson's ratio
ν_m	=	soil matrix Poisson's ratio
σ_1, σ_3	=	major and minor external principal stresses
$\sigma_{xx}, \sigma_{yy}, \sigma_{zz}$	=	stresses in x, y and z directions

Chapter 4: Effects of Inclusion Orientation

4.1 Introduction

In the previous analyses (Chapter 2), the planar reinforcement is oriented in the direction of maximum tensile strain in the soil. Tensile stresses develop in the reinforcement as the soil mass is sheared, with increasing values of σ_1/σ_3 . The experimental results (Chapter 3) confirm that this is an efficient mode of interaction for achieving load transfer with tensile reinforcements. Mechanisms of interaction become more complex when the reinforcement is not coaxial with the maximum tensile strain directions in the soil. These conditions can occur when a) the inclusion is positioned at an angle θ to the minor, external principal stress directions ($\sigma_3=\sigma_h$ when $\tau=0$, Fig. 4.2); and/or b) there is rotation of the external principal stress directions due to shear stresses acting on vertical planes (i.e., $\tau\neq 0$, Fig. 4.2). These situations are common in practical field situations (slopes, embankments, walls and foundations) and have important implications for effective positioning of tensile reinforcements within the soil mass (e.g. Bassett and Last, 1978; McGown et al., 1978).

Many of the existing laboratory studies of soil-reinforcement interaction have focused on the effects of inclusion orientation as shown in Table 4.1. For example, McGown et al. (1978) report measurements of boundary tractions and displacements for plane strain compression tests on sand specimens in a 'unit cell', with single planar reinforcements oriented at angle θ to the external, minor principal stress. The experiments performed at $\theta=0^\circ$ correspond to the same base case geometry used in the design of the APSR cell.

In contrast to the unit cell, there is continuous rotation of principal stress directions in direct simple shear and shear box tests. In these experiments, the specimen is loaded by applying a shear force T at constant normal load N (Fig. 4.1). Direct shear box tests simulate soil-reinforcement interactions for inclusions bisecting the imposed horizontal failure plane (at various angles θ or i) in the soil specimen, and positioned to preserve the symmetry between the top and bottom halves of the shear box. More uniform deformation conditions are achieved in direct simple shear tests such as those reported by Hayashi et al. (1988) (Table 4.1). Direct shear box test data are reported by several authors (Gray and Ohashi, 1983; Jewell and Wroth, 1987; Palmeira and Milligan, 1989; Shewbridge and Sitar, 1989) using a wide range of reinforcing materials and specimen dimensions. In these experiments the primary measurements are the boundary displacements and forces. The effects of reinforcement are interpreted almost exclusively from the limit equilibrium analyses of peak strength conditions. However, photogrammetric and radiographic techniques (Palmeira, 1987; Jewell, 1980) have also been used to observe deformations of the inclusions. The importance of orientation on mechanisms of soil-reinforcement interaction can be appreciated most readily from photo-elastic measurements reported by Dyer and Milligan (1984), using a model granular material (crushed glass). Figure 4.1 shows their results for planar reinforcements (perforated brass) at three different orientations ($i=40^\circ$, 0° and -45°). The light stripes indicate the major principal stress trajectory in the soil, while their intensity indicates the magnitude of the stress. For the inclusion oriented at 40° , there is a large concentration of compressive stress in the surrounding soil, which is indirect evidence of tensile stresses transferred to the reinforcement. In contrast, at $i=-45^\circ$, the inclusion has practically no effect on the soil stresses and, hence, is ineffective as reinforcement. For $i=0^\circ$, compressive stress concentration occurs mainly at the center of the specimen where there is significant distortion of the planar reinforcement. In this case, the shear and bending of the inclusion are important mechanisms of load transfer.

This chapter proposes a simple generalization of the original shear-lag analysis presented previously (Chapter 2) in order to predict tensile stresses in planar reinforcements at arbitrary orientation. The analysis applies to working stress conditions where there are small deformations within the soil mass and assumes that thin planar reinforcements have negligible bending stiffness. Sections 4.2 and 4.3 give full details of the formulation and typical results, while section 4.4 applies the analysis to interpret some of the data reported in the literature (Table 4.1).

4.2 Formulation

Figure 4.2 shows the idealized geometry of a plane strain soil specimen of height m and width w , which contains a single planar reinforcement of length L , oriented at an angle θ to the horizontal. The inclusion is placed symmetrically within the soil specimen (centerline at 0, Fig. 4.2) with local coordinate axes (x, y) rotated relative to the global reference frame, (x^*, y^*) . Initially, the formulation focuses on inclusions at relatively shallow orientations, $|\theta| \leq |\theta_1|$, where θ_1 is defined by:

$$\sin \theta_1 = \left[1 + \left(\frac{w}{m} \right)^2 \right]^{-1} \left\{ \left(\frac{w}{m} \right) \left[1 + \left(\frac{w}{m} \right)^2 - \left(\frac{L}{m} \right)^2 \right]^{1/2} - \left(\frac{L}{m} \right) \right\} \quad (4.1)$$

This condition restricts the orientation such that sections normal to the reinforcement and passing through the tips of the inclusion (i.e., $x = \pm L/2$; Fig. 4.2) bisect the top and bottom boundaries of the soil specimen. Generalizations for arbitrary θ are described in section 4.2.1.

Uniform normal and shear tractions (σ_v, τ) and (σ_h, τ) act on the horizontal and vertical boundaries. Stress components in the local reference frame (x, y) of the unreinforced soil element are given by:

$$\sigma_{xx}^0 = \sigma_h \cos^2 \theta + \sigma_v \sin^2 \theta - \tau \sin 2\theta \quad (4.2a)$$

$$\sigma_{yy}^0 = \sigma_h \sin^2 \theta + \sigma_v \cos^2 \theta + \tau \sin 2\theta \quad (4.2b)$$

$$\sigma_{xy}^0 = \frac{1}{2} \sin 2\theta (\sigma_h - \sigma_v) + \tau \cos 2\theta \quad (4.2c)$$

and the major principal stress is oriented at an angle ξ^* to the vertical direction y^* :

$$\tan 2\xi^* = \frac{2\left(\frac{\tau}{\sigma_v}\right)}{\left(1 - \frac{\sigma_v}{\sigma_h}\right)} \quad (4.2d)$$

The proposed analysis of the reinforced soil composite assumes the following:

1. The soil and reinforcement behave as linear, isotropic and elastic materials (with properties $G_m, \nu_m; E_f, \nu_f$, respectively).
2. The inclusion is very thin ($f \ll w, m, L$) and, hence, has negligible bending stiffness. There is no load transfer at the ends of the inclusion (i.e., $\sigma_{xx}^f = 0$ at $x = \pm L/2$).
3. There is no slippage between soil and reinforcement. This assumption is only valid while the ratio of the local shear to normal tractions are less than the interface friction between the soil and reinforcing materials (i.e., $|\sigma_{xy}^i / \sigma_{yy}^i| < \mu$, where $\mu = \tan \delta$, and δ is the interface friction angle).
4. The 'axial' stress component in the soil matrix σ_{xx}^m is a function of x only, which is the generalization of the condition in equation 2.2 in Chapter 2. For an inclined reinforcement ($\theta \neq 0$), it is essential to separate stress conditions above and below the plane of the reinforcement, as indicated in Figure 4.3. The stress components σ_{xx}^{ma} and σ_{xx}^{mb} refer to average stresses acting in an arbitrary plane $x = x_1$ (where $-L/2 \leq x \leq L/2$; Fig. 4.3) above and below the reinforcement, respectively. The axial stress components can be related to the tensile stress in the reinforcement by considering the equilibrium for an arbitrary cross-section such as A-A in Figure 4.3. Equilibrium forces in the x -direction and moments about O' for the free body (shaded region, Fig. 4.3) give, respectively:

$$\sigma_{xx}^{ma} (y_c + x \tan \theta) + \sigma_{xx}^{mb} (y_c - x \tan \theta) - \sigma_{xx}^f f = \sigma_{xx}^0 m \sec \theta \quad (4.3a)$$

$$\sigma_{xx}^{ma} (y_c + x \tan \theta)^2 - \sigma_{xx}^{mb} (y_c - x \tan \theta)^2 - 2 \sigma_{xx}^0 m x \sec \theta \tan \theta = 0 \quad (4.3b)$$

where $y_c = (m/2 \cos \theta - f/2)$ is the lateral dimension of the soil matrix in the plane $x=0$. Geometric limitations on θ given m , w and L are discussed in section 4.2.1. Equations 4.3a, b can be re-arranged to obtain the components σ_{xx}^m (assuming $f \ll m$):

$$\sigma_{xx}^{ma} = \frac{f (y_c - x \tan \theta)}{2y_c (y_c + x \tan \theta)} \sigma_{xx}^f + \sigma_{xx}^0 \quad (4.4a)$$

$$\sigma_{xx}^{mb} = \frac{f (y_c + x \tan \theta)}{2y_c (y_c - x \tan \theta)} \sigma_{xx}^f + \sigma_{xx}^0 \quad (4.4b)$$

Hence, stresses along the centerline of the element ($x=0$) can be found:

$$\sigma_{xx}^m = \sigma_{xx}^{ma} = \sigma_{xx}^{mb} = \frac{f}{2y_c} \sigma_{xx}^f + \sigma_{xx}^0 \quad (4.5)$$

Neglecting body forces, equilibrium equations in the soil matrix (above and below the plane of the reinforcement) and inclusion can be written:

$$\frac{\partial \sigma_{xx}^m}{\partial x} + \frac{\partial \sigma_{xy}^m}{\partial y} = 0 \quad (4.6a)$$

$$\frac{\partial \sigma_{xy}^m}{\partial x} + \frac{\partial \sigma_{yy}^m}{\partial y} = 0 \quad (4.6b)$$

$$\sigma_{xy}^{ia} - \sigma_{xy}^{ib} = f \frac{d\sigma_{xx}^f}{dx} \quad (4.6c)$$

where σ_{xy}^{ia} , σ_{xy}^{ib} are the shear tractions acting on either side of the soil-reinforcement interface.

Assuming that σ_{xx}^m is constant along any section normal to the reinforcement, the shear stresses in the soil matrix are given by¹:

¹The normal stress distribution in the soil matrix σ_{yy}^m was not determined due to algebraic difficulties.

$$\sigma_{xy}^m = \sigma_{xy}^i - \left[\frac{\left(y - \frac{f}{2}\right)}{(y_c + x \tan \theta)} \right] \left\{ \sigma_{xy}^i - [\tau + (\sigma_{xx}^m - \sigma_v) \tan \theta] \right\} \quad (4.7)$$

where σ_{xy}^m is a linear function of y , which satisfy interface and specimen boundary conditions (cf. Fig. 4.3). The interface tractions above and below the plane of reinforcement can be obtained from equations 4.3 to 4.7:

$$\sigma_{xy}^{ia} = \frac{f}{2y_c} (y_c - x \tan \theta) \frac{d\sigma_{xx}^f}{dx} - \frac{f}{2y_c} \tan \theta \sigma_{xx}^f + \sigma_{xy}^0 \quad (4.8a)$$

$$\sigma_{xy}^{ib} = -\frac{f}{2y_c} (y_c + x \tan \theta) \frac{d\sigma_{xx}^f}{dx} - \frac{f}{2y_c} \tan \theta \sigma_{xx}^f + \sigma_{xy}^0 \quad (4.8b)$$

and

$$\sigma_{yy}^{ia} = \frac{f}{4y_c} (y_c^2 - x^2 \tan^2 \theta) \frac{d^2 \sigma_{xx}^f}{dx^2} - \frac{f}{y_c} \tan \theta (y_c - x \tan \theta) \frac{d\sigma_{xx}^f}{dx} + \frac{f}{2y_c} \tan^2 \theta \sigma_{xx}^f + \sigma_{yy}^0 \quad (4.9a)$$

$$\sigma_{yy}^{ib} = \frac{f}{4y_c} (y_c^2 - x^2 \tan^2 \theta) \frac{d^2 \sigma_{xx}^f}{dx^2} + \frac{f}{y_c} \tan \theta (y_c + x \tan \theta) \frac{d\sigma_{xx}^f}{dx} + \frac{f}{2y_c} \tan^2 \theta \sigma_{xx}^f + \sigma_{yy}^0 \quad (4.9b)$$

Average axial stresses in soil matrix and interface tractions at the center of the inclusion ($x=0$) are given by:

$$\sigma_{xy}^i = \frac{f}{2} \frac{d\sigma_{xx}^f}{dx} + \sigma_{xy}^0 \quad (4.10a)$$

$$\sigma_{yy}^i = \frac{mf}{8 \cos \theta} \frac{d^2 \sigma_{xx}^f}{dx^2} + \frac{f}{2y_c} \tan^2 \theta \sigma_{xx}^f + \sigma_{yy}^0 \quad (4.10b)$$

Following same strategy described in Chapter 2, the shear-lag formulation relates stresses and strains in the direction of the inclusion by decoupling normal and shear stress components in the soil matrix (section 2.2). The decoupled model introduces a fictitious shear spring layer of lateral dimension \bar{y} , in which the matrix shear stress is constant and equal to the interface traction, i.e., $\bar{\sigma}_{xy}^m (|\bar{y}/2 \leq |y| \leq \bar{y}) = \sigma_{xy}^i$. The dimension \bar{y} is obtained by equating the elastic shear strain energy in the physical (real) and decoupled models (after

Budiansky et al. 1986). For thin planar inclusions at shallow orientation ($\theta \leq \theta_1$; eqn. 4.1), the dimension of the shear spring layer is given by:

$$\bar{y} = \frac{m}{3 c_0 \sin \theta} \quad (4.11)$$

The remaining derivation of strains and displacements in the decoupled model follows the original formulation. By combining equations 2.9, 4.5, 4.10 and 4.11 the tensile stress in the reinforcement can be expressed in the form of a second order ordinary differential equation:

$$\frac{d^2 \sigma_{xx}^f}{dx^2} - K_1(\theta) \sigma_{xx}^f + K_2(\sigma_v, \sigma_h, \tau, \theta) = 0 \quad (4.12)$$

where K_1 , K_2 are constant coefficients defined in terms of constituent material properties, orientation θ and boundary tractions (σ_v , σ_h , τ):

$$K_2(\sigma_v, \sigma_h, \tau, \theta) = K_2^v(\theta) \sigma_v + K_2^h(\theta) \sigma_h + K_2^\tau(\theta) \tau \quad (4.13)$$

$$K_1(\theta) = \frac{2}{\bar{y} f} \frac{\left\{ a \left(\cos \theta - \frac{v_m}{\cos \theta} \right) + 2 \frac{G_m}{E_f} (1 + v_f) [(1 - v_f) + a v_f \tan^2 \theta \cos \theta] \right\}}{\left[1 + \frac{1}{4} v_m - \frac{3}{2} \frac{G_m}{E_f} (1 + v_f) v_f \right]} \quad (4.13a)$$

$$K_2^v(\theta) = \frac{2}{\bar{y} f} \frac{\left[v_m - \sin^2 \theta - 2 \frac{G_m}{E_f} (1 + v_f) v_f \cos^2 \theta \right]}{\left[1 + \frac{1}{4} v_m - \frac{3}{2} \frac{G_m}{E_f} (1 + v_f) v_f \right]} \quad (4.13b)$$

$$K_2^h(\theta) = -\frac{2}{\bar{y} f} \frac{\left[\cos^2 \theta - v_m + 2 \frac{G_m}{E_f} (1 + v_f) v_f \sin^2 \theta \right]}{\left[1 + \frac{1}{4} v_m - \frac{3}{2} \frac{G_m}{E_f} (1 + v_f) v_f \right]} \quad (4.13c)$$

$$K_2^\tau(\theta) = \frac{2}{\bar{y} f} \frac{\left[1 - 2 \frac{G_m}{E_f} (1 + v_f) v_f \right] \sin 2\theta}{\left[1 + \frac{1}{4} v_m - \frac{3}{2} \frac{G_m}{E_f} (1 + v_f) v_f \right]} \quad (4.13d)$$

Due to symmetry, the boundary conditions for equation 4.12 are:

$$\begin{aligned}
x = \pm \frac{L}{2} & \quad ; \quad \sigma_{xx}^f = 0 \\
x = 0 & \quad ; \quad \frac{d\sigma_{xx}^f}{dx} = 0
\end{aligned}
\tag{4.14}$$

Hence, the general solution for the tensile stress in the reinforcement is given by:

$$\sigma_{xx}^f = \frac{K_2(\sigma_v, \sigma_h, \tau, \theta)}{K_1(\theta)} \left[1 - \frac{\cosh \sqrt{K_1(\theta)} x}{\cosh \sqrt{K_1(\theta)} \frac{L}{2}} \right]
\tag{4.15}$$

The complete expressions for the interface tractions are given by substituting 4.15 in 4.8 and 4.9, and are presented in Appendix 4.A.

4.2.1. Generalization for Arbitrary θ

In the preceding analysis, the tensile stresses and interface tractions ($\sigma_{xx}^f, \sigma_{xy}^i, \sigma_{yy}^i$) for reinforcements at shallow inclinations $\theta \leq \theta_1$ (eqn. 4.1) are affected by the height of the soil specimen m , but not by its overall width w . For overlength inclusions, the possible configurations are limited by the maximum orientation θ_{\max} , where: 1) for $w > L > m$, $\sin \theta_{\max} = m/L$; or b) $m > L > w$, in which case $\cos \theta_{\max} = w/L$. For inclusions of length $L < m, w$, further generalizations of the shear-lag analysis are needed to describe load transfer at arbitrary orientation, $0 \leq \theta \leq 90^\circ$. Two key assumptions are used in this analysis: 1) equilibrium equations are formulated in the centerline section ($x=0$) of the sample with characteristic dimension y_c ; and 2) the size of the shear spring layer \bar{y} is obtained from the lateral dimension of the specimen ($y^a + y^b$, Fig. 4.3) averaged over the length of the inclusion ($-L/2 \leq x \leq L/2$). Figure 4.4 illustrates the effects of inclusion orientation θ on the dimensions y_c and \bar{y} :

1. For $\theta_1 < \theta < \theta_L$, where $\tan \theta_L = w/m$ (Figs. 4.4c), the width of the soil specimen causes a reduction in the apparent lateral dimension of the shear spring layer \bar{y} , which is related to the area A_1 :

$$\bar{y} = \frac{1}{3} \left[\frac{m}{\cos\theta} - \frac{1}{L \tan\theta} \left(\frac{L}{2\cos\theta} - \frac{w}{2} + \frac{m}{2} \tan\theta \right)^2 \right] \quad (4.16)$$

2. For $\theta_L < \theta < \theta_2$ (Fig. 4.4e), the centerline equilibrium equations are written in terms of the specimen width w , while \bar{y} depends on both m and w as shown in Table 4.2.

3. For $\theta > \theta_2$ \bar{y} is controlled only by the width of the specimen.

Figure 4.5 illustrates variations in the thickness of the shear spring layer \bar{y}/L as a function of orientation θ , for practical values of the aspect ratios w/L and m/L .

Thus, complete solutions for the tensile stress and interface tractions are obtained by substituting the results from Table 4.2 in equations 4.8, 4.9, 4.16, A.1 and A.2.

4.3. Results

The proposed shear lag analysis derives the axial inclusion stress σ_{xx}^f and interface tractions σ_{xy}^i , σ_{yy}^i as functions of the external stresses (σ_v , σ_h , τ). The behavior is affected by the constituent material properties (E_f/G_m , ν_m , ν_f) and specimen geometry (L , m , w , θ and f).

4.3.1. Plane Strain Compression of Soil Specimen

Figure 4.6 presents distributions of σ_{xx}^f , σ_{xy}^i and σ_{yy}^i for an inclusion of length $L=1m$, embedded at different orientations θ , within a soil specimen of dimensions $m=0.8m$ and $w=1.6m$. All results are normalized by the vertical stress σ_v . For this particular geometry ($w>L>m$) $\theta_{max}=53^\circ$, while shallow orientations correspond to $\theta<\theta_1$, where $\theta_1=29.5^\circ$. The composite is sheared in plane strain compression (i.e. $\tau=0$, $\xi^*=0^\circ$) at a stress ratio $\sigma_v/\sigma_h=\sigma_1/\sigma_3=6$. The calculations assume typical/representative values of the constituent material properties. The results show the following:

1. The tensile stress distribution (Fig. 4.6a) is symmetric, $\sigma_{xx}^f(x) = \sigma_{xx}^f(-x)$, with maximum values at the centerline ($x=0$). Maximum load transfer occurs when the inclusion is oriented at $\theta=0^\circ$ (base case geometry considered in Chapter 2), which corresponds to the direction of maximum tensile strains in the unreinforced soil element. There is no load transfer ($\sigma_{xx}^f=0$) when the inclusion is oriented in the zero extension direction of the unreinforced element², $\theta=28^\circ$. For $\theta>28^\circ$, inclusion is loaded in compression ($\sigma_{xx}^f<0$) and, hence, achieves no effective reinforcement of the soil composite.

2. For inclined reinforcements, there is reflective symmetry in the interface shear tractions acting along the top and bottom surfaces of the inclusion, such that $\sigma_{xy}^{ia}(x) = \sigma_{xy}^{ib}(-x)$ (Fig. 4.6b). The interface shear traction (on either side of the inclusion) increases as the proximity to the lateral boundary reduces, with maximum and minimum values at either end of the inclusion. The gradient $d\sigma_{xy}^i/dx$ is non-zero at the centerline and confirms previous observations (section 2.4.1) that full load-transfer is not achieved for the selected material properties and inclusion geometry. At $\theta=28^\circ$, $\sigma_{xy}^{ia}/\sigma_v = \sigma_{xy}^{ib}/\sigma_v = 0.35$ corresponding to the shear stress in the unreinforced soil element ($\sigma_{xy}^0/\sigma_v = 0.5 \sin 2\theta [1 - \sigma_h/\sigma_v]$).

3. The normal interface traction (Fig. 4.6c) also exhibits reflective symmetry between top and bottom faces of the inclusion. In all cases, $\sigma_{yy}^i/\sigma_v < 1$ as the inclusion is too short to achieve full load transfer (cf. Fig. 2.3). Minimum values of σ_{yy}^i occur at the ends of inclusion where σ_{xy}^i is a maximum. At $\theta=28^\circ$, $\sigma_{yy}^i/\sigma_v = \sigma_{yy}^0/\sigma_v = 0.82$ is uniform at all locations along the inclusion.

The principal factors affecting the maximum load transfer at the center of the inclusion, σ_{max}^f/σ_v (i.e., $\sigma_{xx}^f(0)/\sigma_v$) are: 1) the relative soil reinforcement stiffness E_f/G_m ;

²For an elastic soil element in plane strain compression, the zero extension direction, ψ , is given by:
 $\cos 2\psi = (1 - 2\nu_m)(R + 1)/(R - 1)$.

2) inclusion length L and orientation θ ; and 3) the magnitude and directions of principal strains in the soil, described by σ_v/σ_h and ν_m (for an isotropic, elastic soil). Figure 4.7 shows predictions of the maximum load transfer ratio as functions of the orientation, $|\theta| \leq 45^\circ$, for practical ranges of these parameters. The inclusion length and stiffness ratio ($L, E_f/G_m$) affect the magnitude of the tensile stresses in the reinforcement (previously characterized by the 'pickup' length for the base case analysis, $\theta=0^\circ$, section 2.4.2), but do not alter the relative performance at different orientations (Fig. 4.7b, c). Figure 4.7a shows that the stress ratio σ_v/σ_h affects both the maximum load transfer σ_{max}^f/σ_v , and also the orientation range over which the inclusion is in tension. For an incompressible soil matrix ($\nu_m=0.5$), the zero extension directions in the soil are independent of the shear stress level and, hence, the range for which the inclusion is in tension is $0^\circ \leq |\theta| \leq 45^\circ$. Oriented inclusions (i.e., $\theta \neq 0^\circ$) consolidated under K_0 stress conditions carry compressive stresses.

4.3.2. Direct Shear

Direct shear constitutes a second independent mode of interaction for the reinforced soil composite. In this hypothetical case, the specimen is loaded with boundary shear tractions τ only (i.e., $\sigma_v=\sigma_h=0$ hence, $\xi^*=45^\circ$). For an unreinforced, elastic isotropic soil matrix, the zero extension directions are $\psi=0^\circ$ and 90° , while principal compressive and tensile strains are oriented at -45° and $+45^\circ$, respectively. Figure 4.8 shows analytical solutions for the distribution of tensile stress, σ_{xx}^f/τ , and interface tractions, σ_{xy}^i/τ , σ_{yy}^i/τ , in simple shear of a composite element with the inclusion oriented at $\theta=0^\circ$ to 45° . This example uses the same specimen geometry and constituent material properties presented in the previous sections:

1. The tensile stress distribution is symmetric, with maximum load transfer at the centerline ($x=0$), while the interface tractions exhibit reflective symmetry between the top and bottom surfaces of the inclusion (e.g. $\sigma_{xy}^{ia}(x)=\sigma_{xy}^{ib}(-x)$).

2. There is no load transfer when the reinforcement is oriented at $\theta=0^\circ$. Tensile stresses develop when $\theta>0^\circ$ ($\leq\theta_{\max}=53^\circ$, in this case), with maximum load transfer for $\theta=45^\circ$ where $\sigma_{\max}^f/\tau=280$. The analytical solutions describe load transfer in direct shear as an odd function of inclusion orientation such that $\sigma_{xx}^f(-\theta)=-\sigma_{xx}^f(\theta)$. Thus, for $\theta<0^\circ$ the inclusion is loaded in compression and, hence, is not effective in reinforcing the soil. The analyses are not considered reliable in compression, where mechanisms of buckling have not been considered in the formulation.

The principal factors affecting the maximum load transfer in direct shear are the inclusion length L , relative stiffness ratio E_f/G_m and orientation θ . Figure 4.9 shows predictions of σ_{\max}^f/τ as function of the orientation $-45^\circ\leq\theta\leq+45^\circ$, for practical range of these parameters. Similarly to the plane strain compression mode, the inclusion length and stiffness ratio ($L, E_f/G_m$) affect the magnitude of the tensile stresses in the reinforcement, but do not alter the relative performance at different orientations.

4.3.3. Direct Simple Shear Tests

Direct simple shear tests can be simulated in the proposed analysis by combining the linear solutions from the plane strain and direct shear modes. The composite soil element is initially consolidated to a prescribed confining pressure σ_v , usually under K_0 -conditions such that $\sigma_h=K_0\sigma_v$. Shear stresses τ are then imposed on the horizontal boundaries of the specimen at constant confining pressure. Figure 4.10 illustrates the distribution of the tensile stress and interface tractions for a 1.0m long inclusion oriented at $\theta=30^\circ$ at prescribed stress ratios, τ/σ_v (using the reference geometry and material properties). Initial K_0 -consolidation ($K_0=\sigma_h/\sigma_v=0.43$) induces compressive stresses in the inclusion. The tensile reinforcement only becomes effective when $\tau/\sigma_v\geq 0.17$, corresponding to a mobilized friction angle $\phi\geq 28^\circ$ in the unreinforced soil element.

Figure 4.11 shows the analytical solutions for maximum load transfer σ_{\max}^f/σ_v , in simple shear tests as a functions of the inclusion orientation θ (for $-45^\circ \leq \theta \leq +45^\circ$) and shear stress, τ/σ_v . The results can be obtained by direct superposition of the plane strain compression and direct shear modes (also shown). The results show the following:

1. There are residual compressive stresses in the reinforcement due to K_0 -consolidation of the composite element for $\theta \neq 0^\circ$.
2. As the specimen is sheared, the tensile reinforcement becomes effective for inclinations $0 < \theta \leq \theta_0$, where θ_0 is a function of the external shear stress τ/σ_v . The orientation of maximum tensile load transfer is also a function of shear stress level. For example, at $\tau/\sigma_v = 0.5$ ($\phi = 54^\circ$ in the unreinforced element) maximum reinforcement benefit occurs when $\theta \cong 30^\circ$.
3. There is no load transfer predicted in simple shear tests with $\theta = 0^\circ$.

4.3.4. Behavior of Long Inclusions

The preceding examples have presented results of the analysis for inclined reinforcements using typical material properties, and specimen geometry typical of a large scale laboratory test ($m=0.8\text{m}$, $w=1.6\text{m}$). For very long inclusions, the proposed shear-lag analysis predicts the there is a maximum tensile stress in the reinforcement, σ_∞^f , which is obtained as a linear function of σ_H/σ_v , τ/σ_v from equation 4.13:

$$\frac{\sigma_\infty^f}{\sigma_v} = \frac{K_2(\sigma_H/\sigma_v, \tau/\sigma_v, \theta)}{K_1(\theta)} \quad (4.17)$$

where the coefficients K_1 , K_2 are given by 4.13a to d and Table 4.2.

Figures 4.12a, b summarize the behavior of these very long inclusion at various orientations ($0^\circ \leq \theta \leq 45^\circ$) in both plane strain compression and simple shear tests. These

results confirm the critical importance of inclusion orientation and external principal stress directions on the effectiveness of tensile soil reinforcements.

In practical field situations, the length of horizontal reinforcements ($\theta=0^\circ$) is usually sufficient to achieve the full load transfer predicted in equation 4.17. However, for inclined reinforcements ($\theta\neq 0^\circ$) the vertical spacing between layers m imposes a constraint on the inclusion length. Figure 4.13 shows the maximum load transfer ratio, $\sigma_{\max}^f/\sigma_\infty^f$ (which is independent of the shearing mode) as a function of the inclusion half length $L/2$. The results confirm previous findings (Fig. 2.4) that inclusions of 'pickup' length $L_I > 3.0m$ (defined as length for which $\sigma_{\max}^f/\sigma_\infty^f \geq 0.95$) are required to achieve the maximum possible load transfer for relatively inextensible reinforcing materials ($E_f/G_m=10^5$). For short inclusions ($L < L_I$), there is a reduction in the load transfer ratio with inclusion orientation, which becomes significant with inextensible reinforcements. For example, when $E_f/G_m=10^5$ and $L=1m$, the load transfer ratio $\sigma_{\max}^f/\sigma_\infty^f=0.35$ at $\theta=0^\circ$, but is only 0.13 at $\theta=45^\circ$.

4.3.5. Comparison with Finite Element Results

One method for evaluating the proposed shear-lag analysis is to compare the results with finite element computations. In the numerical calculations, the reinforcement is fully bonded to the soil matrix and, hence, there is load transfer at the tips of the inclusion. Alternative solutions using gap and frictional interface elements introduce non-linearities in the solution, creating other problems of numerical accuracy. The difference in boundary conditions at the tips can become important when either a) the inclusion is short (i.e., $L < L_I$) or b) the tips of the inclusion are in close proximity to the boundary of the soil specimen. This latter problem is particularly significant for the simple shear interaction mode with $\theta \equiv \pm 45^\circ$, where there are very large shear stresses acting near the end of the inclusion. Overall, it is not possible to make comprehensive evaluations of the shear-lag analysis using the finite element method. Instead, this section illustrates calculations which show

that the trends in the centerline load transfer are well described as functions of the inclusion orientation. Figure 4.14 shows a typical finite element mesh³ used in the evaluations. The model describes the full geometry of the composite reinforced soil specimen (i.e., there are no convenient planes of symmetry) and comprises 864 plane strain, 8-noded isoparametric elements which describe both the soil matrix and the reinforcement. Uniform shear and normal boundary tractions are imposed along the surfaces OABC.

Figure 4.15 summarizes comparisons of the centerline tensile stress for inclined reinforcements in plane strain compression tests. The results show the stress reduction $\sigma_{\max}^f(\theta)/\sigma_{\max}^f(0)$ as a function of the inclination and external stress ratio, σ_v/σ_h . The material properties and specimen geometry differ slightly from previous examples and are listed in the figure. There is excellent agreement (within 3% in most cases) between the finite element solutions and the shear-lag analyses. Figure 4.16 compares the numerical and analytical solutions of σ_{\max}^f/σ_v for simple shear tests on K_0 -consolidated soil specimens reinforced with a relatively extensible material, $E_f/G_m=10^2$. In this case, the material properties and test geometry were selected to ensure that the tensile stress at the inclusion tip did not exceed 30% of the expected centerline stress. Again there is excellent agreement with the finite element calculations, which confirms the general pattern of load-transfer behavior described by the shear-lag analysis for inclined reinforcements.

4.4. Interpretation of Tests Results Available in the Literature

4.4.1. Plane Strain Tests

McGown et al. (1978) present results of boundary tractions and deformations from a plane strain shear device containing a single planar inclusion oriented in various directions to the horizontal (θ , Fig. 4.17). The test device contains a soil specimen of dimensions

³All calculations were performed using the ABAQUS code.

152x102x102mm which is confined by a constant vacuum pressure, $\sigma_3=70\text{kPa}$. The major principal stress is obtained through rigid top and bottom platens, with test performed at a constant displacement rate. The side walls are lubricated and incorporate a thick glass plate to permit photographic measurements of internal deformations during the test and provide nominal plane strain conditions. Tests were performed using dry Leighton Buzzard Sand (LBS) deposited at three densities (Table 4.1, figure 4.20) and reinforced with three different materials (aluminum foil, aluminum mesh and a melt-bonded, non-woven fabric-T140), positioned at $\theta=0^\circ$, 30° , 60° and 90° .

Figure 4.19a, b shows typical stress ratio-axial strain measurements for tests with horizontal inclusions ($\theta=0^\circ$) on medium dense ($D_r=58$ to 65%) and loose ($D_r=11$ to 18%) LBS, respectively. The unreinforced, dense sand reaches a peak stress ratio, $R_{\max}=8.1$, at an axial strain, $\epsilon_1\approx 2.3\%$, followed by post-peak strain softening associated with shear planes formed within the specimen. The addition of horizontal inclusions, particularly the aluminum mesh and T-140 fabric, cause large changes in the externally measured composite behavior, while the behavior for the thin aluminum foil is similar to the unreinforced sand. Although there are relatively large increases in the shear resistance (e.g. $R_{\max}=13.0$, 10.5 for the aluminum mesh and T-140, respectively), the reinforcements have little influence on the strain mobilized at peak conditions. McGown et al. (1978) summarize their measurements of R_{\max} as functions of the inclusion orientation and specimen density (Fig. 4.21).

The boundary conditions in the unit cell do not correspond exactly to conditions assumed in the proposed analysis. In the laboratory tests, the major principal stress is obtained through rigid platens which force uniform displacements along the top and bottom of the device. As a result, the vertical stresses acting on the soil specimen are not uniform across these boundaries. The principal effect of this boundary condition is to force

failure to occur through the center of the unit cell⁴. This behavior can be seen most clearly from contours of volumetric and shear strains (obtained from photogrammetric measurements of the displacement field) as shown in Figure 4.18. In the proposed shear-lag analysis, uniform boundary tractions ensure that local failure will initiate at the edges of the soil specimen.

The proposed shear-lag analysis can be applied to predict and interpret failure conditions within the unit cell by considering the local distribution of stresses within the soil matrix. In general, failure will occur when the peak friction is mobilized in the soil matrix such that $\sin\phi = (R^m - 1)/(R^m + 1)$, where R^m is the ratio of principal stresses within the soil matrix ($R^m = \sigma_1^m / \sigma_3^m$), and ϕ depends on the initial density and external confining stress. In the shear-lag analysis, the average stress component $\sigma_{xx}^m(x)$ only varies axially along the length of the reinforcement, while σ_{xy}^m and σ_{yy}^m vary both laterally and axially. Average stress conditions within the reinforced soil matrix can be obtained from stresses at the interface and at the specimen boundary as follows:

$$\bar{\sigma}_{xx}^m = \frac{1}{L} \int_{-L/2}^{L/2} \sigma_{xx}^m dx \quad (4.18a)$$

$$\bar{\sigma}_{xy}^m = \frac{1}{y_c L} \int_{-L/2}^{L/2} \int_{-y_b}^{y_a} \sigma_{xy}^m dy dx = \frac{1}{2L} \int_{-L/2}^{L/2} (\sigma_{xy}^i + \sigma_{xy}^{ma}) dx \quad (4.18b)$$

$$\bar{\sigma}_{yy}^m = \frac{1}{y_c L} \int_{-L/2}^{L/2} \int_{-y_b}^{y_a} \sigma_{yy}^m dy dx = \frac{1}{L} \int_{-L/2}^{L/2} \left(\frac{1}{3} \sigma_{yy}^i + \frac{2}{3} \sigma_{yy}^{ma} \right) dx \quad (4.18c)$$

where analytical expressions for σ_{xx}^m , σ_{xy}^i , σ_{yy}^i in equations 4.5 and 4.10 and σ_{xy}^{ma} , σ_{yy}^{ma} in Figure 4.3 are related to the tensile stress in the reinforcement σ_{xx}^f (eqn. 4.15). The average stresses in the soil matrix can be written as follows:

⁴ If tractions were truly uniform, local failures would initiate at the edges of the specimen and the external stress ratio would be little affected by the presence of the inclusion. This behavior occurs in the APSR cell (Larson, 1992).

$$\bar{\sigma}_{xx}^m = \frac{1}{2y_c} \bar{\sigma}_{xx}^f + \sigma_{xx}^0 \quad (4.19a)$$

$$\bar{\sigma}_{xy}^m = \frac{1}{2} \left[\left(\frac{f}{2y_c} \bar{\sigma}_{xx}^f + \sigma_{xx}^0 - \sigma_v \right) \tan\theta + \sigma_{xy}^0 \right] \quad (4.19b)$$

$$\begin{aligned} \bar{\sigma}_{yy}^m = \frac{1}{3} \left[\frac{m}{2L\cos\theta} \left(-\frac{f}{2} \frac{K_2(\sigma_v, \sigma_h, \tau, \theta)}{\sqrt{K_1(\theta)}} \tanh\sqrt{K_1(\theta)} L/2 - \sigma_{xy}^0 \right) + \frac{f}{2y_c} \tan^2\theta \bar{\sigma}_{xx}^f + \sigma_{yy}^0 \right] + \\ + \frac{2}{3} \left[\bar{\sigma}_{xx}^m + \sigma_v (1 - \tan^2\theta) \right] \end{aligned} \quad (4.19c)$$

where $\bar{\sigma}_{xx}^f$ is the average inclusion stresses:

$$\bar{\sigma}_{xx}^f = \frac{1}{L} \int_{-L/2}^{L/2} \sigma_{xx}^f dx = \frac{K_2(\sigma_v, \sigma_h, \tau, \theta)}{K_1(\theta)} \left[1 - \frac{\tanh\sqrt{K_1(\theta)} L/2}{\sqrt{K_1(\theta)} L/2} \right] \quad (4.19d)$$

Hence, the stress ratio within the soil matrix, R^m , can be related to the boundary tractions σ_v , σ_h and external stress ratio, $R (= \sigma_v/\sigma_h)$. It should be noted that this interpretation of the shear-lag analysis does not consider the "edge effects" for $x < -L/2$ and $x > L/2$. Therefore, the predictions are expected to overestimate the measured values of R .

Input parameters for the proposed shear-lag analysis are listed in Table 4.3. The behavior of unreinforced Leighton Buzzard sand (LBS) in plane strain compression has been reported by Deterling (1984), Figure 4.20a.

The elastic properties of the aluminum foil reinforcement are obtained from the uniaxial tension tests reported in Figure 4.20b. The T-140 non-woven fabric exhibits a highly non-linear stress-strain response in unconfined uniaxial tension. Data for similar heat bonded non-woven fabrics (e.g. Ling et al., 1992) show that soil confinement (at $\sigma_3=70\text{kPa}$) can increase the secant modulus by up to 30%. Elastic parameters for the proposed shear-lag analysis are based on the initial tangent modulus (from the unconfined, uniaxial test). This parameter selection is subsequently justified from the predictions of tensile stress levels in the reinforcement.

Figures 4.21a and b compare the shear-lag predictions and measured peak stress ratios R_{\max} ($=(\sigma_v/\sigma_h)_{\max}$) for the unit cell tests with aluminum foil and T-140 reinforcement, respectively:

1. The analytical predictions and measured data show similar trends in the variation of R_{\max} with orientation θ , for both reinforcing materials and at all three sand densities. The stress ratio of the composite is maximum when $\theta=0^\circ$ (horizontal inclusions) and is larger than the unreinforced soil for $0 \leq \theta \leq 45^\circ$. For $\theta \geq 60^\circ$, there is a small net loss of strength in the composite and minor difference in the maximum stress ratios measured at $\theta=60^\circ$, 90° .
2. The aluminum foil is extremely thin ($f=0.02\text{mm}$) and, hence, gives very small changes in R_{\max} compared to the T-140 fabric ($f=0.55\text{mm}$), even though the relative stiffness is larger ($E_f/G_m \cong 120$ and 35 for aluminum foil⁵ and T-140 in dense LBS, respectively).
3. The shear-lag analysis tends to overestimate the measured strength for $\theta < 30^\circ$ and underestimate for $\theta \geq 60^\circ$, especially for T-140 reinforcement on loose LBS. This behavior is qualitatively in accordance with the "edge" effects which are not included in the analysis. At higher inclination angles, the analysis predicts axial compression of the inclusion which causes local amplification of shear stresses mobilized in the soil matrix and, hence, reduces the overall strength of the composite. McGown et al. (1978) attribute the measured reduction in R_{\max} at $\theta=60^\circ$, 90° to local slippage at the soil-reinforcement interface. Interface slippage effects are not considered in the analysis of inclined reinforcements. Although this mechanism is plausible for smooth aluminum sheet, it is unlikely for the T-140 non-woven fabric.

⁵This stiffness is quoted by Andrawes et al. (1978), and is much lower than the Young's modulus of aluminum.

Figure 4.22 illustrates the shear-lag predictions of axial stresses in the reinforcements at peak stress ratio conditions in the composite. The results are shown for dense Leighton Buzzard Sand at the four inclusion orientations used in the unit cell tests. These results demonstrate that the full load transfer is achieved due to the low stiffness of the particular reinforcements.

4.4.2. Direct Shear Box Tests

Several authors have described measurements of boundary tractions and displacements from direct shear box tests on specimens of dry sand reinforced by inclusion which bisect the imposed horizontal failure plane at various orientations (Table 4.1). This section describes the application of the proposed shear-lag analysis for interpreting one set of direct shear tests performed on dense Leighton Buzzard Sand reinforced by a steel grid (Jewell, 1908). Figure 4.23 summarizes the test geometry and measured data. These particular experiments were conducted in a relatively small direct shear apparatus (DSA), of height $m=0.15\text{m}$, width $w=0.25\text{m}$ and depth $B=0.15\text{m}$. The inclusions are made from a square grid of steel bars (diameter 0.82mm) with length $L=0.13\text{m}$, and were positioned centrally within the DSA in order to preserve the symmetry between the upper and lower halves of the box. All tests were performed using very dense LBS (with initial $D_r=90\%$) at a constant average vertical pressure $\sigma_v=29\text{kPa}$.

The principal measurements during the test are the external shear force T , the lateral displacement \bar{x} (which describes the non-uniform shear strain) and the vertical displacement \bar{y} , which indicates the volume change within the specimen. Figure 4.23 show the results for inclusions oriented at $-30^\circ \leq \theta \leq 60^\circ$ together with data for the unreinforced sand:

1. For inclusions oriented at $\theta > 0^\circ$, there is a significant increase in the peak shear resistance, with maximum improvement $\tau_r/\tau_{ur}=1.55$, measured for an inclusion rotated at $\theta=60^\circ$. In contrast, there is a 10% reduction in peak shear resistance when $\theta=-30^\circ$.

2. Peak strength conditions are mobilized at horizontal displacements $\bar{x}=1$ to 2mm, at which the specimen exhibits significant dilation.
3. The reinforcement has little influence on the initial response of the composite element for $\bar{x}\leq 0.2$ mm. However, there is a significant change in shear resistance for horizontal displacements in the range $\bar{x}=0.4$ to 0.7mm, with no volume change in the sample ($\bar{y}=0$ mm).

The existing interpretations of reinforced direct shear tests apply limit equilibrium methods to evaluate the peak shear resistance. For example, Jewell (1980) considers equilibrium in the upper half of the DSA (Fig. 4.24a) in which a tensile force at the center of the inclusion P_R reinforces the failure plane with two mechanisms: 1) the horizontal component, $P_R\cos\theta$, reduces the shear force acting in the sand; and 2) the vertical component, $P_R\sin\theta$, increases the confining stress acting at the centerplane. The net change in shear resistance is then given by:

$$\frac{\tau_{ext}}{\sigma_v} = \frac{P_R}{A\sigma_v} (\sin\theta \tan\phi + \cos\theta) \quad (4.20)$$

where τ_{ext} is the additional shear resistance and ϕ is the peak friction angle or plane strain shearing of the soil specimen (at the appropriate confining stress and density). In practice, P_R is not usually measured in the tests and, hence, equation 4.20 provides only a conceptual model of the reinforced soil behavior. Jewell and Wroth (1987) estimate τ_{ext}/σ_v using limiting values for P_R based on pullout bond resistance of the inclusion and obtain good agreement with the measured data. For a planar inclusion, $P_{Rlim}=\sigma_n L \tan\delta$, where σ_n is the average normal interface traction along the inclusion and δ is the interface friction angle.

Palmeira and Milligan (1989) have recently proposed a refined limit equilibrium calculation (Fig. 4.24b) which includes more realistic calculation of stress conditions in the

central shear zone. In this calculation, the centerline axial stress in the reinforcement P_R can be computed from the measured direct shear behavior of the unreinforced sand, ϕ_{ds} ($\tan^{-1}\tau/\sigma_v$) and the distortion of the inclusion within the shear zone (measured by photogrammetry).

There are two principal difficulties in developing more refined interpretations of the reinforced direct shear tests: 1) the stress and strain fields are highly non-uniform within the soil specimen; and 2) the stress state within the shear zone is not known and is difficult to estimate due to principal stress rotations. Figure 4.25 offers one plausible interpretation of the behavior of dense LBS in direct shear box test. Initially, the soil is consolidated under K_0 conditions (typically $\sigma_{h0}=0.4$ to $0.5 \sigma_{v0}$ during 1-D compression of sand). The initial measured response (O-A) can be assumed to be approximately linear. If the soil is treated as isotropic, then $\Delta\sigma_h=0$, and the Mohr circle can be defined at state A. In this condition, failure initiates in the sample along planes of maximum stress obliquities which are controlled by the friction angle measured in plane strain shearing $\phi_{ps}=54^\circ$ (after Jewell and Wroth, 1987). Subsequent shearing from A to B generates irrecoverable (plastic) deformations, non-linear stress-strain behavior and principal stress rotations ($\Delta\sigma_h>0$). Dilation begins for loading beyond B, where $\sigma_h>\sigma_v$ (and, hence, $\bar{y}>0$). Thus, the stress state at B ($\sigma_h\cong\sigma_v$, $\tau/\sigma_v=0.82$) represents the maximum deformation, $\bar{x}=0.5\text{mm}$, for which elastic soil properties can represent the unreinforced behavior of the sand. For peak strength conditions C, Jewell and Wroth (1987) relate ϕ_{ps} and ϕ_{ds} through the dilation rate $\eta=d\bar{y}/d\bar{x}$ through assumptions of co-axiality, $\tan\phi_{ds}=(\sin\phi_{ps}\cos\eta)/(1-\sin\phi_{ps}\sin\eta)$.

The proposed shear-lag analysis can be applied to interpret the reinforced direct shear tests of Jewell (1985) when $\bar{x}\leq 0.5\text{mm}$. The analysis predicts the axial stress at the centerline of the inclusion for the specified geometry, material properties and boundary tractions (σ_v , σ_h , τ , assumed uniform). It is apparent from equilibrium of the upper half of

the box that tensile forces in the reinforcement reduce the shear stress acting in a horizontal plane. The change in shear stress due to the reinforcement is given by:

$$\frac{\tau_{ext}}{\sigma_v} = \frac{f}{w} \frac{\sigma_{max}^f}{\sigma_v} \cos\theta \quad (4.21)$$

where $\sigma_{max}^f = \sigma_{xx}^f(x=0)$ and is given by equations 4.13 and 4.15. This analysis makes no assessment of the potential improvement in shear strength due to changes in confining pressure along the centerplane.

Figure 4.26 summarizes the comparison between the predicted and measured values of τ_{ext}/σ_v at $\bar{x}=0.5\text{mm}$. Small error bands in the measured data reflect variations in the behavior of the unreinforced sand. Input parameters for the sand are obtained from the measured data at state B using the assumptions described in Figure 4.25. Although the properties of the grid are not known precisely, uncertainties in E_f and f have little effect on the predictions of τ_{ext}/σ_v . In this case, the reinforcements are effectively inextensible as $E_f/G_m > 10^4$. The results show the following:

1. The measured data for inclusions oriented at $\theta=15^\circ, 30^\circ, 45^\circ$ and 60° all show increased shear resistance, with maximum reinforcing benefit $\tau_{ext}/\sigma_v \approx 0.20$, at $\theta=60^\circ$. There is a reduction in shear resistance in the test with $\theta = -60^\circ$. The shear-lag analysis is in good overall agreement with these data but tends to underestimate τ_{ext}/σ_v for $\theta=60^\circ$ and 90° . The analyses show maximum reinforcing benefit ($\tau_{ext}/\sigma_v \approx 0.17$) for $\theta \approx 40^\circ$, which corresponds approximately to the direction of maximum tensile strains (45°) for an elastic soil matrix with uniform boundary tractions (σ_v, σ_h, τ).
2. The analysis predicts no reinforcing effects for inclusions at $\theta=0^\circ$ or 90° . Although the measurements also show $\tau_{ext}/\sigma_v = 0$ at $\theta=0^\circ$, there is a 10% increase in shear resistance at $\theta=90^\circ$. This behavior can be attributed to the onset of dilation, \bar{y} , which has a particularly pronounced effect on the mobilization of tensile stress for reinforcements

oriented at $\theta=90^\circ\pm 30^\circ$. Figure 4.26 also presents the measurements at peak strength conditions, where the maximum improvement in shear resistance, $\tau_{exl}/\sigma_v \cong 0.55$, occurs at $\theta=60^\circ$. Although the shear-lag analysis cannot describe this behavior, it is particularly interesting to note the dramatic improvement in shear resistance at $\theta=90^\circ$ relative to conditions at $\bar{x}=0.5\text{mm}$. The results suggest that most of the reinforcing action at $\theta=90^\circ$ can be attributed to dilation.

This result is evaluated more closely using data from a very large cubic shear box (1m^3) reported by Palmeira (1987). Figure 4.27 summarizes the dilation and additional shear resistance as functions of \bar{x} , for a 0.6m long aluminum sheet reinforcement at $\theta=90^\circ$. Dilation in the large shear box begins at $\bar{x}\cong 10\text{mm}$, corresponding to an average shear strain $\bar{\gamma}=\bar{x}/m\cong 1.0\%$. In comparison, $\bar{\gamma}\cong 0.3\%$ at state B in the small shear box tests, showing an important scale effect associated with these devices. The close correlation between $\bar{\gamma}$ and τ_{exl}/σ_v , with small reinforcing effect for $\bar{x}<10\text{mm}$, supports the assumptions of elastic response for the shear-lag analysis in working load conditions.

4.5. Conclusions

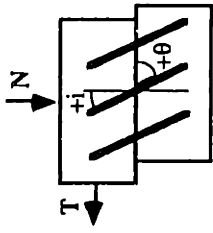
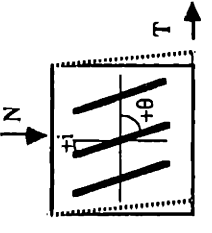
This chapter has proposed an approximate shear-lag analysis for a single, thin planar reinforcement inclined at arbitrary orientation within a soil specimen which is loaded by uniform normal and shear boundary tractions (i.e., arbitrary direction and magnitude of principal stresses). The analysis generalizes the basic formulation described in Chapter 2 assuming 1) linear, isotropic and elastic properties of the constituent materials; 2) no slippage at the soil-reinforcement interface; and 3) negligible bending resistance for thin reinforcing inclusions. The formulation also proposes a simple method for estimating the dimensions of the shear spring layer used in the shear-lag approximation.

The analyses provide closed form expressions for the axial stress and interface tractions as functions of the specimen geometry, material properties and boundary loads.

The results show the effects of inclusion orientation in two fundamental modes of interaction, plane strain compression (σ_v , σ_h) and direct shear (τ). The behavior of reinforcements in simple shear tests can then be interpreted from superposition of the linear solutions. In all cases, the reinforcement is most effective (i.e., highest tensile stress) when it is oriented in the direction of maximum tensile strains in the (unreinforced) soil.

Partial evaluation of the shear-lag analyses is achieved through comparisons with linear, finite element calculations. The numerical analyses show good agreement with reductions of the effects of orientation on stresses at the centerline of the inclusion for a limited range of material properties and specimen geometries. Complete comparisons are not possible as the shear-lag analysis assumes no load transfer at the tips of the inclusion. Differences between the two analyses arise when the finite element calculations predict large axial stresses at the tips of the inclusion.

The shear-lag analyses have been used to interpret the effects of inclusion orientation measured in laboratory plane strain compression and direct shear box tests. In the plane strain unit cell tests of McGown et al. (1978), the improvement in shear resistance of the soil composite was interpreted consistently from shear-lag predictions of the average stress state within the soil mass. There is excellent agreement with the measured data obtained at three different soil densities using aluminum foil and non-woven reinforcing materials. Changes in the shear resistance for reinforced direct shear box tests (e.g. Jewell, 1989; Jewell and Wroth, 1987) are due, in large part, to the dilation of the soil within the central failure zone of the specimen. This behavior cannot be modeled by the proposed analysis. However, there are also improvements in the shear resistance which occur at small strain levels. This behavior is well described by the proposed shear-lag analysis.

Apparatus	References	Dimensions (cm)	Sand	Reinforcing Materials	σ_c (kPa)	D_r (%)	Principal Variables
Direct (Box) Shear 	Gray and Ohashi (1983)	not given	Muskegon	fibers: reeds, PVC copper wire	34-68	20, 100	length, L diameter, d concentration, c orientation, $-60^\circ \leq i \leq 30^\circ$
	Jewell & Wroth (1987) Jewell (1980)	25.4x15.2x15.2	LBS ¹	steel tension springs	25-85	90	axial stiffness, E_f orientation, $0^\circ \leq i \leq 180^\circ$
	Palmeira et al. (1989) Palmeira (1987)	100x100x100	LBS ¹	geogrid, non-woven fabric, metal strip	30	87	grid type orientation, $i=0^\circ, 30^\circ$
	Shewbridge et al. (1989)	76.1x40.2x13.5	Monterey	nylon cord, wood/metal rods	10.25	71	material type large deformations ²
Direct Simple Shear 	Hayashi et al. (1988)	20x20x20	Toyoura	geogrid, bronze bars	25-150	82	material type confining stress, σ_c orientation, $-20^\circ \leq i \leq 20^\circ$
	McGown et al. (1978)	152x102x102mm	LBS ¹	non-woven fabrics, aluminum foil and mesh	70	11, 70	material type sand density orientation, $0^\circ \leq \theta \leq 90^\circ$

¹Leighton Buzzard Sand

Table 4.1: Laboratory Measurements for Reinforced Soils with Inclined Inclusions and Principal Stress Rotations.

θ	Thickness of Shear Spring Layer, \bar{y}	Centerline Thickness, y_c
$0 \leq \theta \leq \theta_1$	$\frac{m}{3 \cos \theta}$	$\left(\frac{m}{2 \cos \theta} - \frac{f}{2} \right)$
$\theta_1 \leq \theta \leq \theta_L$	$\frac{m}{3 \cos \theta} - \frac{1}{3 L \tan \theta} \left(\frac{L}{2 \cos \theta} - \frac{w}{2} + \frac{m}{2} \tan \theta \right)^2$	
$\theta_L \leq \theta \leq \theta_2$	$\frac{w}{3 \sin \theta} - \frac{1}{3 L \tan \theta} \left(\frac{L}{2 \cos \theta} + \frac{w}{2} - \frac{m}{2} \tan \theta \right)^2$	$\left(\frac{w}{2 \sin \theta} - \frac{f}{2} \right)$
$\theta_2 \leq \theta \leq \pi/2$	$\frac{w}{3 \sin \theta}$	

$$\sin \theta_1 = \left[1 + \left(\frac{w}{m} \right)^2 \right]^{-1} \left\{ \left(\frac{w}{m} \right) \left[1 + \left(\frac{w}{m} \right)^2 - \left(\frac{L}{m} \right)^2 \right]^{1/2} - \left(\frac{L}{m} \right) \right\}$$

$$\cos \theta_2 = \left[1 + \left(\frac{m}{w} \right)^2 \right]^{-1} \left\{ \left(\frac{m}{w} \right) \left[1 + \left(\frac{m}{w} \right)^2 - \left(\frac{L}{w} \right)^2 \right]^{1/2} - \left(\frac{L}{w} \right) \right\}$$

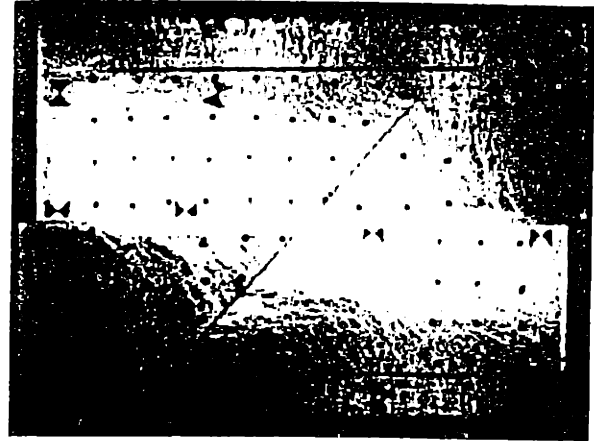
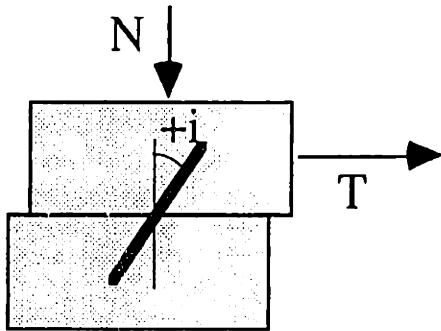
$$\tan \theta_L = \frac{w}{m}$$

a) Effect of Orientation on Parameters \bar{y} , y_c

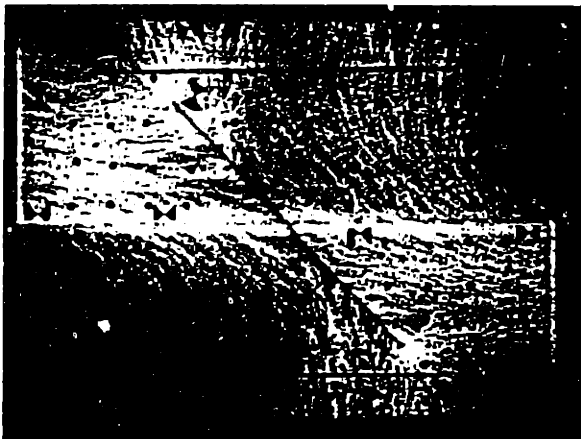
$K_1(\theta)$	$\frac{2}{\bar{y} f} \frac{\left[a \left(\sin \theta - \frac{v_m}{\sin \theta} \right) + 2 \frac{G_m}{E_f} (1 + v_f) \left[(1 - v_f) + a v_f \cotan^2 \theta \sin \theta \right] \right]}{\left[1 + \frac{1}{4} v_m - \frac{3}{2} \frac{G_m}{E_f} (1 + v_f) v_f \right]}$
$K_2^v(\theta)$	$\frac{2}{\bar{y} f} \frac{\left[v_m - \cos^2 \theta - 2 \frac{G_m}{E_f} (1 + v_f) v_f \sin^2 \theta \right]}{\left[1 + \frac{1}{4} v_m - \frac{3}{2} \frac{G_m}{E_f} (1 + v_f) v_f \right]}$
$K_2^h(\theta)$	$-\frac{2}{\bar{y} f} \frac{\left[\sin^2 \theta - v_m + 2 \frac{G_m}{E_f} (1 + v_f) v_f \cos^2 \theta \right]}{\left[1 + \frac{1}{4} v_m - \frac{3}{2} \frac{G_m}{E_f} (1 + v_f) v_f \right]}$
$K_2^T(\theta)$	$\frac{2}{\bar{y} f} \frac{\left[1 - 2 \frac{G_m}{E_f} (1 + v_f) v_f \right] \sin 2\theta}{\left[1 + \frac{1}{4} v_m - \frac{3}{2} \frac{G_m}{E_f} (1 + v_f) v_f \right]}$

b) Shear-Lag Coefficients for $\theta \geq 45^\circ$ (eqn. 4.13)

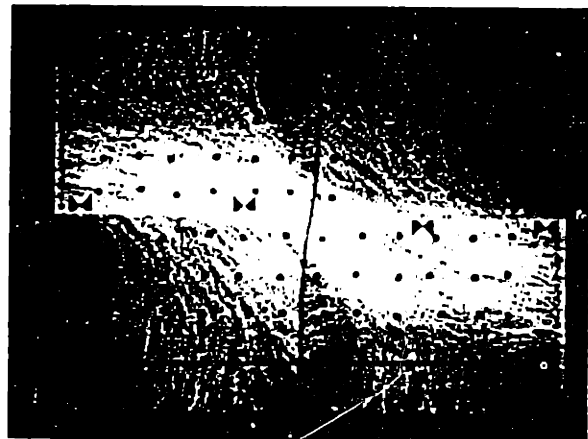
Table 4.2: Parameters for Proposed Shear-Lag Analysis.



a) Reinforcement at $i=40^\circ$



b) Reinforcement at $i=-45^\circ$



c) Reinforcement at $i=0^\circ$

Figure 4.1: Effects of Inclusion Orientation on Reinforced Direct Shear Tests.

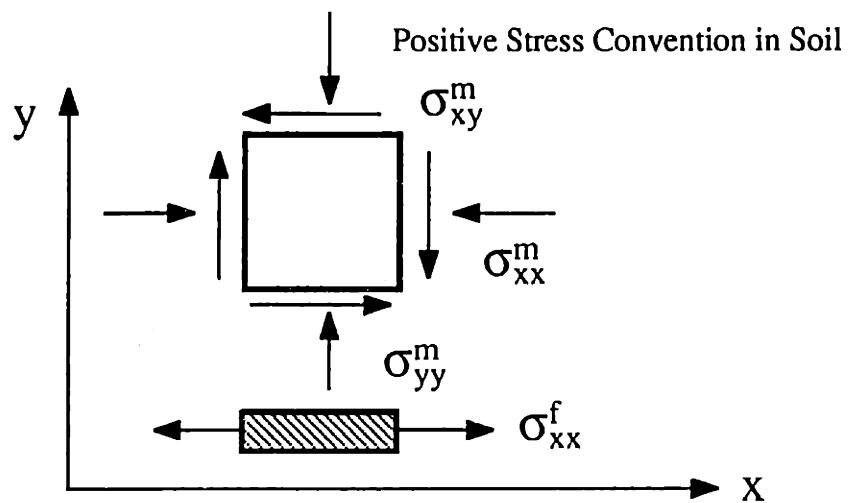
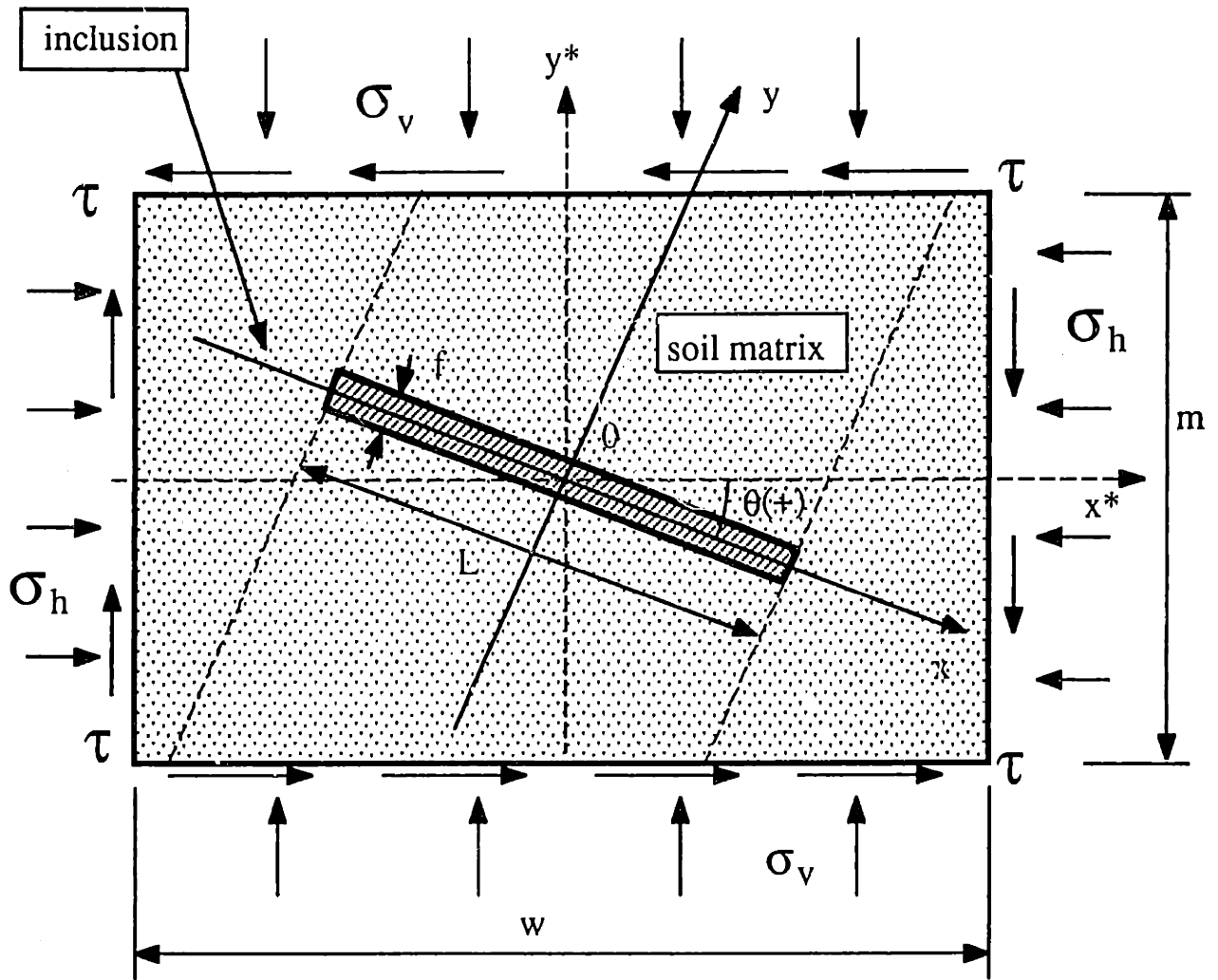
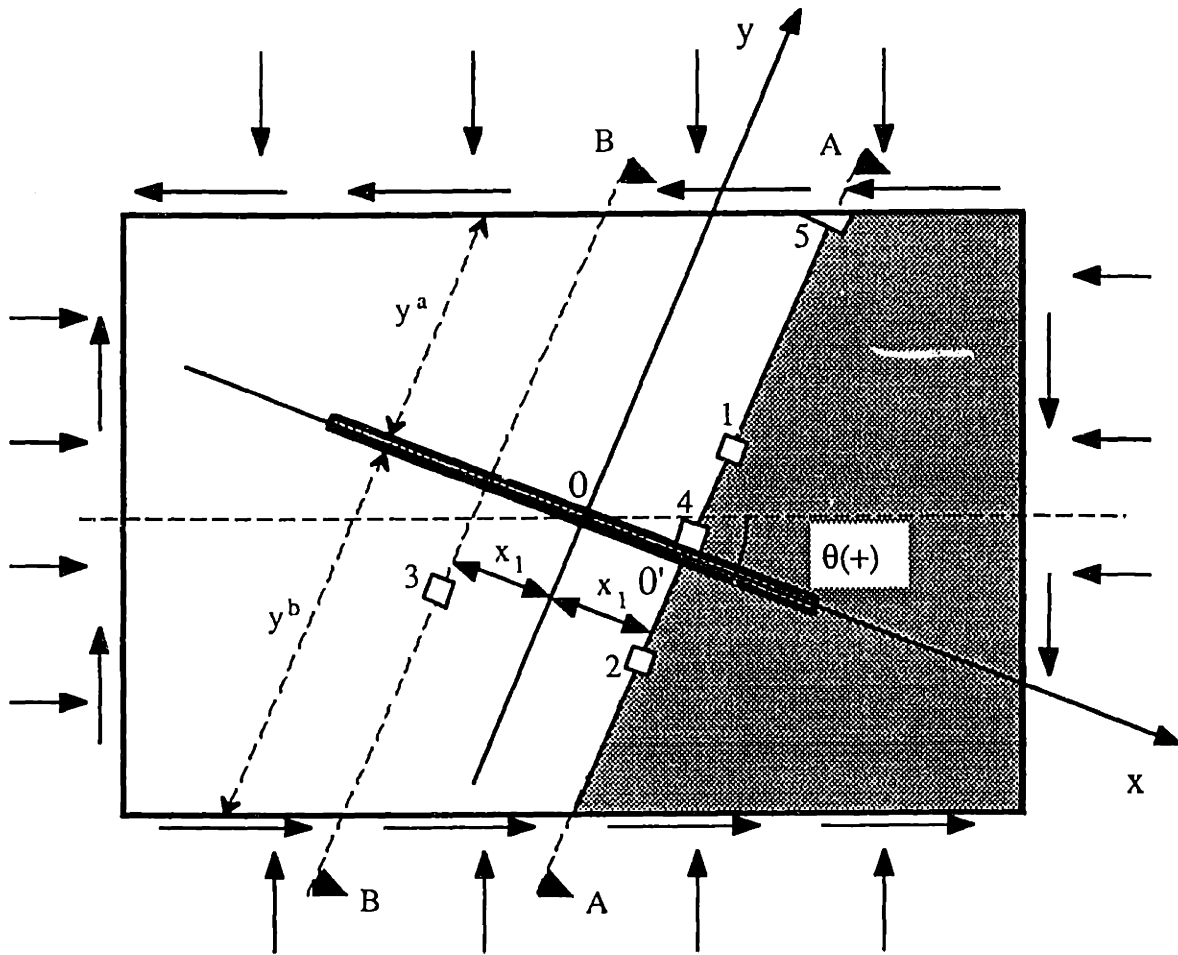


Figure 4.2 Plane Strain Geometry for Composite Reinforced Soil Element with General Inclusion Orientation and Principal Stress Directions.



Selected Location	State of Stress
1. Generic location, (x_1, y_1) (superscript 'a' for $y > 0$) $-L/2 \leq x_1 \leq L/2$	$\{\sigma_{xx}^{ma}(x_1), \sigma_{yy}^{ma}(x_1, y_1), \sigma_{xy}^{ma}(x_1, y_1)\}$
2. Equivalent location below reinforcement, $(x_1, -y_1)$ (superscript 'b' for $y < 0$)	$\{\sigma_{xx}^{mb}, \sigma_{yy}^{mb}, \sigma_{xy}^{mb}\}$
3. Reflective symmetry $(-x_1, -y_1)$	$\sigma_{xx}^{mb}(-x_1, -y_1) = \sigma_{xx}^{ma}(x_1, y_1)$ $\sigma_{yy}^{mb}(-x_1, -y_1) = \sigma_{yy}^{ma}(x_1, y_1)$ $\sigma_{xy}^{mb}(-x_1, -y_1) = \sigma_{xy}^{ma}(x_1, y_1)$
4. Interface with reinforcement, $(x, f/2)$ $\sigma_{xy}^i \sigma_{yy}^i$: interface traction components	$\{\sigma_{xx}^{ia}, \sigma_{xy}^{ia}, \sigma_{yy}^{ia}\}$
5. Boundary of specimen, $(x_1, m/2\cos\theta + x_1\tan\theta)$	σ_{xx}^{ma} $\sigma_{yy}^{ma} = \sigma_{xx}^{ma}\tan^2\theta + \sigma_v(1 - \tan^2\theta) + 2\tau\tan\theta$ $\sigma_{xy}^{ma} = (\sigma_{xx}^{ma} - \sigma_v)\tan\theta + \tau$

Figure 4.3: Soil Stress Conditions Assumed in Proposed Analysis.

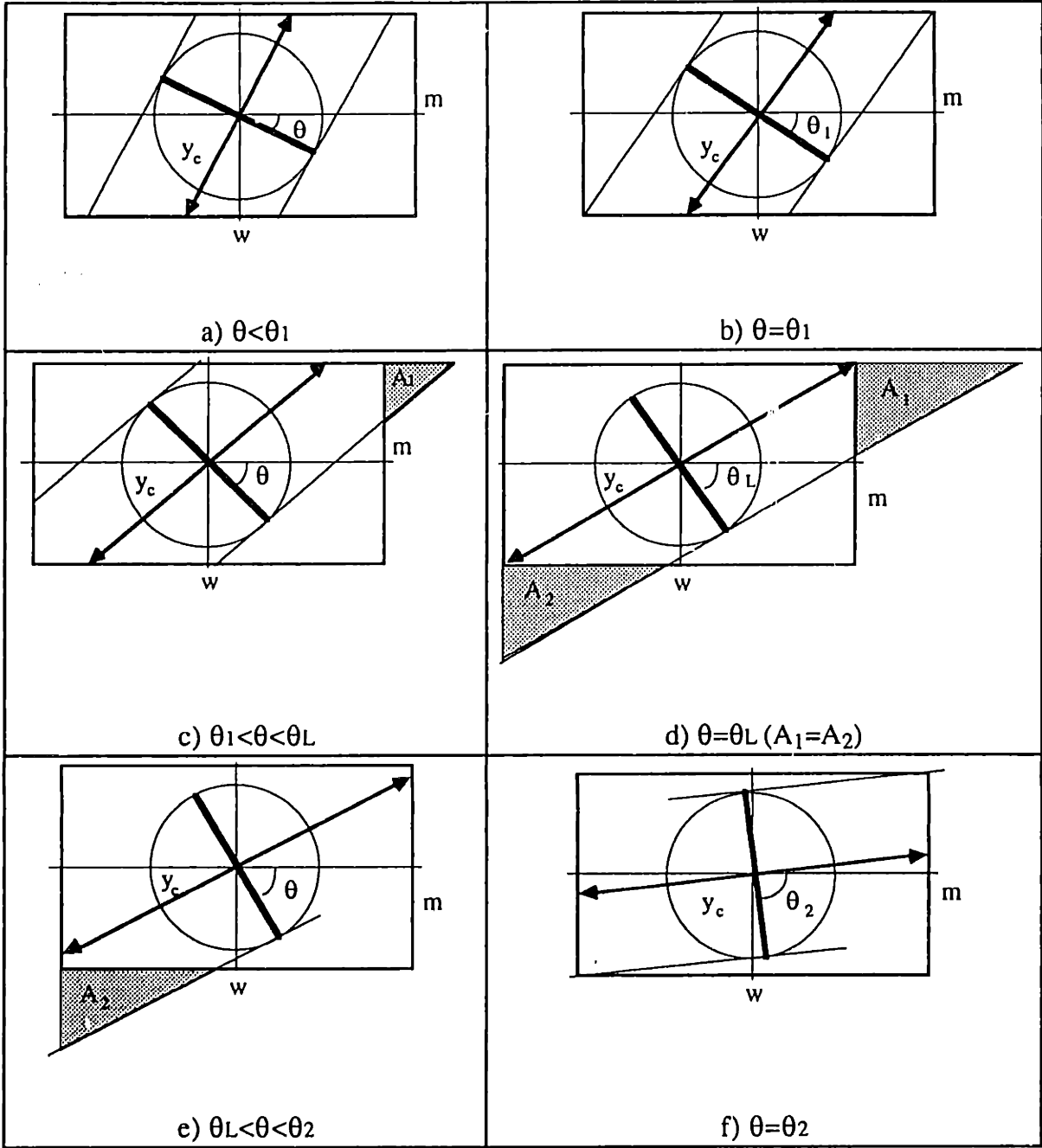


Figure 4.4: Effect of Inclusion Orientation on Shear-Lag Approximations.

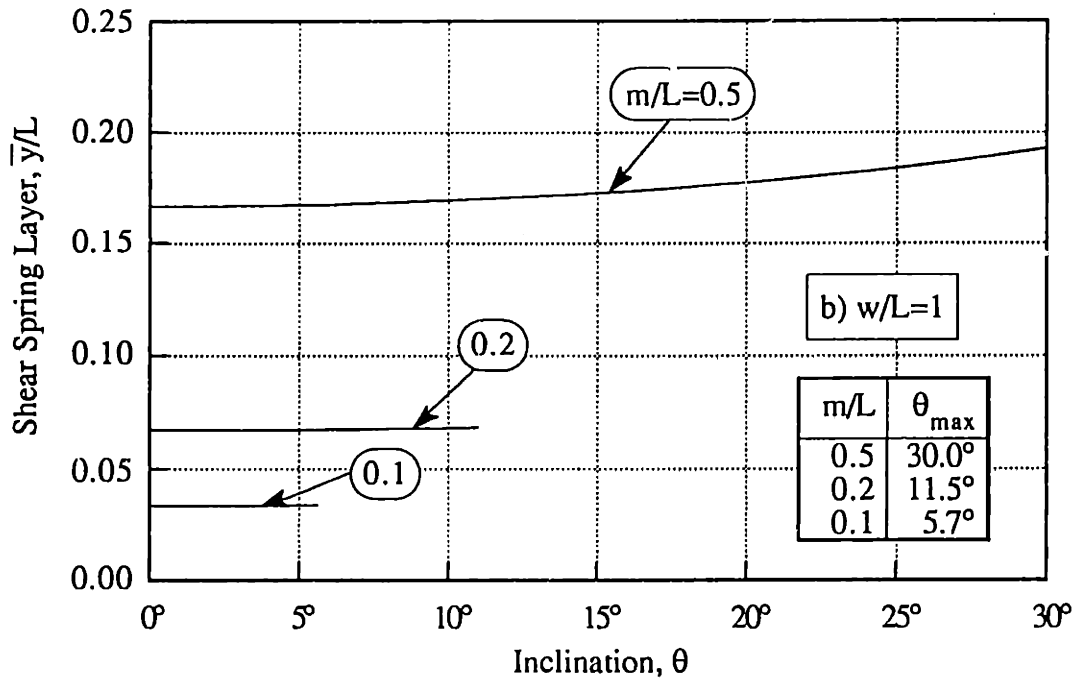
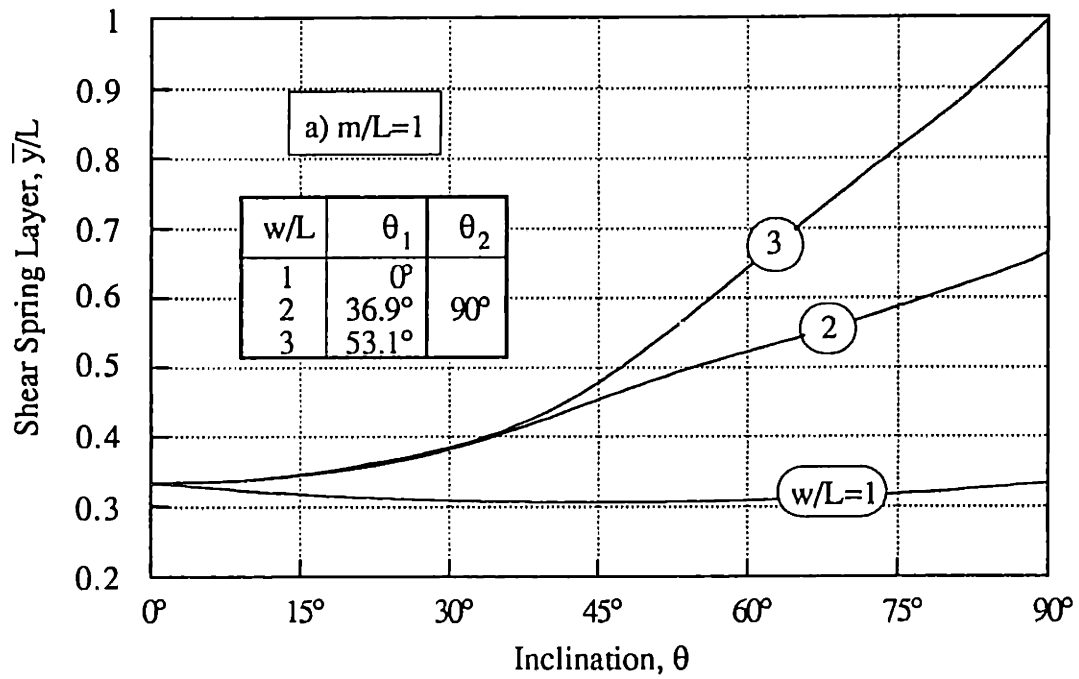


Figure 4.5: Influence of Geometric Parameters on Shear Spring Layer.

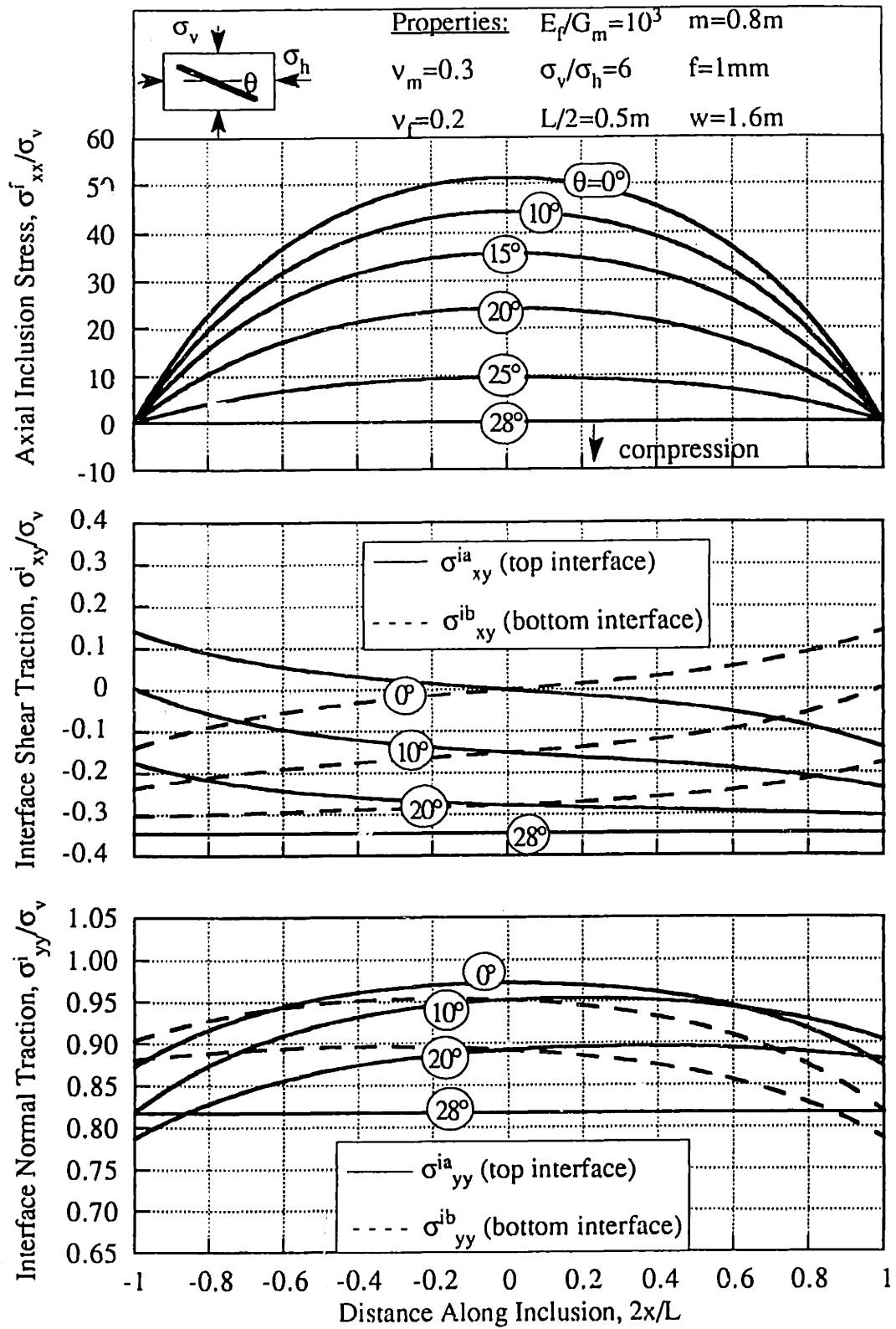
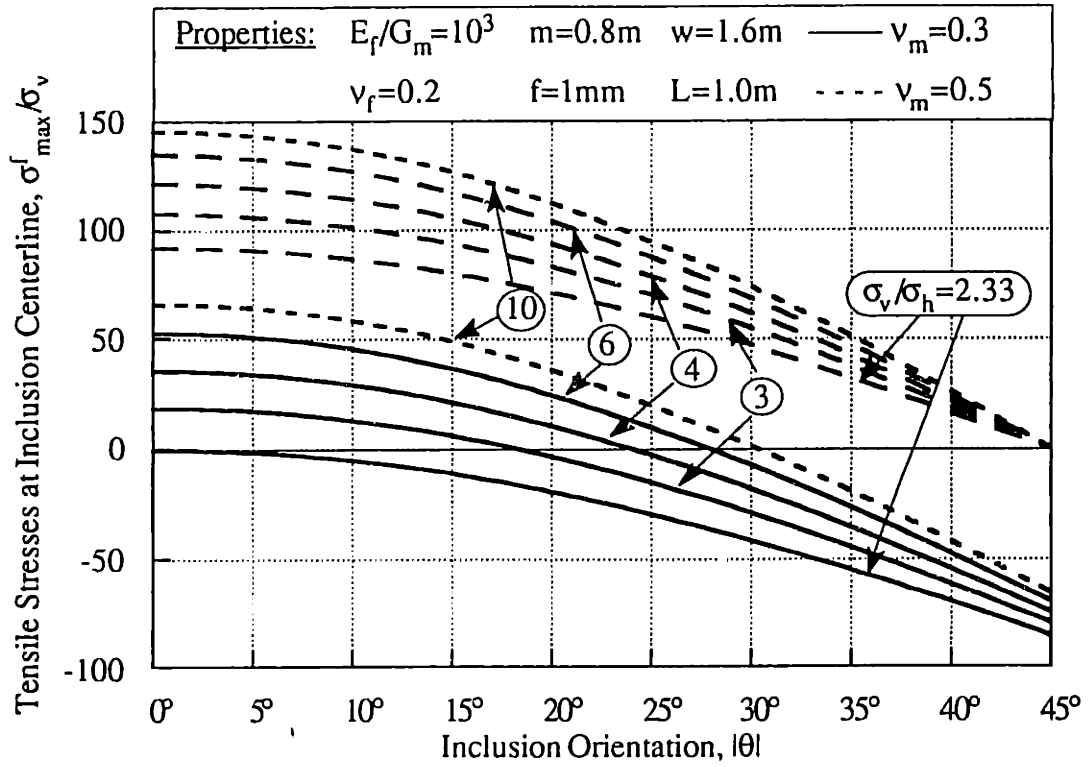
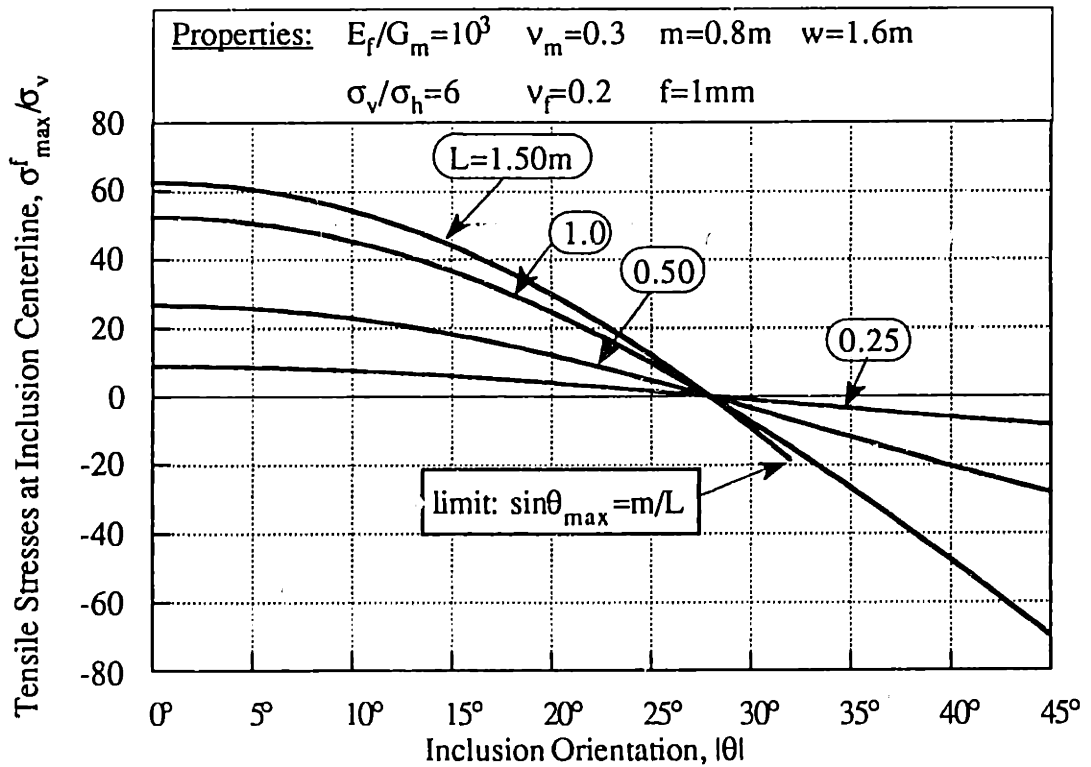


Figure 4.6: Effects of Inclusion Orientation on Tensile Inclusion Stresses and Interface Tractions.

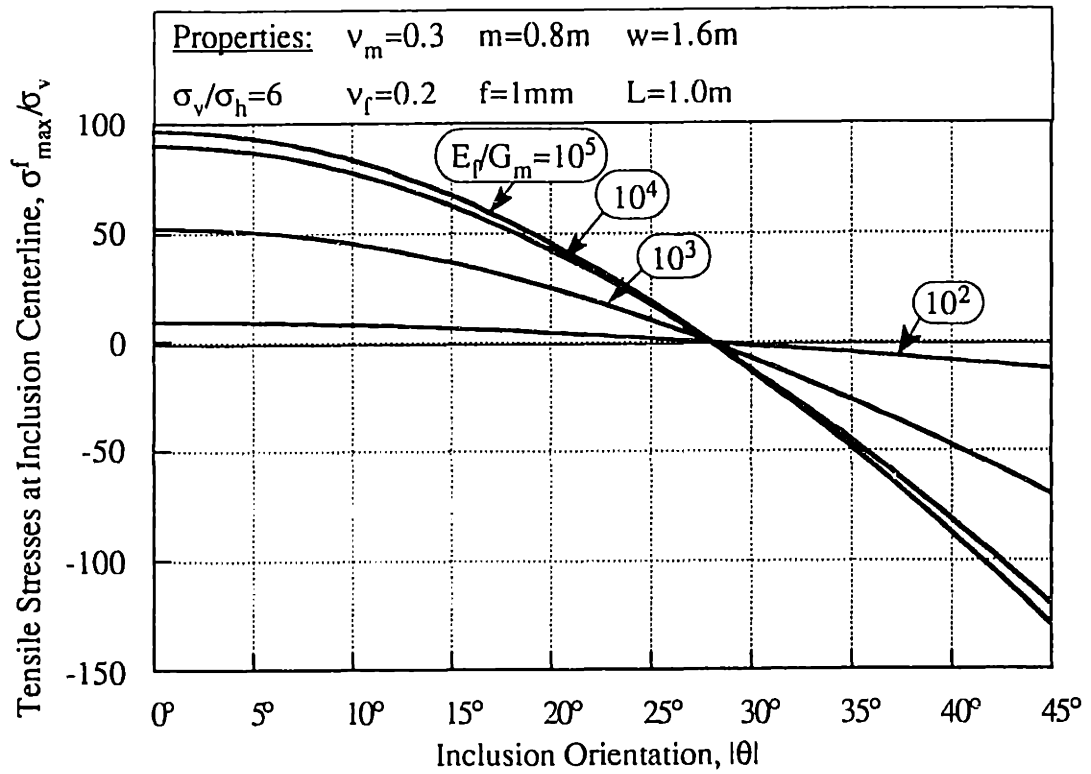


a) Effect of Shear Stress Level



b) Effect of Length

Figure 4.7 : Factors Affecting Maximum Load Transfer in Plane Strain Compression.



c) Effect of Relative Stiffness Ratio

Figure 4.7 (cont.): Factors Affecting Maximum Load Transfer in Plane Strain Compression.

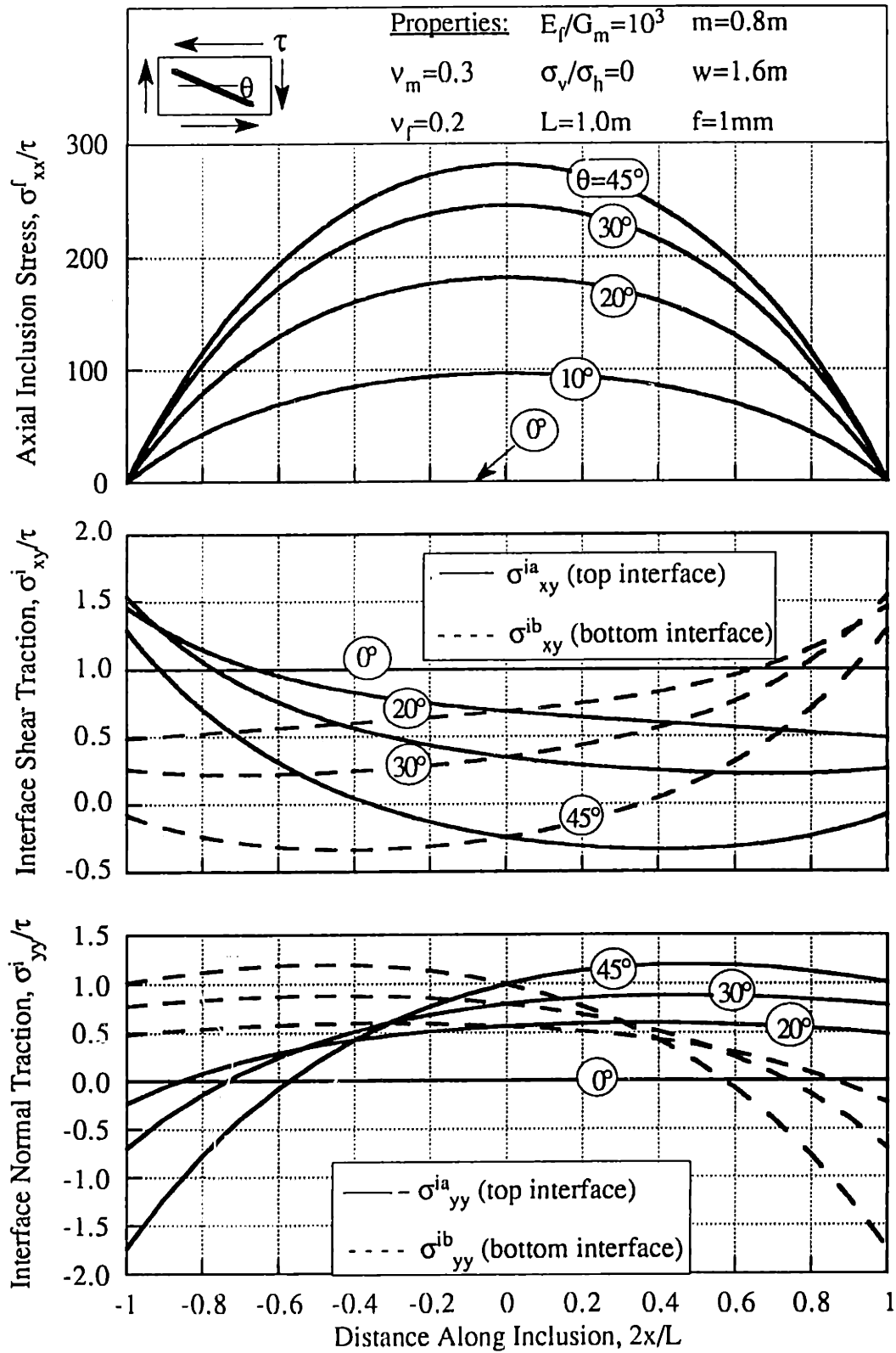


Figure 4.8: Effect of Inclusion Orientation on Load Transfer in Direct Shear.

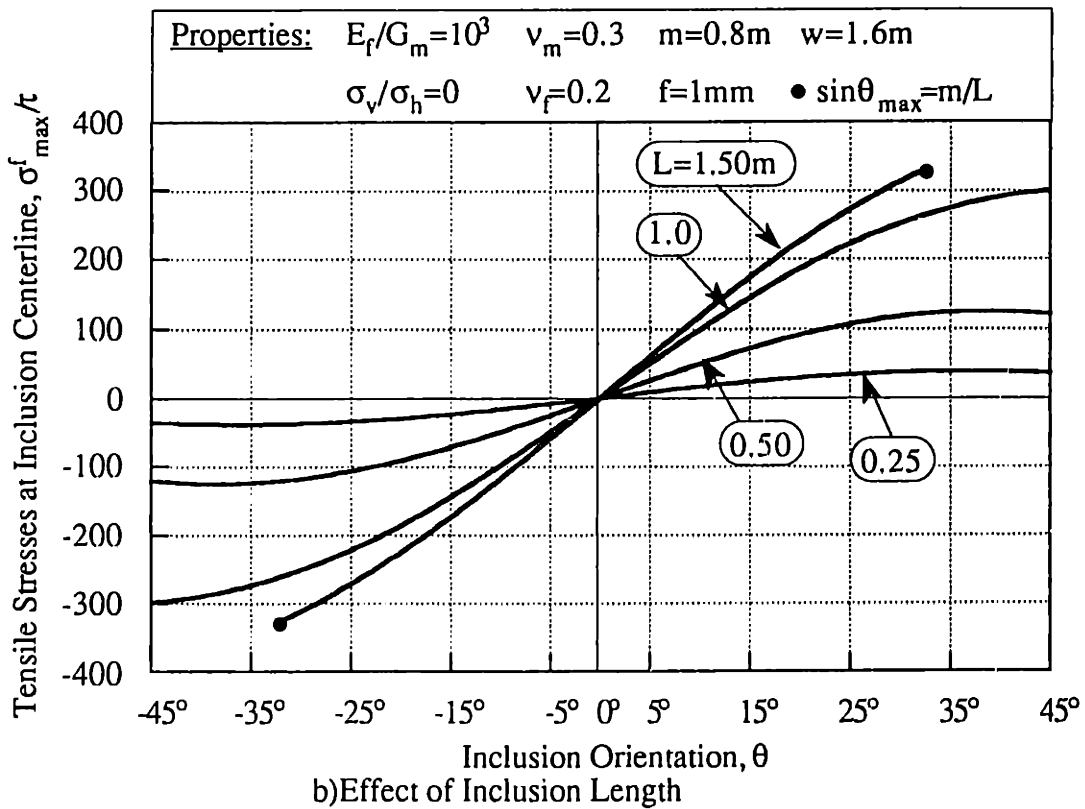
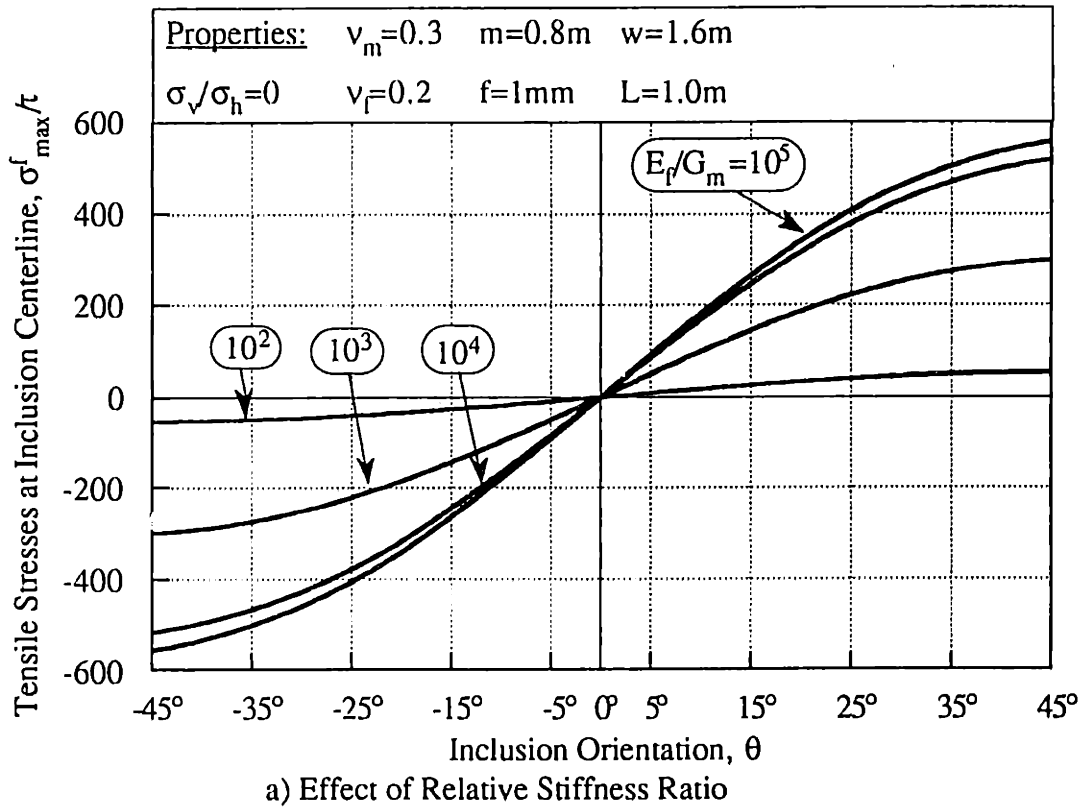


Figure 4.9: Factors Affecting Maximum Load Transfer in Direct Shear.

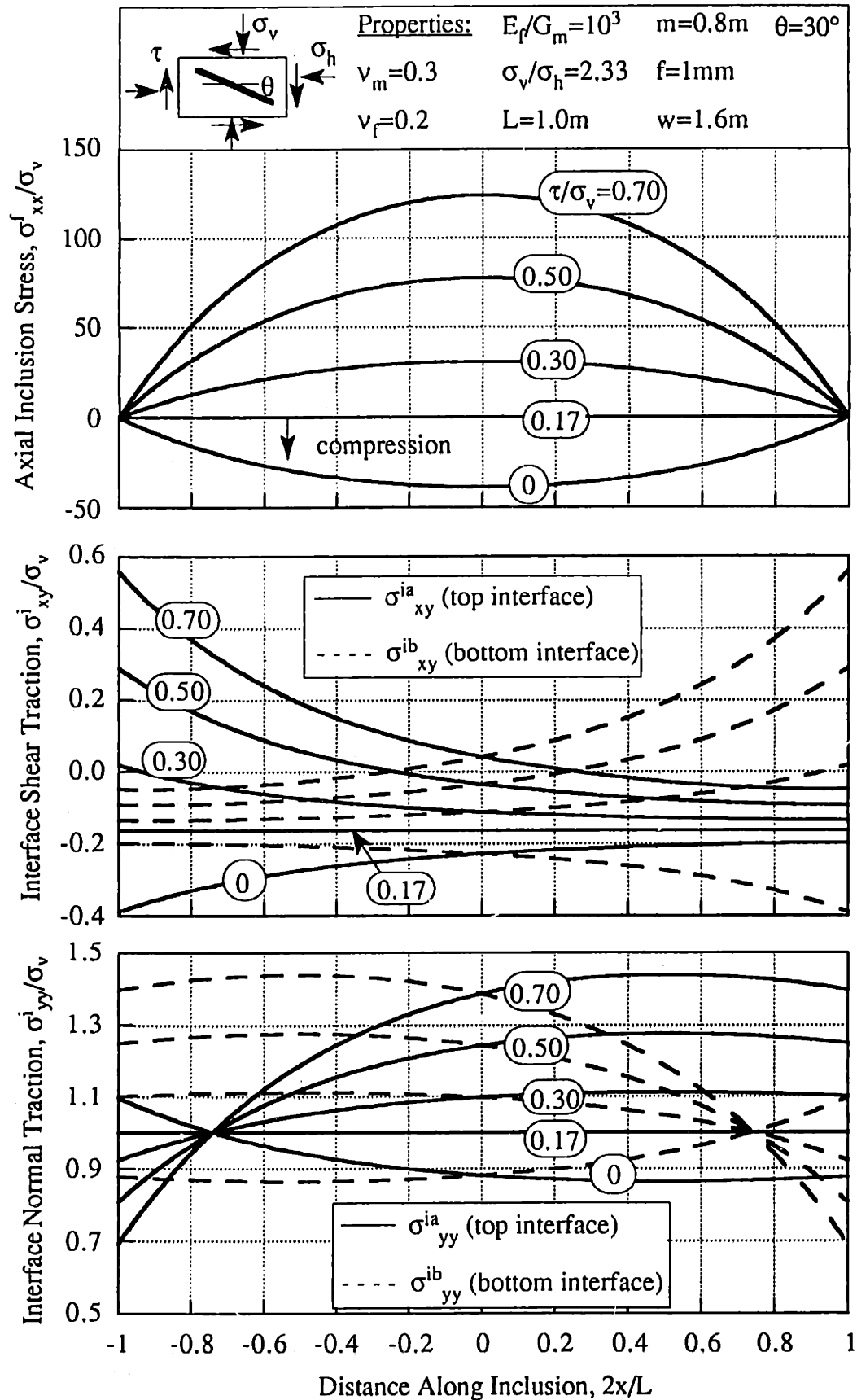


Figure 4.10: Inclusion Tensile Stresses and Interface Traction during Simple Shear Tests.

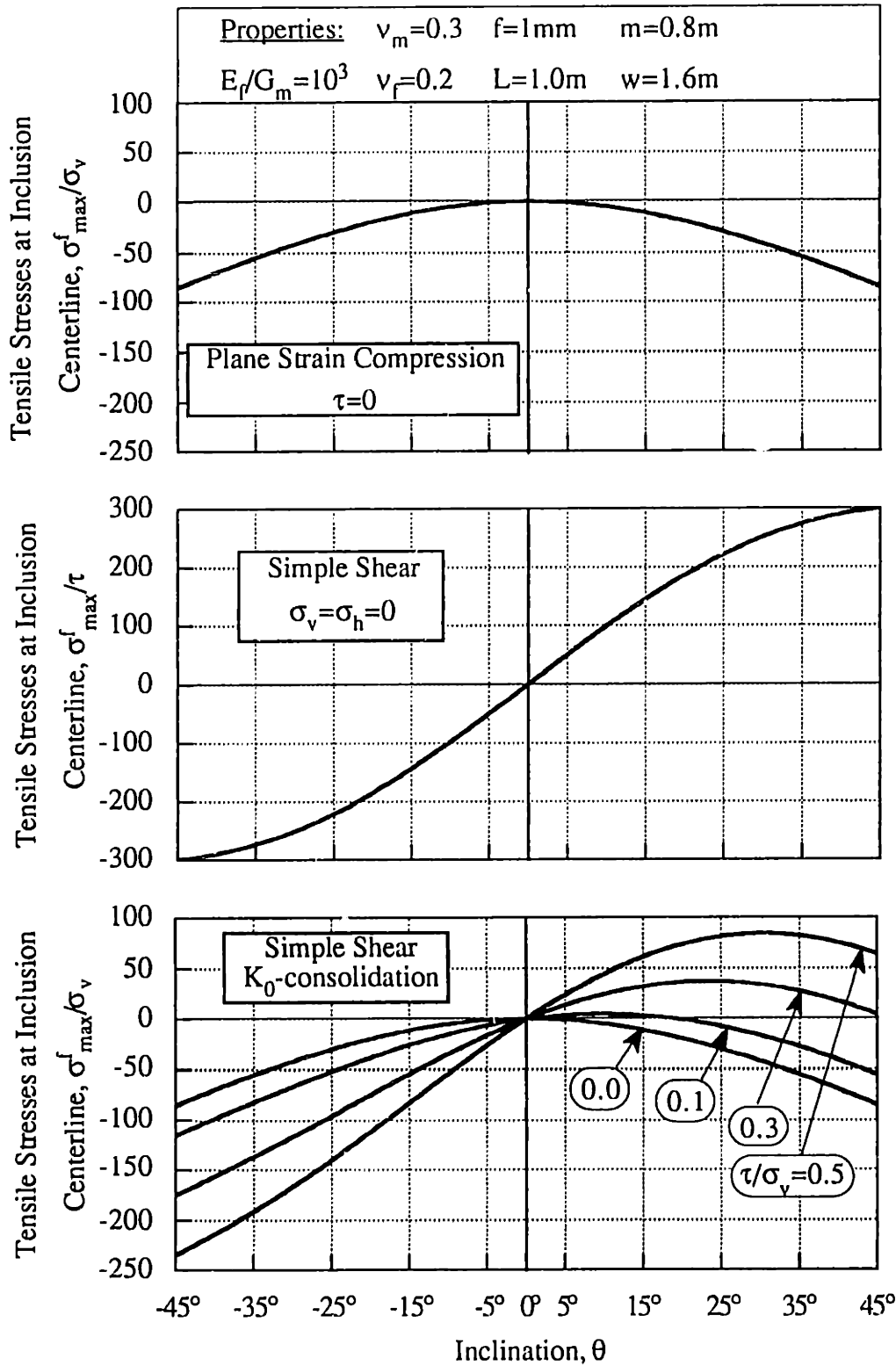
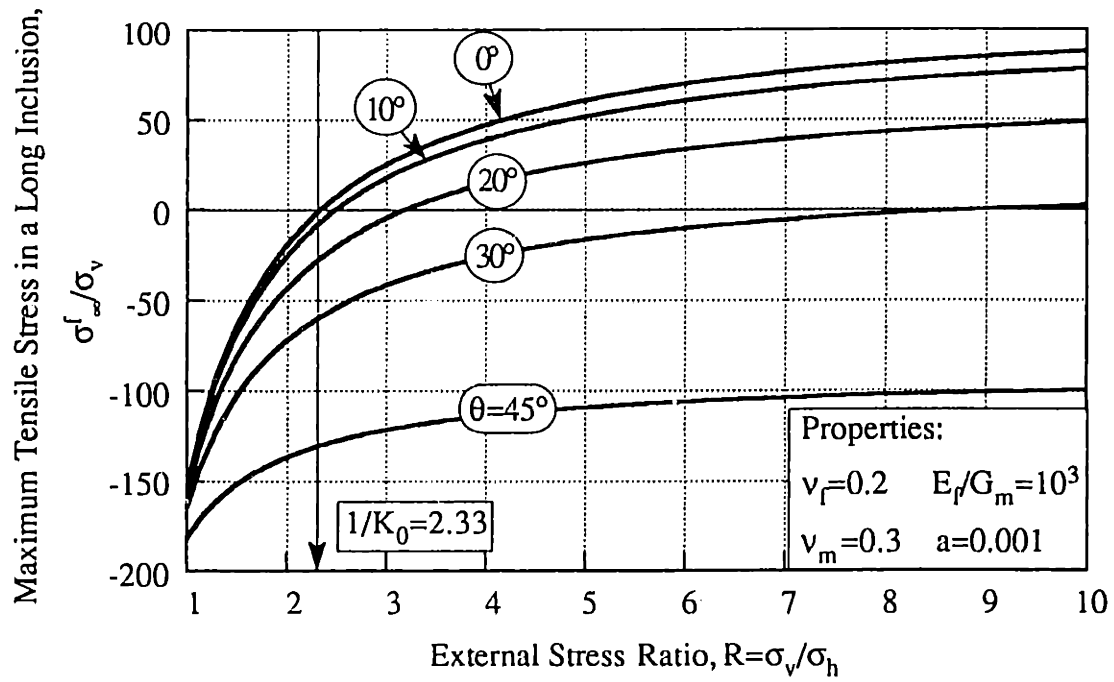
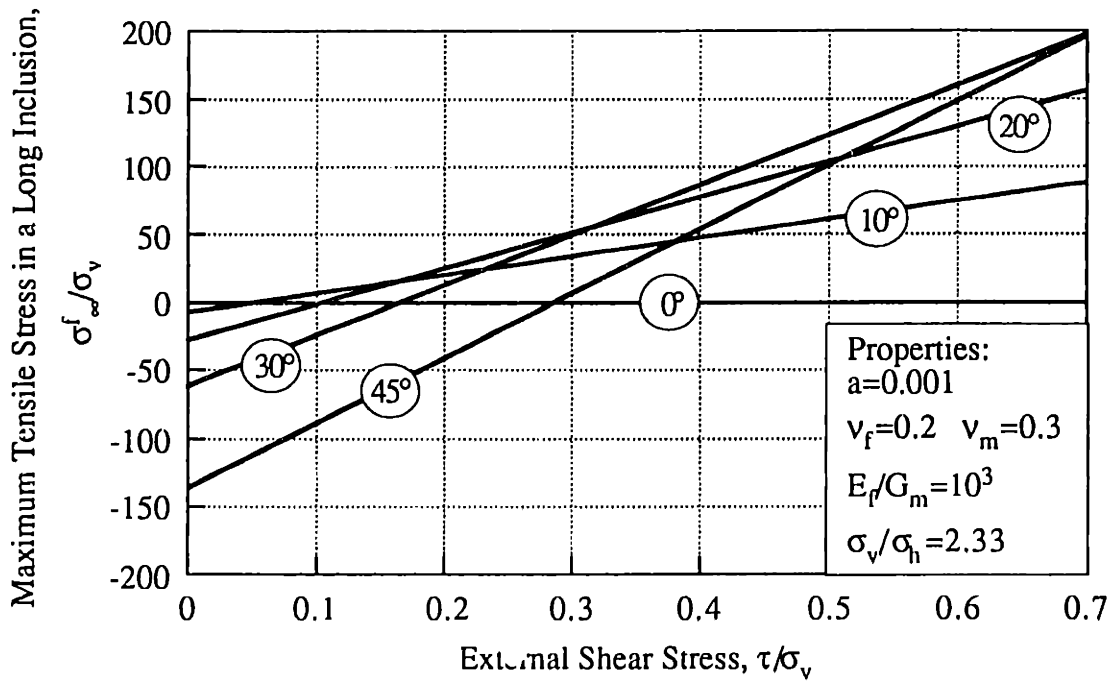


Figure 4.11: Effect of Inclusion Orientation on Maximum Load Transfer in Simple Shear Tests.



a) Plane Strain Compression



b) Simple Shear

Figure 4.12: Maximum Stresses Carried by Long Inclusions.

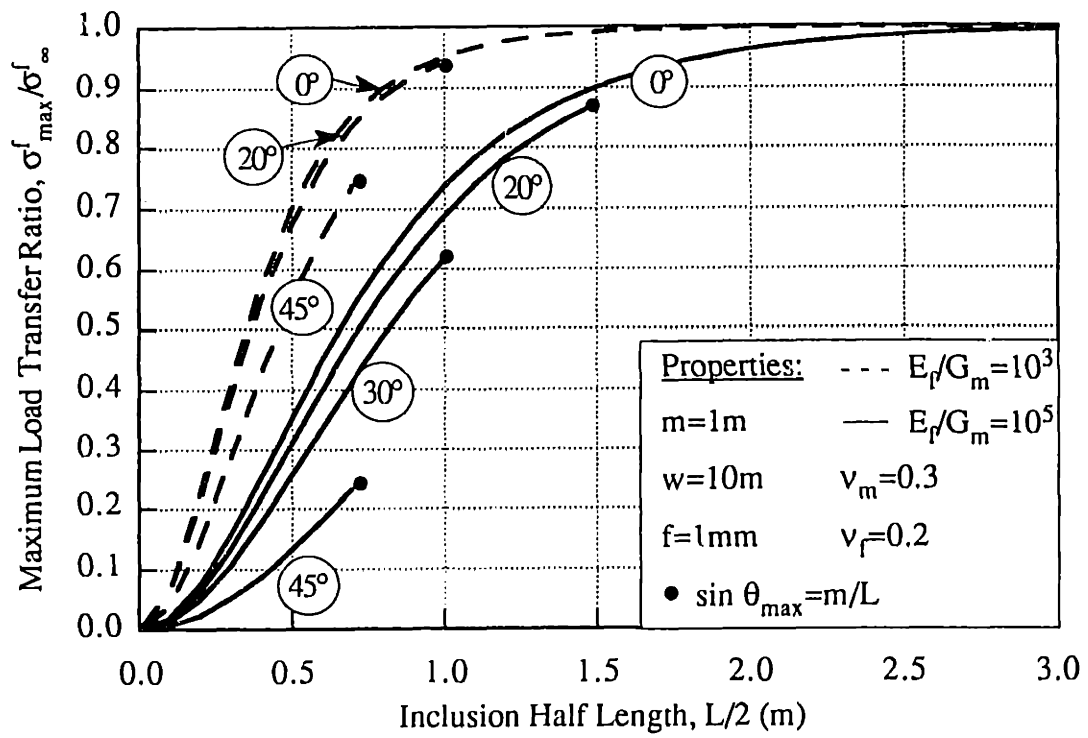
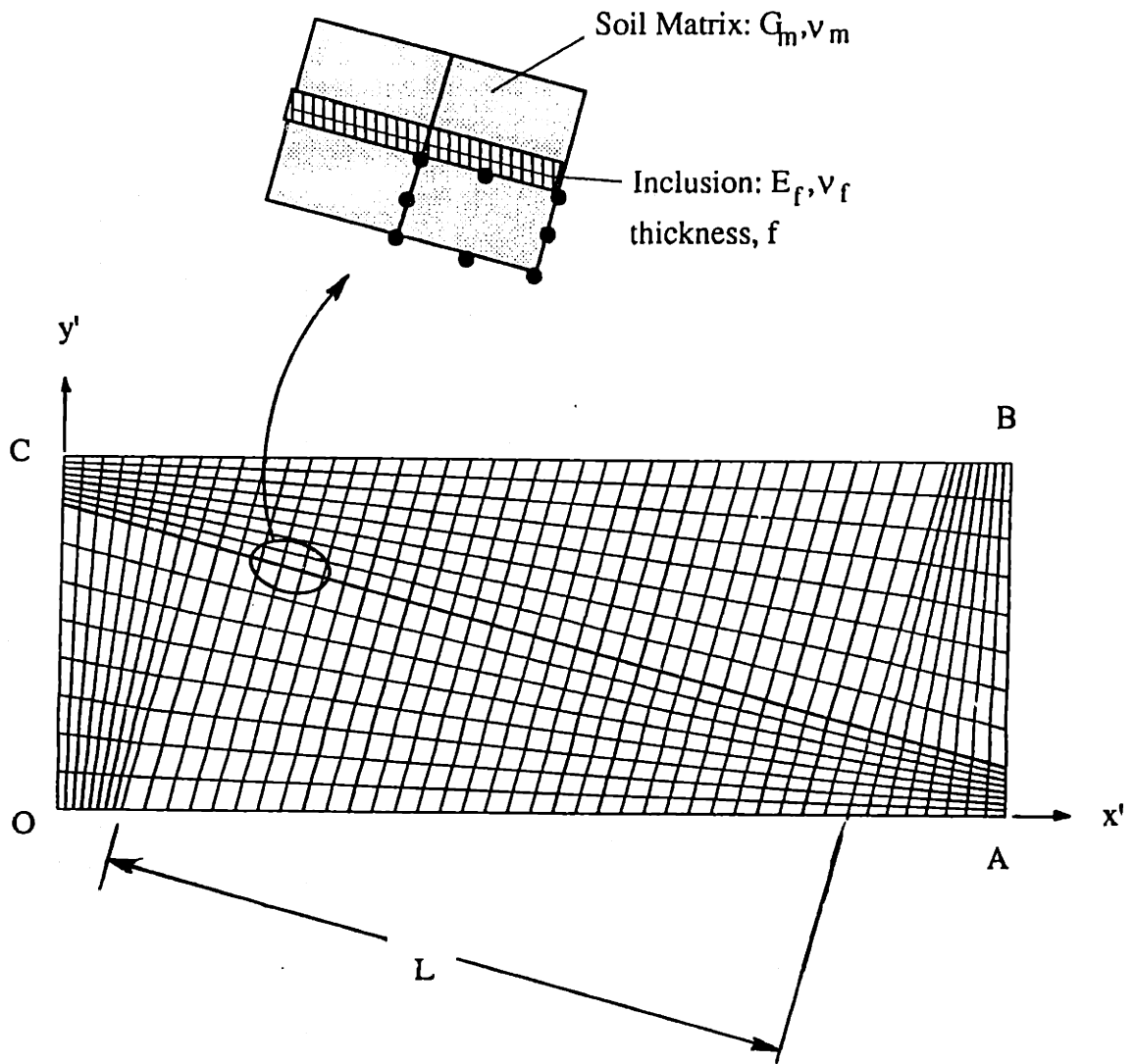


Figure 4.13: Effect of Inclusion Length, Orientation and Stiffness on the Maximum Load Transfer Ratio.



$L(m)$	1.0
$w(m)$	1.5
$m(m)$	0.5
$f(mm)$	1.0
θ	15°

Figure 4.14: Typical Finite Element Model for Computing Axial Stress in a Thin Inclined Reinforcement.

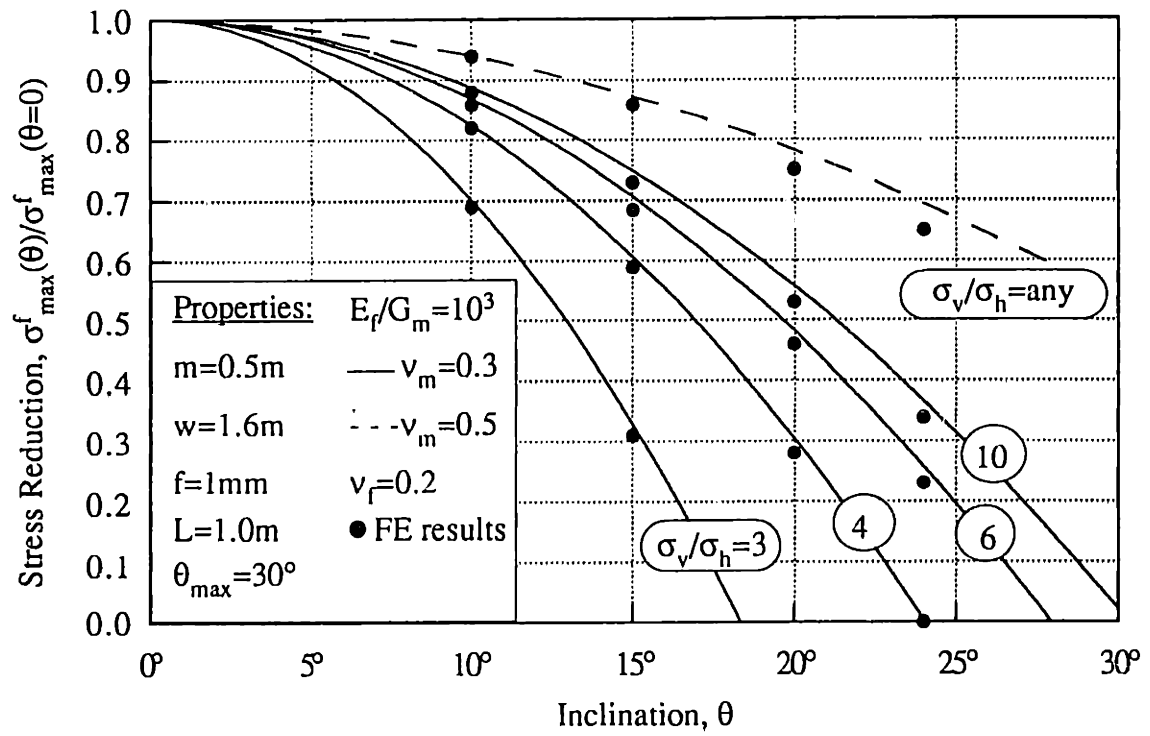


Figure 4.15: Reduction in Maximum Axial Inclusion Stress at Centerline.

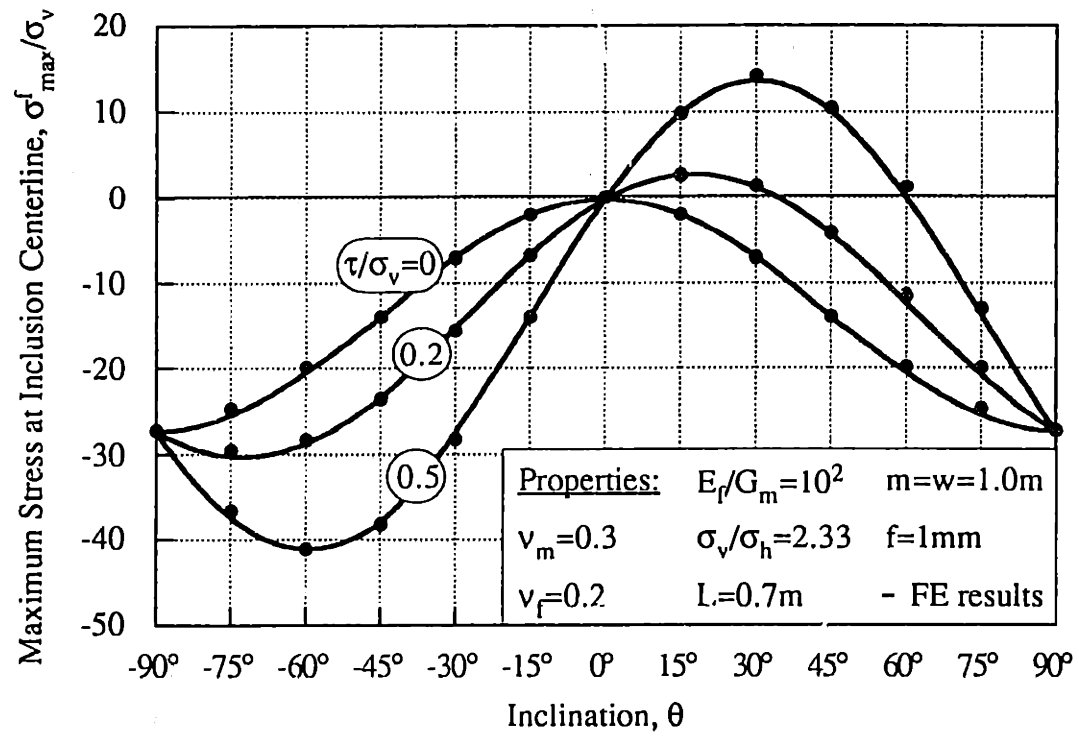


Figure 4.16: Influence of Inclusion Orientation on Maximum Stress at Inclusion Centerline and Comparison with Finite Element Results.

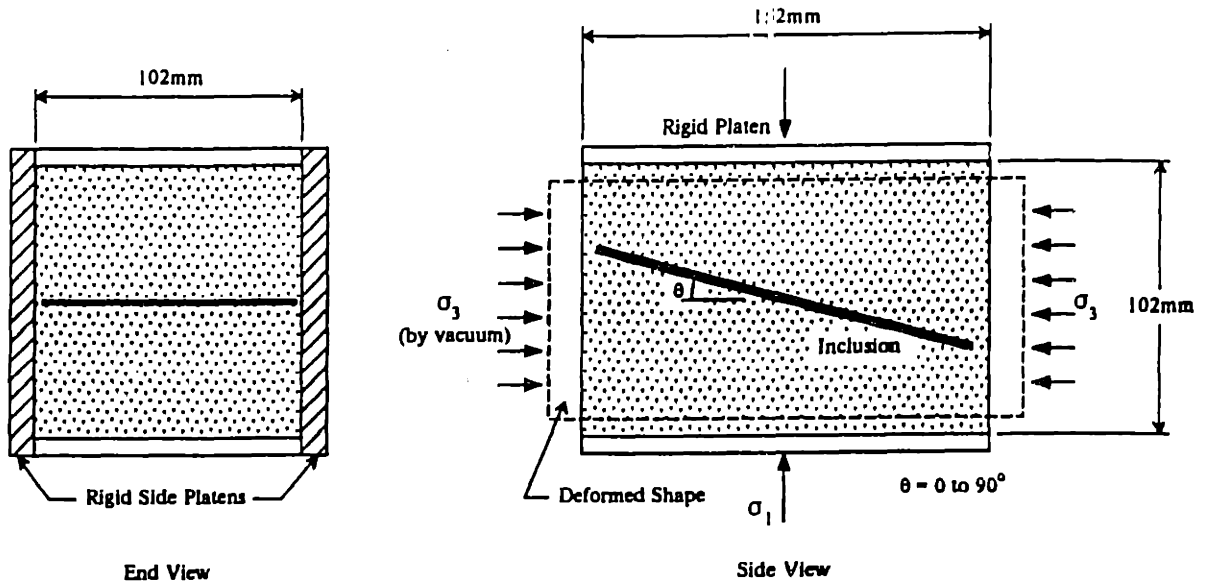


Figure 4.17: Unit Cell for Plane Strain Tests on Leighton Buzzard Sand (McGown et al., 1978).

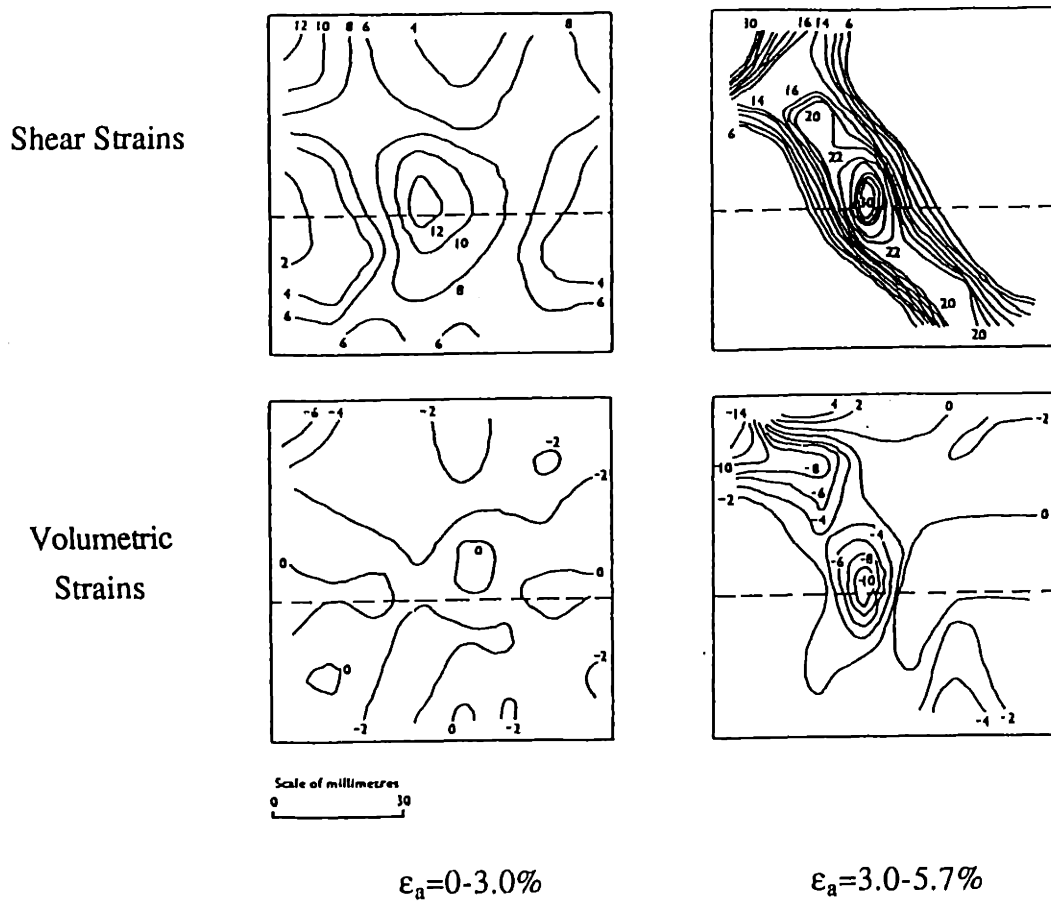
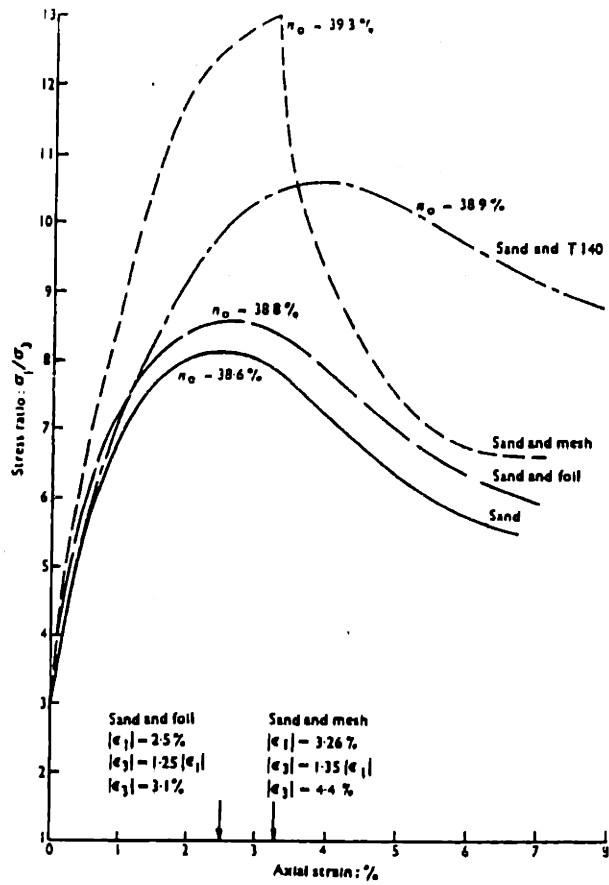
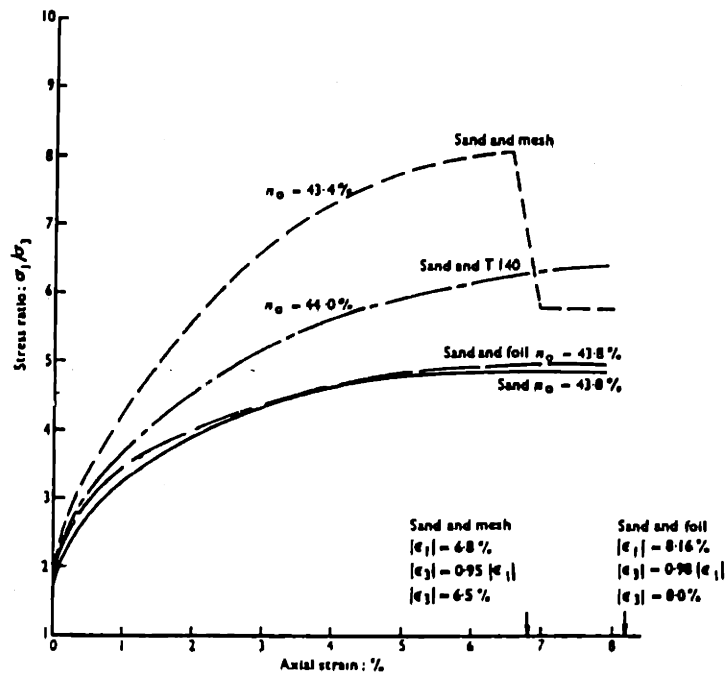


Figure 4.18: Contours of Volumetric and Shear Strains for Plane Strain Shear with a Horizontal Reinforcement (McGown et al., 1978).

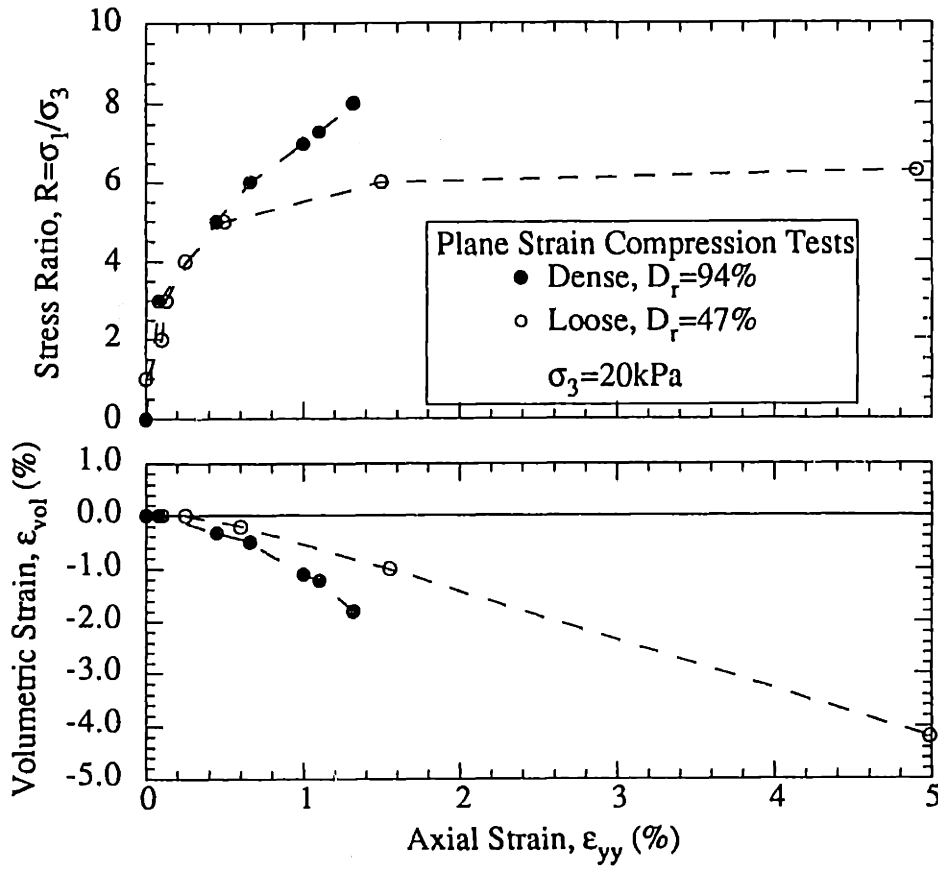


(a) Dense Leighton Buzzard sand

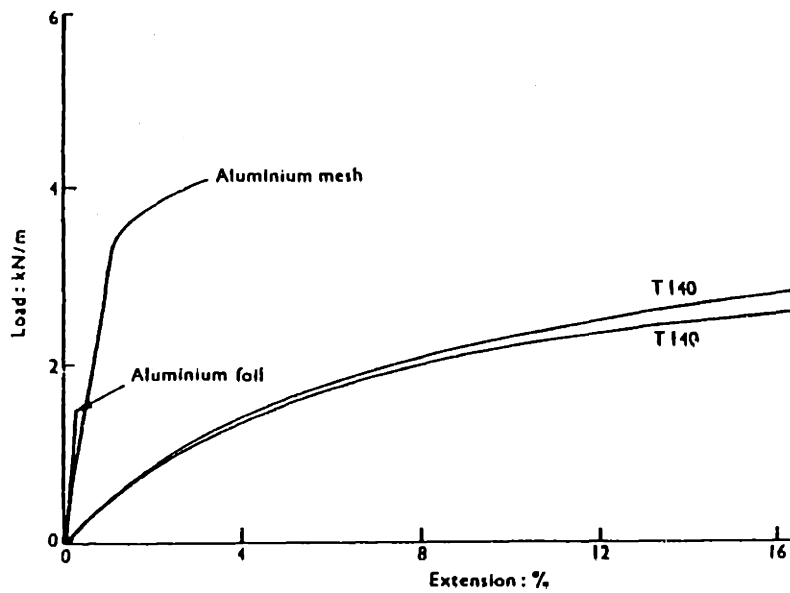


(b) Loose Leighton Buzzard sand

Figure 4.19: Effect of Reinforcements on External Stress-Strain Behavior Measured in Plane Strain Shear Tests (McGown et al., 1978).

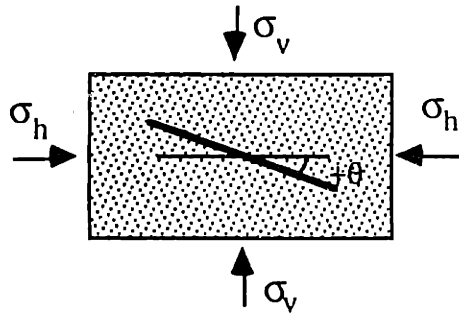


a) Leighton Buzzard Sand (after Deterling, 1984).



b) Unconfined Uniaxial Tension Tests on Reinforcing Materials (McGown et al., 1978).

Figure 4.20: Constituent Material Properties for Unit Cell Tests.



Dimensions:

$m=0.10\text{m}$

$w=0.15\text{m}$

$L^*=0.10\text{m}$

*Not given in texts; estimate is maximum length for full rotation ($L \leq m, w$).

a) Specimen Geometry and Test Conditions

State	Relative Density $D_r, (\%)$	Void Ratio	$\sigma_h(\text{kPa})$	${}^+G_m$ (MPa)	${}^+v_m$	Peak Friction ϕ°	Peak $R=\sigma_v/\sigma_h$
Dense	65	0.63	70	4.0	0.5	51	8.1
Medium	51	0.67	70	3.0	0.5	48	6.9
Loose	27	0.74	70	1.7	0.5	44	5.5

+Ref. Figure 4.20a.

b) Properties of Leighton Buzzard Sand.

Thickness, $f(\text{mm})$	E_f (MPa)	v_f
0.02	440*	0.3

* Provided in Andrawes et al. (1978).

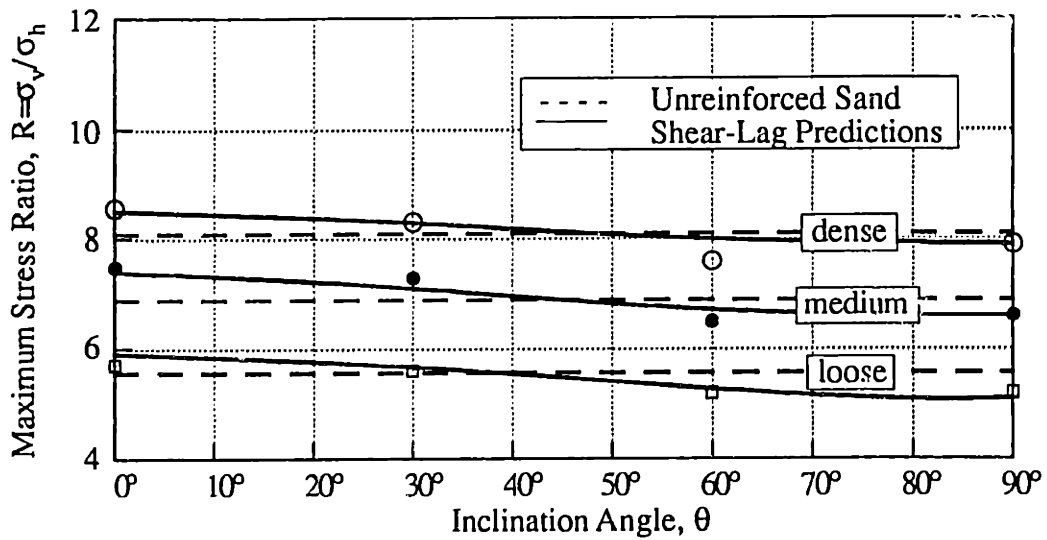
c) Properties of Aluminum Foil Reinforcement.

Thickness (mm)	$\epsilon_f (\%)$	$\sigma_h(\text{kPa})$	${}^+E_f$ (MPa)	v_f
0.55	3.3		130	0.3
	5.5	70	115	
	8.0		100	

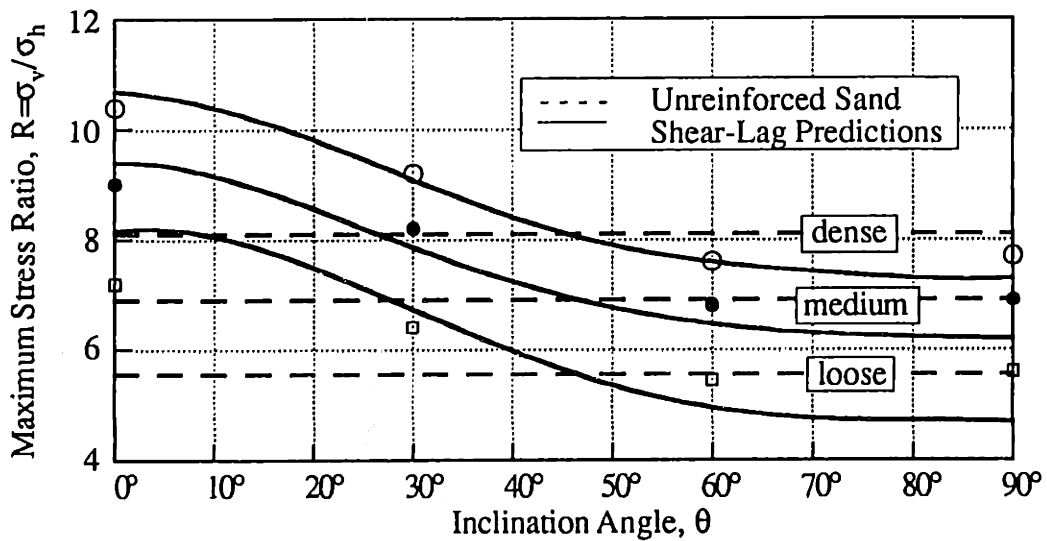
+ Secant modulus based on unconfined uniaxial tests, Figure 4.20b.

d) Properties of Non-Woven T-140 Fabric.

Table 4.3: Input Parameters for Shear-lag Analysis of Plane Strain Unit Cell Tests Reported by McGown et al. (1978).



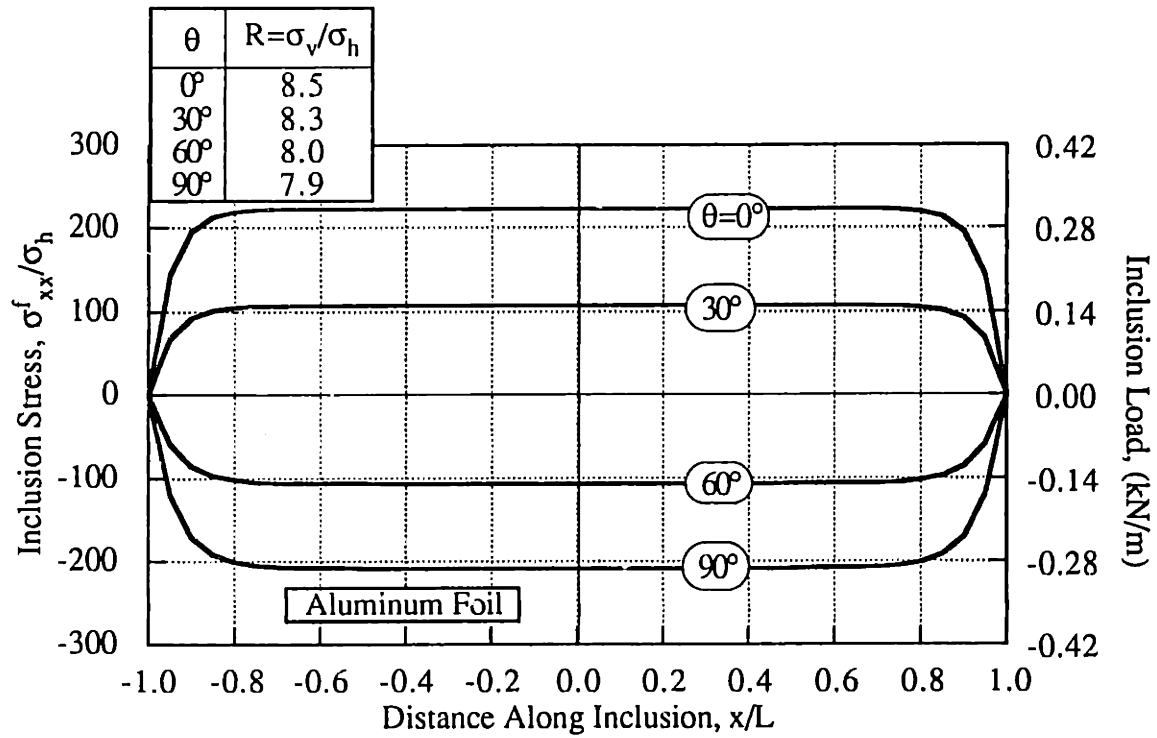
a) Aluminum Foil Reinforcement



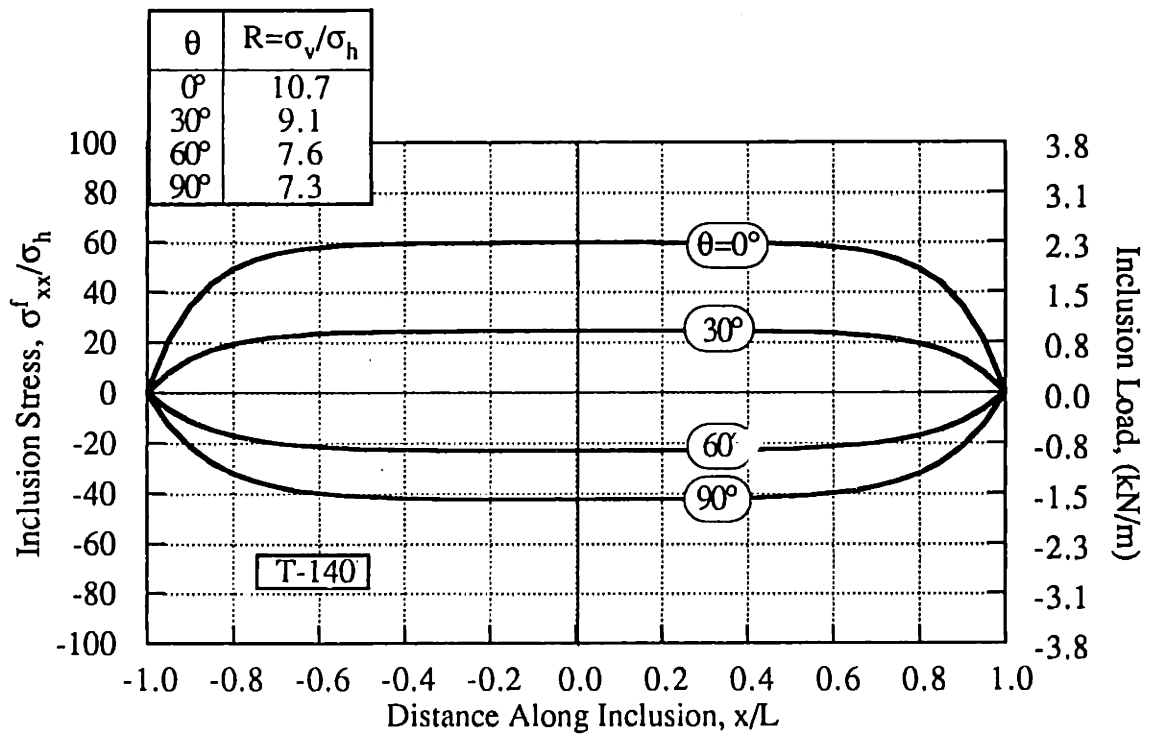
b) T-140 Non-Woven Fabric Reinforcement

Measured Data: Leighton Buzzard Sand			
Symbol	Void Ratio, e	σ_h (kPa)	Density
○	0.63	70	Dense
●	0.67		Medium
□	0.74		Loose

Figure 4.21: Comparison of Shear-Lag Predictions and Measured Peak Stress Ratio for Unit Cell Tests.



a) Aluminum Foil in Dense Sand.



b) T-140 Reinforcement in Dense Sand.

Figure 4.22: Stresses Predicted for Reinforcements in Dense Sand at Peak Strength Conditions in Unit Cell Tests.

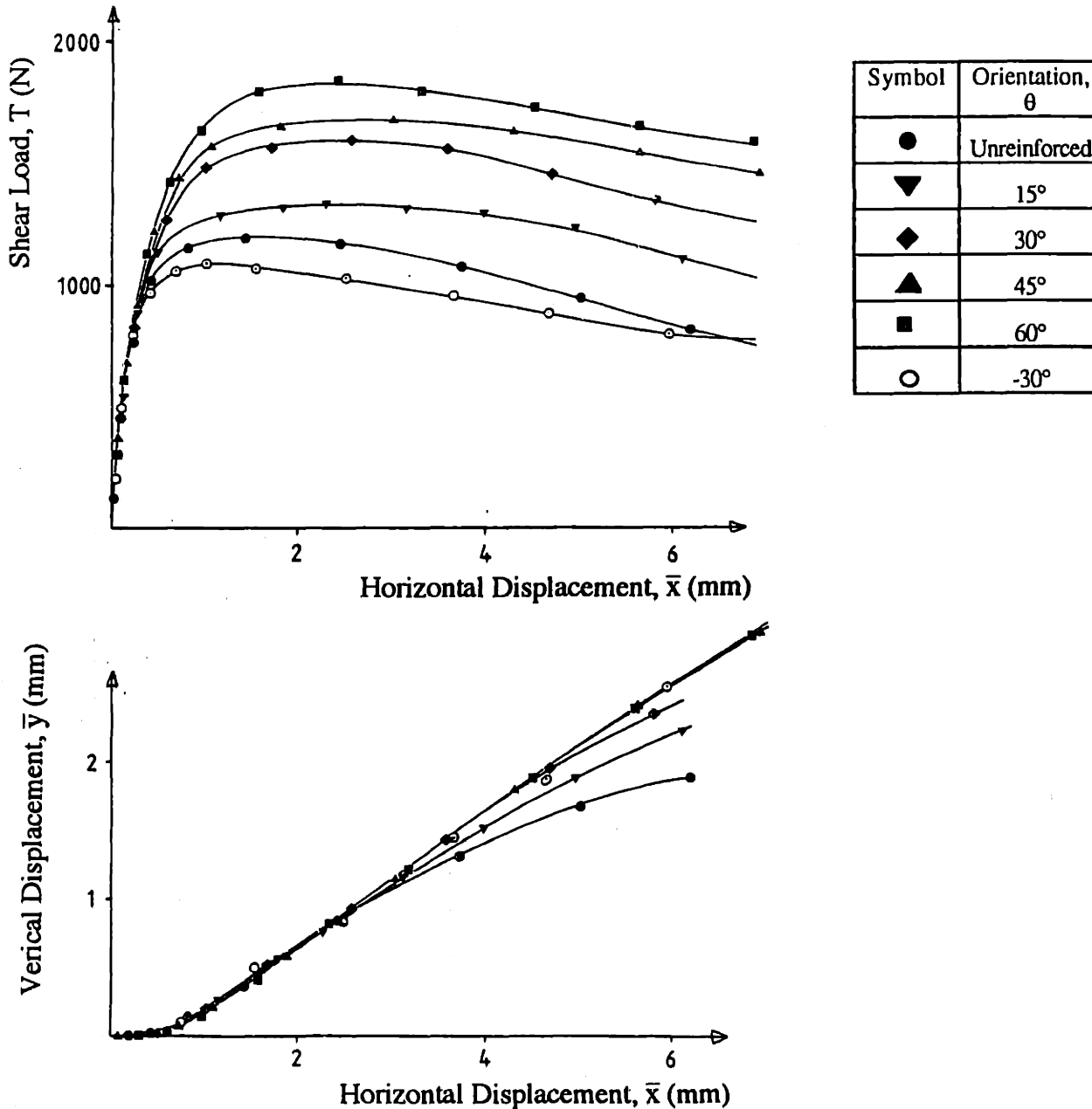
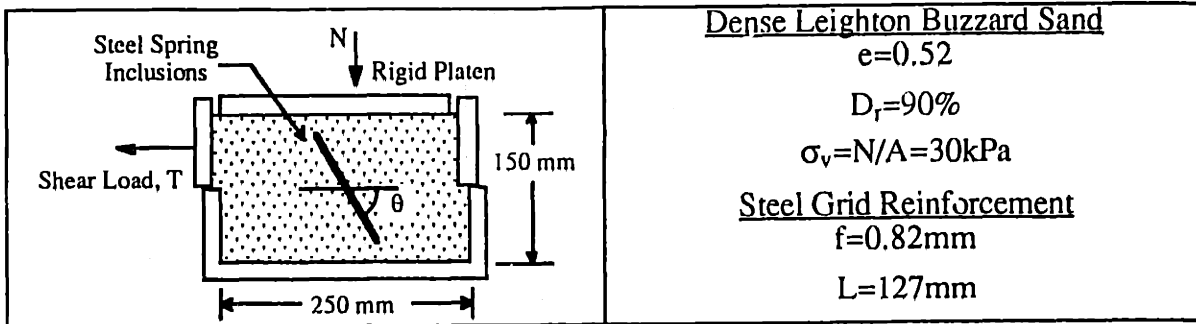
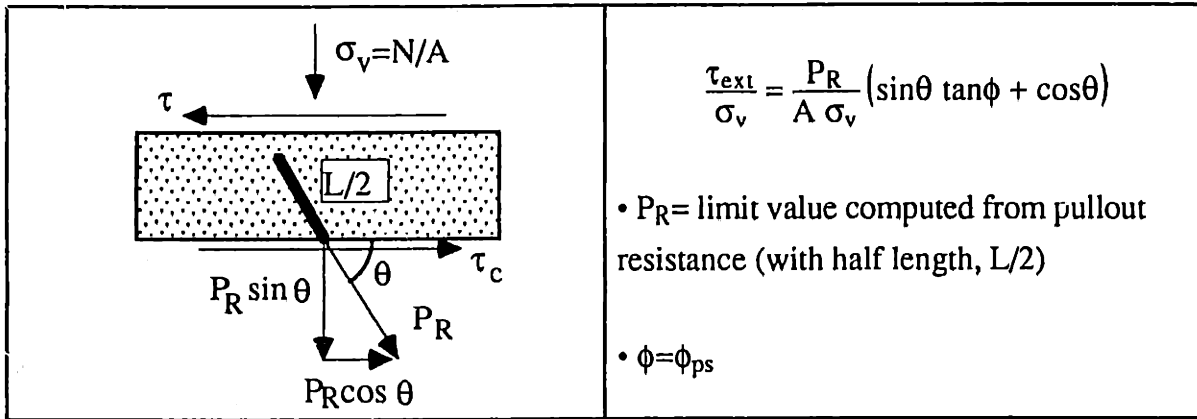
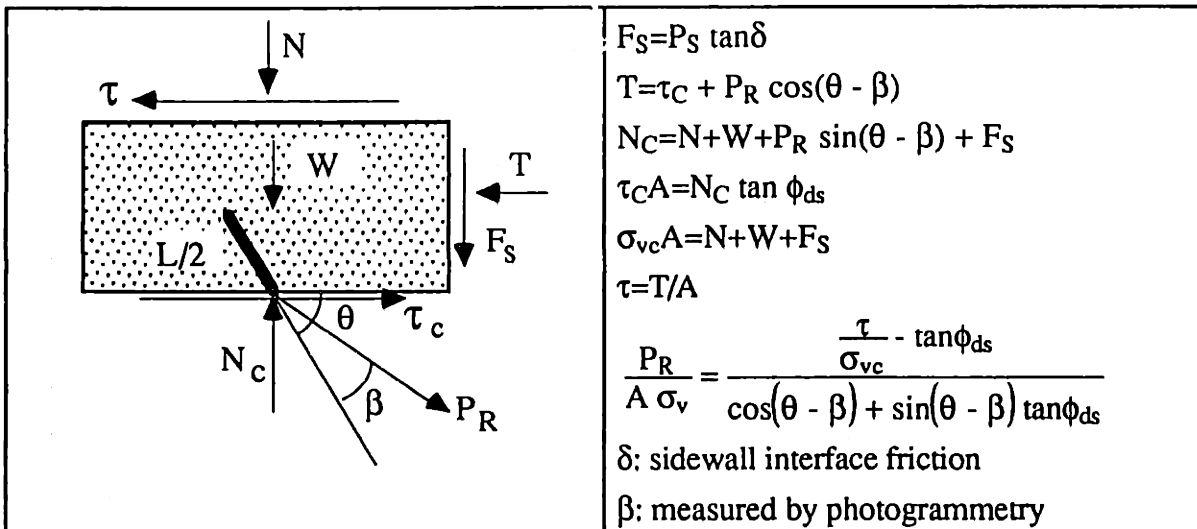


Figure 4.23: Typical Results of Direct Shear Tests on Leighton Buzzard Sand Reinforced by a Single Steel Grid at Different Orientations (Jewell, 1980).

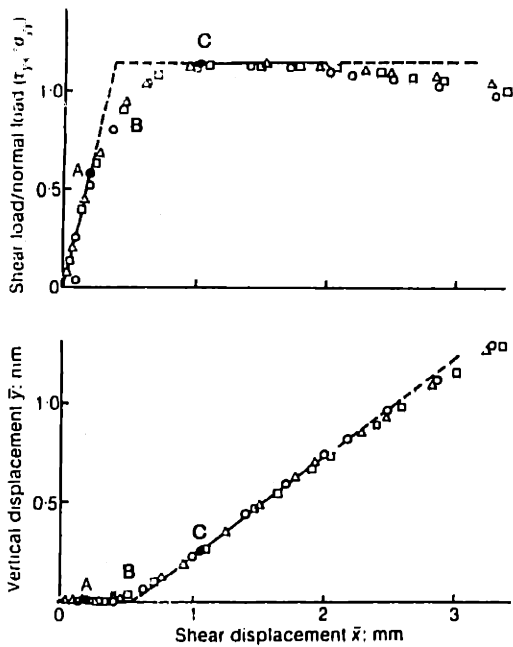


a) Interpretation of Additional Shear Resistance
(after Jewell, 1980).



b) Interpretation of Force at Center of Reinforcement
(after Palmeira, 1987).

Figure 4.24: Limit Equilibrium Interpretation of Direct Shear Tests.



O-A	Elastic	$\sigma_h = K_0 \sigma_{v0}$
I	First Yield	$\phi_{ps} = 54^\circ$
B II	Dilation Begins	$\bar{x} = 0.5 \text{ mm}$ $\sigma_h \cong \sigma_v$
C III	Peak Resistance	$\sigma_h > \sigma_v$

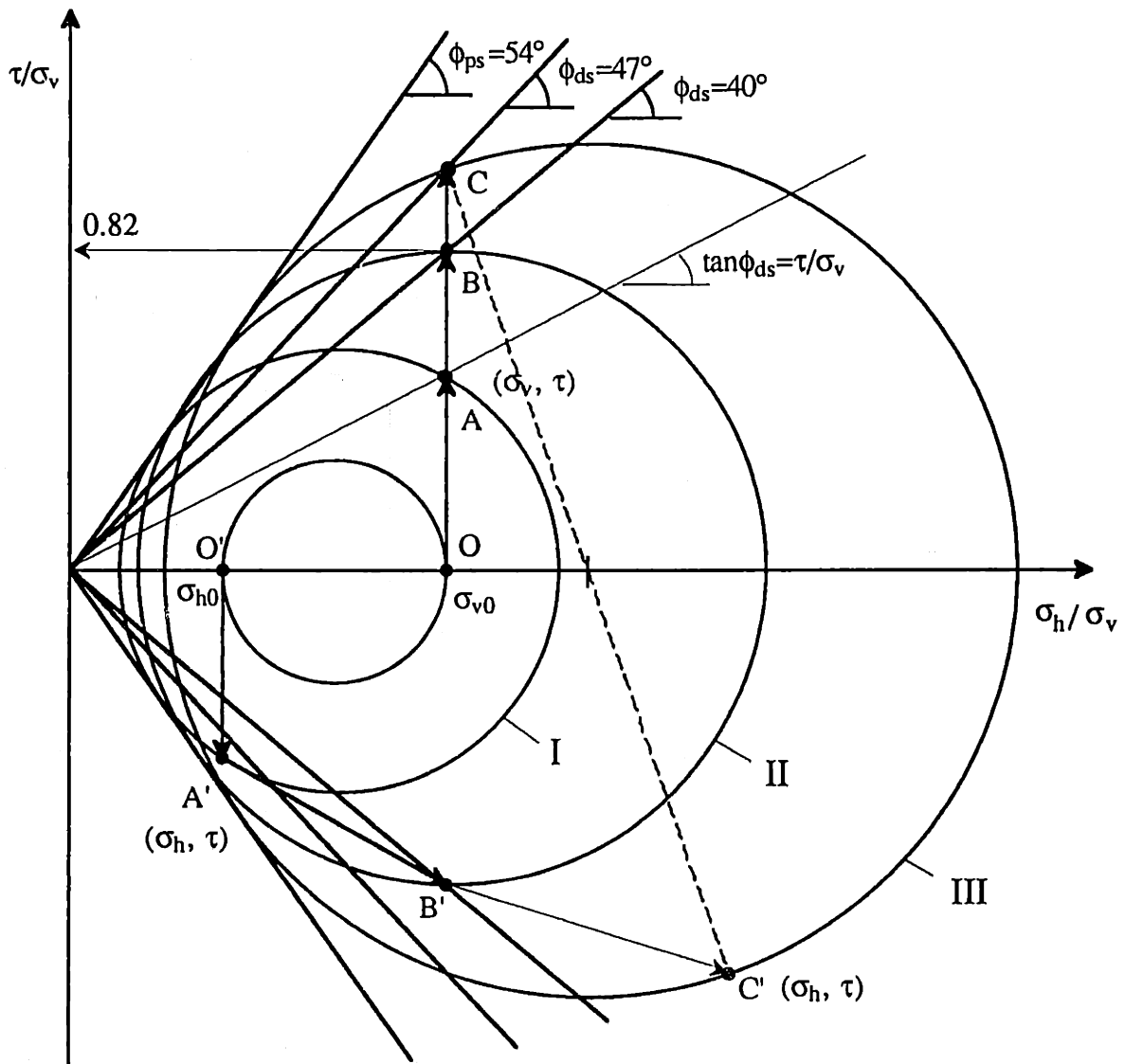
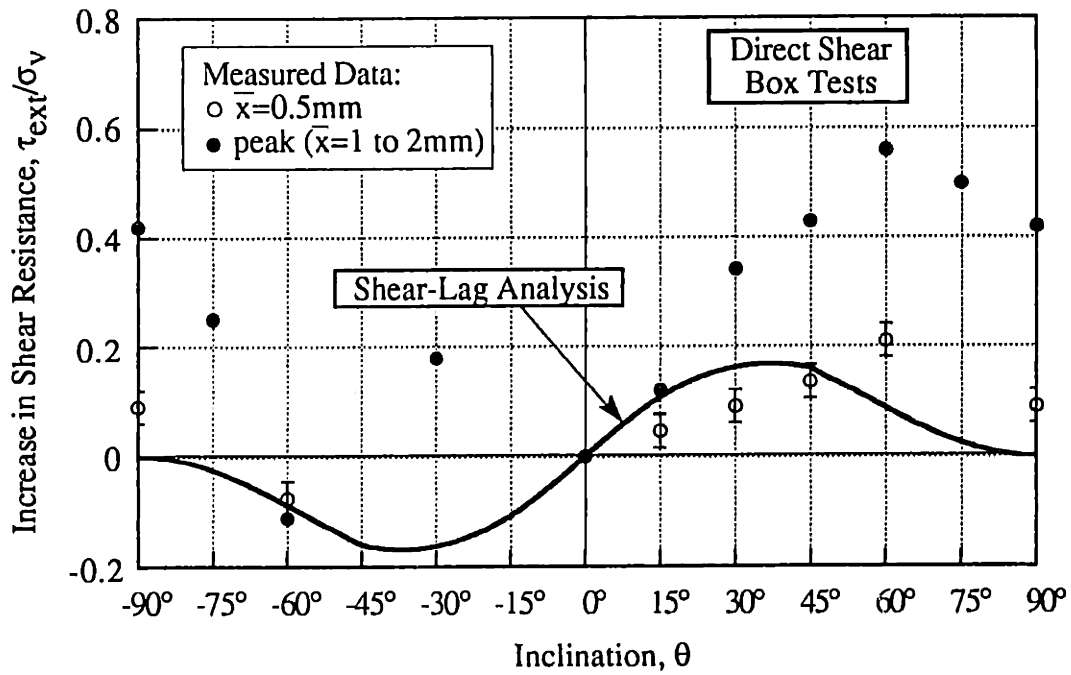


Figure 4.25: Proposed Interpretation of Direct Shear Box Tests on Unreinforced Dense Leighton Buzzard Sand.



a) Comparison of Predictions and Measurements of Improvement in Shear Resistance.

Stress Conditions (state B, Fig. 4.25)	$\tau/\sigma_v=0.82$	$\sigma_h/\sigma_v=1$	$\sigma_v=29.4\text{kPa}$
Dense LBS	$\phi_{ps}=54^\circ$	$G_m=4.0\text{MPa}$	$\nu_m=0.5$
Steel Grid ⁺	$E_f=2 \times 10^8\text{kPa}$	$\nu_f=0.3$	

⁺Treated as rough sheet of same overall dimensions.

b) Input Parameters for Shear-Lag Analysis.

Figure 4.26: Comparison of Shear-Lag Analysis and Results of Direct Shear Tests in Reinforced Leighton Buzzard Sand (Jewell and Wroth, 1987).

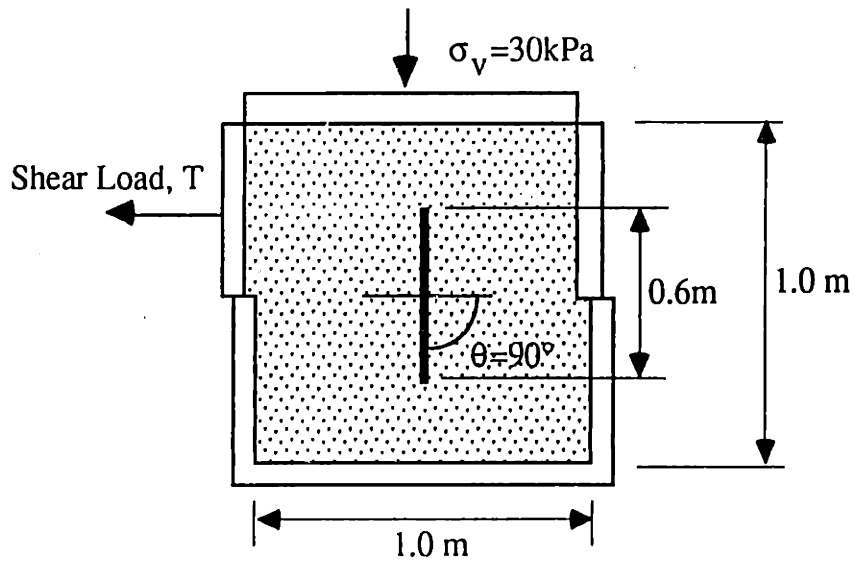
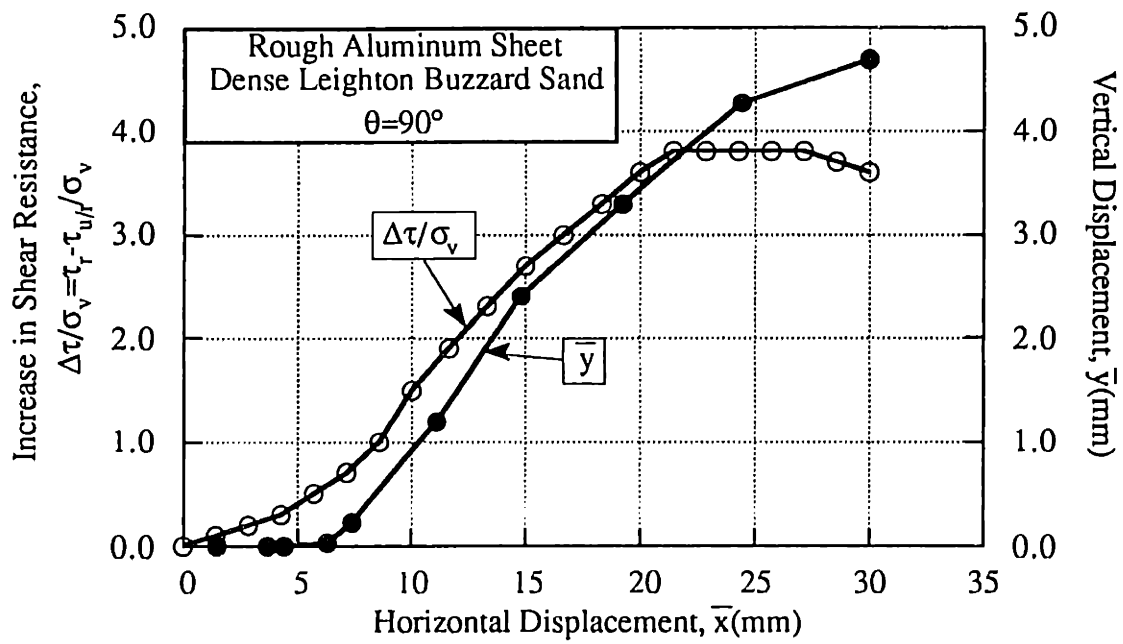


Figure 4.27: Link Between Reinforcing Effect and Soil Dilation in Large Direct Shear Box Test at $\theta=90^\circ$ (after Palmeira, 1987).

Appendix 4.A: Complete Expressions for the Interface Traction

The expressions for interface tractions are given by substituting σ_{xx}^f from 4.18 in 4.7 and 4.9. The interface shear tractions are:

$$\sigma_{xy}^{ia} = -\frac{f(\omega - x \tan\theta)}{2\omega} \frac{K_2}{\sqrt{K_1}} \left[\frac{\sinh\sqrt{K_1} x}{\cosh\sqrt{K_1} \frac{L}{2}} \right] - \frac{f \tan\theta}{2\omega} \frac{K_2}{K_1} \left[1 - \frac{\cosh\sqrt{K_1} x}{\cosh\sqrt{K_1} \frac{L}{2}} \right] + \sigma_{xy}^0 \quad \text{A.1a}$$

$$\sigma_{xy}^{ib} = \frac{f(\omega + x \tan\theta)}{2\omega} \frac{K_2}{\sqrt{K_1}} \left[\frac{\sinh\sqrt{K_1} x}{\cosh\sqrt{K_1} \frac{L}{2}} \right] - \frac{f \tan\theta}{2\omega} \frac{K_2}{K_1} \left[1 - \frac{\cosh\sqrt{K_1} x}{\cosh\sqrt{K_1} \frac{L}{2}} \right] + \sigma_{xy}^0 \quad \text{A.1b}$$

And the interface normal tractions are:

$$\begin{aligned} \sigma_{yy}^{ia} = & -\frac{f}{4y_c} (y_c^2 - x^2 \tan^2\theta) K_2 \left[\frac{\cosh\sqrt{K_1} x}{\cosh\sqrt{K_1} \frac{L}{2}} \right] + \frac{f}{y_c} x \tan^2\theta \frac{K_2}{\sqrt{K_1}} \left[\frac{\sinh\sqrt{K_1} x}{\cosh\sqrt{K_1} \frac{L}{2}} \right] + \\ & -\frac{f}{2y_c} \tan^2\theta \frac{K_2}{K_1} \left[1 - \frac{\cosh\sqrt{K_1} x}{\cosh\sqrt{K_1} \frac{L}{2}} \right] + \sigma_{yy}^0 \end{aligned} \quad \text{A.2a}$$

$$\begin{aligned} \sigma_{yy}^{ib} = & -\frac{f}{4y_c} (y_c^2 - x^2 \tan^2\theta) K_2 \left[\frac{\cosh\sqrt{K_1} x}{\cosh\sqrt{K_1} \frac{L}{2}} \right] - \frac{f}{y_c} x \tan^2\theta \frac{K_2}{\sqrt{K_1}} \left[\frac{\sinh\sqrt{K_1} x}{\cosh\sqrt{K_1} \frac{L}{2}} \right] + \\ & -\frac{f}{2y_c} \tan^2\theta \frac{K_2}{K_1} \left[1 - \frac{\cosh\sqrt{K_1} x}{\cosh\sqrt{K_1} \frac{L}{2}} \right] + \sigma_{yy}^0 \end{aligned} \quad \text{A.2b}$$

Appendix 4.B: References

- Abramanto, M., and Whittle, A.J. (1993), "Shear-Lag Analysis of a Planar Soil Reinforcement in Plane Strain Compression," *ASCE Journal of Mechanical Engineering*, February.
- Andrawes, K.Z., McGown, A., and Al-Hasani, M.M. (1978) "Alteration of Soil Behaviour by the Inclusion of Materials with Different Properties", *Ground Engineering*, 35-42.
- Basset, R.H. and Last, N.C. (1978) "Reinforcing Earth Below Footings and Embankments", *Symposium on Earth Reinforcement*, Pittsburgh, PA, 202-231.
- Budiansky, B., Hutchinson, J. W. and Evans, A. G. (1986) "Matrix Fracture in Fiber-Reinforced Ceramics", *Journal of the Mechanics and Physics of Solids*, 34(2), 167-189.
- Deterling, P.A. (1984) "*Behavior of Sand Stressed under Three Independently Controlled Principal Stresses*", S.M. Thesis, Massachusetts Institute of Technology, Cambridge, MA.
- Dyer, M.R. (1985) "*Observation of the Stress Distribution in Crushed Glass with Applications to Soil Reinforcement*", Ph.D. Thesis, University of Oxford.
- Dyer, M.R. and Milligan, G.W.E. (1984) "A Photo-Elastic Investigation of the Interaction of a Cohesionless Soil with Reinforcement Placed at Different Orientations", *Proc. Int. Conf. on Insitu Soil and Rock Reinforcement*, Paris, 257-262.
- Gray, D.H. and Ohashi, H. (1983) "Mechanics of Fiber Reinforcement in Sand", *ASCE Journal of Geotechnical Engineering*, 109(3), 335-353.

- Hayashi, S., Ochiai, H., Yoshimoto, A., Sato, K., and Kitamura, T. (1988) "Functions and Effects of Reinforcing Materials in Earth Reinforcement", *International Geotechnical Symposium on Theory and Practice of Earth Reinforcement*, Fukuoka, Japan, 99-104.
- Jewell, R.A. (1980) "*Some Effects of Reinforcement on the Mechanical Behaviour of Soils*", Ph.D. Thesis, University of Cambridge.
- Jewell, R.A., and Wroth, C.P. (1987) "Direct Shear Tests on Reinforced Sand", *Géotechnique*, 37(1), 53-68.
- Larson, D. G. (1992) "*A Laboratory Investigation of Load Transfer in Reinforced Soil*", PhD Thesis, MIT, Cambridge, MA.
- Ling, H-I; Wu, J.T.H. and Tatsuoka, F. (1992) "Short-Term Strength and Deformation Characteristics of Geotextiles Under Typical Operational Conditions", *Geotextiles and Geomembranes*, 11, 185-219.
- McGown, A.; Andrawes, K.Z. and Al-Hasani, M.M. (1978) "Effect of Inclusion Properties on the Behaviour of Sand", *Géotechnique*, 28(3), 327-346.
- Palmeira, E.M. (1987) "*The Study of Soil-Reinforcement Interaction by means of Large Scale Laboratory Tests*", Ph.D. Thesis, University of Oxford.
- Palmeira, E.M. and Milligan, G.W.E. (1989) "Scale and other Factors Affecting the Results of Pullout Tests of Grids Buried in Sand", *Géotechnique*, 39 (3), 511-524.
- Shewbridge, S.E. and Sitar, N. (1989) "Deformation Characteristics of Reinforced Sand in Direct Shear", *ASCE Journal of Geotechnical Engineering*, 115(8), 1134-1147.

Appendix 4.C: Notation

The following symbols are used in Chapter 4:

a	=	inclusion ratio (f/m)
D_r	=	relative density
E_f	=	inclusion elastic modulus
E_m	=	soil matrix elastic modulus
f	=	inclusion thickness
G_m	=	soil matrix shear modulus
i	=	inclusion inclination with vertical
K_0	=	coefficient of lateral stress at rest
K_1	=	shear lag parameter (eqn. 4.13a)
K_2^v, K_2^h, K_2^f	=	expressions defined in eqns. 4.13b, c, d
L	=	inclusion length
L_I	=	length of zone I (pickup length)
m	=	soil matrix height
N	=	consolidation load in direct shear tests
P_R	=	reinforcement load in direct shear tests
R_{max}	=	maximum σ_1/σ_3 in plane strain tests
R^m	=	ratio of principal stresses within soil matrix
T	=	external shear load in direct shear tests
x, y	=	distance along inclusion and soil matrix (x, y local coordinate system)
x^*, y^*	=	global coordinate system
y^a, y^b	=	lateral dimensions of soil specimen (Fig. 4.3)
\bar{y}	=	dimension of shear spring layer
y_c	=	lateral dimension of soil matrix at $x=0$
w	=	soil matrix width

δ	=	soil-inclusion interface friction
ϕ	=	mobilized soil friction angle
ϕ_{ps}, ϕ_{ds}	=	friction angle measured in plane strain and direct shear, respectively
η	=	dilation rate
μ	=	soil-inclusion interface friction coefficient
ν_f	=	inclusion Poisson's ratio
ν_m	=	soil matrix Poisson's ratio
γ	=	shear strain
σ_1, σ_3	=	major and minor external principal stresses
σ_1^m, σ_3^m	=	major and minor principal stresses in soil matrix
σ_v, σ_h	=	vertical and horizontal external stresses
σ_{h0}, σ_{v0}	=	consolidation stresses in direct shear tests
σ_{∞}^f	=	maximum axial stress carried by long inclusions
σ_{max}^f	=	maximum axial stress at inclusion centerline
σ_{xx}^f	=	axial stress along inclusion (positive in tension)
$\sigma_{xx}^0, \sigma_{xy}^0, \sigma_{yy}^0$	=	unreinforced soil matrix axial, shear and normal stresses
$\bar{\sigma}_{xx}^f, \bar{\sigma}_{xy}^m, \bar{\sigma}_{yy}^m$	=	average stresses (eqn. 4.19)
$\sigma_{xy}^i, \sigma_{yy}^i$	=	average interface shear and normal stresses
$c_{xy}^{i a,b}, \sigma_{yy}^{i a,b}$	=	upper/lower interface shear and normal stress
$\sigma_{xx}^m, \sigma_{xy}^m, \sigma_{yy}^m$	=	soil matrix axial, shear and normal stresses
$\sigma_{xx}^{m a,b}, \sigma_{xy}^{m a,b}, \sigma_{yy}^{m a,b}$	=	soil matrix axial, shear and normal stresses in upper/lower regions
θ	=	inclusion inclination to horizontal
θ_L	=	limit orientation defined as $\tan^{-1}w/m$
θ_{max}	=	maximum orientation for long inclusions ($=\sin^{-1}m/L$ or $\cos^{-1}w/L$)
θ_1, θ_2	=	defined in equation 4.1 and Figure 4.4, respectively
τ	=	external shear stress
τ_{ext}	=	$\tau_r - \tau_{ur}$

- τ_r = reinforced external shear
- τ_{ur} = unreinforced external shear
- ξ^* = orientation of principal stresses with y^*
- ψ = zero extension direction

Chapter 5: Analysis of Pullout Tests for Planar Soil Reinforcement

5.1. Introduction

Pullout tests simulate the action of a reinforcing inclusion as a tensile anchorage embedded in the soil mass. The test data are widely used to estimate the soil-reinforcement bond capacity for design calculations based on limit equilibrium analyses (e.g. Jewell, 1990). In practice, pullout measurements have been reported from a variety of experimental configurations, ranging from full scale field tests (e.g., Chang et al., 1977; Schlosser and Elias, 1978) to laboratory models (walls and embankments) and pullout boxes (e.g. Shen et al, 1979; Ingold, 1984; Delmas et al, 1979; Rowe et al, 1985). Figure 5.1 shows some of the typical geometries used in laboratory pullout tests and demonstrates the wide range of boundary conditions which are possible. The principal variations in test geometry are associated with three design considerations:

1. The uniformity of vertical stresses imposed externally on the soil;
2. The boundary conditions at the front face of the cell where pullout loads are applied;
3. The control of the embedded length of the inclusion.

Recent data from test devices using rigid top platens and flexible pressure bags (e.g. Palmeira, 1987; Fig. 5.1b) suggest that the vertical boundary condition does not affect significantly the pullout measurements (for pullout boxes with height to length aspect ratios $h/L \geq 0.6$). Similarly, the control of embedment length is expected to influence the bond resistance only at large displacements and has little effect on the peak bond capacity for reinforcing materials of practical interest.

The boundary condition at the front wall, however, can affect significantly the measured data. In conventional pullout experiments, there are large shear stresses acting at the soil-reinforcement interface, close to the front wall of the cell. Palmeira and Milligan (1989) found that wall roughness could increase the apparent bond resistance by 100% for pullout tests on steel grid reinforcements in dense sand. As a result, they recommended either lubricating the front face or increasing the scale of the test to minimize the effects of the boundary conditions. These authors assumed that the wall friction causes overestimation of the bond capacity for design. An alternative strategy to ameliorate the effects of wall friction is to use an intruded slot (e.g. Juran and Christopher, 1989; Figs. 5.1d, e, f), which separates the inclusion from the front face. To date there have been no systematic studies to compare pullout measurements from different shear boxes. However, it is apparent that much of the scatter reported in the literature for similar constituent material properties (soil and reinforcement) may be attributed to differences in boundary conditions.

For reinforcements with planar surfaces, the mechanism of interaction in pullout tests is controlled by the skin friction mobilized between the soil and reinforcement. In the standard interpretation of these tests, the apparent friction coefficient, $\bar{\delta}$, is reported at the maximum pullout load, P_p :

$$\tan \bar{\delta} = \frac{P_p}{A_r \sigma_v} = \frac{\bar{\tau}}{\sigma_v} \quad (5.1)$$

where A_r is the surface area of the embedded inclusion, $\sigma_v = N/A_s$ (Fig. 5.1) is the external vertical stress at the boundary of the specimen, A_s is the cross-sectional area of the cell, and $\bar{\tau}$ is the average shear resistance acting along the interface.

There is much discussion in the literature regarding the correct interpretation of $\bar{\delta}$. If the inclusion is rigid (inextensible), it can be assumed that the shear resistance is mobilized uniformly over the embedded surface area at the pullout load. In this case, the apparent

friction $\bar{\delta}$ should be comparable to the interface friction measured in a direct shear box apparatus. However, for extensible reinforcements (including most geosynthetics), the deformations of the inclusion can introduce a progressive failure mechanism, in which the shear resistance varies with position. Hence $\bar{\delta}$ will be affected by the length of the inclusion, constituent material properties (deformation and strength of the soil and reinforcement) as well as the interface friction.

Measurements of the apparent friction coefficient are often compared with the frictional shear strength of the soil ϕ' through the bond ratio, $f = \tan \bar{\delta} / \tan \phi'$. Pullout data compiled by Palmeira (1987) for planar reinforcements (metal strips and geosynthetics) in dry, cohesionless materials show bond ratios ranging from a minimum $f = 0.3-0.4$ up to values $f \geq 2$. Schlosser and Elias (1978) report f values in excess of 5 from field pullout tests on steel strips. This wide variation in f reflects differences in test geometry and boundary conditions as well as differences in the intrinsic material properties (shear strength of the soil, interface friction, etc.). The interpretation of bond ratio is further complicated by two mechanistic factors:

1. Most authors do not provide specific information regarding the selection of the reference friction ϕ' . In conventional practice, ϕ' refers to the friction angle mobilized at peak shear resistance (i.e., $\phi' = \phi'_p$). It is well known that ϕ'_p is a function of the confining effective stress and density (e.g. Bolton, 1986), and is also affected by the mode of shearing¹, compaction procedures, etc. In contrast, the constant volume friction angle, ϕ'_{cv} , corresponding to shear resistance at large shear strains, is a more reliable material

¹The friction angle is usually measured in triaxial compression, ϕ'_{tc} , or direct shear box tests, ϕ'_{ds} . Marachi et al. (1981) report consistent differences between the plane strain ϕ'_{ps} and triaxial compression friction ϕ'_{tc} , while Rowe (1989) explains the difference between ϕ'_{ps} and ϕ'_{ds} in terms of the dilation rate in the soil.

property which is largely independent of the initial state of the material (typically $\phi'_{cv}=30^\circ\pm 3^\circ$).

2. The normal tractions σ_N acting locally at the soil-reinforcement interface during pullout are generally not known. Experimental measurements of local normal stresses have been obtained from pullout tests on instrumented model piles (e.g. Wernick, 1977; Plumelle, 1987; Lehane et al., 1993); however, there is currently no data for thin planar inclusions. Schlosser and Elias (1978) postulated that measurements of bond ratio in excess of unity ($f>1$) could be attributed to increases in the normal stresses σ_N through a loosely defined mechanism of 'restrained dilatancy' within the soil. Similar mechanisms were proposed by Hettler (1982) and Boulon and Foray (1986) for tensile loading of axisymmetric piles. Schlosser and DeBuhan (1990) then suggest that the pullout bond resistance ($\tan \bar{\delta}$) should be compared with the interface friction measured in shear box tests at constant normal stiffness (e.g. Boulon et al, 1990), $\bar{k}=\Delta\sigma_N/\Delta u$, where Δu is the lateral displacement in the soil during pullout. The case when $\bar{k}=0$ corresponds to a standard shear box test at constant confining stress, while $\bar{k}=\infty$ corresponds to a constant volume direct shear box test ($\Delta u=0$). For axisymmetric piles or nails, Boulon and Foray (1986) propose $\bar{k}=E_p/R$, where E_p , R are the Young's modulus and radius of the pile, respectively. For thin, planar reinforcements, $\bar{k}\rightarrow 0$ (i.e., $R\rightarrow\infty$) and hence this model predicts $\Delta\sigma_N=0$ during pullout.

The widespread application of polymeric geogrid reinforcements (e.g. ICE, 1985) has spurred considerable research efforts to evaluate the load capacity of these materials in pullout tests. The grid geometry generates a complex set of interactions, including surface friction, particle interlocking within the apertures, and passive thrust (bearing resistance) against the transverse elements. These mechanisms can be appreciated most readily from

photo-elastic measurements of stress fields in the surrounding 'soil'² during pullout, as shown in Figure 5.2 (Dyer, 1985; Milligan et al, 1990). The orientation of the white lines in these figures corresponds approximately to the trajectory of the major compressive stress, while their brightness is an indication of the maximum shear stress intensity (Allersma, 1982). The results show that highly non-uniform stress fields develop around the transverse elements of the grid and hence the bond resistance is not directly comparable to that of a rough sheet inclusion (Fig. 5.2a). Jewell et al. (1985) and Palmeira and Milligan (1989) have proposed semi-empirical expressions for estimating the bond capacity of grids based on the interference between successive bearing members. In this analysis, the bond capacity is a function of the grid geometry, particle size (d_{50}) and peak friction angle of the soil. However, the analysis does not consider the progressive failure mechanisms for long, extensible reinforcements.

Overall, it is apparent from the preceding discussions that pullout tests have several major limitations: 1) the results are significantly affected by the boundary conditions; 2) deformation of extensible reinforcements introduces a progressive failure mechanism, which complicates the evaluation of bond capacity even for planar, frictional reinforcements; and 3) mechanisms of interaction are highly complex for grid reinforcements which are widely used in practice.

This chapter presents a new analysis which is capable of describing the complete load-transfer behavior for pullout tests with extensible, planar reinforcements. The proposed formulation uses the shear-lag approximations described in Chapter 2 (Abramanto and Whittle, 1993; Budiansky et al, 1986), in order to predict the development

²These measurements were obtained using a model granular material comprised of crushed glass saturated with paraffin (same refractive index) and viewed through a polariscope using circularly polarized light. The photo-elastic method measures the forces at individual grain contacts from the bi-refracting effect of optically sensitive material in polarized light.

and distribution of tensile stresses and interface tractions along the inclusion as functions of the constituent material properties and test geometry. The principal advantage of the proposed analysis is its simplicity, which enables clear physical interpretation of the effects of individual parameters and avoids the complexities associated with non-linear numerical analyses using frictional interface elements (e.g. Gens et al, 1988; Schellekens and DeBorst, 1993). The analytical predictions are evaluated in Chapter 6 through direct comparison with pullout tests performed on instrumented inclusions in the APSR cell.

5.2. Shear-Lag Formulation

5.2.1. Governing Equations

Figure 5.3 shows the idealized geometry and boundary conditions considered in the proposed analysis of pullout tests for planar soil reinforcements. The reinforcing inclusion has thickness f and length L , and is embedded in the soil matrix in a box of overall vertical dimensions $m+f$. The soil specimen is initially subjected to uniform boundary tractions σ_1 and σ_3 . In conventional pullout tests, σ_3/σ_1 corresponds to the K_0 -stress condition associated with 1-D compression of the specimen³. Pullout loads σ_p [FL^{-2}] are applied at the active end of the inclusion ($x=0$) and generate tensile stresses within the reinforcement, $\sigma_{xx}^f(x)$, which reflect the distribution of normal and shear tractions along the interface (σ_{xy}^i and σ_{yy}^i , respectively). Figure 5.3 also shows the positive sign convention for stresses within the soil matrix (σ_{xx}^m , σ_{yy}^m , σ_{xy}^m). The proposed analysis assumes the following:

1. The soil matrix and reinforcing material behave as linear, isotropic and elastic materials with properties G_m , ν_m and E_f , ν_f , respectively (Fig. 5.3).

³The results in Chapter 2 show that no tensile stresses develop in the inclusion due to K_0 -consolidation of the soil specimen. Compaction of the sand or other modifications of the stress ratio σ_1/σ_3 can induce residual stresses in the inclusion, as discussed in section 5.3.1.2.

2. The soil-reinforcement interface is frictional and described by a constant angle of friction δ , such that $|\sigma_{xy}^i| / \sigma_{yy}^i \leq \tan \delta$.
3. There is no axial stress acting at the 'passive end' of the inclusion (i.e., $\sigma_{xx}^f = 0$ at $x = L$), as the inclusion is thin and is not physically bonded to the soil matrix.
4. The axial stresses in the soil matrix and in the inclusion are functions of x only (i.e., $\sigma_{xx}^m(x)$, $\sigma_{xx}^f(x)$). Thus, the horizontal stresses in the inclusion and the soil can be related by:

$$\bar{\sigma}_{xx}^m = \sigma_{xx}^m = a \sigma_{xx}^f + \sigma_3 (1 + a) \quad (5.2)$$

where $a=f/m$ is the 'inclusion ratio' and $\bar{\sigma}_{xx}^m$ is the 'average' horizontal stress in the soil matrix.

Based on these assumptions, the complete traction boundary conditions in the soil for the pullout analyses can be defined as follows:

$$x = 0 \quad ; \quad |y - f/2| \leq m/2 \quad : \quad \sigma_{xx}^m = \bar{\sigma}_{xx}^m \quad (5.3a)$$

$$: \quad \sigma_{xy}^m = \sigma_{xy}^i \left[1 - a \left(\frac{2y}{f} - 1 \right) \right] \quad (5.3b)$$

$$x = L \quad ; \quad |y - f/2| \leq m/2 \quad : \quad \sigma_{xx}^m = \sigma_3 \quad (5.3c)$$

$$0 \leq x \leq L \quad ; \quad |y - f/2| = 0 \quad : \quad \sigma_{xy}^m = \sigma_{xy}^i \quad \text{and} \quad \sigma_{yy}^m = \sigma_{yy}^i \quad (5.3d)$$

$$0 \leq x \leq L \quad ; \quad |y - f/2| = m/2 \quad : \quad \sigma_{xy}^m = 0 \quad \text{and} \quad \sigma_{yy}^m = \sigma_1 \quad (5.3e)$$

The analytical boundary conditions at the active face of the specimen ($x=0$) correspond to an average normal traction ($\bar{\sigma}_{xx}^m$; eqn. 5.3a after eqn. 5.2) and a shear traction which varies linearly from the interface to the upper and lower boundary of the soil specimen (eqn. 5.3b). These idealized conditions are not achieved in practical pullout box designs (cf. Fig. 5.1), but are most closely related to box designs with intruded slots (Figs. 5.1d, e, f).

Following the general shear-lag derivation based on the substitute-single-stringer method (Kuhn, 1956; section 2.2), tensile stresses in a planar reinforcement are obtained from the solution of the following ordinary differential equation:

$$\frac{d^2\sigma_{xx}^f}{dx^2} - K_1 \sigma_{xx}^f + K_2\sigma = 0 \quad (5.4)$$

where:

$$K_2 \sigma = K_2^1 \sigma_1 + K_2^3 \sigma_3 \quad (5.4a)$$

and K_1 , K_2^1 , K_2^3 are constants defined in terms of the material properties and geometry:

$$K_1 = \frac{6}{mf} \frac{\left[(1 - \nu_m) a + 2 \frac{G_m}{E_f} (1 + \nu_f) (1 - \nu_f) \right]}{\left[1 + \frac{1}{4} \nu_m - \frac{3}{2} \frac{G_m}{E_f} (1 + \nu_f) \nu_f \right]} \quad (5.5a)$$

$$K_2^1 = \frac{6}{mf} \frac{\left[\nu_m - 2 \frac{G_m}{E_f} (1 + \nu_f) \nu_f \right]}{\left[1 + \frac{1}{4} \nu_m - \frac{3}{2} \frac{G_m}{E_f} (1 + \nu_f) \nu_f \right]} \quad (5.5b)$$

$$K_2^3 = - \frac{6}{mf} \frac{(1 - \nu_m) (1 + a)}{\left[1 + \frac{1}{4} \nu_m - \frac{3}{2} \frac{G_m}{E_f} (1 + \nu_f) \nu_f \right]} \quad (5.5c)$$

The distribution of shear and normal stresses in the soil matrix are selected in order to satisfy the quasi-static equilibrium and boundary conditions:

$$\text{Linear: } \sigma_{xy}^m = \sigma_{xy}^i \left[1 - a \left(\frac{2y}{f} - 1 \right) \right] \quad (5.6a)$$

$$\text{Parabolic: } \sigma_{yy}^m = \sigma_{yy}^i + \frac{4}{m} (\sigma_1 - \sigma_{yy}^i) \left[y^2 \left(-\frac{1}{m} \right) + y (1 + a) - \frac{f}{2} \left(1 + \frac{a}{2} \right) \right] \quad (5.6b)$$

Hence, the interface tractions can then be related to the tensile stress distribution in the reinforcement:

$$\sigma_{xy}^i = \frac{f}{2} \frac{d\sigma_{xx}^f}{dx} \quad (5.7a)$$

$$\sigma_{yy}^i = \sigma_1 + \frac{mf}{8} \frac{d^2\sigma_{xx}^f}{dx^2} \quad (5.7b)$$

Tensile stresses in the reinforcement are given by the general solution of equation 5.4:

$$\sigma_{xx}^f = C_1 \cosh \sqrt{K_1} x + C_2 \sinh \sqrt{K_1} x + K \quad (5.8a)$$

where $K=K_2\sigma/K_1$, and C_1, C_2 are constants to be determined from appropriate boundary conditions and subject to the constraints imposed by the local frictional resistance at the inclusion-soil interface (δ , Fig. 5.3). Finally, general solutions for the interface tractions are obtained from equations 5.7 and 5.8a:

$$\sigma_{xy}^i = \frac{f}{2} \sqrt{K_1} (C_1 \sinh \sqrt{K_1} x + C_2 \cosh \sqrt{K_1} x) \quad (5.8b)$$

$$\sigma_{yy}^i = \sigma_1 + \frac{mf}{8} K_1 (C_1 \cosh \sqrt{K_1} x + C_2 \sinh \sqrt{K_1} x) \quad (5.8c)$$

5.2.2. Particular Solutions

Figure 5.4 illustrates schematically the sequence of events predicted during a pullout test, based on particular solutions of the general equations described in the previous section. The analysis identifies four successive phases in the response of the inclusion during pullout:

1. No interface slippage: Initially, the pullout stress σ_p is resisted by shear tractions at the soil-reinforcement interface. No slippage occurs until the ratio of local shear to normal traction mobilizes the interface frictional resistance. Sliding initiates from the active end of the inclusion (i.e., $-\sigma_{xy}^i/\sigma_{yy}^i = \tan \delta$ at $x=0$) at a first 'yield' stress, σ_p^I . The yield stress marks the onset of non-linearity in the load-elongation response (Fig. 5.4b).
2. Active slipping front (one-way debonding): As the pullout stress increases ($\sigma_p > \sigma_p^I$), the zone of sliding progresses along the inclusion and is characterized by a length x_{d1} . A second or upper yield load σ_p^II is identified when the interface friction is mobilized at the

passive end of the inclusion (i.e., $-\sigma_{xy}^i/\sigma_{yy}^i = \tan \delta$ at $x=L$). The length of the active slipping front at σ_p^{II} is given by x_{d1}^{II} .

3. Active and passive slipping fronts: For pullout stresses $\sigma_p > \sigma_p^{\text{II}}$, the analysis describe a two-way slipping mechanism (two-way debonding), with a passive sliding front of length x_{d2} moving to connect with the active slipping front (with maximum pullout force σ_{pp}).
4. Full slippage occurs when the local interface friction angle δ is mobilized at all points along the inclusion (i.e., $x_{d1} - x_{d2} \rightarrow 0$), corresponding to a residual pullout load, σ_{pr} . This does not imply necessarily that the interface shear traction σ_{xy}^i is uniform along the length of the inclusion.

For situations (combinations of geometric and material properties) where $x_{d1}^{\text{II}} \rightarrow L$, the active slip front reaches the passive end of the inclusion and hence $\sigma_p^{\text{II}} \cong \sigma_{pp} = \sigma_{pr}$. The following paragraphs summarize the particular analytical solutions during each phase of the pullout test.

5.2.2.1 No Slippage

The particular solution for equation 5.4 is obtained with boundary conditions $\sigma_{xx}^f = \sigma_p$ for $x=0$ and $\sigma_{xx}^f = 0$ for $x=L$, for which the integration constants are given by:

$$C_1^0 = \sigma_p - K \quad ; \quad C_2^0 = - \frac{K + (\sigma_p - K) \cosh \sqrt{K_1} L}{\sinh \sqrt{K_1} L} \quad (5.9)$$

The constant K ($=K_2\sigma/K_1$; cf. eqns. 5.4, 5.5) represents the tensile stresses within the inclusion due to the consolidation stresses (σ_1, σ_3). For samples consolidated under K_0 -conditions ($K_0 = \sigma_3/\sigma_1$), $K=0$; however, high compaction stresses can induce significant residual stresses prior to pullout (section 5.3.1.2).

5.2.2.2 One-Way Debonding

As the pullout stress σ_p increases, frictional sliding starts to occur at the active end. The first yield stress σ_p^I is determined by imposing the constraint - $\sigma_{xy}^i/\sigma_{yy}^i = \mu = \tan \delta$ at $x=0$:

$$\sigma_p^I = \frac{\beta \sigma_1 - K \operatorname{csch} \sqrt{K_1} L}{\operatorname{coth} \sqrt{K_1} L - \alpha^{-1/2}} + K \quad (5.10a)$$

where the dimensionless constants α and β are expressed by:

$$\alpha = \frac{16}{m^2 \mu^2 K_1} \quad ; \quad \beta = \frac{2 \mu}{f \sqrt{K_1}} \quad (5.10b, c)$$

For conditions where $\sigma_p > \sigma_p^I$, the inclusion can be subdivided into two regions (Fig. 5.4c): A) a no-slide 'anchor length' of reinforcement, $x_{d1} \leq x \leq L$; and B) a zone of sliding at constant friction ratio μ , defined by $0 \leq x \leq x_{d1}$. Tensile stresses in zone A satisfy the governing equation 5.4 and are described by the general solution, equation 5.8a, with boundary conditions 1) $\sigma_{xx}^f = \sigma_{t1}$ at $x=x_{d1}$, and 2) $\sigma_{xx}^f = 0$ at $x=L$. The constants C_1 and C_2 become:

$$C_1^I = - \frac{(\sigma_{t1} - K) \sinh \sqrt{K_1} L + K \sinh \sqrt{K_1} x_{d1}}{\sinh \sqrt{K_1} (x_{d1} - L)} \quad (5.11a)$$

$$C_2^I = \frac{(\sigma_{t1} - K) \cosh \sqrt{K_1} L + K \cosh \sqrt{K_1} x_{d1}}{\sinh \sqrt{K_1} (x_{d1} - L)} \quad (5.11b)$$

where σ_{t1} is the transition stress acting at the sliding front. The governing equation for the sliding zone B is determined by imposing the frictional resistance directly in the governing equilibrium equations:

$$\text{Zone B: } 0 \leq x \leq x_{d1}: \quad \frac{d^2 \sigma_{xx}^f}{dx^2} - \frac{4}{\mu m} \frac{d\sigma_{xx}^f}{dx} - \frac{8}{mf} \sigma_1 = 0 \quad (5.12)$$

With boundary conditions a) $\sigma_{xx}^f = \sigma_p$ at $x=0$, and b) $\sigma_{xx}^f = \sigma_{t1}$ at $x=x_{d1}$, the particular solution for the tensile stress in zone B becomes:

$$\sigma_{xx}^{iB} = \sigma_p - \beta \sqrt{K_1} \sigma_1 x - \frac{\sigma_p - \beta \sigma_1 \sqrt{K_1} x_{d1} - K}{[(1 + \alpha) \exp(\sqrt{\alpha} K_1 x_{d1})] - 1} [\exp(\sqrt{\alpha} K_1 x) - 1] \quad (5.13a)$$

and the corresponding interface tractions are obtained from equations 5.7a, b:

$$\sigma_{xy}^{iB} = -\mu \sigma_1 - \frac{\sigma_p - \beta \sigma_1 \sqrt{K_1} x_{d1} - K}{[(1 + \alpha) \exp(\sqrt{\alpha} K_1 x_{d1})] - 1} \frac{2}{a \mu} \exp(\sqrt{\alpha} K_1 x) \quad (5.13b)$$

$$\sigma_{yy}^{iB} = -\frac{\sigma_{xy}^{iB}}{\mu} \quad (5.13c)$$

The solution for zones A and B (equations 5.11/5.8 and 5.13, respectively) is completed by determining the transition stress, σ_{t1} , and debond length, x_{d1} , through matching of the axial stresses and interface tractions:

$$\text{At } x=x_{d1}: \quad \sigma_{t1} = \sigma_{xx}^{iA} = \sigma_{xx}^{iB} \quad (5.14a)$$

$$\sigma_{xy}^{iA} = \sigma_{xy}^{iB} \quad (5.14b)$$

$$\sigma_{yy}^{iA} = \sigma_{yy}^{iB} \quad (5.14c)$$

The transition stress is obtained as follows:

$$\sigma_{t1} = \frac{\sigma_p - \beta \sigma_1 \sqrt{K_1} x_{d1} - K}{[(1 + \alpha) \exp(\sqrt{\alpha} K_1 x_{d1})] - 1} \alpha \exp(\sqrt{\alpha} K_1 x_{d1}) + K \quad (5.15)$$

while x_{d1} is solved numerically from the following non-linear equation:

$$\begin{aligned} & \frac{[\sqrt{\alpha} + \alpha \coth \sqrt{K_1} (x_{d1} - L)] \exp(\sqrt{\alpha} K_1 x_{d1})}{[(1 + \alpha) \exp(\sqrt{\alpha} K_1 x_{d1})] - 1} [(\sigma_p - K) - \beta \sigma_1 \sqrt{K_1} x_{d1}] + \\ & + K \operatorname{csch} \sqrt{K_1} (x_{d1} - L) + \beta \sigma_1 = 0 \end{aligned} \quad (5.16)$$

Equation 5.16 was solved numerically using the commercially available software MATLAB⁴.

⁴MATLABTM is a trademark of "The Math Works, Inc.". The solution is based on the subroutine "fsolve", and is based on Newton's method, including a line search to ensure global convergence when the initial estimate is poor.

5.2.2.3. Two-Way Debonding

Slippage initiates at the passive end of the inclusion when the interface friction is mobilized such that $-\sigma_{xy}^i/\sigma_{yy}^i = \mu$ at $x=L$. The upper yield stress σ_p^{II} is then determined by imposing the frictional constraint in the equations describing the distribution of interface tractions for one-way debonding (i.e., equations 5.8, 5.11, 5.13b, c and 5.15):

$$\sigma_p^{\text{II}} = \left[\left(\beta \sigma_1 - \alpha^{-1/2} K \right) \sinh \sqrt{K_1} (L - x_{d1}^{\text{II}}) - K \cosh \sqrt{K_1} (L - x_{d1}^{\text{II}}) \right] \quad (5.17)$$

$$\left[\frac{(1 + \alpha) \exp(\sqrt{\alpha} K_1 x_{d1}^{\text{II}}) - 1}{\alpha \exp(\sqrt{\alpha} K_1 x_{d1}^{\text{II}})} \right] + K + \beta \sigma_1 \sqrt{K_1} x_{d1}^{\text{II}}$$

where x_{d1}^{II} describes the length of the slip zone from the active end at the initiation of two-way debonding, which can be computed analytically as follows:

$$x_{d1}^{\text{II}} = L - \frac{1}{\sqrt{K_1}} \left\{ \operatorname{arcsinh} \left[\frac{2 \left(\frac{1}{\sqrt{\alpha}} + \frac{K}{\beta \sigma_1} \frac{\alpha - 1}{\alpha} \right)}{1 - \left(\frac{1}{\sqrt{\alpha}} + \frac{K}{\beta \sigma_1} \frac{\alpha - 1}{\alpha} \right)^2} \right] \right\} \quad (5.18)$$

Solutions for the tensile stress distributions for the two-way debonding mechanism are obtained by defining the length of the passive slipping front, x_{d2} , as shown in Figure 5.4c. The tensile stresses and interface tractions in zone B (slipping zone from active end) are given in equations 5.13. In the no-slip zone (zone A), the integration constants C_1 , C_2 (eqn. 5.8) are obtained as follows:

$$C_1^{\text{II}} = - \frac{(\sigma_{t2} - K) \sinh \sqrt{K_1} x_{d1} - (\sigma_{t1} - K) \sinh \sqrt{K_1} x_{d2}}{\sinh \sqrt{K_1} (x_{d2} - x_{d1})} \quad (5.19)$$

$$C_2^{\text{II}} = \frac{(\sigma_{t2} - K) \cosh \sqrt{K_1} x_{d1} - (\sigma_{t1} - K) \cosh \sqrt{K_1} x_{d2}}{\sinh \sqrt{K_1} (x_{d2} - x_{d1})}$$

where σ_{t2} is the transition stress at the passive end slipping front x_{d2} .

Tensile stresses and boundary tractions in zone C (sliding zone at the passive end of the inclusion) must satisfy the following general equation (cf. eqn. 5.12 in active slip zone):

$$\text{Zone C: } x_{d2} \leq x \leq L: \quad \frac{d^2 \sigma_{xx}^f}{dx^2} + \frac{4}{m\mu} \frac{d\sigma_{xx}^f}{dx} + \frac{8}{mf} \sigma_1 = 0 \quad (5.20)$$

subject to boundary conditions: a) $\sigma_{xx}^f = \sigma_{t2}$ at $x=x_{d2}$; and b) $\sigma_{xx}^f = 0$ at $x=L$:

$$\sigma_{xx}^{fC} = \beta \sigma_1 \sqrt{K_1} (L - x) - \frac{\beta \sigma_1 \sqrt{K_1} (L - x_{d2}) - K}{[(1 - \alpha) \exp(-\sqrt{\alpha} K_1 x_{d2})] - \exp(-\sqrt{\alpha} K_1 L)} \frac{1}{[\exp(-\sqrt{\alpha} K_1 x) - \exp(-\sqrt{\alpha} K_1 L)]} \quad (5.21a)$$

$$\sigma_{xy}^{iC} = -\mu \sigma_1 + \frac{\beta \sigma_1 \sqrt{K_1} (L - x_{d2}) - K}{[(1 - \alpha) \exp(-\sqrt{\alpha} K_1 x_{d2})] - \exp(-\sqrt{\alpha} K_1 L)} \frac{2}{a \mu} \exp(-\sqrt{\alpha} K_1 x) \quad (5.21b)$$

$$\sigma_{yy}^{iC} = -\frac{\sigma_{xy}^{iC}}{\mu} \quad (5.21c)$$

Finally, the transition stresses σ_{t1} , σ_{t2} and slip zone lengths x_{d1} , x_{d2} must be computed by matching simultaneously the axial stresses and interface tractions at x_{d1} and x_{d2} :

$$\begin{array}{ll} \text{At } x=x_{d1}: & \text{At } x=x_{d2}: \\ \sigma_{t1} = \sigma_{xx}^{fA} = \sigma_{xx}^{fB} & \sigma_{t2} = \sigma_{xx}^{fA} = \sigma_{xx}^{fC} \end{array} \quad (5.22a)$$

$$\sigma_{xy}^{iA} = \sigma_{xy}^{iB} \quad \sigma_{xy}^{iA} = \sigma_{xy}^{iC} \quad (5.22b)$$

$$\sigma_{yy}^{iA} = \sigma_{yy}^{iB} \quad \sigma_{yy}^{iA} = \sigma_{yy}^{iC} \quad (5.22c)$$

The transition stress σ_{t1} at $x=x_{d1}$ is given by equation 5.15, while σ_{t2} is obtained as:

$$\sigma_{t2} = \frac{[K - \beta \sigma_1 \sqrt{K_1} (L - x_{d2})] \alpha \exp(-\sqrt{\alpha} K_1 x_{d2})}{[(1 - \alpha) \exp(-\sqrt{\alpha} K_1 x_{d2})] - \exp(-\sqrt{\alpha} K_1 L)} + K \quad (5.23)$$

The two slip zone lengths (x_{d1} , x_{d2}) are determined numerically from the simultaneous solution of the following non-linear equations:

$$\begin{aligned} & \frac{[(\sigma_p - K) - \beta \sigma_1 \sqrt{K_1} x_{d1}] \alpha \exp(\sqrt{\alpha K_1} x_{d1})}{[(1 + \alpha) \exp(\sqrt{\alpha K_1} x_{d1})] - 1} \left[\frac{1}{\sqrt{\alpha}} - \frac{1}{\tanh \sqrt{K_1} (x_{d2} - x_{d1})} \right] - \\ & - \frac{[-K + \beta \sigma_1 \sqrt{K_1} (L - x_{d2})] \alpha \exp(-\sqrt{\alpha K_1} x_{d2})}{[(1 - \alpha) \exp(-\sqrt{\alpha K_1} x_{d2})] - \exp(-\sqrt{\alpha K_1} L)} \left[\frac{1}{\sinh \sqrt{K_1} (x_{d2} - x_{d1})} \right] + \\ & + \beta \sigma_1 = 0 \end{aligned} \quad (5.24a)$$

$$\begin{aligned} & \frac{[(\sigma_p - K) - \beta \sigma_1 \sqrt{K_1} x_{d1}] \alpha \exp(\sqrt{\alpha K_1} x_{d1})}{[(1 + \alpha) \exp(\sqrt{\alpha K_1} x_{d1})] - 1} \left[-\frac{1}{\sinh \sqrt{K_1} (x_{d2} - x_{d1})} \right] + \\ & + \frac{[-K + \beta \sigma_1 \sqrt{K_1} (L - x_{d2})] \alpha \exp(-\sqrt{\alpha K_1} x_{d2})}{[(1 - \alpha) \exp(-\sqrt{\alpha K_1} x_{d2})] - \exp(-\sqrt{\alpha K_1} L)} \left[-\frac{1}{\sqrt{\alpha}} - \frac{1}{\tanh \sqrt{K_1} (x_{d2} - x_{d1})} \right] + \\ & + \beta \sigma_1 = 0 \end{aligned} \quad (5.24b)$$

Convergence of solution is always achieved for $\sigma_p \leq \sigma_{pp}$. In these cases, x_{d1} and x_{d2} are calculated directly from equations 5.16 or 5.24 for a given pullout stress σ_p . However, the peak pullout stress σ_{pp} ($\sigma_{pp} = \sigma_p^{\text{II}}$ in K_0 -consolidation) corresponds to a bifurcation point in the analysis, marking the initiation of the snap-through process. Therefore, the solution for the range $\sigma_{pp} > \sigma_p > \sigma_{pr}$ is achieved by combining expressions 5.24a and b and eliminating σ_p :

$$\begin{aligned} & \frac{[K - \beta \sigma_1 \sqrt{K_1} (L - x_{d2})] (1 - \alpha) \exp(-\sqrt{\alpha K_1} x_{d2})}{[(1 - \alpha) \exp(-\sqrt{\alpha K_1} x_{d2})] - \exp(-\sqrt{\alpha K_1} L)} + \\ & + \beta \sigma_1 \left[\frac{1}{\sinh \sqrt{K_1} (x_{d2} - x_{d1})} - \frac{1}{\tanh \sqrt{K_1} (x_{d2} - x_{d1})} + \frac{1}{\sqrt{\alpha}} \right] = 0 \end{aligned} \quad (5.25)$$

In this case ($\sigma_{pp} > \sigma_p > \sigma_{pr}$), x_{d2} is obtained for a given value of x_{d1} in equation 5.25 (using the MATLAB library 'fsolve', as in one-way debonding). These values of slipped lengths are subsequently substituted in 5.24a or b in order to obtain the corresponding pullout stress σ_p .

5.2.2.4. Representation of Pullout Response

The conventional method for presenting the results of pullout tests is to report the load-displacement response, σ_p - u_p , where u_p is the displacement measured at the active end of the inclusion. However, this approach cannot be used reliably in the proposed analysis as there is no fixed reference frame; Figure 5.3 shows that all boundaries have specified shear and normal tractions and hence the displacements are undefined. Figure 5.4 illustrates two methods for describing the pullout response, in terms of a) the slip length ratio, and b) the elongation of the inclusion. The slip length ratio, L_s/L ($=1-[x_{d2}-x_{d1}]/L$) is a method for representing the physical pullout mechanisms described in previous paragraphs, but cannot be used for practical comparisons with measured data. The elongation, Δu_x^f , can be obtained by integrating the elastic strains in the inclusion based on the distributions of tensile stresses and interface tractions:

$$\Delta u_x^f = \int_x \left\{ \frac{1 + \nu_f}{E_f} [- (1 - \nu_f) \sigma_{xx}^f - \nu_f \sigma_{yy}^i] \right\} dx \equiv \int_x \frac{-(1 - \nu_f^2)}{E_f} \sigma_{xx}^f dx \quad (5.26)$$

Appendix 5.A gives complete expressions for the inclusion elongation at successive stages of pullout. Experimental measurements of elongation can be achieved by measuring the relative displacements between the active and passive ends of the inclusion (e.g. Johnston and Romstad, 1989).

5.3. Interpretation of Pullout Behavior

5.3.1. Typical Results

The analytical solutions in the preceding section relate the pullout response (σ_p - Δu_x^f), tensile stress and interface traction distributions (σ_{xx}^f , σ_{xy}^i , σ_{yy}^i) to the material properties (E_f , ν_f ; G_m , ν_m), geometry (L , m , f), interface friction (δ) and external consolidation stress state (σ_1 , σ_3). Figure 5.5 presents typical results of the development of tensile stress and interface tractions for pullout of a planar reinforcement of length $L=1\text{m}$

and thickness $f=1\text{mm}$, embedded in a K_0 -consolidated soil specimen ($v_m=0.3$, then $K_0=v_m/(1-v_m)=0.429$ and hence $\sigma_1/\sigma_3=2.33$) of overall depth $m=0.5\text{m}$. Reinforcing materials used in practice have stiffness ratios ranging from $E_f/G_m=100$ (low stiffness non-woven geotextiles) to $E_f/G_m=10^5$ (steel or other metallic reinforcements). This example simulates a relatively large laboratory experiment (cf. Fig. 5.1), with an average reinforcement-soil stiffness ratio ($E_f/G_m=10^3$) and a relatively smooth interface ($\delta=20^\circ$, $\mu=0.35$). The results show the following:

1. At the start of the test ($\sigma_p=0$) there are no residual stresses in the inclusion due to the assumed K_0 -consolidation conditions in the soil and, hence $\sigma_{xx}^f=\sigma_{xy}^i=0$ while the normal interface traction $\sigma_{yy}^i=\sigma_1$.
2. Interface slippage initiates at a first yield stress, $\sigma_p^f/\sigma_1=156$. At this load level, there is a non-linear distribution of tensile stress within the reinforcement and a corresponding build up in both the shear and normal interface tractions at the active end of the inclusion ($x=0$). Sliding initiates at the active end of the inclusion when $\mu=-\sigma_{xy}^i/\sigma_{yy}^i=\tan \delta=0.35$. The results show that the maximum shear traction at yield, $\sigma_{xy}^i/\sigma_1=0.47$, occurs at $x=0$ and is due to the local amplification of the normal stress, $\sigma_{yy}^i/\sigma_1=1.35$.
3. At subsequent stages of the test ($\sigma_p=300, 500$; Fig. 5.5), the mechanism of pullout is characterized by the progress of the sliding front ($x=x_{d1}$, Fig. 5.4) along the inclusion ('one-way debonding'). The results show a local concentration of shear and normal interface tractions at the sliding front, with maximum values and discontinuous gradients of both components at $x=x_{d1}$. In contrast, the analysis describes a continuous, smooth distribution of tensile stress along the inclusion. Stress conditions ahead of the sliding front ($x>x_{d1}$, no slip zone) are qualitatively similar to the pre-yield behavior described above ($\sigma_p<\sigma_p^f$). For $x<x_{d1}$, sliding occurs at a constant stress ratio, $\mu=0.35$, while the normal interface traction approaches its initial value, $\sigma_{yy}^i\rightarrow\sigma_1$ (and, hence,

$\sigma_{xy}^i \rightarrow 0.35\sigma_1$). For this particular example, the tensile stresses (σ_{xx}^f/σ_1) are distributed approximately linearly within the slip zone.

4. Sliding initiates from the passive end of the inclusion ($x=L=1\text{m}$) at the upper yield stress, $\sigma_p^{\text{II}}/\sigma_1=708$, with the active sliding front located at $x_{d1}^{\text{II}}\cong 0.91\text{m}$. In this particular example, σ_p^{II} corresponds to the peak pullout load (σ_{pp}) and the subsequent two-way debonding mechanism is associated with a reduction in pullout resistance ("snap-through", as discussed in section 5.3.1.3). The upper yield stress is slightly larger than the limit pullout stress (i.e., corresponding to limit equilibrium for a rigid planar inclusion), $\sigma_L/\sigma_1=2\mu L/f=700$ ($\sigma_p^{\text{II}}/\sigma_L=1.01$). The tensile stress distribution is almost exactly linear at the peak pullout load, while small non-uniformities in the interface tractions are limited to the vicinity of the two sliding fronts ($x=0.9\pm 0.1\text{m}$).

Overall, the analytical solutions described in Figure 5.5 show a number of characteristic features which have not been identified in previous studies of pullout. Local increases in the normal interface traction σ_{yy}^i are associated with the formation and position of the sliding front and must be carefully distinguished from the effects of soil dilation speculated upon by previous authors (e.g. Schlosser and Elias, 1978). Mobilization of the peak shear resistance along the interface is controlled by the predicted normal interface tractions, while the true interface friction can be interpreted locally from the residual resistance (i.e., where $\sigma_{yy}^i \rightarrow 1$).

5.3.1.1. Effect of Reinforcement-Soil Stiffness Ratio

Figure 5.6 shows further analytical predictions of pullout behavior for a more 'extensible' reinforcement with stiffness ratio $E_f/G_m=100$ (close to the lower limit for practical soil reinforcements), using the same reference geometry, consolidation stresses and interface friction selected previously (cf. Fig. 5.5). Although the results in Figure 5.6

are qualitatively similar to those described previously, more detailed comparisons show the following:

1. Local amplification of the interface normal and shear tractions at the sliding front are accentuated for the analysis using more extensible reinforcement. The results in Figure 5.6 show maximum tractions $\sigma_{yy}^i/\sigma_1=3.0$ and $\sigma_{xy}^i/\sigma_1=-1.10$ at the sliding front.
2. Differences in the tensile stress distributions within the reinforcement can be explained using the concept of a 'characteristic anchor length' \tilde{L} . This dimension corresponds to the length of reinforcement in the no-slip zone which is required to achieve full transfer of the tensile load acting at the sliding front (i.e., all tensile load is transferred into the soil). Figure 5.6 shows that the characteristic anchor length is $\tilde{L}\approx 0.25\text{m}$ for the extensible reinforcement, at a pullout stress $\sigma_p/\sigma_1=500$, while $\tilde{L}\approx 0.70\text{m}$ for the base case analysis (Fig. 5.5). For relatively extensible reinforcements, \tilde{L} is small and the sliding front corresponds to an inflexion point in the tensile stress distribution (Fig. 5.6a). The net effect of these observations is that higher stresses are required to achieve pullout of the more extensible reinforcement. The results in Figure 5.6a show the peak pullout stress $\sigma_{pp}/\sigma_1(=\sigma_p^{\text{II}}/\sigma_1)=784$, which is significantly larger than the limit stress ($\sigma_{pp}/\sigma_L=1.12$). There is a large post-peak reduction in pullout resistance associated with energy release in the two-way debonding mechanism.

5.3.1.2. Effect of Residual Stresses

When the soil is compacted, or consolidated under non- K_0 conditions, residual tensile stresses may exist in the reinforcement prior to pullout. These effects can be examined in the proposed analysis through the external stress ratio, σ_1/σ_3 . Figure 5.7 shows the predicted pullout behavior following consolidation under an external stress ratio $\sigma_1/\sigma_3=6$ (corresponding to a mobilized friction angle $\phi_{\text{mob}}=45.6^\circ$), using the reference material properties and geometry:

1. At $\sigma_p=0$, the maximum tensile stress occurs at the center of the reinforcement (i.e., at $x=0.5m$), where $\sigma_{xx}^f/\sigma_1=50$. The interface shear traction is anti-symmetric about the centerline with maximum stresses mobilized at either end of the inclusion ($|\sigma_{xy}^i|/\sigma_1=0.17$ at $x=0, L$), where the local normal traction is a minimum ($\sigma_{yy}^i/\sigma_1=0.88$); the mobilized interface friction at $x=0, L$ is $\mu=0.19$.
2. The residual stress does not affect the peak pullout resistance $\sigma_{pp}/\sigma_1=708$, but does alter the yield stresses σ_p^I and σ_p^{II} . Additional pullout loads are required in order to overcome the residual stress and, hence, initiate sliding at the active end of the reinforcement ($\sigma_p^I/\sigma_1=211=156+55$; cf. Figs. 5.5a, 5.7a). In contrast, the residual stresses promote slippage at the passive end of the reinforcement and, hence, there is a reduction in σ_p^{II} ($\sigma_p^{II}/\sigma_1=680$) and the subsequent two-way debonding mechanism is stable.

5.3.1.3. Pullout-Elongation Response

Figures 5.8a and b summarize the load-elongation behavior for the pullout tests described above. The pullout loads are normalized with respect to the limit stress σ_L , obtained from limit equilibrium, while the elongation is presented in a dimensionless format, $(\Delta u_x^f + a E_f)/(\sigma_1 L)$. Although the elongation can be normalized by σ_1 and E_f , it is affected independently by all three geometric parameters (m, f, L ; cf. Appendix 5.A). In all cases, the pullout response is linear until first yield (σ_p^I), when sliding initiates at the active end of the inclusion. Figure 5.8a confirms the effects of the reinforcement-soil stiffness ratio (E_f/G_m) on the peak pullout stress observed previously. For the more extensible reinforcement ($E_f/G_m=10^2$; Fig. 5.6), the post-peak response is characterized by a reduction in the elongation as sliding propagates from the passive end of the inclusion. This "snap-through" mechanism corresponds to a recovery of elastic strain energy associated with the local concentration of interface tractions at the sliding front.

Figure 5.8b⁵ confirms that residual tensile stresses associated with sample compaction (characterized by σ_1/σ_3) do have a small effect on the initial yield and subsequent response, but do not influence the peak pullout stress.

5.3.2. Yield, Peak and Residual Pullout Stresses

The discussion of typical results has identified basic mechanisms of pullout in the proposed analysis and related this behavior to concentrations of the interface tractions at the sliding front. In principle, these results can be evaluated through comparison with numerical analysis using finite element methods. In practice, it is difficult to achieve accurate non-linear numerical analysis for sliding along a frictional interface between two materials with a large contrast in stiffness (e.g. Griffiths, 1985; Gens et al., 1988; Schellekens and DeBorst, 1993). As a result of these difficulties, more reliable evaluations can be achieved through comparisons with experimental data in well controlled laboratory tests, described in Chapter 6. This section considers the factors affecting the analytical predictions of yield ($\sigma_p^I, \sigma_p^{II}$), peak and residual (σ_{pp}, σ_{pr}) pullout stresses.

5.3.2.1. Factors Affecting Pullout Response

Figures 5.9a, b summarize the effects of test geometry on the pullout load-elongation behavior. The inclusion thickness f and height of the soil specimen m have little influence on the normalized pre-peak pullout load-elongation response (σ_p/σ_L vs. $\Delta u_x^f a E_f / L \sigma_1$; Fig 5.9a). However, very low volume fractions ($a \leq 0.05\%$) generate higher peak resistance (i.e., $\sigma_{pp}/\sigma_L > 1$), with associated snap-through in two-way debonding. The length of the reinforcement L has little influence on the peak pullout stress ratio (σ_{pp}/σ_L), but does affect significantly both the elongation required to mobilize this resistance as well as the first yield stress.

⁵Figure 5.8 shows only the elongations generated during pullout, i.e., does not include elongations due to residual stresses.

This behavior is most clearly illustrated in Figure 5.10 which compares the tensile stress and interface tractions at a reference pullout load, $\sigma_p/\sigma_L=0.5$, for inclusions with lengths $L=1.0, 2.0$ and $4.0m$. The characteristic dimensions of the traction concentration (amplification factor, $\Delta\sigma_{yy}^i/\sigma_1$, and anchor length, \tilde{L}) are not affected by the length of the inclusion. Hence, the load-elongation response is controlled by the relative position of the sliding front, x_{d1}/L (Fig. 5.10b).

The principal material properties affecting load-elongation response are the reinforcement-soil stiffness ratio E_f/G_m (Fig. 5.8a), Poisson's ratio in the soil ν_m (Fig. 5.11a), and interface friction angle δ (or friction ratio, $\mu=\tan \delta$, Fig. 5.11b). The parameter ν_m primarily affects the initial yield stress σ_p^I and causes an offset in the subsequent load-elongation response (Fig. 5.11a) due to residual stresses in the inclusion prior to pullout (as $\sigma_1/\sigma_3=2.33$ in all cases). However, if the external stress ratio corresponds to a K_0 -consolidation (i.e., $\sigma_1/\sigma_3=(1-\nu_m)/\nu_m$), then the Poisson's ratio has negligible effect on the pullout-elongation response. In contrast, E_f/G_m and μ (Figs. 5.8a, 5.11b) affect the initial (pre-yield) behavior, the peak pullout ratio (σ_{pp}/σ_L) and post-peak response. The interface friction is the most important parameter controlling the load-elongation response during one-way debonding.

5.3.2.2. Initial Yield

The preceding results confirm that the initial yield stress σ_p^I is affected by specimen geometry, constituent material and interface properties (cf. eqn.5.10). Yield occurs when the interface friction ratio μ is mobilized at the active end of the inclusion. For certain combinations of properties, it is possible to achieve a condition where $\sigma_{xy}^i(0)/\sigma_{yy}^i(0)<\tan\delta$ at any applied load σ_p . In these cases, there is no interface slippage ($\sigma_p^I \rightarrow \infty$) and failure occurs in the soil, as discussed in section 5.3.3. This limiting condition (for the case where there are no residual stresses in the reinforcement) occurs when:

$$\frac{m \mu}{4} \sqrt{K_1} = 1 \quad (5.27)$$

where $K_1(E_f/G_m, v_m, v_f, a)$ is the shear-lag parameter, and $\tanh \sqrt{K_1} L = 1$ for all practical pullout test geometries.

For a given specimen geometry $a=f/m$ and material properties E_f/G_m (other properties v_m, v_f have minor influence), equation 5.27 gives an estimate of the maximum interface friction $\mu_{\max}(=\tan \delta_{\max})$ for which sliding will take place at the soil-reinforcement interface. Figure 5.12 summarizes relations between the limiting interface friction δ_{\max} , soil-reinforcement stiffness ratio E_f/G_m , and inclusion ratio $a(=f/m)$. Values of δ_{\max} are only of practical importance for combinations of small inclusion ratio ($a \leq 0.1\%$) and relatively low stiffness ratio ($E_f/G_m \leq 10^3$). For example, when $a=0.01\%$ and $E_f/G_m=10^3$, interface sliding will not occur for friction angles $\delta_{\max} > 20^\circ$ ($\mu=0.36$; marked X in Figure 5.12). If $\delta > \delta_{\max}$, then the pullout resistance will be controlled either by shear failure of the soil (section 5.3.3) or tensile yield of the reinforcement itself.

5.3.2.3. Comparison with Limit Equilibrium Solutions

The peak pullout stress σ_{pp} , obtained from the proposed analysis, is affected by non-uniformities in the interface shear (and normal) traction mobilized along the interface and, hence, is generally not equal to the limit stress $\sigma_L/\sigma_1(=2\mu L/f)$. Previous results show that the ratio σ_{pp}/σ_L is a function of inclusion geometry (L, f, m), material properties and interface friction ($E_f/G_m, \delta$).

The limit equilibrium calculation of σ_L assumes that the reinforcement is inextensible and that the soil is a frictional material with no pre-failure deformations. In contrast, the shear-lag analysis describe pre-slip deformations, post-yield hardening of the load-elongation response during one-way debonding, and post-peak snap-through associated with two-way mechanism.

The shear-lag solutions can be compared with σ_L for the limit case when $G_m/E_f=0$ (inextensible reinforcement). Figure 5.13a summarizes values of $\sigma_p^{\text{II}}/\sigma_L$ for this situation as a function of the key parameters in equation 5.17 (L, m, δ). The results show clearly that $\sigma_p^{\text{II}}/\sigma_L \rightarrow 1$ as $L/m \rightarrow \infty$ (or $\tan\delta \rightarrow 0$, as expected), but $\sigma_p^{\text{II}}/\sigma_L \approx 1.0$ to 1.1 for most values of L/m and $\tan\delta$.

Further matching with the limit equilibrium calculations can be made by evaluating the conditions for which $\sigma_p^{\text{I}} \rightarrow \sigma_L$. This corresponds to the situation where the interface friction is mobilized simultaneously at both ends of the inclusion (and, hence, there is no post-yield hardening of the load-elongation response). Figure 5.13b shows that this limiting condition, $\sigma_p^{\text{I}}/\sigma_L=1$, is achieved only for very small values of L/m ($L/m=0.2$ to 0.6, depending on the interface friction considered).

5.3.2.4. Residual Pullout Stress

In the shear-lag analysis, the 'residual' pullout stress σ_{pr} corresponds to the 'idealized' equilibrium condition where the interface friction is mobilized equally at all points along the inclusion, i.e., $|\sigma_{xy}^i|/\sigma_{yy}^i = \tan\delta$ for $0 \leq x \leq L$. The values obtained for σ_{pr} are slightly higher than the limit stress σ_L , due to residual non-uniformities in interface shear and normal tractions at the limiting condition (e.g. Fig. 5.6, $\sigma_{pr}/\sigma_L=746$). In laboratory pullout tests, however, once this condition is reached the inclusion is extracted from the box and any residual non-uniformities in interface tractions are expected to vanish. The input parameter used as interface friction in the shear-lag formulation corresponds therefore to this residual 'kinetic' friction angle (lowest energy state possible).

5.3.3. Soil Failure

The preceding discussions have focused exclusively on conditions for sliding along the soil-reinforcement interface. Stress conditions in the soil can also be estimated from the

shear-lag analysis. Equations 5.6a, b relate the shear and vertical stresses in the soil matrix ($\sigma_{xy}^m, \sigma_{yy}^m$) to the boundary conditions and interface tractions (σ_1, σ_3 and $\sigma_{yy}^i, \sigma_{xy}^i$, respectively). Figures 5.14a and b show contours which describe the development of these stresses at various stages of the pullout test (using reference properties originally in Fig. 5.5). The results show clearly the concentration of interface tractions as the sliding front progresses along the inclusion.

The analysis assumes that horizontal stresses in the soil are functions of position x only (i.e., $\sigma_{xx}^m(x)$, eqn. 5.2). As a result, the complete stress state at a given point in the soil is not known. However, as a first approximation the average horizontal stress $\bar{\sigma}_{xx}^m$ (given by eqn. 5.2) can be combined with the distributions of σ_{yy}^m and σ_{xy}^m in order to estimate the friction mobilized in the soil. Figure 5.14c presents contours of the mobilized 'pseudo-friction' $\tilde{\phi}$ (where $\sin \tilde{\phi} = (\tilde{R} - 1)/(\tilde{R} + 1)$, and $\tilde{R} = \tilde{\sigma}_1^m/\tilde{\sigma}_3^m$ is the pseudo-stress ratio in the soil) generated during the pullout tests. The results again show a concentration of $\tilde{\phi}$ at the sliding front. It is important to note that the approximation for $\tilde{\phi}$ always leads to an overestimation of the true friction mobilized in the soil, ϕ , at points close to the inclusion, and underestimates ϕ at points close to the specimen boundary. Thus, the contours of $\tilde{\phi}$ give a conservative estimate of failure conditions occurring within the soil.

Figures 5.15a, b and c show analogous solutions for the more extensible reinforcing material considered previously ($E_f/G_m=100$; Fig. 5.6). In this example, stress concentrations are much more pronounced and the mobilized pseudo-friction is in the range $20^\circ \leq \tilde{\phi} \leq 55^\circ$. It is highly probable that these stress conditions will cause failure within the soil mass ($35^\circ \leq \phi \leq 57^\circ$ for failure of typical sands in plane strain shearing; e.g. Ladd et al., 1977), and may provide the basis for the 'restrained dilatancy' described by previous researchers.

The proposed analysis assumes elastic behavior of the soil and hence, is less reliable when there is a significant zone of failure around the inclusion. In order to evaluate

the occurrence of failure within the soil, the maximum pseudo-friction angle $\tilde{\phi}_{\max}$ can be related to the geometry, material properties and interface friction (a , E_f/G_m , δ , respectively). Figure 5.16 summarizes these results for four particular values of $\tilde{\phi}_{\max}$ ($\tilde{R}_{\max}=4, 6, 8, 10$), which can be equated with the peak friction measured in plane strain shear tests in the soil. For inextensible reinforcements ($E_f/G_m > 10^5$; Fig 5.16) and for all cases where $\tanh\sqrt{K_1}L \approx 1$ (practical pullout conditions), $\tilde{\phi}_{\max}$ is independent of the test geometry (a, L) and is related uniquely to the interface friction as follows⁶:

$$E_f/G_m \rightarrow \infty : \sin \tilde{\phi}_{\max} = \tan \delta (= -\sigma_{xy}^i/\sigma_{yy}^i) \quad (5.28)$$

For more extensible reinforcements, much lower interface friction is required to mobilize the shear strength of the soil. The data in Figure 5.16 provide a useful but approximate basis for discriminating between pullout failure due to interface sliding and to shear failure within the soil.

5.4 Conclusions

This chapter describes a new shear-lag analysis for interpreting pullout tests on planar soil reinforcements. The formulation uses the shear-lag approximations described in Chapter 2, together with idealized boundary conditions at the active end of the reinforcement where pullout loads are applied. Closed-form analytical expressions are presented for the tensile stress and interface tractions along the inclusion, as functions of the pullout and consolidation stresses, test geometry, elastic material properties and interface friction.

⁶In an ideal, drained simple shear test on a soil, the failure condition is given by $\tau/\sigma_{v0} = 0.5[(1+K_0)^2 \sin^2 \phi - (1-K_0)^2]^{1/2}$, where τ/σ_{v0} is the stress ratio acting on horizontal planes in the sample and $K_0 = \sigma_{h0}/\sigma_{v0}$ is the consolidation stress ratio. For $K_0=1$, $\tau/\sigma_{v0} = \sin \phi$. Equating τ/σ_{v0} with $\tan \delta$ in equation 5.28, the results in Figure 5.16 imply that $K_0 \rightarrow 1$ in pullout tests.

The analysis provide new insights on the underlying mechanisms of pullout for extensible reinforcements. The complete pullout response (load-elongation) comprises four successive phases: 1) The initial linear behavior, characterized by a build up of interface tractions at the active end of the inclusion. 2) The development of a sliding front from the active end of the inclusion, generating a non-linear hardening response in pullout. The results show that stress concentrations develop at the sliding front and are most significant when reinforcements are relatively extensible. 3) The peak pullout resistance, associated with a two-way failure mechanism, with sliding fronts progressing from both the active and passive ends of the inclusion. The peak resistance coincides with the initiation of sliding at the passive end of the reinforcement when there are no residual tensile stresses in the inclusion. 4) The post-peak regime, when the sliding fronts coalesce causing a net reduction in pullout resistance and elongation, which give rise to a 'snap-through' mechanism of behavior.

Detailed interpretations of the analytical solutions have shown that the principal parameters controlling the load-elongation response are the reinforcement-soil stiffness ratio E_f/G_m , inclusion length L , and interface friction δ . The peak pullout resistance in the proposed analysis can be significantly larger (>10-20%) than that estimated from conventional limit equilibrium. This effect is due to local concentrations of the interface tractions and suggests an underlying source of error in the interpretation of interface friction from peak pullout measurements. Approximate calculations of stress fields around the inclusion show that pullout can induce shear failure in the soil. The chapter presents solutions for estimating conditions for failure in a frictional soil (ϕ), based on specified material properties, geometry and interface friction.

The shear-lag solutions are evaluated in Chapter 6 through direct comparison with experimental pullout tests performed in the APSR cell.

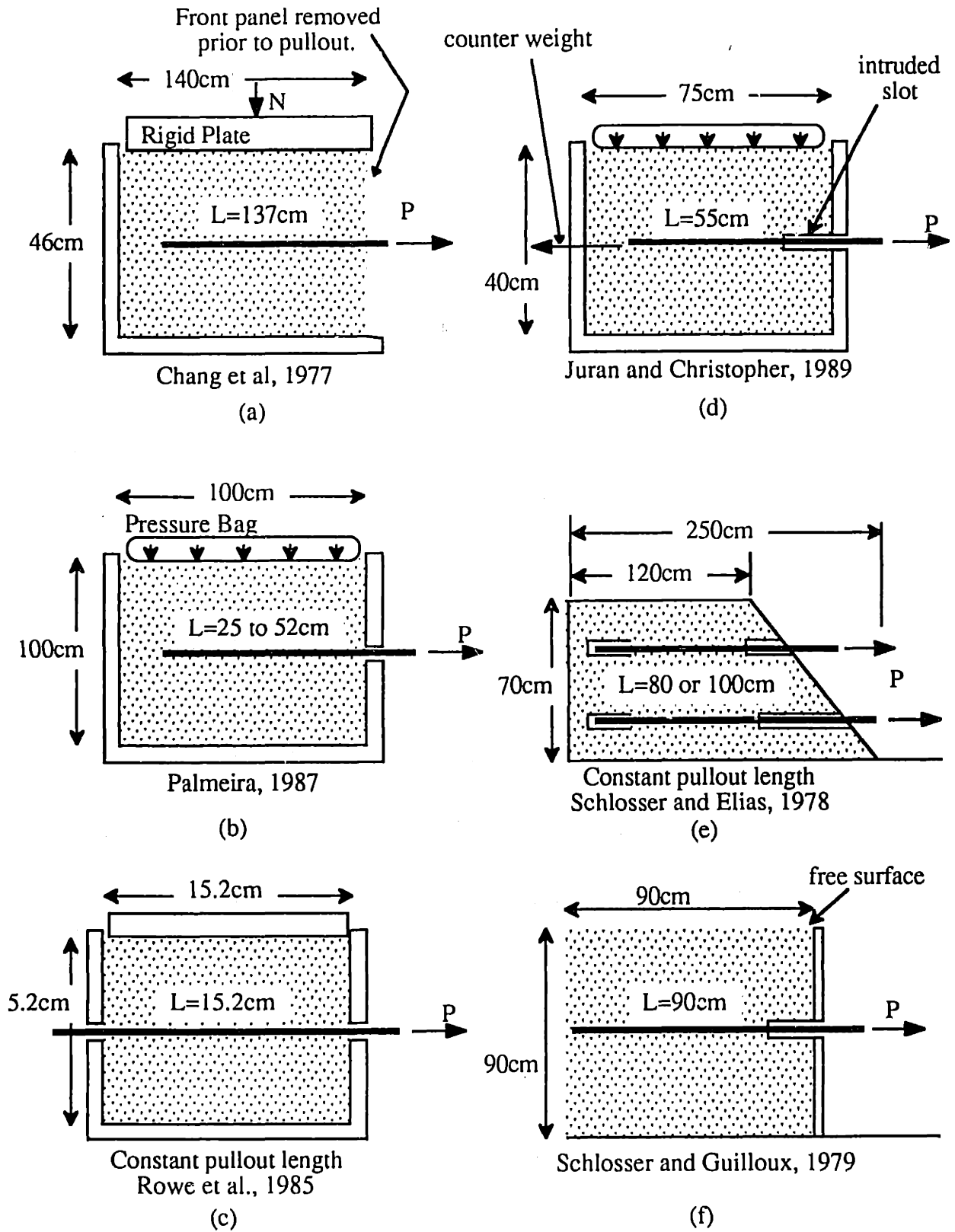
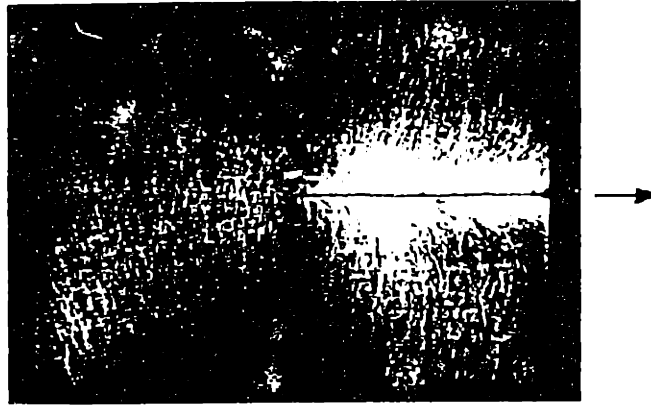
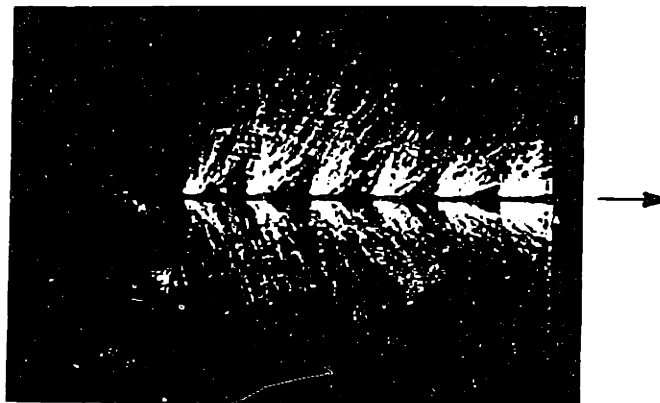


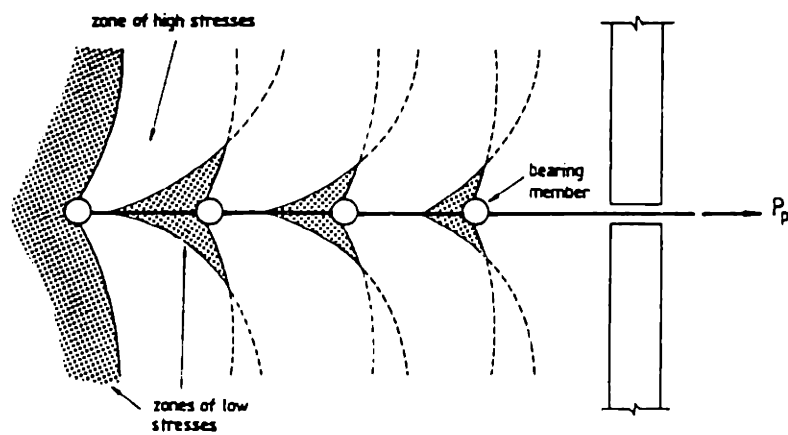
Figure 5.1: Boundary Conditions in Laboratory Pullout Tests.



a) Photoelastic observations of stresses (rough sheet)



b) Photoelastic observations of stresses (grid)



c) Schematic illustration of the effect of interference between bearing members (grid inclusion).

Figure 5.2: Stresses around a Rough Sheet and a Grid in a Pullout Test (after Dyer, 1985 and Palmeira, 1987).

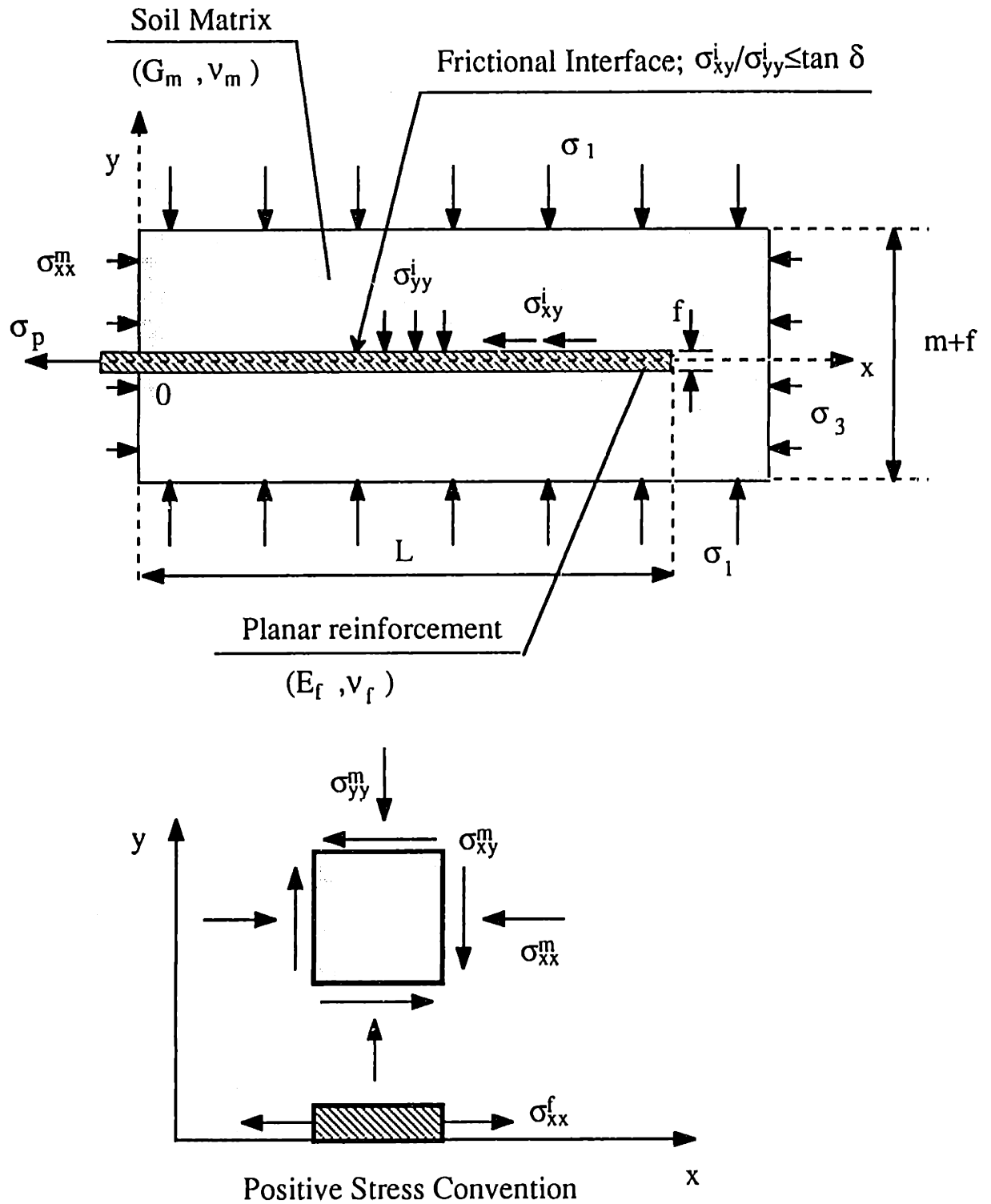
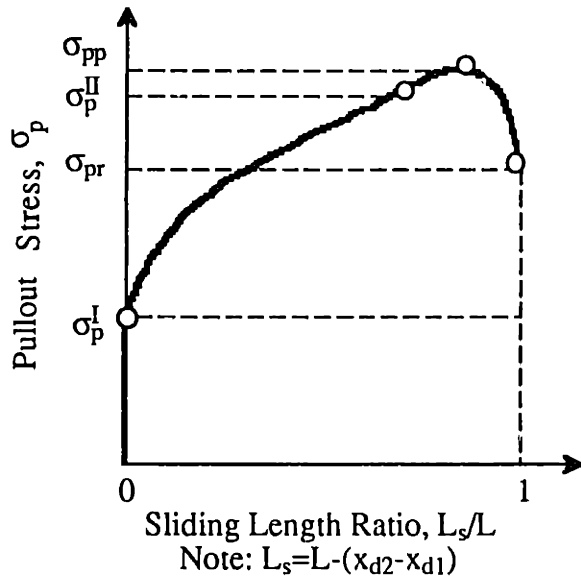
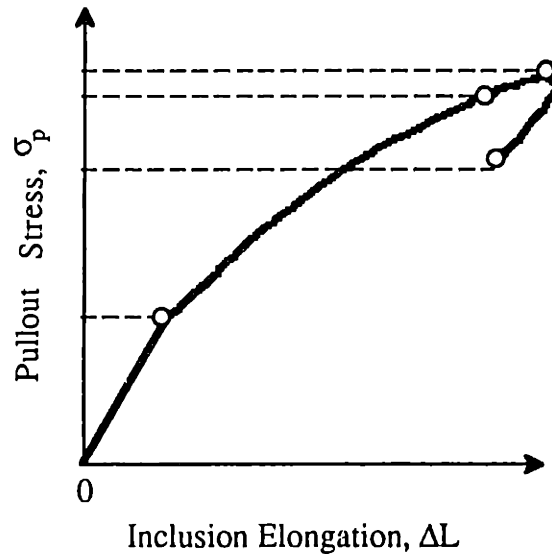


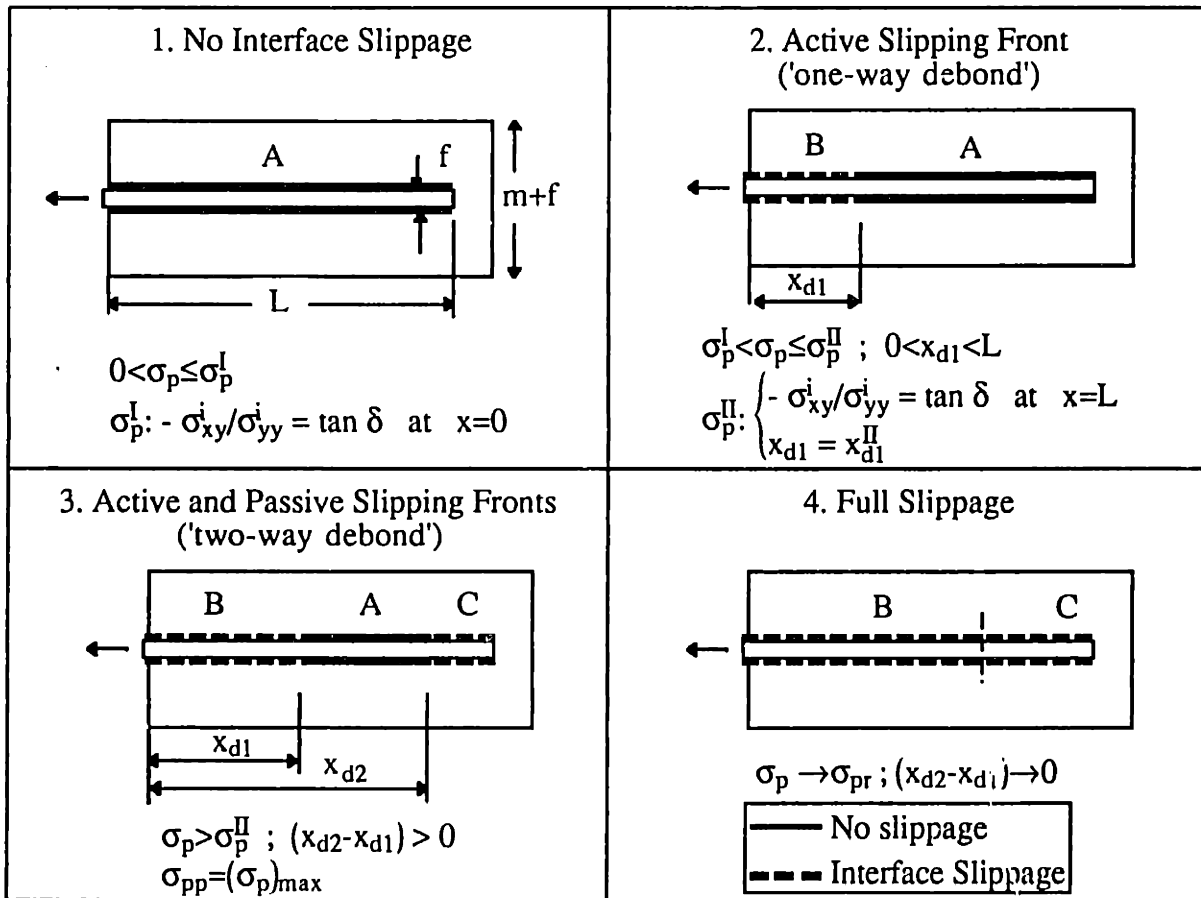
Figure 5.3: Geometry and Boundary Conditions used in Analysis of Pullout Tests for Planar Soil Reinforcements.



a) Load-Slip Length Response



b) Load-Elongation Response



c) Interface Conditions

Figure 5.4: Schematic Sequence of Events during Pullout of Planar Inclusions.

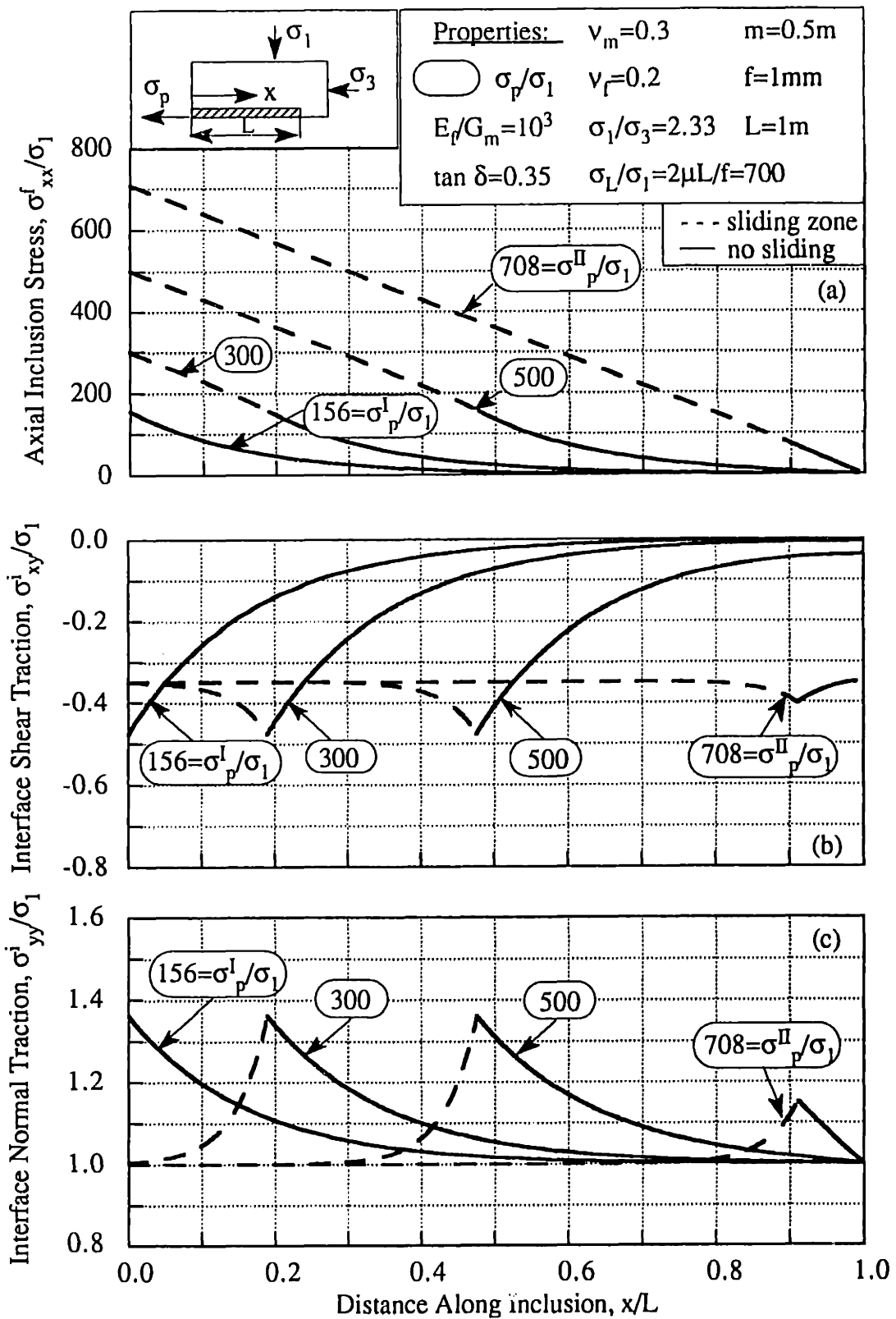


Figure 5.5: Axial Inclusion Stress and Interface Traction During Pullout Test: Base Case Analysis.

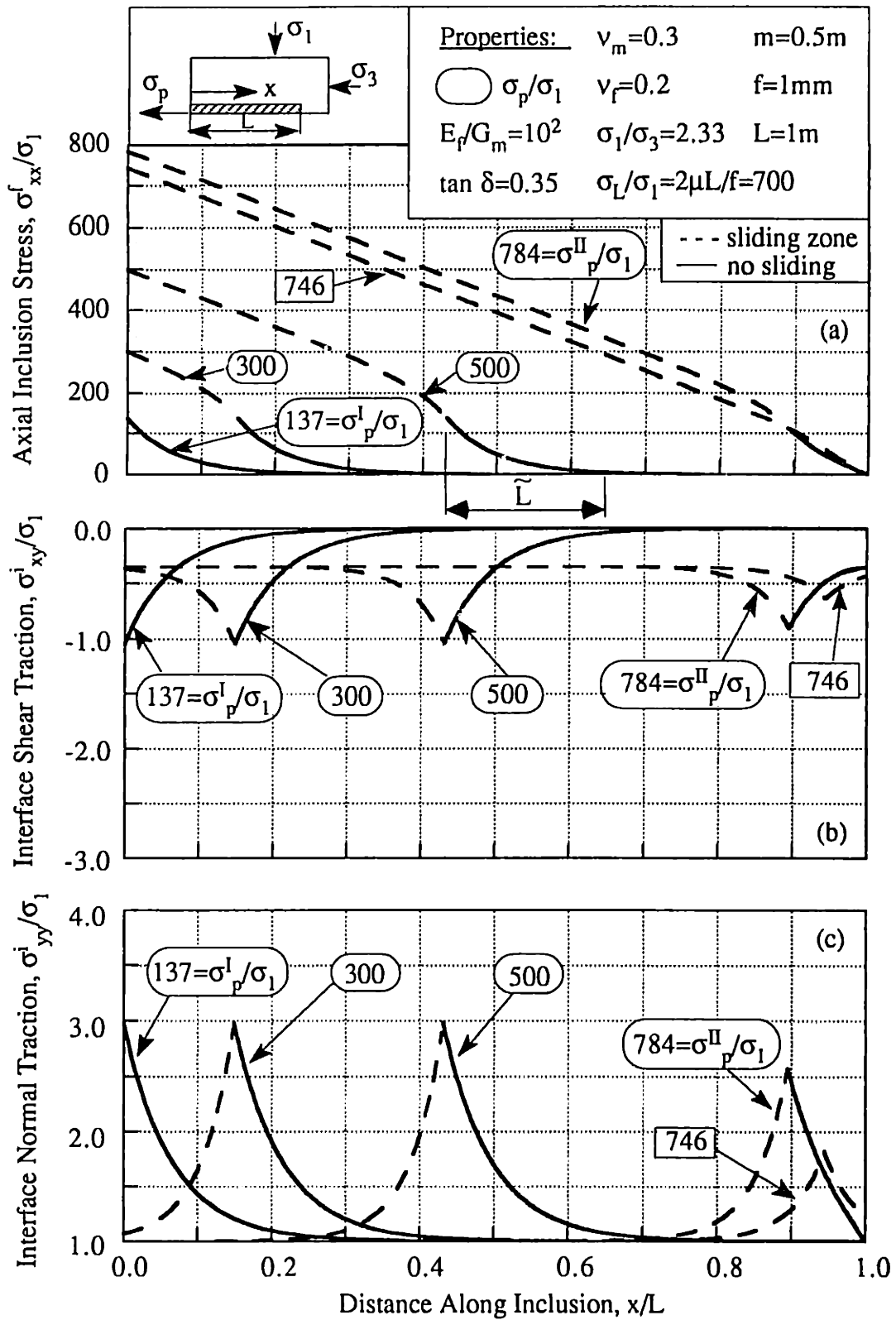


Figure 5.6: Tensile Stress and Interface Traction During Pullout Tests:
 Extensible Inclusion under K_0 Compression.

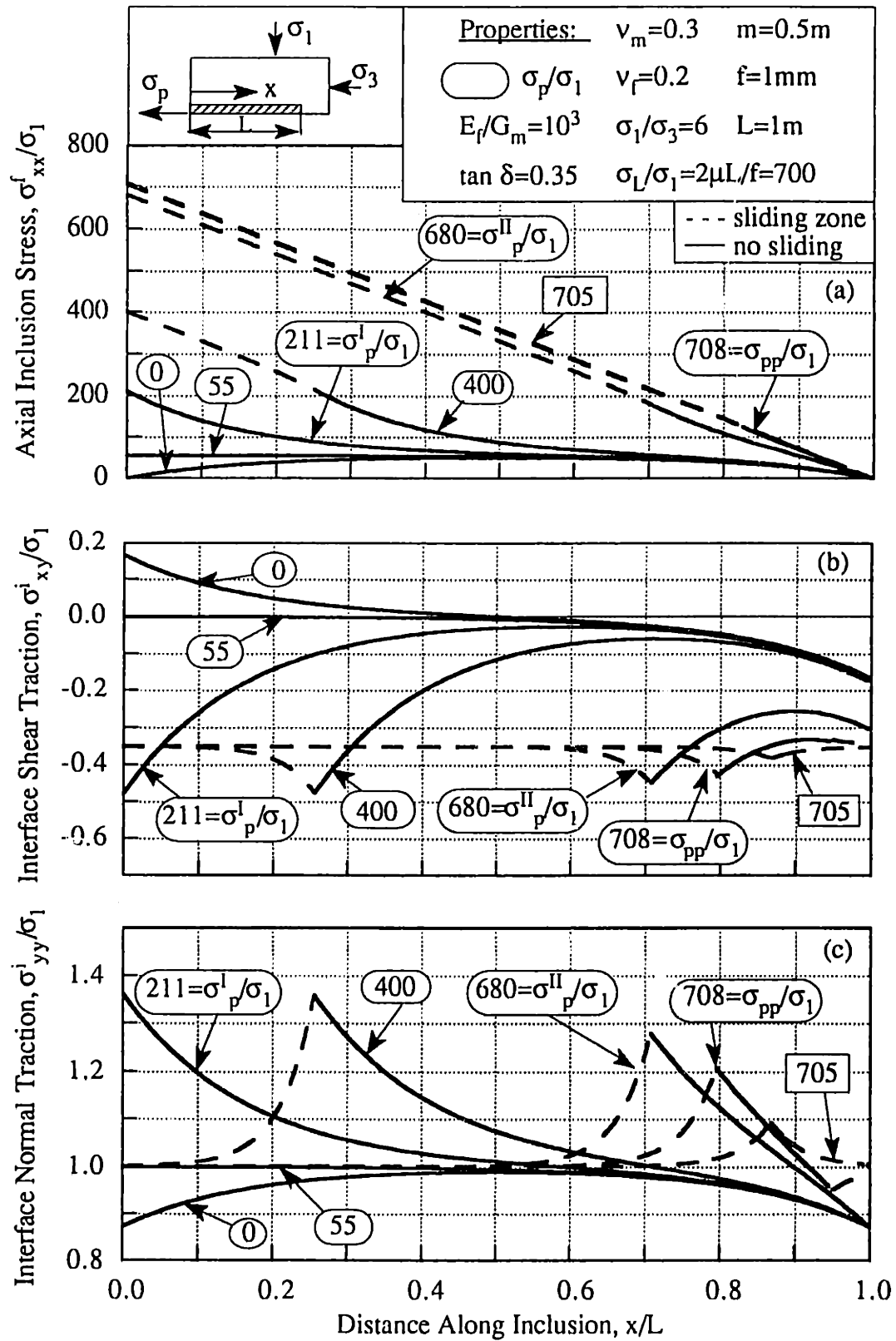
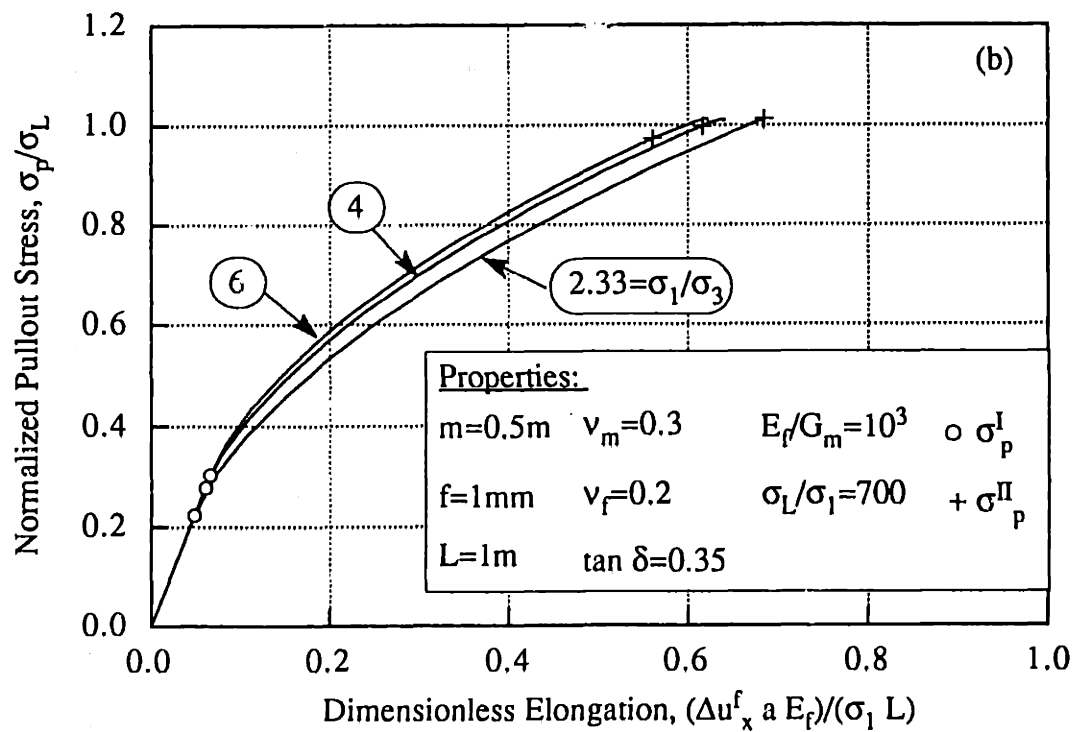
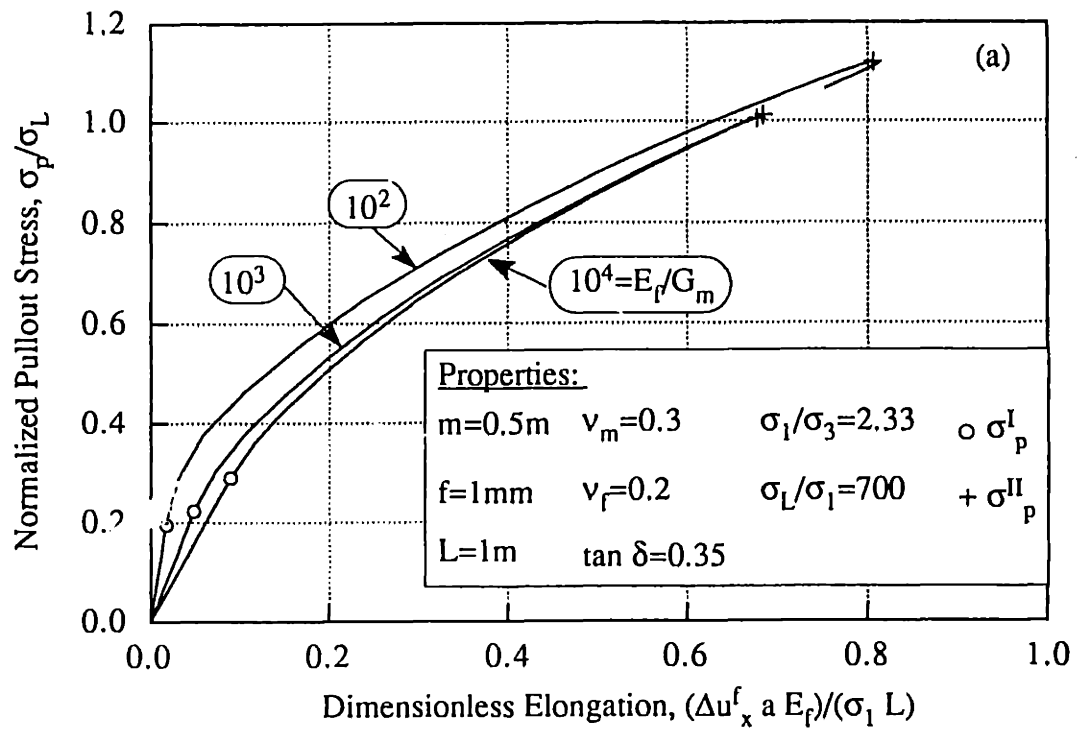
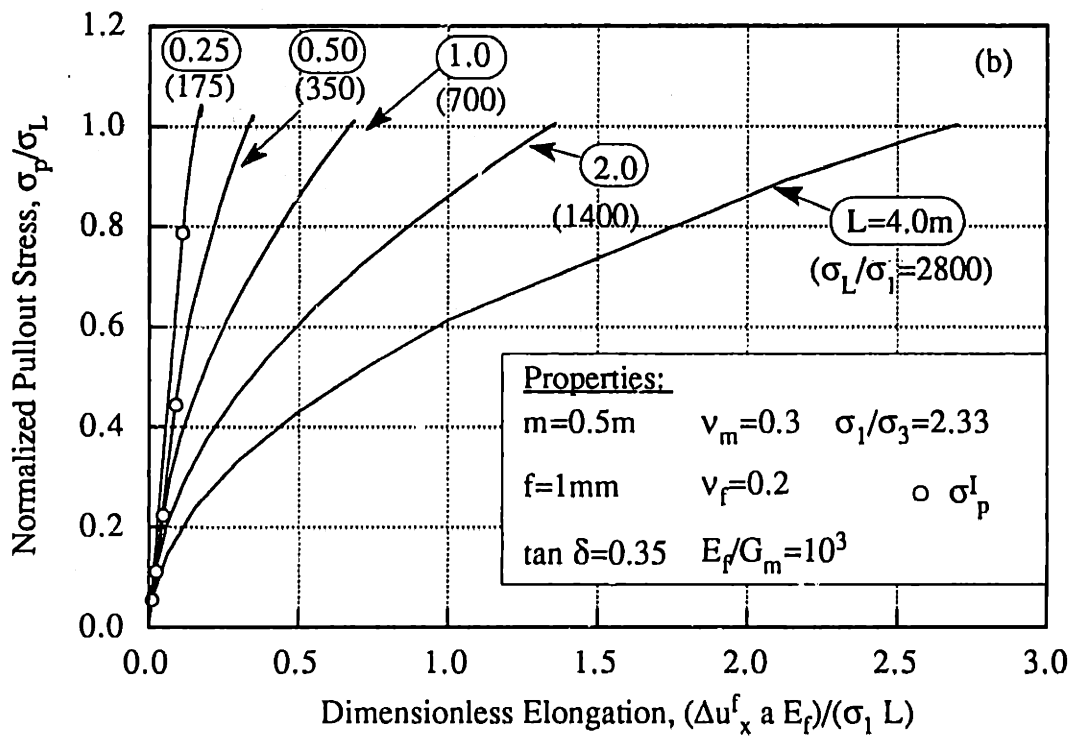
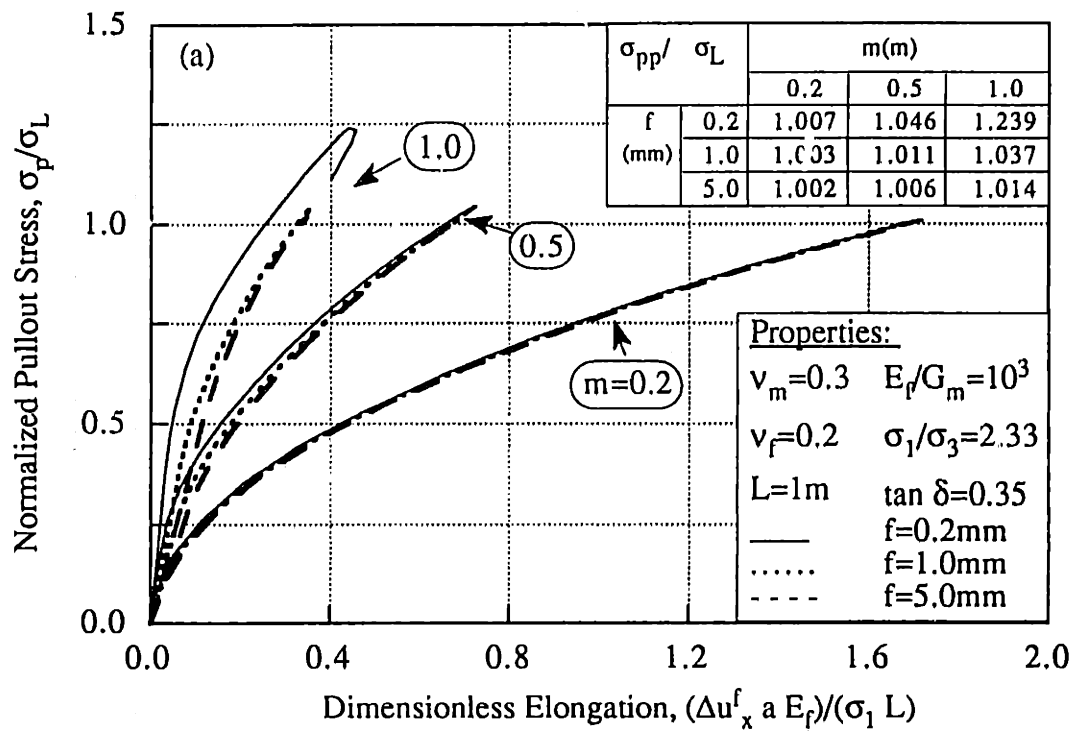


Figure 5.7: Effects of Residual Stresses on Tensile Stress and Interface Tractions During Pullout Tests.



Figures 5.8 a, b: Effects of Stiffness Ratio E_f/G_m and Residual Stresses (σ_1/σ_3) on Pullout Response.



Figures 5.9 a, b: Effects of Geometry on Load-Elongation Response.

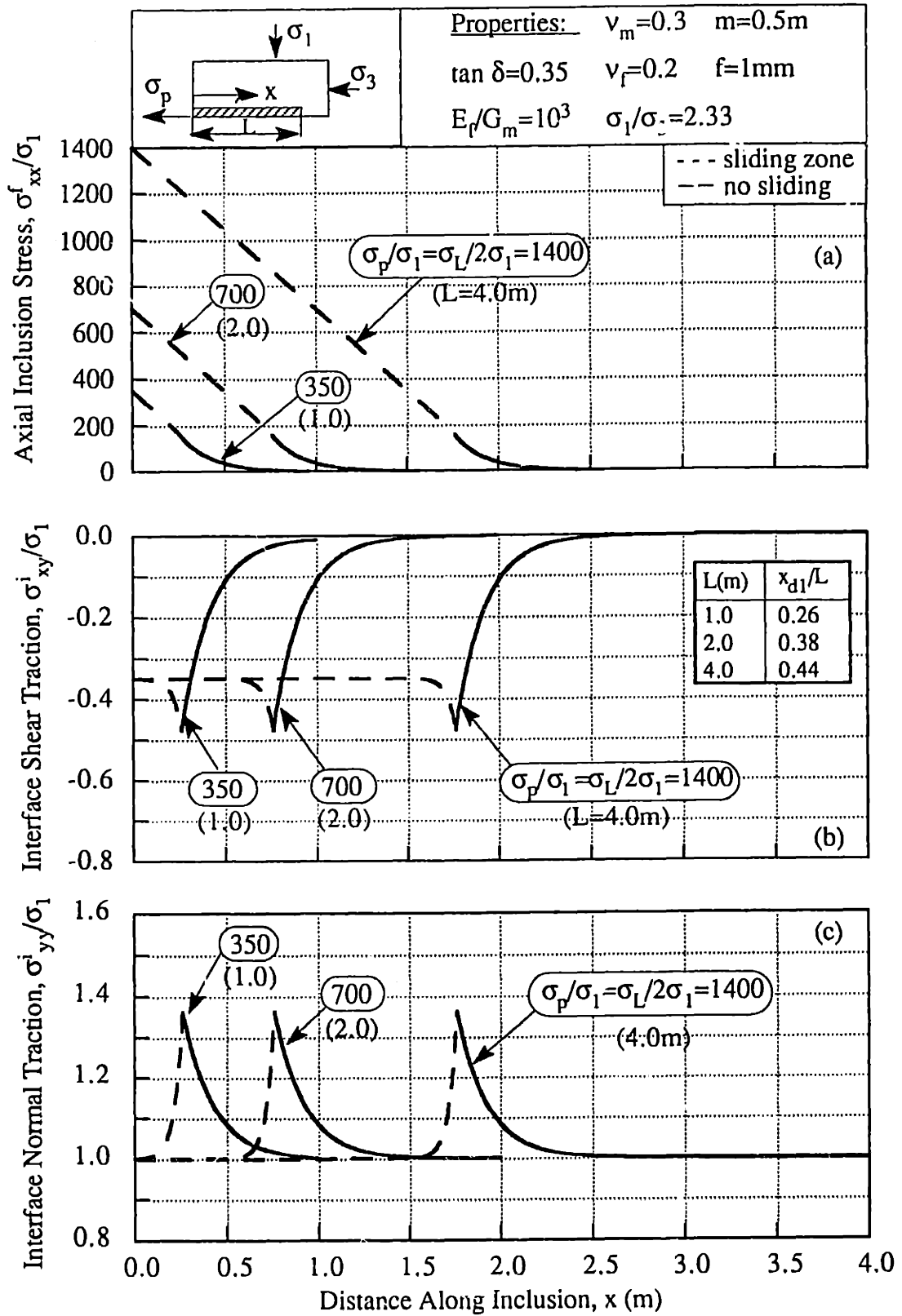


Figure 5.10: Effects of Inclusion Length on Axial Inclusion Stress and Interface Tractions.

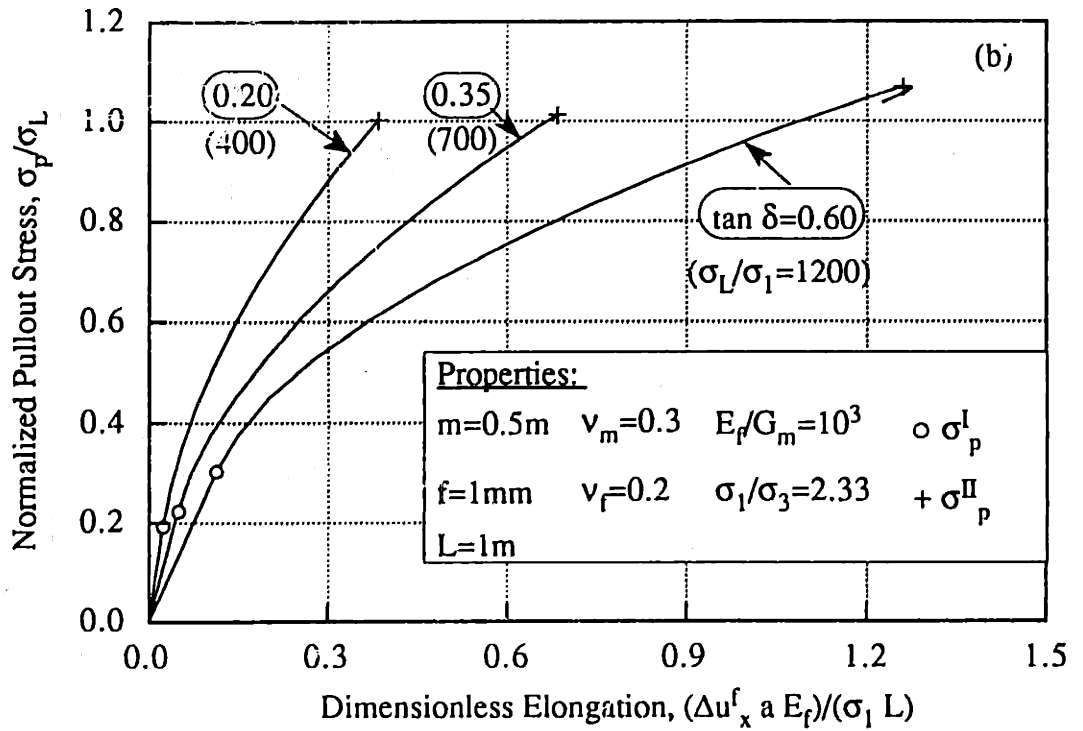
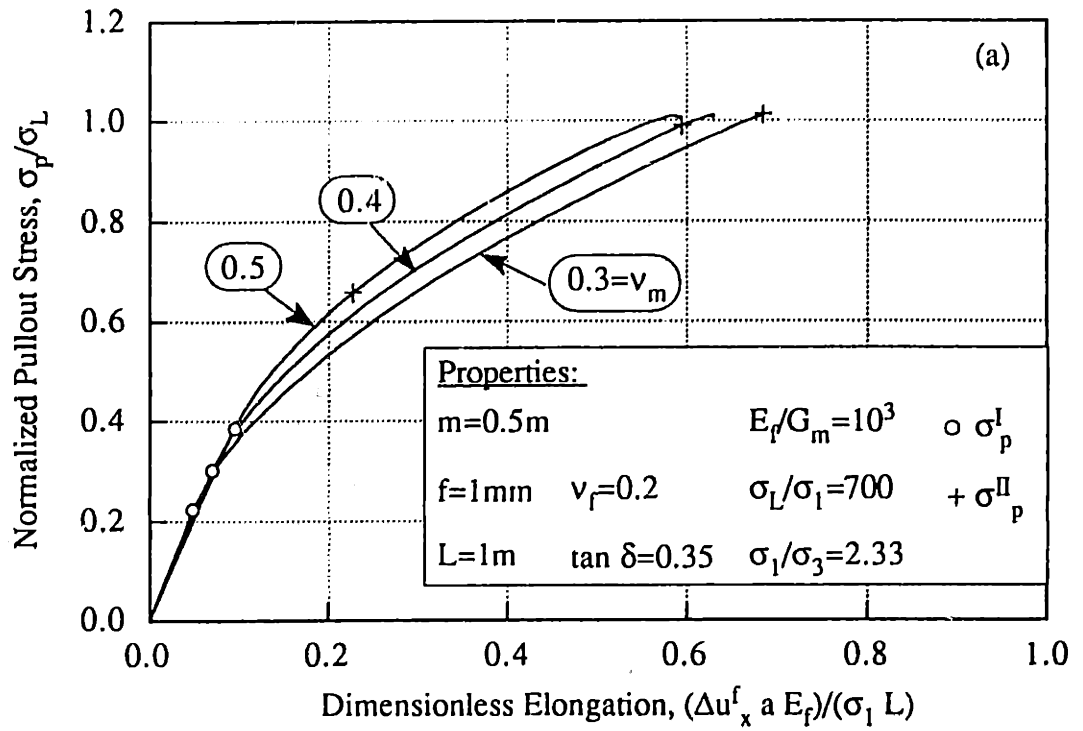


Figure 5.11 a, b: Effect of Material and Interface Properties on Load-Elongation Response.

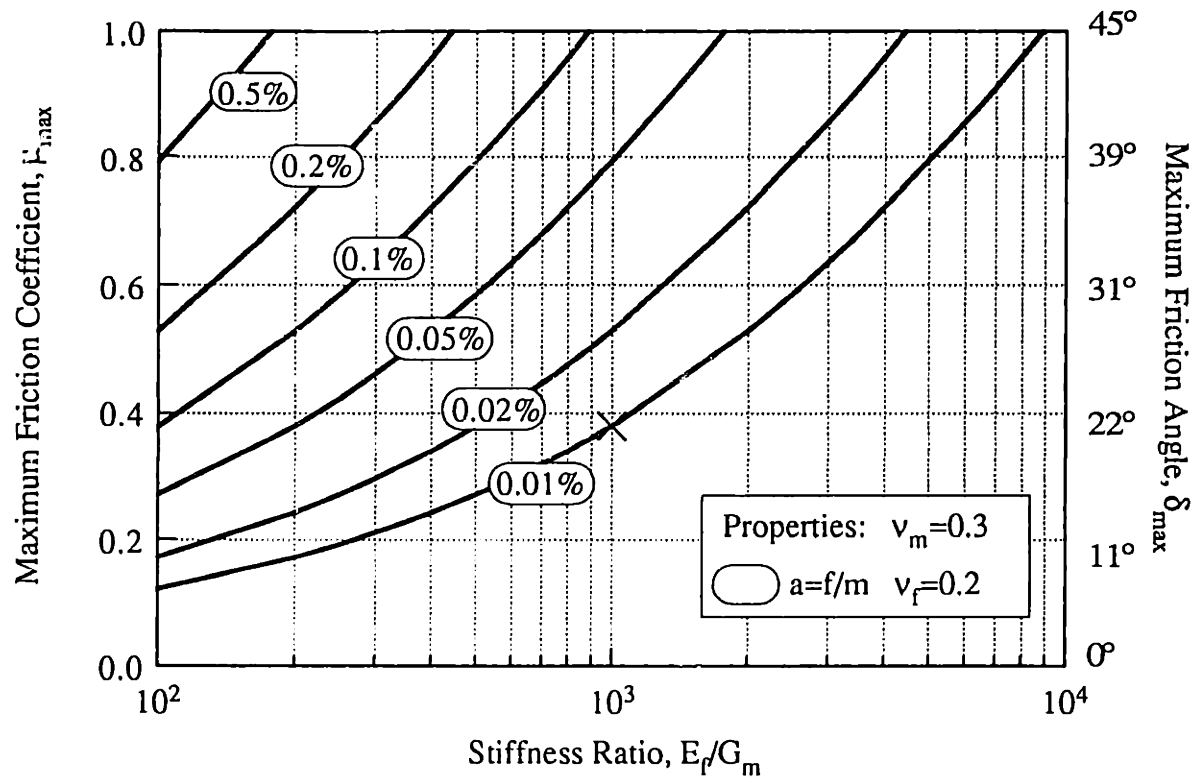


Figure 5.12: Limiting Friction for Sliding at Soil-Reinforcement Interface.

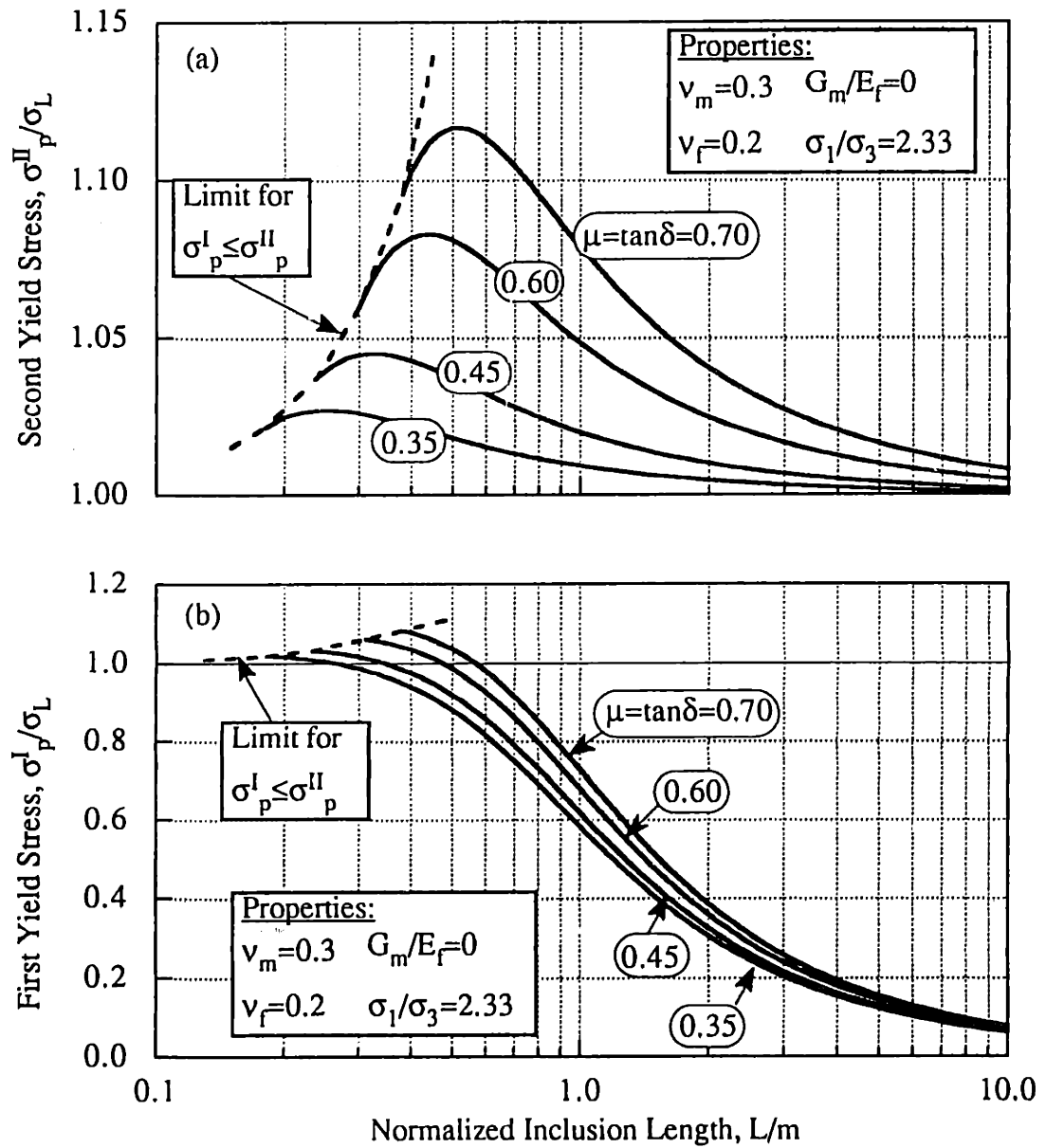
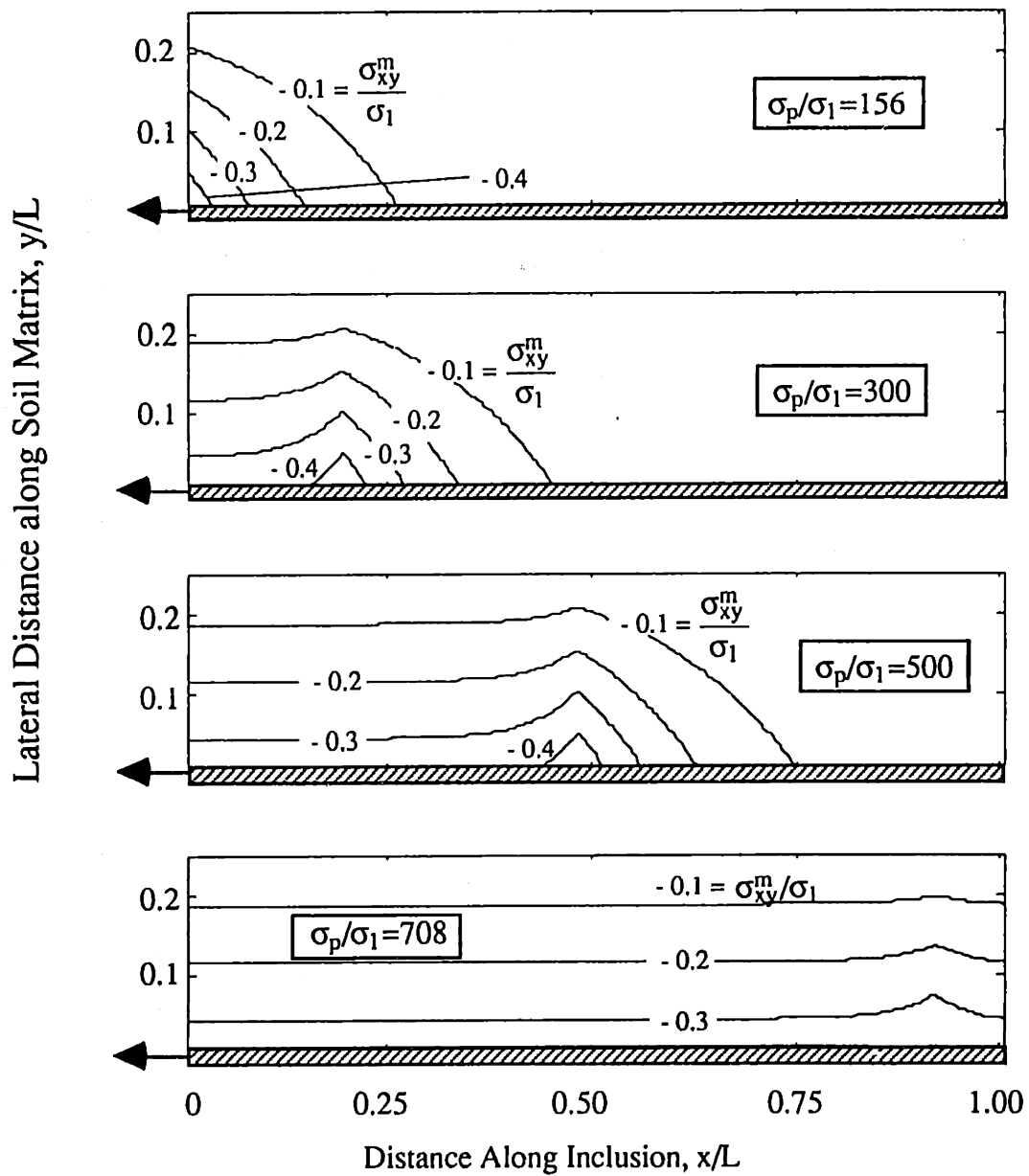
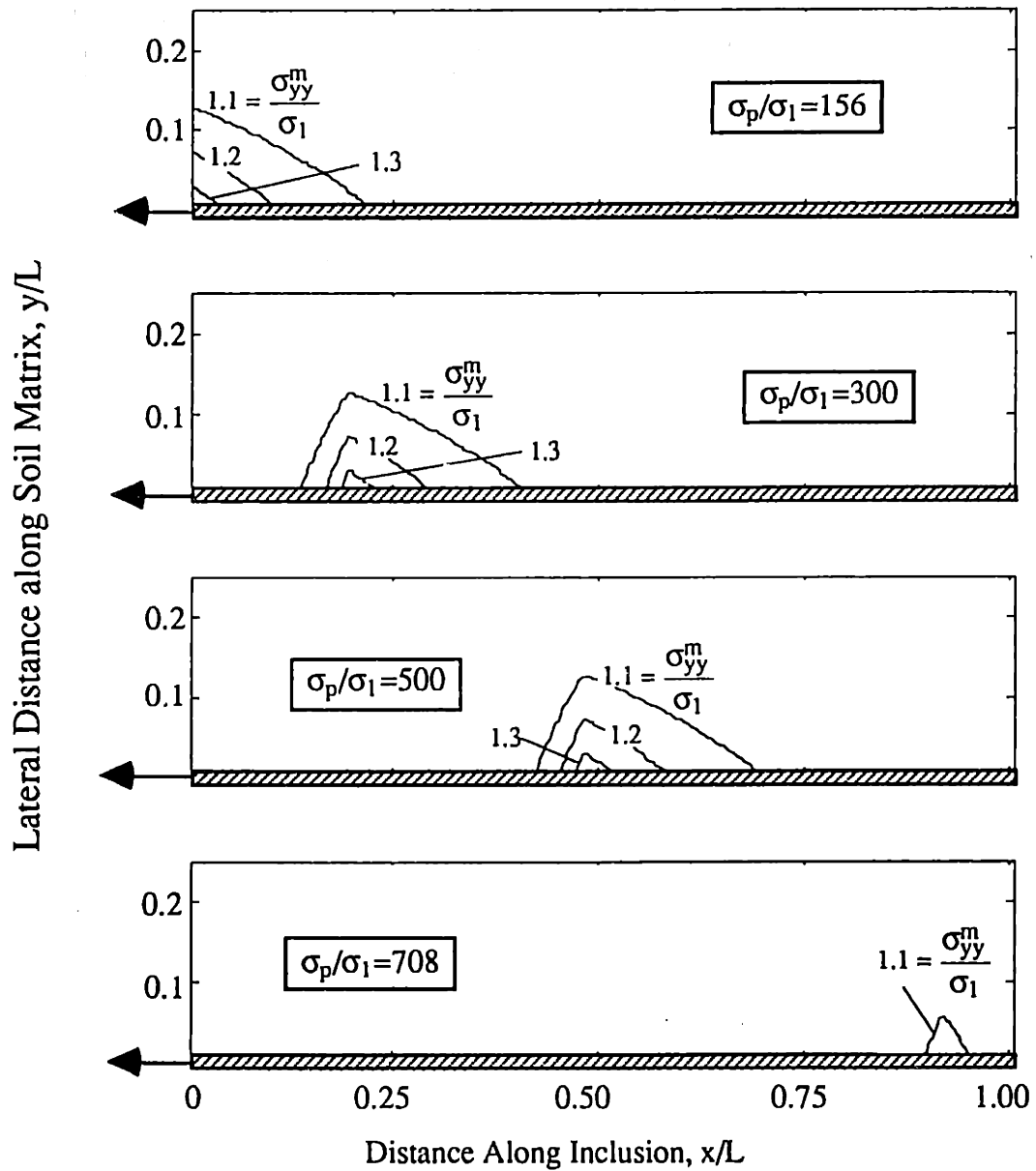


Figure 5.13: Limit Values of Yield Stresses for Inextensible Reinforcements.



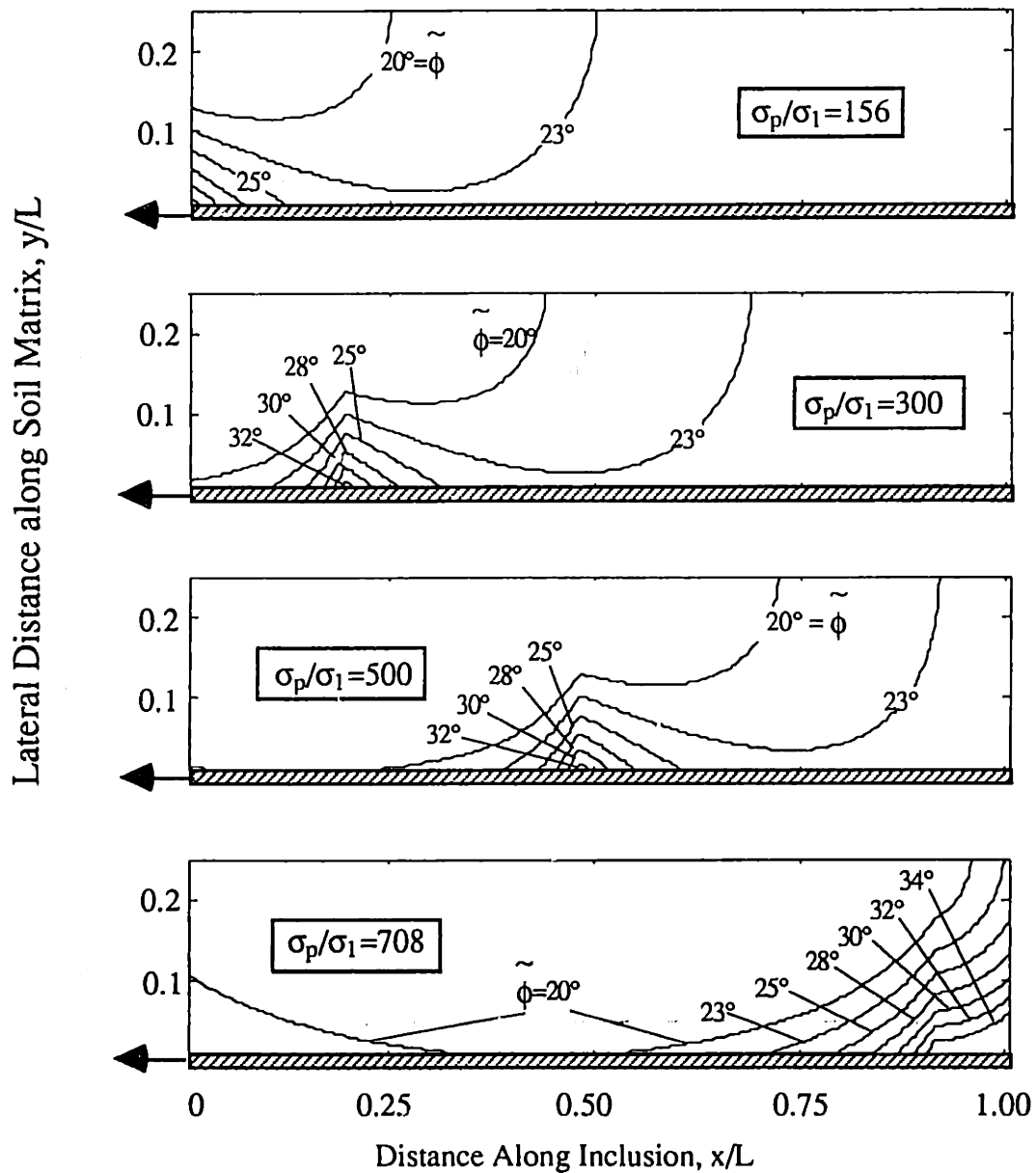
Properties		
$\sigma_1/\sigma_3=2.33$	$\nu_m=0.3$	$m=0.5m$
$E_f/G_m=10^3$	$\nu_f=0.2$	$f=1mm$
$\tan \delta=0.35$	$\sigma_1/\sigma_1=700$	$L=1m$

Figure 5.14 a: Contours of Shear Stresses in the Soil Matrix During Pullout Test for Reference Properties.



Properties		
$\sigma_1/\sigma_3=2.33$	$\nu_m=0.3$	$m=0.5m$
$E_f/G_m=10^3$	$\nu_f=0.2$	$f=1mm$
$\tan \delta=0.35$	$\sigma_1/\sigma_1=700$	$L=1m$

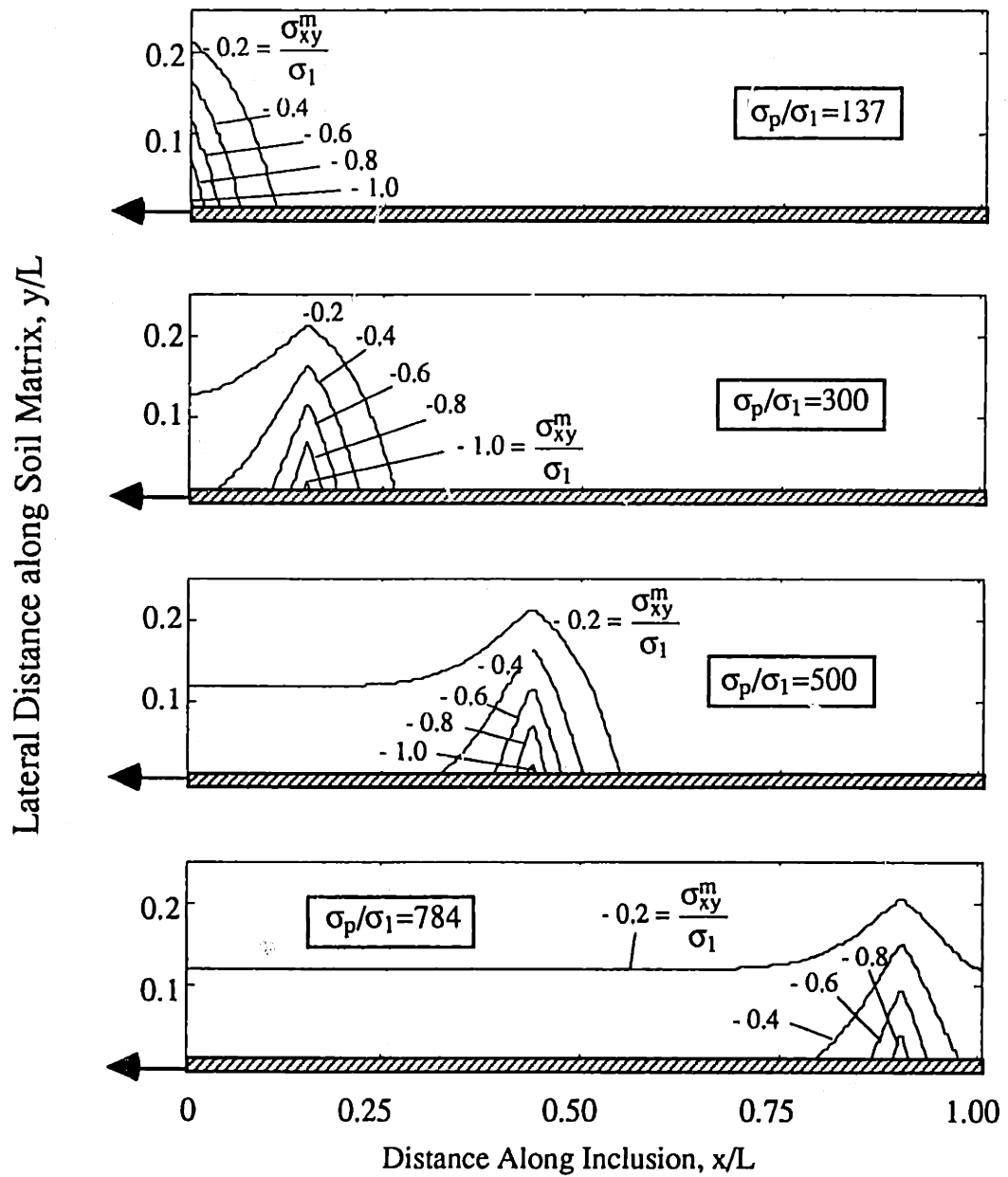
Figure 5.14 b: Contours of Normal Stresses in the Soil Matrix During Pullout Test for Reference Properties.



Properties		
$\sigma_1/\sigma_3=2.33$	$\nu_m=0.3$	$m=0.5m$
$E_f/G_m=10^3$	$\nu_f=0.2$	$f=1mm$
$\tan \delta=0.35$	$\sigma_L/\sigma_1=700$	$L=1m$

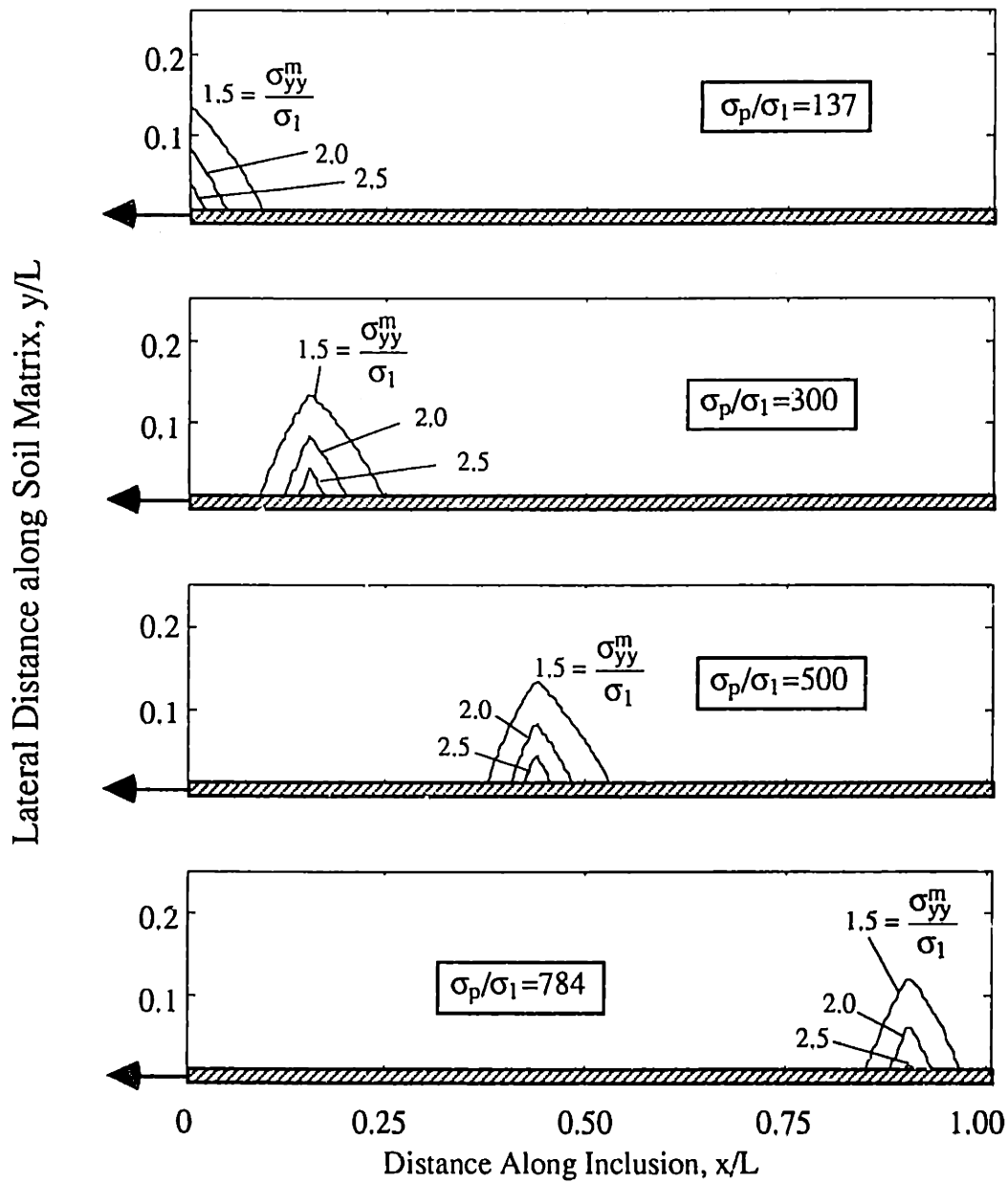
$\tilde{\phi}$	σ_1/σ_3
20°	2.00
23°	2.25
25°	2.50
28°	2.75
30°	3.00
32°	3.25

Figure 5.14 c: Contours of Mobilized Pseudo-Friction Angle in the Soil Matrix During Pullout Test for Reference Properties.



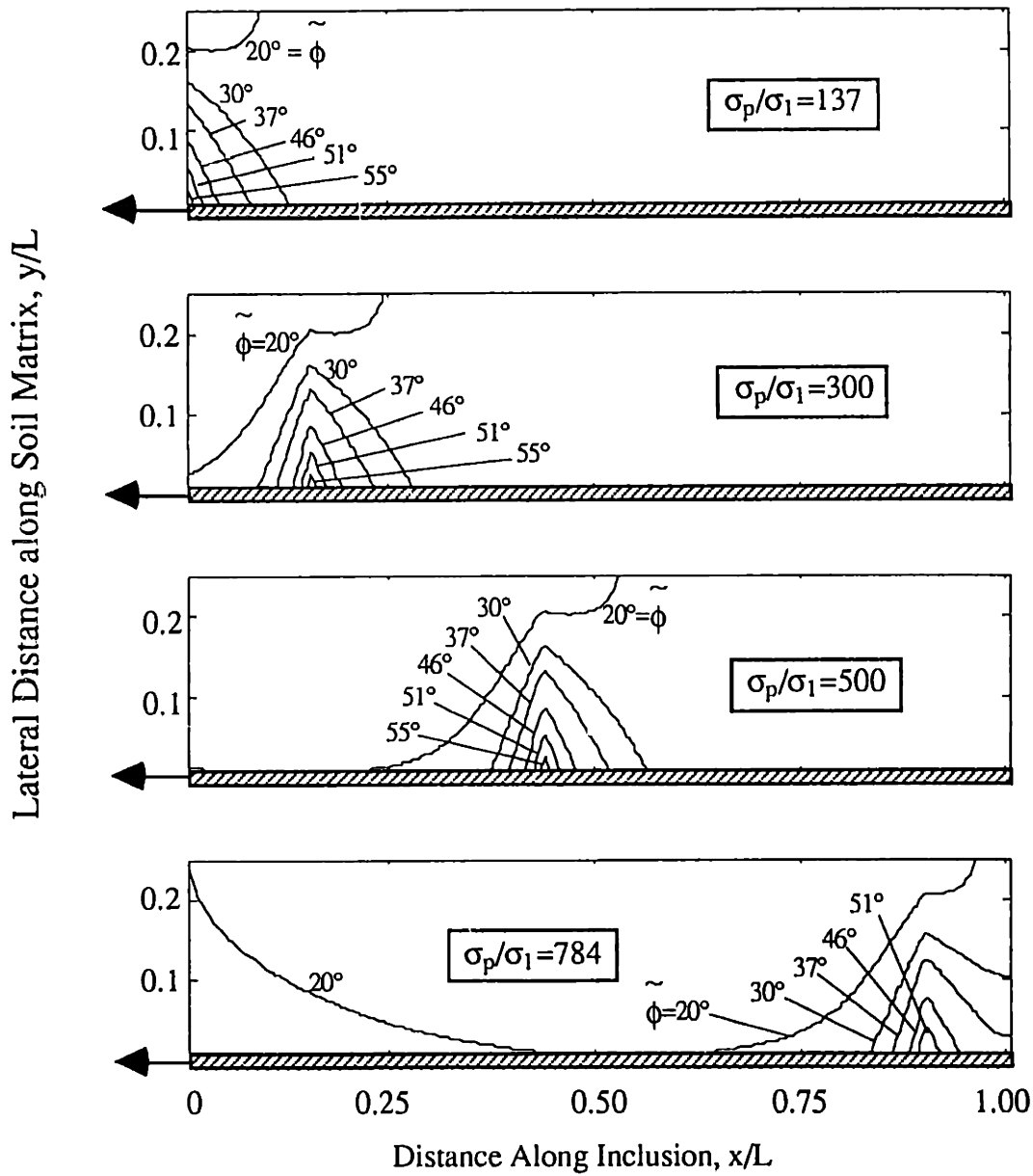
Properties		
$\sigma_1/\sigma_3=2.33$	$\nu_m=0.3$	$m=0.5m$
$E_f/G_m=10^2$	$\nu_f=0.2$	$f=1mm$
$\tan \delta=0.35$	$\sigma_L/\sigma_1=700$	$L=1m$

Figure 5.15 a: Contours of Shear Stresses in the Soil Matrix During Pullout Test in Extensible Inclusion.



Properties		
$\sigma_1/\sigma_3=2.33$	$\nu_m=0.3$	$m=0.5m$
$E_f/G_m=10^2$	$\nu_f=0.2$	$f=1mm$
$\tan \delta=0.35$	$\sigma_L/\sigma_1=700$	$L=1m$

Figure 5.15 b: Contours of Normal Stresses in the Soil Matrix During Pullout Test in Extensible Inclusion.



Properties		
$\sigma_1/\sigma_3=2.33$	$\nu_m=0.3$	$m=0.5m$
$E_f/G_m=10^2$	$\nu_f=0.2$	$f=1mm$
$\tan \delta=0.35$	$\sigma_L/\sigma_1=700$	$L=1m$

$\tilde{\phi}$	σ_1/σ_3
20°	2
30°	3
37°	4
46°	6
51°	8
55°	10

Figure 5.15 c: Contours of Mobilized Pseudo-Friction Angle in the Soil Matrix During Pullout Test in Extensible Inclusion.

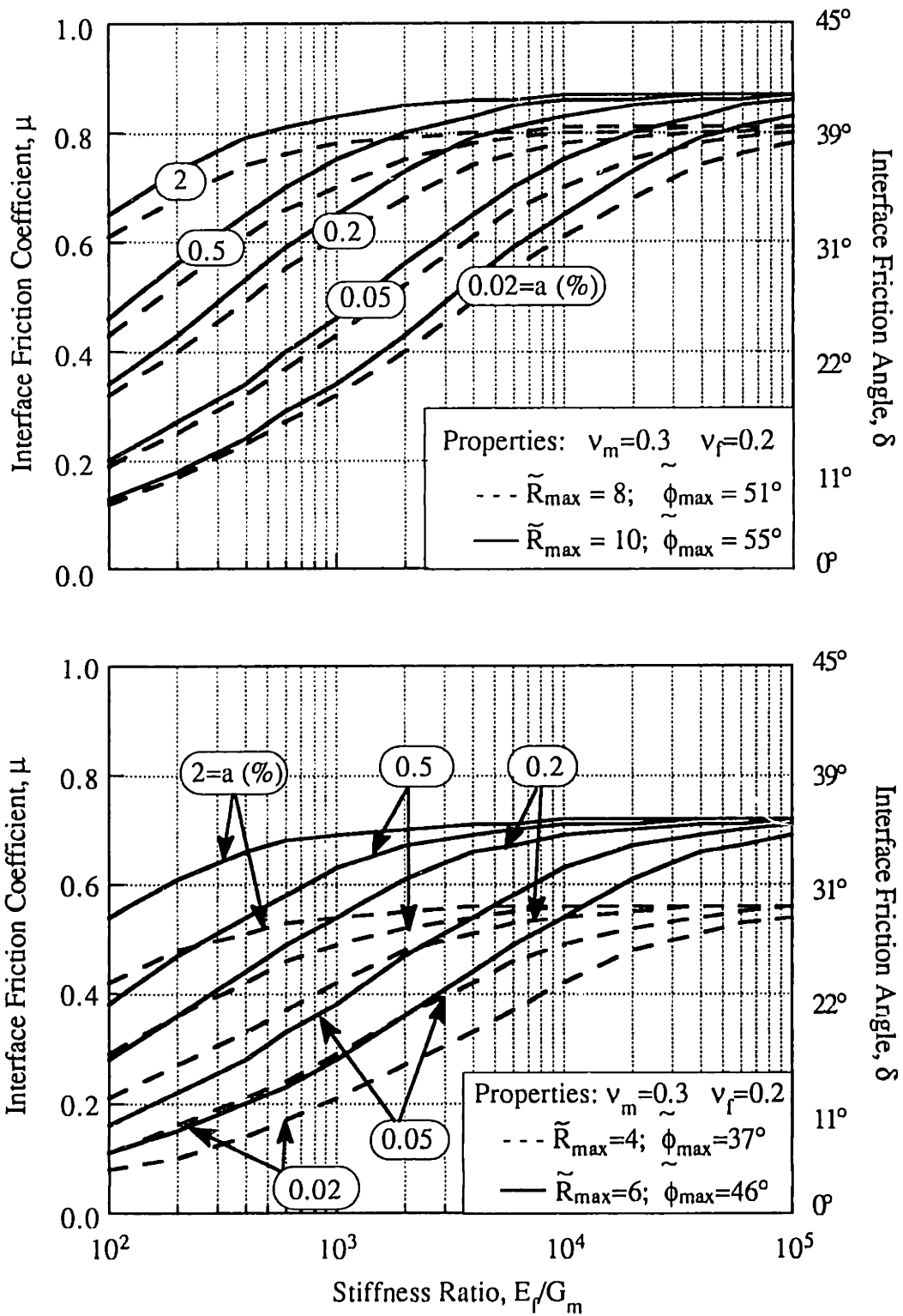


Figure 5.16: Evaluation of Conditions for Soil Failure in Pullout Tests.

Appendix 5.A: Complete Expressions for Pullout Curves

This appendix summarizes analytical expressions for the inclusion elongation (equation 5.26) for specified dimensions of the slippage zone x_{d1} and x_{d2} (zones B, C in figure 5.4):

1. Initial/residual elongation: For soil specimens consolidated under 1-D conditions ($K_0=\sigma_1/\sigma_3$), the reinforcement is initially unstressed. However, for non- K_0 consolidation there is potential for residual stresses to develop in the inclusion. The initial elongation (at $\sigma_p=0$) is computed as follows:

$$\Delta u_x^f = \frac{(1+\nu_f)}{E_f} \left\{ 2K \left[\frac{(1-\cosh\sqrt{K_1}L)}{\sinh\sqrt{K_1}L} \right] \left[\frac{(1-\nu_f)}{\sqrt{K_1}} + \nu_f \frac{mf\sqrt{K_1}}{8} \right] + [(1-\nu_f)K + \nu_f\sigma_1]L \right\} \quad (A.1)$$

2. No slippage: The elongation is computed from equations 5.8 and 5.9:

$$\Delta u_x^f = \frac{(1+\nu_f)}{E_f} \left\{ (2K-\sigma_p) \left[\frac{(1-\cosh\sqrt{K_1}L)}{\sinh\sqrt{K_1}L} \right] \left[\frac{(1-\nu_f)}{\sqrt{K_1}} + \nu_f \frac{mf\sqrt{K_1}}{8} \right] + [(1-\nu_f)K + \nu_f\sigma_1]L \right\} \quad (A.2)$$

3. One-way debonding: In this case, the total elongation is obtained by integrating the strains in the slipped and no-slip regions (zones A, B; Fig. 5.4) through equations 5.8/5.11 and 5.13, respectively:

$$\begin{aligned} \Delta u_x^f = & \frac{(1+\nu_f)}{E_f} \left\{ (2K-\sigma_{t1}) \left[\frac{1-\cosh\sqrt{K_1}(L-x_{d1})}{\sinh\sqrt{K_1}(L-x_{d1})} \right] \left[\frac{(1-\nu_f)}{\sqrt{K_1}} + \nu_f \frac{mf\sqrt{K_1}}{8} \right] + \right. \\ & + (1-\nu_f) \left[\sigma_p x_{d1} - \beta \sigma_1 \sqrt{K_1} \frac{x_{d1}^2}{2} - \frac{\sigma_p - \beta \sigma_1 \sqrt{K_1} x_{d1} - K}{[(1+\alpha)\exp(\sqrt{\alpha K_1} x_{d1})] - 1} \right. \\ & \left. \left. \frac{(\exp(\sqrt{\alpha K_1} x_{d1}) - 1 - \sqrt{\alpha K_1} x_{d1})}{\sqrt{\alpha K_1}} + K(L-x_{d1}) \right] + \right. \\ & \left. + \nu_f \left[\sigma_1 x_{d1} + \frac{\sigma_p - \beta \sigma_1 \sqrt{K_1} x_{d1} - K}{[(1+\alpha)\exp(\sqrt{\alpha K_1} x_{d1})] - 1} \frac{(\exp(\sqrt{\alpha K_1} x_{d1}) - 1)}{\beta \sqrt{K_1}} \right] \right\} \quad (A.3) \end{aligned}$$

4. Two-way debonding: The elongation involves contributions from the three regions A, B, C, as shown in Figure 5.4. The relevant equations are 5.8/5.19, 5.13 and 5.21:

$$\begin{aligned}
\Delta u_x^f = & \frac{(1+\nu_f)}{E_f} \left\{ (2K - \sigma_{t1} - \sigma_{t2}) \left[\frac{1 - \cosh \sqrt{K_1} (x_{d2} - x_{d1})}{\sinh \sqrt{K_1} (x_{d2} - x_{d1})} \right] \left[\frac{(1-\nu_f)}{\sqrt{K_1}} + \nu_f \frac{mf \sqrt{K_1}}{8} \right] + \right. \\
& + (1-\nu_f) \left[K(x_{d2} - x_{d1}) + \sigma_p x_{d1} - \beta \sigma_1 \sqrt{K_1} \frac{x_{d1}^2}{2} - \frac{\sigma_p - \beta \sigma_1 \sqrt{K_1} x_{d1} - K}{[(1+\alpha) \exp(\sqrt{\alpha K_1} x_{d1})] - 1} \right. \\
& \frac{\exp(\sqrt{\alpha K_1} x_{d1}) - 1 - \sqrt{\alpha K_1} x_{d1}}{\sqrt{\alpha K_1}} + \beta \sigma_1 K_1 \frac{(L - x_{d2}^2)}{2} - \frac{\beta \sigma_1 \sqrt{K_1} (L - x_{d2}) - K}{[(1-\alpha) \exp(-\sqrt{\alpha K_1} x_{d2})] - \exp(-\sqrt{\alpha K_1} L)} \\
& \left. \left. \frac{[\sqrt{\alpha K_1} (x_{d2} - L) - 1] \exp(-\sqrt{\alpha K_1} L) + \exp(-\sqrt{\alpha K_1} x_{d2})}{\sqrt{\alpha K_1}} \right] + \right. \\
& + \nu_f \left[\sigma_1 (2x_{d2} - x_{d1} - L) + \frac{\sigma_p - \beta \sigma_1 \sqrt{K_1} x_{d1} - K}{[(1+\alpha) \exp(\sqrt{\alpha K_1} x_{d1})] - 1} \frac{\exp(\sqrt{\alpha K_1} x_{d1}) - 1}{\beta \sqrt{K_1}} - \right. \\
& \left. \left. \frac{\beta \sigma_1 \sqrt{K_1} (L - x_{d2}) - K}{[(1-\alpha) \exp(-\sqrt{\alpha K_1} x_{d2})] - \exp(-\sqrt{\alpha K_1} L)} \frac{\exp(-\sqrt{\alpha K_1} L) - \exp(-\sqrt{\alpha K_1} x_{d2})}{\beta \sqrt{K_1}} \right] \right\}
\end{aligned} \tag{A.4}$$

In these expressions, the terms multiplied by ν_f correspond to the inclusion elongations due to increase in normal interface tractions. These elongations are expected to be very small, and can therefore be neglected.

Appendix 5.B: References

- Abramento, M. and Whittle, A.J. (1993) "Shear-Lag Analysis of a Planar Soil Reinforcement in Plane Strain Compression", *ASCE Journal of Engineering Mechanics*, 119(2), 270-291.
- Allersma, H.G.B. (1982) "Photo-Elastic Stress Analysis and Strains in Simple Shear", *IUTAM Conf. on Deformation and Failure of Granular Materials*, Delft, Holland, 345-353.
- Bolton, M.D. (1986) "The Strength and Dilatancy of Sands", *Géotechnique*, 36(1), 65-79.
- Boulon, M.; Plytas, C. and Foray, P. (1990) "Comportement d'Interface et Prévion du Frottement Latéral le Long des Pieux et Tirants d'Ancrage", *Revue Française de Géotechnique*, 2, 31-48.
- Boulon, M. and Foray, P. (1986) "Physical and Numerical Simulation of Lateral Shaft Friction along Offshore Piles in Sand", *Proc. Third Int. Conf. on Num. Methods in Offshore Piling*, Nantes, France, 127-148.
- Budiansky, B., Hutchinson, J. W. and Evans, A. G. (1986) "Matrix Fracture in Fiber-Reinforced Ceramics", *Journal of the Mechanics and Physics of Solids*, 34(2), 167-189.
- Chang, J.C., Hannon, J.B. and Forsyth, R.A. (1977) "Pull-out Resistance and Interaction of Earth Reinforcement and Soil," *Transport Research Record No. 640*, Washington, D.C.

- Delmas, P.; Gourc, J.P. and Giroud, J.P. (1979) "Analyse Expérimentale de l'interaction Mécanique Sol-Géotextile", *Proc. International Conference on Soil Reinforcement, Paris*, 1, 29-34.
- Dyer, M.R. (1985), "*Observation of the Stress Distribution in Crushed Glass with Applications to Soil Reinforcement*", Ph.D. Thesis, University of Oxford.
- Gens, A.; Carol, I. and Alonso, E.E. (1988) " An Interface Element Formulation for the Analysis of Soil-Reinforcement Interaction", *Computers and Geotechnics*, 7, 133-151.
- Griffiths, D.V. (1985) "Numerical Modelling of Interfaces Using Conventional Finite Elements", *Proc. of the Fifth International Conference on Numerical Methods in Geomechanics*, Nagoya, 837-844.
- Hettler, A. (1982) "Approximation Formulae for Piles Under Tension", *IUTAM Conf. on Deformation and Failure of Granular Materials*, Delft, Holland, 603-608.
- ICE (1985) "*Conference on Polymer Grid Reinforcement*", Institute of Civil Engineers, Thomas Telford, London, 391 pp.
- Ingold, T.S. (1984) "A Laboratory Investigation of Soil-Geotextile Friction," *Ground Engineering*, 17(11), 21-28.
- Jewell, R.A. (1990) "Strength and Deformation in Reinforced Soil Design", *Proc. Fourth International Conference on Geotextiles, Geomembranes and Related Products*, The Hague, 79 pp.
- Jewell, R.A., Milligan, G.W.E., Sarsby, R.W., and Dubois, D. (1985) "Interaction Between Soils and Geogrids," *Polymer Grid Reinforcement*, Thomas Telford, London, 18-30.

- Johnston, R. S. and Romstad, K.M. (1989) "Dilation and Boundary Effects in Large Scale Pullout Tests", *Proceedings of the XII International Conference on Soil Mechanics and Foundation Engineering*, Rio de Janeiro, 1263-1266.
- Juran, I. and Christopher, B. (1989), "Laboratory Model Study on Geosynthetic Reinforced Soil Retaining Walls," *ASCE Journal of Geotechnical Engineering*, 115(7), 905-926.
- Kuhn, P. (1956) *Stresses in Aircraft and Shell Structures*, McGraw-Hill, 435 pp.
- Ladd, C. C., Foott, R., Ishihara, K., Schlosser, F. and Poulos, H. G. (1977) "Stress-Deformation and Strength Characteristics", *Proceedings of the 9th International Conference on Soil Mechanics and Foundation Engineering*, Tokyo, 2, 421-494.
- Lehane, B.M.; Jardine, R.J.; Bond, A.J. and Frank, R. (1993) "Mechanisms of Shaft Friction in Sand from Instrumented Pile Tests", *ASCE Journal of Geotechnical Engineering*, 119(1), 19-35.
- Marachi, N.D.; Duncan, J.M.; Chan, C.K. and Seed, H.B. (1981) "Plane-Strain Testing of Sand", *Laboratory Shear Strength of Soil*, *ASTM STP 740*, R.N. Young and F. C. Townsend, Eds. , American Society for Testing and Materials. 294-302.
- Milligan, G.W.E.; Earl, R.F. and Bush, D.I. (1990) "Observations of Photo-Elastic Pullout Tests on Geotextiles and Geogrids", *Fourth Int. Conf. on Geotextiles, Geomembranes and Related Products*, Rotterdam, 2, 747-751.
- Palmeira, E.M. (1987), *The Study of Soil-Reinforcement Interaction by means of Large Scale Laboratory Tests*, Ph.D. Thesis, University of Oxford.
- Palmeira, E.M., and Milligan, G.W.E. (1989) "Scale and Other Factors Affecting the Results of Pullout Tests of Grids Buried in Sand", *Géotechnique*, 39(3), 511-524.

- Plumelle, C. (1987) "Experimentation en Vraie Grandeur d'une Paroi Clouée", *Revue Française de Géotechnique*, 3, 45-50.
- Rowe, P.W. (1969) "The Relation Between the Shear Strength of Sands in Triaxial Compression, Plane Strain and Direct Shear", *Géotechnique*, 19(1), 75-86.
- Rowe, R.K.; Ho, S.K. and Fisher, D.G. (1985) "Determination of Soil-Geotextile Interface Strength Properties", *Proceedings of the Second Canadian Symposium on Geotextiles and Geomembranes*, Edmonton, Canada, 25-34.
- Schellekens, J.C.J. and DeBorst, R. (1993) "On the Numerical Integration of Interface Elements", *International Journal for Numerical Methods in Engineering*, 36, 43-66.
- Schlosser, F. and Elias, V. (1978), "Friction in Reinforced Earth", *Proceedings of the ASCE Symposium on Earth Reinforcement*, Pittsburgh, PA, 735-762.
- Schlosser, F., and Guilloux, A. (1979), "Friction Between Soil and Strips in Reinforced Earth Structures," *Proceedings of the 1st International Conference on Soil Reinforcement*, Paris, 151-156.
- Schlosser, F. and DeBuhan, P. (1990) "Theory and Design Related to the Performance of Reinforced Soil Structures", *Performance of Reinforced Soil Structures*, State-of-the-Art Report, British Geotechnical Society, 1-14.
- Shen, C.K.; Mitchell, J.K.; deNatale, J.S. and Romstad, K.M. (1979) "Laboratory Testing and Model Studies of Friction in Reinforced Earth", *Proc. International Conference on Soil Reinforcement*, Paris, 1, 169-174.
- Wernick, E. (1977) "Stresses and Strains on the Surface of Anchors", *Revue Française de Géotechnique*, 3, 113-119.

Appendix 5.C: Notation

The following symbols are used in Chapter 5:

a	= inclusion ratio (f/m)
C_1, C_2	= constants in equations 5.8
C_1^0, C_2^0	= integration constants defined by eqn. 5.9 for no debonding
C_1^I, C_2^I	= integration constants defined by eqn. 5.11 for one-way debonding
C_1^{II}, C_2^{II}	= integration constants defined by 5.19 for two-way debonding
E_f	= Young's modulus for reinforcement
f	= inclusion thickness
G_m	= soil matrix shear modulus
K	= maximum axial stress carried by long inclusions ($= K_2\sigma/K_1$)
K_0	= coefficient of earth pressure at rest
K_1	= shear lag parameter (eqn. 5.5a)
$K_2\sigma$	= expression defined by eqns. 5.4a and 5.5b, c
L	= inclusion length
\tilde{L}	= characteristic anchor length (Fig. 5.5)
L_s	= slip length = $L - (x_{d2} - x_{d1})$
m	= soil matrix height
\tilde{R}	= pseudo-stress ratio in soil matrix
\tilde{R}_{max}	= maximum pseudo-stress ratio in soil matrix
x	= distance along inclusion from active end
x_{d1}, x_{d2}	= debonded length at active, passive ends of inclusion
x_{d1}^{II}	= slipped length at active end when $\sigma_p = \sigma_p^{II}$
y	= distance along soil matrix
α, β	= parameters defined by eqns. 5.10b, c

δ	=	interface friction angle
δ_{\max}	=	maximum interface friction angle for first yield
δ_{mob}	=	mobilized interface friction angle
Δu_x^f	=	inclusion elongation (eqn. 5.26)
$\Delta u_x^f \text{ res}$	=	residual inclusion elongation from non- K_0 condition (eqn. A.1)
$\Delta \sigma_{yy}^i / \sigma_1$	=	amplification factor
ϕ	=	true friction in soil matrix
ϕ_{mob}	=	mobilized friction in soil matrix
$\tilde{\phi}$	=	pseudo-mobilized friction in soil matrix
$\tilde{\phi}_{\max}$	=	maximum pseudo-mobilized friction in soil matrix
μ	=	interface friction coefficient
μ_{\max}	=	maximum interface friction coefficient for first yield
ν_f	=	inclusion Poisson's ratio
ν_m	=	soil matrix Poisson's ratio
σ_1, σ_3	=	major and minor external principal stresses
$\tilde{\sigma}_1^m, \tilde{\sigma}_3^m$	=	pseudo-major and minor principal stresses in soil matrix
σ_L	=	limit stress $2\mu L \sigma_1 / f$ (based on limit equilibrium assumptions)
σ_p	=	pullout stress
σ_p^I	=	first yield initiation of sliding at active end ($x=0$)
σ_p^{II}	=	upper/second yield initiation of sliding at passive end ($x=L$)
σ_{pp}	=	peak pullout stress
σ_{pr}	=	residual pullout stress
σ_{t1}, σ_{t2}	=	transition stresses bonded-debonded region at active, passive ends
σ_{xx}^f	=	axial stress along fiber
$\sigma_{xy}^i, \sigma_{yy}^i$	=	interface shear and normal tractions
$\bar{\sigma}_{xx}^m$	=	average horizontal stress in soil matrix
$\sigma_{xx}^m, \sigma_{xy}^m, \sigma_{yy}^m$	=	soil matrix axial, shear and normal stresses

$\sigma_{xx}^f, \sigma_{xy}^i, \sigma_{yy}^i =$ axial, shear and normal stresses at interface in the active slipping zone

$\sigma_{xx}^f, \sigma_{xy}^i, \sigma_{yy}^i =$ axial, shear and normal stresses at interface in the passive slipping zone

Chapter 6 : Pullout Tests of Planar Inclusions in the APSR Cell

6.1. Introduction

The previous chapter has proposed a new analysis for describing pullout tests on planar soil reinforcements. The formulation uses shear-lag approximations, previously applied for studying soil-reinforcement interactions in plane strain shear tests (Chapters 2 and 4), in order to develop analytical solutions for the tensile stresses and interface tractions as functions of the pullout and consolidation stresses, test geometry, elastic material properties and interface friction. The proposed analysis clarifies the underlying mechanisms of pullout for extensible reinforcements and shows a number of characteristic features not previously identified in the literature, including: a) local stress concentrations at the sliding front, which affect the distribution of tensile stresses; b) peak pullout resistance, which can be significantly larger than the bond capacity computed by limit equilibrium; and c) post-peak 'snap-through' in the load-elongation response, associated with the coalescence of sliding fronts progressing from the active and passive ends of the inclusion.

In principle, the proposed pullout analysis can be evaluated using either numerical analysis (based on non-linear finite element methods) or experimental measurements with instrumented inclusions. In practice, there are significant difficulties in achieving reliable numerical analyses of pullout using non-linear, frictional interface elements (e.g. Griffiths, 1985; Gens et al., 1988; Schellekens and DeBorst, 1993), while experimental data are often affected by the boundary conditions used in the tests (e.g. Fig. 5.1). A detailed literature survey revealed that there are very few pullout tests performed with instrumented inclusions. Most authors report only the pullout load-deformation response at the active end

of the inclusion. Tell-tale measurements at the passive end are reported by Johnston and Romstad (1989). Although Guilloux et al. (1979) did report tensile stress distributions for instrumented steel strips, most of the recent experimental studies of pullout have focused on grid or non-linear geosynthetic reinforcements (e.g. Palmeira and Milligan, 1989).

This chapter describes the results of a short program of pullout experiments for instrumented planar reinforcements which are used to evaluate the proposed shear-lag analysis. The experiments were performed in the APSR cell using steel and nylon 6/6 sheet reinforcements embedded in dense Ticino sand. The selected reinforcing materials both exhibit a linear, elastic stress-strain response and low interface friction; nylon 6/6 has an axial stiffness which is approximately two orders of magnitude lower than that of steel. The chapter gives full details of the test procedures, results and comparisons with the shear-lag analysis.

6.2. Experimental Program

Table 6.1 presents a summary of the pullout experiments performed in the APSR cell, which comprise one multi-stage (4 stage) test using steel sheet reinforcement, and four separate tests on nylon 6/6 inclusions.

The tests on the steel sheet reinforcement (APSR 50-1 to 50-4), were performed in multiple stages: 1) the sand was initially consolidated to the prescribed stress (σ_1, σ_3); 2) pullout loads were applied at a constant displacement rate until a stable, limiting pullout resistance was achieved; 3) the inclusion was then unloaded, the sand was reconsolidated to a higher confining stress at which a further pullout test was performed. The first three stages (APSR 50-1, 50-2 and 50-3) were performed using a consolidation stress ratio $\sigma_3/\sigma_1=1/2.33=1/R$, which is approximately equal to the K_0 -stress ratio for the soil (Baldi et al., 1985) and were used to evaluate the effect of confining stress on the pullout behavior. In the fourth stage of the test (APSR 50-4), residual tensile stresses were induced in the

inclusion using a consolidation stress ratio $R=\sigma_1/\sigma_3=4$. Premature failure in this test occurred due to slippage at the grips.

The four tests on nylon 6/6 sheet were performed at a low confining pressure¹ $\sigma_3=10.5$ kPa ($R=2.33$) in order to ensure that the stress levels during pullout did not exceed the linear range of the stress-strain response. Tests APSR 57 and 59 were conducted at a lower displacement rate in order to evaluate the post-peak pullout response of the nylon 6/6 sheet.

6.3. Test Procedure

The APSR cell (Larson, 1992; Whittle et al., 1992; 1993) was originally designed to measure the tensile stresses which develop in a planar inclusion as the surrounding soil is sheared in plane strain compression. Figure 6.1 compares the boundary conditions used in the 'standard' APSR tests with the pullout procedures. In the 'standard' APSR test, the soil specimen is sheared by increasing the major principal stress σ_1 at a fixed confining pressure σ_3 , while the tensile forces (F , Fig. 6.1) are applied to ensure that there is no displacement of the inclusion relative to the rear wall of the cell at the reference point, X . The rear wall of the cell (and plane strain surfaces) are lubricated to minimize friction. In this mode of operation, the force F corresponds to the tensile stress at the center of a planar inclusion of equivalent length $2L$ (Fig. 6.1). Chapter 3 compares results from standard APSR tests with steel sheet reinforcements and shear-lag analyses developed in Chapter 2. The APSR cell is fully automated and, hence, it is possible to simulate a wide variety of test conditions using the same apparatus. In the simulation of pullout tests, the soil specimen is

¹In tests APSR 51, 53 and 57, the specimens were preloaded to a confining pressure $\sigma_3=30$ kPa ($R=2.33$), in order to calibrate special strain gauges used to measure normal stress. These gauges did not perform to an acceptable standard, and are not reported further in this chapter.

consolidated with prescribed stresses σ_1 , σ_3 . The inclusion is then pulled out from the soil matrix at a fixed displacement rate, $\dot{u}_x(0)$, with a corresponding measured pullout stress σ_p . This displacement control ensures that the post-peak response can be measured reliably. The rear wall of the cell is lubricated and, hence, approximates a smooth interface (i.e., zero shear traction). Larson (1992) shows that the interface shear resistance is very low and is controlled by the cohesive strength of the silicon grease. Similar boundary conditions are recommended by Palmeira and Milligan (1989), but are rarely achieved in practical pullout tests.

The following paragraphs describe the procedures for performing pullout tests in the APSR cell including: 1) preparation of instrumented inclusions; 2) APSR cell and specimen preparation; and 3) consolidation and pullout.

6.3.1. Preparation of Instrumented Inclusions

The inclusions were made from a 15.2 cm wide roll of 0.127 mm thick steel shim stock, and a 15.2 cm wide roll of 0.254 mm thick nylon 6/6 sheet. In each case, the inclusions comprise two sheets of the material bonded together using a flexible adhesive, with four BLH SR-4 bonded resistance strain gauges (gauge number FAE-50-35 S13 EL, each 12.7mm long, or FAE-25-35 S13 EL, 6.35 mm long) with a nominal resistance of 350 Ω , spaced as shown in Figure 6.2. The gauges are manufactured with an average “Gauge Factor” (GF), expressing the change in resistance of the gauge for a given amount of strain. The gauges used in this research have $GF \approx 2.0$. A wheatstone bridge circuit is used to provide a sensitive voltage response to the small changes in resistance across a strain gauge. The strain gauges are mounted on the inside face of one of the sheets, such that the gauges and electrical leads are protected from abrasion by the surrounding sand. Any curvatures of the nylon 6/6 or steel sheet rolls are counteracted by bonding the sheets back-to-back in order to produce a flat inclusion.

Figure 6.2 shows the geometry and instrumentation of the inclusions used in the pullout tests. The length of the sheet includes the embedment L plus 5.7 cm at each end to attach grips for the uniaxial tension test and an additional 2 cm corresponding to the clearance between the grips and the rear wall of the APSR cell. After the uniaxial tension test, the dummy end of each inclusion (Fig. 6.2) is trimmed and the inclusions are cut to a width of 13.3 cm. The APSR cell is 15.2 cm wide so that the inclusion has a clearance of approximately 1 cm to the sidewalls which prevents the sharp edge of the steel from damaging the specimen membrane.

The preparation of the instrumented inclusion includes the following steps:

1. The inside surface of one of the sheets is cleaned with cloth and acetone to remove rust or surface contamination. Two perpendicular lines are drawn to mark the centerpoint where the gauge will be mounted. The gauges are attached to the surface with BLH EPY-150 strain gauge epoxy. The epoxy layer is as thin as possible to minimize its effect on the strains transmitted to the gauge.
2. Each gauge has two short wires for connection to a voltage source. For the steel inclusions, a piece of insulating tape is placed under the strain gauge leads to prevent them from short-circuiting against the steel surface. Two insulated wires (30 gauge) are soldered to the strain gauge and run along the length of the reinforcement to an amphenol connector (Fig. 6.2). When the connections are completed, the exposed leads are covered with insulating tape. The wires must be placed carefully near the end of the inclusion so they are not damaged when drilling holes for the grips.
3. After the gauges and connecting wires are in place and the epoxy has thoroughly cured, the two sheets are bonded together with 3M Rubber and Vinyl Adhesive. The hole pattern for the grips is then drilled with a 3/8" drill bit.

In-isolation uniaxial tensile tests are performed on each inclusion in order to: a) ensure that all strain gauges respond accurately to an applied load; and b) determine the actual elastic modulus for the inclusion. Figure 6.3 shows the experimental arrangement by which the inclusion is attached to the Instron tensile test machine via a pair of custom built chucks. The ends of the inclusion are bolted to a set of grips through 1.5 mm thick rubber pads.

6.3.1.1. Steel Sheet

Larson (1992) has presented detailed measurements of the gauge strain as a function of applied stress for uniaxial tensile tests on steel sheet reinforcements. The displacement rate used in these tests ($\dot{x}=0.042$ mm/s) is similar to that used in the APSR cell (Table 6.1). The elastic moduli computed from these data are generally not identical for each of the strain gauges and range from $E_f=180$ to 260 GPa (compared with the reference property, $E_f=207$ GPa). This variability is due to factors such as the non-uniform curvature over the inclusion length, small misalignments of the gauges, variations in gauge factor and steel thickness. Overall, the in-isolation tests on the steel sheet yielded an average elastic modulus $E_f=209$ GPa, within 1% of the reference modulus. Data from the pullout tests are interpreted using the gauge factors and this average modulus value.

6.3.1.2. Nylon 6/6 Sheet

Uniaxial tension tests on the instrumented nylon 6/6 inclusions were carried out at three different displacement rates, $\dot{x}=0.00042$, 0.0042 and 0.042 mm/s, in order to evaluate possible time dependency in the material response. The stress-strain response of nylon 6/6 was not affected by this range of displacement rates.

Figure 6.4 presents typical results from three loading cycles of uniaxial tension tests performed on nylon 6/6, for a loading velocity of 0.042mm/s. Figure 6.4a shows the external stress-external axial strain response; the stress is computed by dividing the applied

load by the cross-sectional area of the inclusion, and the external strain by dividing the inclusion elongation (as measured by an external LVDT) by the inclusion initial length. A linear regression analysis of the initial loading curve for the range of axial stresses expected in the pullout tests ($\sigma_p=0$ to 20 MPa) yields $E_f=1.92$ GPa.

Figure 6.4b shows a typical plot of the external stress (applied external load) as a function of the local axial strain around one of the gauges, as measured from the gauge output (using the strain gauge factor GF). The gauges reinforce the inclusion locally (they are stiffer than the nylon inclusion), so that the strains around it are approximately 1.9 times smaller than the global inclusion strain, as measured by the external LVDT (Fig. 6.4c). Figure 6.4b yields the local axial stress in the inclusion during the pullout test, given the local gauge response.

6.3.2. APSR Cell and Specimen Preparation

Soil specimens in the APSR cell are contained within a thin rubber membrane made from 0.38 mm thick material rubber (sold under the trade name 'dental dam'). The membrane is cut to fit the dimensions of the cell with a minimum number of seams which are sealed using a latex contact adhesive. The assembled membrane is then checked for leaks by filling with water. The reinforcing inclusion is attached to the membrane via a rubber collar seal, as shown in Figure 6.5. A thin bead of RTV (silicon rubber adhesive) is used to seal the connection between the reinforcement and collar (Fig. 6.5c).

Figure 6.6 illustrates the installation of the membrane inside the APSR cell. Initially the interior surfaces of the cell are cleaned and coated with a thin layer of grease (50-50 mixture of Dow-Corning high vacuum grease and Compound 7). The membrane is laid inside the cell with the inclusion passing through the entry slot (position X in Fig. 6.1). The membrane is then fitted around the specimen mold (Fig. 6.6 b, c). The vacuum tube is attached by piercing a small hole through the membrane collar.

The sand specimen is formed by dry pluviation in the plane normal to the consolidation stresses and pullout loads (σ_1 , σ_3 and σ_p). The raining apparatus (section 3.2.6 and Figure 3.5) produces a uniform specimen of dense Ticino sand ($D_r=79\pm3\%$). Specimen preparation is completed by removing the excess sand to produce a smooth flat surface. The top surface of the membrane is sealed with rubber latex (and RTV to eliminate leaks) and is placed under a vacuum ($\sigma_3\cong 90\text{kPa}$), while the mold is removed and the top cover is bolted in position.

6.3.3. Consolidation and Pullout Test Procedures

Once the top plate of the APSR is bolted in place, the specimen is confined under air pressure (σ_3) and the vacuum is gradually released. The load platens for the major principal stress are brought into contact with the ends of the sand specimen (using displacement or stress control procedures described by Larson, 1992), and the specimen is consolidated to a prescribed stress state.

The inclusion is prepared for the pullout test by connecting the active end via a grip assembly to the external arch piston (Fig. 6.7). The inclusion is then disconnected from the sample membrane in order to avoid pulling it through the entry slot. This is accomplished by cutting the membrane around the inclusion at the entry slot with a pair of scissors, and applying high vacuum grease around the cut surface to prevent sand particles escaping from the cell.

Pullout loads are applied at a controlled displacement rate (Table 6.1) by pumping water into the arch jack (Fig. 6.7) and monitoring the movement of the inclusion via a LVDT connected to the clamping mechanism. In test APSR 59 the LVDT is connected directly to the inclusion at the exit slot. The pullout force is measured directly by the load cell throughout this process. The pullout force, displacement at the active end of the

inclusion and local strain gauge measurements are all recorded by the MIT geotechnical laboratories central data acquisition control unit (HP3497A).

6.4. Results

6.4.1. Steel Sheet Inclusion

Figure 6.8 summarizes the load-displacement (F_p vs. u_p) measurements obtained in the four pullout tests (APSR 50-1, 2, 3 and 4), performed on a steel sheet inclusion of length $L=36$ cm. Displacements at the active end of the inclusion, u_p , are actually measured at a reference point on the clamping mechanism by the LVDT shown in Figure 6.7. The peak pullout resistance is well defined in the first three tests (APSR 50-1, 50-2, 50-3), while premature failure in 50-4 occurred due to slippage at the grips. The results show the following:

1. Displacements at the active end of the inclusion were not monitored continuously through the successive loading and unloading stages of APSR test 50. Thus, the results in Figure 6.8 show relative displacements in a series of successive pullout tests. The offset pullout force at zero displacement corresponds to the seating load ($F_p \approx 0.4$ kN) which is applied at the start of test APSR 50-1 (i.e., when the load cell is first connected to the inclusion).
2. The maximum pullout force in tests 50-2 and 50-3 occurs at a displacement $u_p=3.5-4.0$ mm, but there is no apparent post-peak reduction in resistance for continued loading up to $u_p=5.5-6.0$ mm. The displacement at peak load in test 50-1 is somewhat smaller ($u_p=2.3-3.0$ mm), but also shows no post-peak softening. The peak resistance measurements in the three complete pullout tests give highly consistent estimates of the apparent interface friction, $\mu=0.4$ ($\delta=22^\circ$). This result is in close agreement with well documented direct shear box and simple shear measurements of interface friction for dry sand against smooth steel interfaces reported by Kishida and Uesugi (1987). Figure 6.9

shows values of μ for Fujigawa sand as a function of the relative roughness of the steel interface, $R_n = R_{\max 50}/D_{50}$, where $R_{\max 50}$ is the maximum roughness over a gauge length of surface D_{50} .

3. The load-deformation response in the first three pullout tests are replotted in a dimensionless format (σ_p/σ_1 vs. u_p/L) in Figure 6.10. This figure confirms that the maximum pullout resistance is proportional to the confining stress σ_1 , and shows the very close agreement in the pre-peak response for tests 50-2 and 50-3. Higher pre-peak stiffness is measured in 50-1, and may be due to factors such as initial misalignment of the inclusion.

Figures 6.11a, 6.12a, 6.13a and 6.14a show the development of tensile stresses within the inclusion interpreted from strain gauge measurements at 4 locations along the inclusion:

1. In test 50-1, the initial tensile stresses σ_{xx}^f/σ_1 , measured in gauges 3 and 4 may reflect residual stresses or bending of the inclusion during specimen preparation and consolidation. In contrast, there are minimal residual stresses measured by the gauges at the start of tests 50-2 and 50-3. Further consolidation of the sand under a shear stress ratio $R=4$ in test 50-4 is witnessed by strain gauge measurements of tensile stresses (with maximum residual stress at the center of the inclusion, $\sigma_{xx}^f/\sigma_1 \cong 70$).
2. Strain gauge measurements of the tensile stress distribution along the inclusion are generally less reliable (more erratic) during the initial stages of the pullout tests, particularly for $u_p \leq 0.5-1.0$ mm. One factor affecting the behavior may be the imprecision of strain gauge response at low stress levels.
3. Steel is among the least extensible of materials used to reinforce soils. Therefore, it is of interest to compare the measured load-transfer with that of an ideal rigid inclusion which is characterized by uniform shear resistance over the length of the inclusion. For this ideal case, $\sigma_{xy}^i = \text{constant}$ and, therefore, $d\sigma_{xx}^f/dx = \text{constant}$. Thus, the tensile stress is

distributed linearly along the inclusion. Figure 6.11b through 6.14b present the results of the apparent mobilized friction δ_i mobilized over sub-lengths of the inclusion $L_i=L-x_i$, where x_i is the location of strain gauge i from the active end of the inclusion:

$$\mu_i = \tan \delta_i = \frac{\sigma_{xx}^f(x_i)}{\sigma_1} \frac{f}{2 L_i} \quad (6.1)$$

For a rigid inclusion, μ_i should be constant for all sub lengths L_i ($i=1$ to 4 and external load cell). The measurements from APSR 50-1, 50-2 and 50-3 show variations of approximately 3° - 7° in μ_i during the early stages of the tests, but give almost unique response at the peak pullout loads (i.e., at $u_p=2.2, 4.1$ and 4.2 mm, respectively), in which $\mu_i=\mu=0.40$. The results in tests 50-1 are slightly more erratic than those in 50-2 and 50-3. The post-peak response of tests 50-2 and 50-3 consistently show $\mu_i=22^\circ$ - 25° , reflecting fluctuations in the individual gauge response. Overall, these results show that the shear resistance is most uniform along the inclusion at peak pullout load.

4. Figure 6.15 show further representations of the measured tensile stress distribution at four specific pullout load levels corresponding to $\sigma_p/\sigma_L=0.25, 0.5, 0.67$ and 1.0 (i.e., at factors of safety $FS=4.0, 2.0, 1.5$ and 1.0). There is excellent agreement in the load distribution for tests 50-1, 50-2 and 50-3 at each of these load levels, while differences in 50-4 (due to residual stresses) are only significant for $\sigma_p/\sigma_L \leq 0.5$. The inclusion elongation was not measured directly and can be estimated from these results by simple numerical integration:

$$\Delta u_x^f = \frac{1}{2E_f} \sum_{i=1}^5 [\sigma_{xx}^f(x_{i-1}) + \sigma_{xx}^f(x_i)] [L_{i-1} - L_i] \quad (6.2)$$

where $(i-1)=0$ and $i=5$ correspond to the passive and active ends of the inclusion, respectively. Figure 6.16 shows that the load-elongation behavior from the four tests are very consistent. The response is linear for normalized pullout stress ratio $\sigma_p/\sigma_1 < 900$, while non-linear behavior is only significant for $\sigma_p/\sigma_1 > 1000$.

6.4.2. Nylon 6/6 Sheet Inclusions

This section describes the results from 3 pullout tests on instrumented nylon 6/6 inclusions (APSR 51, 57 and 59) of length $L=0.42\text{m}$, embedded in dense Ticino sand. The data from APSR 53 are not considered reliable due to difficulties in sand pluviation (Table 6.1), and are not discussed further. Although the same consolidation stress conditions were applied in all of these tests, different displacement rates were used during pullout ($\dot{u}=0.058, 0.035$ and 0.0035 mm/s were used in successive tests). Figure 6.17a summarizes the load-displacement response from tests 57 and 59 (there were no load cell data obtained in test APSR 51):

1. Large differences in the initial load-deformation response in APSR 57 and 59 are due to changes in the referencing system used to measure the displacement u_p . In tests 51, (53) and 57, the displacements are monitored by an LVDT at a point located on the clamping mechanism, as shown in Figure 6.7 (also used for steel inclusions). Test 59 used a refined design (Fig. 6.7) in which the displacement is measured by and LVDT at the exit point from the APSR cell. This latter mechanism gives a much stiffer initial load-displacement response, and hence indicates the problems associated with system compliance in earlier measurements of u_p . It should be noted that one additional difference in test procedure was the K_0 -precompression of the sand in tests 51 and 57, which was used to calibrate special normal stress gauges. It is believed that these procedures do not affect the pullout data reported in this section.
2. The three tests give very consistent measurements of the maximum pullout force (Figs. 6.17a, b), $F_p=1.37\text{kN}$ (corresponding to an apparent interface friction $\mu=(\sigma_{pp}/\sigma_1)(f/2L)=0.5$ or $\delta=26^\circ$), while the displacement required to mobilize this resistance increases slightly as \dot{u} decreases ($u_p=2.3, 2.7$ and 4.5mm for tests 51, 57 and 59, respectively). There is a significant post-peak reduction in resistance which is

accompanied by oscillation in the pullout force with continued displacement. This 'stick-slip' behavior was observed in tests 57 and 59, but was absent from test APSR 51. This phenomenon is discussed in more detail below.

Figures 6.18, 6.19 and 6.20 give complete details of tensile stresses σ_{xx}^f/σ_1 in the three tests, estimated from local strain gauge measurements. The data show significant differences from the load-transfer response shown previously for the steel sheet inclusion. For example, there are no significant tensile loads measured by strain gauge 1 ($x/L=0.76$) for load levels $\sigma_p/\sigma_1 < 550$, or $u_p/L < 0.0037$ ($u_p < 2\text{mm}$). Non-linearities in the tensile stress distribution are shown most clearly by the apparent interface friction δ_i , in Figures 6.18b, 6.19b and 6.20b. At peak pullout load, there are large differences in the computed values of δ_i over different sub-lengths of the inclusion. In particular, the results show maximum values $\delta_i \cong 31^\circ$ (tests APSR 51, 59) occurring at the passive end and hence demonstrate important variations in the shear resistance along the inclusion.

Figure 6.20c examines the post-peak pullout response for APSR 59 in more detail for active end displacements $u_p/L = 0.030$ ($u_p = 13\text{ mm}$). Although the stresses oscillate in 'stick-slip', there is a well defined residual resistance (measured in all gauges) which is stable over relatively large displacements, $u_p/L = 0.012$ to 0.030 ($u_p = 5$ to 12 mm).

In test APSR 59, the load cell, displacement transducer and strain gauge signals were recorded on the data acquisition system at 3 seconds intervals. Figure 6.20d shows the complete data set recorded over a displacement range $u_p/L = 0.014$ to 0.017 ($u_p = 6.0$ to 7.0mm). The results show clearly the stick-slip phenomena in which the sudden reduction in load is associated with a jump in displacement rate (i.e., the actual displacement rate is unsteady). The actual velocity of slip is much higher than the active end displacement rate \dot{u} and can only be estimated using much higher speed data acquisition. Bouden and Tabor (1950) have explained the underlying mechanism for this behavior through differences between the static and kinetic friction, μ_s and μ_k , respectively. They describe a simplified

1-D analysis for the relative motion between two surfaces, one of which is displaced at a constant speed, while the other is supported by an elastic system such that its deflection during sliding is a measure of the frictional force. In this calculation, the maximum frictional force (e.g. point A in Figure 6.20d) is controlled by the static friction μ_s , while the minimum resistance immediately after slip (point C; Fig. 6.20d) is related to $(2\mu_k - \mu_s)$. Hence, the differential stress oscillation is a measure of the difference between the static and kinetic friction (i.e., $\Delta\mu = \mu_s - \mu_k$). Experiments performed on metallic surfaces (Bowden and Tabor, 1950) show that, with a given apparatus, the intermittent motion does not depend on the shape of the surfaces or on the load, i.e., $\Delta\mu$ remains approximately constant for a given combination of surface materials. However, $\Delta\mu$ generally decreases as the displacement rate increases and, hence, there is a critical value \dot{u}_c above which there is no apparent stick-slip motion. This latter observation is consistent with the three pullout tests on nylon 6/6. There was no stick-slip observed in APSR 51, where $\dot{u} = 0.058 \text{ mm/s}$, while the measurements in tests 57 and 59 imply a static-kinetic friction difference in the range $\Delta\mu \approx 0.03$ to 0.07 (i.e., $\Delta\delta \approx 2^\circ - 4^\circ$).

Figure 6.21 compares the tensile stress distribution measurements for the three pullout tests at four load levels, $\sigma_p/\sigma_{pp} = 0.25, 0.5, 0.67$ and 1.0 (i.e., FS=4, 2, 1.5 and 1.0, respectively). These results confirm the repeatability of experimental measurements and demonstrate the non-linearity in the tensile stress distribution throughout the load test. The elongation of the inclusion is estimated by numerical integration of the measured tensile stresses, assuming elastic material behavior, as shown in Figure 6.22. Although the initial load-elongation response is linear, non-linearities become significant for $\sigma_p/\sigma_1 \geq 200$ (i.e., for $\sigma_p/\sigma_{pp} \geq 0.3$). For steel sheet inclusions, non-linearities only develop at $\sigma_p/\sigma_{pp} > 0.8$. This representation also shows that post-peak reductions in pullout resistance are associated with reduced elongation of the inclusion, which corresponds to the 'snap-through' response described in Chapter 5.

Overall, the pullout measurements for instrumented nylon 6/6 inclusion are more difficult to interpret than those reported previously for steel sheet. Computed values of interface friction δ , at peak pullout load, range from 31° (based on local strain gauge data, Figs. 6.18b, 6.19b, 6.20b) to 26° (averaged over the inclusion length), while post-peak data give residual (kinetic) friction from 20° to 23° . These values are averages computed from all three tests (51, 57, 59). Stick-slip is interpreted by the methods of Bowden and Tabor (1950); extreme values of residual friction range from 18° to 24° .

There are no measurements of sand-nylon 6/6 interface friction reported in the literature. However, O'Rourke et al. (1990) have presented data from an extensive program of shear box interface tests between sand and a variety of smooth polymeric materials. Figure 6.23 summarizes measurements of δ' as a function of sand density for medium density polyethylene (MDPE) and four different types of sands. The authors report that the interface friction is a function of sand type (i.e., grain size and shape distribution, grain hardness, etc.), formation density and hardness of the polymer surface (characterized by the shore-D hardness number, ASTM D2240-85). The pullout tests in this chapter were performed in dense Ticino sand (with physical properties similar to both the Ottawa and fluvioglacial sands, Figs. 6.23a, b) at a dry density $\gamma_d=16 \text{ kN/m}^3$, while the nylon 6/6 has a shore-D hardness number of 80 to 85 (compared to 62 for MDPE). The measured data at the same dry density show $\delta=22^\circ\text{-}26^\circ$, which is comparable to the range interpreted from pullout tests.

6.5 Comparison with Analytical Predictions

This section compares the measured pullout response for the steel and nylon 6/6 sheet inclusions with the analytical predictions described in Chapter 5. Table 6.2 summarizes the input parameters for the proposed shear-lag analyses. Approximate elastic parameters for the dense Ticino sand ($G_m=6.0 \text{ MPa}$, $\nu_m=0.35$) were obtained from plane strain compression shear tests performed in the APSR cell at a confining pressure of

$\sigma_3=31\text{kPa}$, and described in section 3.4.1. In principle, the shear modulus of sand is a function of the confining stress and, hence, small variations in G_m are expected for pullout tests performed at different confining stress levels. In practice, small variations in E_f/G_m (within a factor of 2) have little impact on shear-lag predictions of pullout response, as shown in Figure 5.8a. Similarly, uncertainties in $\nu_m=0.33$ to 0.42 are also of secondary importance in pullout analyses. The elastic moduli E_f of the steel and nylon 6/6 were evaluated from in-isolation, uniaxial tension tests. The sand-steel interface friction angle $\delta=22^\circ$ is well defined from the pullout tests, and is much lower than the peak friction mobilized in shearing of the sand ($\phi_p\cong 53^\circ-55^\circ$). The interface friction angle for nylon 6/6 and sand cannot be interpreted unambiguously from the pullout tests. Estimates from the residual pullout resistance range from $\delta=20^\circ$ to 23° ($\mu=0.37$ to 0.42).

6.5.1. Steel Inclusions

Figure 6.24 compares the predicted and measured (dimensionless) load-elongation response for the four pullout tests on steel sheet inclusions. The measured peak pullout resistance is in good agreement with both the shear-lag prediction and the limit equilibrium calculation, as expected for a relatively inextensible inclusion ($E_f/G_m\cong 3.5\times 10^4$). The shear-lag analysis predicts a linear load-elongation response for $\sigma_p/\sigma_1\leq 900$, which is consistent with the measured behavior (especially for test 50-4, Figure 6.24b). However, there is a discrepancy between the predictions and measurements in the initial stages of the test due to the offset tensile load (at zero elongation) which is applied to compensate for the load system compliance (cf. section 6.4.1.).

Figure 6.25 compares the shear-lag predictions and measurements of the tensile stress distributions at four successive stages in each pullout test. There is very good agreement between predictions and measurements, with relatively small deviations from the linear load distribution expected for an inextensible inclusion.

6.5.2. Nylon 6/6 Inclusions

Figure 6.26 compares the measurements of pullout load-elongation response for nylon 6/6 inclusions with shear-lag predictions using three different values of the interface friction, $\delta=20^\circ$, 22° and 23° ($\mu=0.37$, 0.40 and 0.42 , respectively). The results for $\delta=22^\circ$ describe accurately the key elements of the measured pullout response: 1) the initial response is linear for $\sigma_p/\sigma_1 \leq 300$ to 400 ; 2) the peak pullout resistance occurs at $\sigma_p/\sigma_1=820$; and 3) there is a significant post-peak reduction in pullout resistance associated with 'snap-through'. Shear-lag predictions for $\delta=20^\circ$ and 23° provide lower and upper bounds to the measured peak pullout load, while limit equilibrium calculations (for the same interface friction angles) underestimate σ_p/σ_1 by 15 to 25%. Figure 6.26b shows further comparisons of load-elongation response for sub-length $L_4=0.36\text{m}$ (i.e., length from passive end to position of strain gauge 4 in Fig. 6.2) in three nylon 6/6 pullout tests (APSR 51, 57 and 59). The results show good agreement with shear-lag predictions using $\delta=20^\circ$ to 22° .

Detailed comparisons between predictions and measurements of the tensile stress distributions in each of the three pullout tests are shown in Figure 6.27. These results show that the shear-lag analysis gives remarkably accurate predictions of the highly non-linear stress distribution at successive stages of pullout tests on an extensible reinforcement (in this case $E_f/G_m=320$). It should be noted that the analysis slightly underestimates the tensile stresses measured in strain gauge 1 ($x/L=0.76$) for high values of σ_{xx}^f/σ_1 (>800).

The results in figure 6.27 provide the first truly insightful evaluation of the proposed shear-lag pullout analysis. Further aspects of the analysis, such as the stress concentration at the sliding front, require more comprehensive experimental measurements, which were beyond the scope of the current test program. One aspect of the tests which deserves further attention is the possibility of soil failure (hence, dilation) during the tests.

The results in Chapter 5 show that the shear-lag analysis can be used to provide a conservative (i.e., lowest possible values of δ necessary to cause soil failure at a given value of $\tilde{\phi}$) estimate of the mobilized friction $\tilde{\phi}$ (referred to as pseudo-friction) as a function of test geometry, interface friction and relative soil-inclusion stiffness. Figure 6.28 compares the interface friction for the steel and nylon 6/6 inclusions with the conditions for failure of dense Ticino sand (with $\tilde{\phi} = 55^\circ$). For the steel inclusion ($E_f/G_m \cong 3.5 \times 10^4$, $a=f/m=0.04\%$), sand failure will only occur for $\delta > 40^\circ - 42^\circ$ and, hence, the pullout tests described in this chapter are associated with interface failure. However, for the nylon 6/6 sheet ($E_f/G_m \cong 320$, $a=0.09\%$), soil failure is expected for $\delta > 23^\circ - 24^\circ$; therefore, the pullout tests in nylon may promote failure conditions in the soil.

6.6 Conclusions

This chapter has described results of pullout tests performed on instrumented steel and nylon 6/6 sheet inclusions. The primary goal of these tests was to evaluate the shear-lag pullout analyses described in Chapter 5. The selected inclusion materials have linear, elastic (and time independent) stress-strain properties, smooth surfaces with relatively low interface friction, and represent upper and lower limits of extensibility (relative soil-reinforcement stiffness) for practical soil reinforcements. The pullout experiments were performed in the APSR cell on inclusions of lengths $L=0.36$ and 0.42 m, embedded in dense Ticino sand whose properties have been described previously in Chapter 3. Tensile stresses within the inclusion were measured by strain gauges and were calibrated from uniaxial, tensile tests.

There were significant experimental difficulties in measuring accurately the initial load-displacement response for steel sheet inclusions. However, in all cases, the load distribution and load-elongation response are approximately linear, and the interface friction ($\delta=22^\circ$) can be well defined from repeatable measurements of the peak pullout load. There is good agreement between shear-lag analyses and the measured data for tests performed at

confining pressures ranging from $\sigma_3=30$ to 98 kPa, while residual tensile stresses (associated with soil shearing) had little effect on the predicted or measured pullout behavior.

Test data for nylon 6/6 inclusions showed much more non-linearity in both the load distribution and load-elongation response. The measurements show a pronounced post-peak reduction in pullout resistance, which is further complicated by stick-slip behavior for tests performed at low displacement rates. The shear-lag analyses describe accurately and consistently the measured data for an assumed interface friction angle $\delta=22^\circ$, which corresponds closely with residual conditions measured in the pullout tests. The analysis shows that the peak pullout load is controlled by the non-linear load distribution and is significantly higher (approximately 20%) than would be expected from a conventional limit equilibrium calculation. The proposed shear-lag analysis provides a consistent mechanical explanation for the measured post-peak 'snap-through' response of the nylon 6/6 inclusions.

The data in this chapter provide a very encouraging assessment of the proposed shear-lag pullout analysis. More comprehensive experimental measurements are now required to evaluate other aspects of the analytical predictions such as stress concentrations at the sliding front.

Test ¹	Inclusion			External Consolidation Stress State in Soil (kPa)				Displacement Rate (mm/s)	Stick-Slip	Notes
	Type	Length L (m)	Thickness f (mm)	σ_1	σ_3	R= σ_1/σ_3				
APSR50-1	steel	0.356	0.254	49.0	21.0	2.33	0.058	no	Test in 4 stages. Stages 1, 2, 3: Effect of confining stress σ_3 . Stage 4: Effect of residual stress. Premature failure at grips in stage 4.	
APSR50-2				73.5	31.5	2.33				
APSR50-3				98.0	42.0	2.33				
APSR50-4				168	42.0	4.0				
APSR51 ²	nylon 6/6	0.420	0.508				0.058	no	External loading readings not available.	
APSR53 ²				24.5	10.5	2.33				
APSR57 ²										
APSR59							0.0035	yes	Slower pullout speed for verification of stick-slip.	

Notes:

¹All tests were performed in dense Ticino sand ($D_r=79\%$).

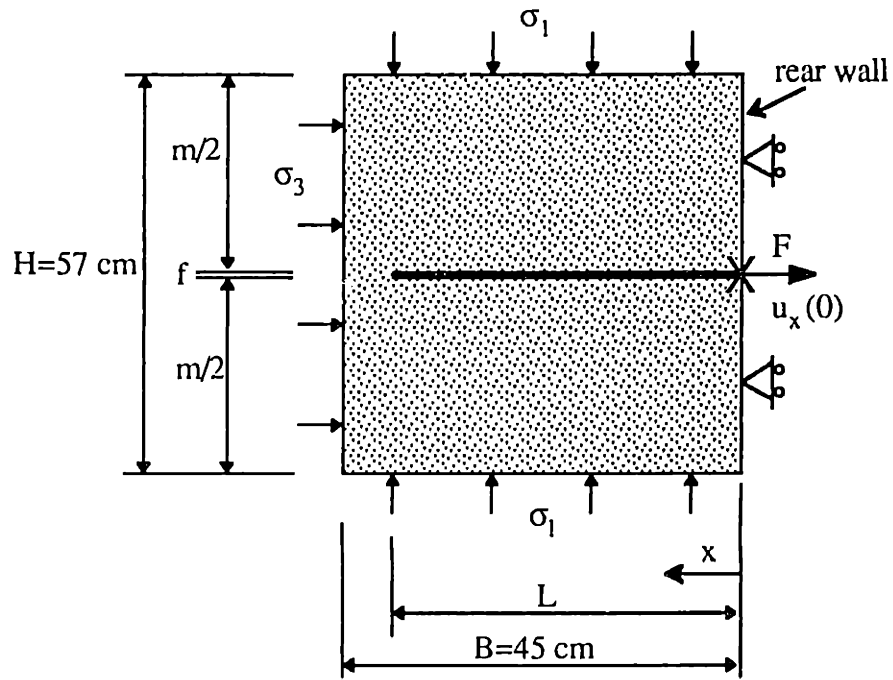
²Specimens were precompressed to a maximum stress $\sigma_3=30$ kPa (at $R=2.33$) in these tests.

Table 6.1: Pullout Tests Performed in the APSR cell.

Material	Modulus (kPa)	E_f/G_m	Poisson's Ratio	Lateral Dimension	Length L(m)	Interface Friction δ ($\mu=\tan\delta$)
Dense Ticino Sand	$G_m=6000$ (at $\sigma_3=30$ kPa)	-	$\nu_m=0.35$	$m=0.57m$	-	$\phi'_p=53^\circ-55^\circ$
Steel Sheet	$E_f=2.07 \times 10^8$	34500	$\nu_f=0.20$	$f=0.25mm$	0.36	22° (0.40)
Nylon 6/6 Sheet	$E_f=1.92 \times 10^6$	320	$\nu_f=0.20$	$f=0.51mm$	$0.42^{(1)}$	20° (0.37) to 23° (0.42)

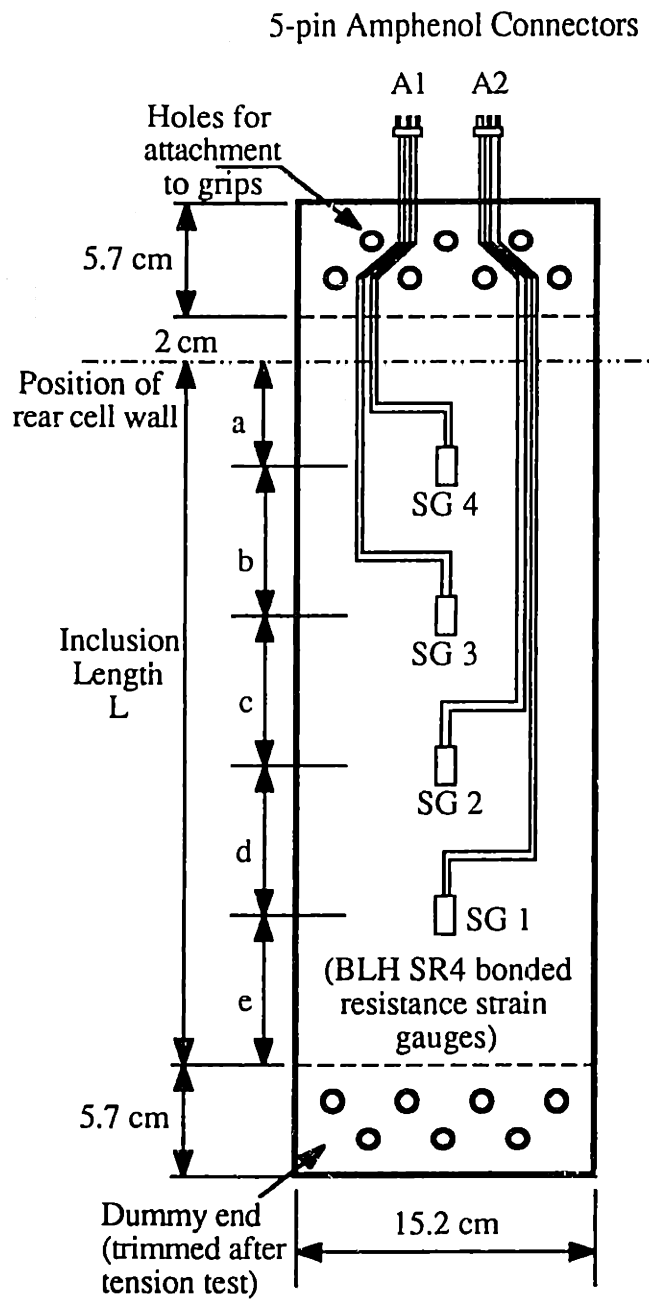
¹For test APSR 51, effective inclusion length, $L=0.36m$.

Table 6.2: Input Parameters for Shear-Lag Analysis of Pullout Tests in the APSR cell.



Test	Boundary Condition		Measured Response at X
	In soil	At X	
Standard APSR Test	$\sigma_3 = \text{constant}$ $\sigma_1 = \text{increases}$ $R = \text{increases}$	$u_x = 0$ No displacement at X	$\sigma_{xx}^f = F/A$ Centerline load
Pullout Test in APSR	$\sigma_1, \sigma_3 = \text{constant}$ $(\sigma_1/\sigma_3 = R)$	$u_x(0), \dot{u}_x(0)$ Applied displacement rate	$\sigma_p = F/A$ vs. $u_x(0)$ Pullout response

Figure 6.1: Comparison of Boundary Conditions used in the APSR Cell.



Dimensions (cm)

	a	b	c	d	e	L
Steel	5.6	7.6	7.6	7.6	7.6	36.0
Nylon	6.4	7.6	7.6	10.2	10.2	42.0

Figure 6.2: Schematic of the Instrumented Inclusion for Pullout Tests.

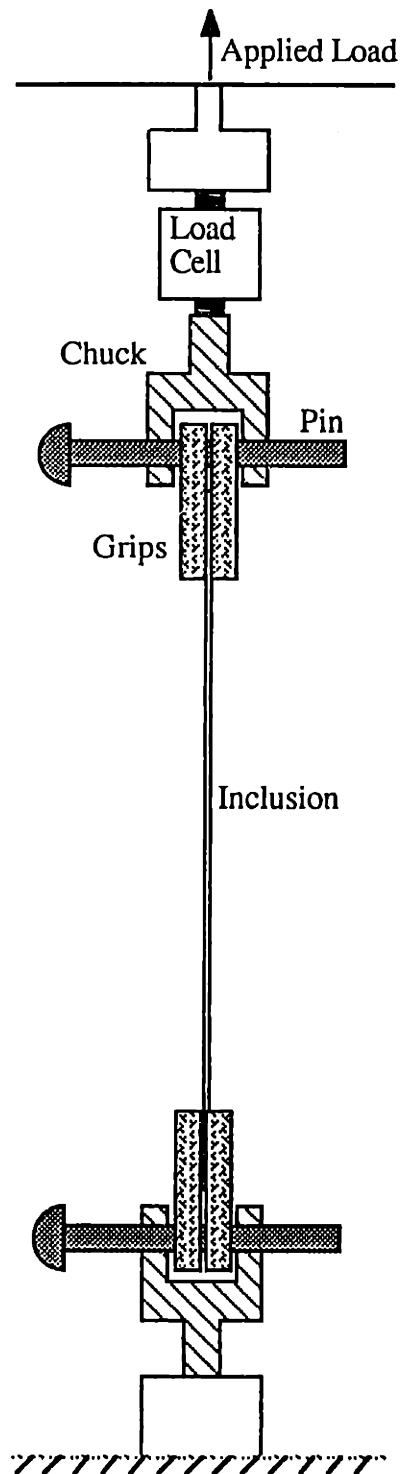


Figure 6.3: In-isolation Test Setup in Instron Machine.

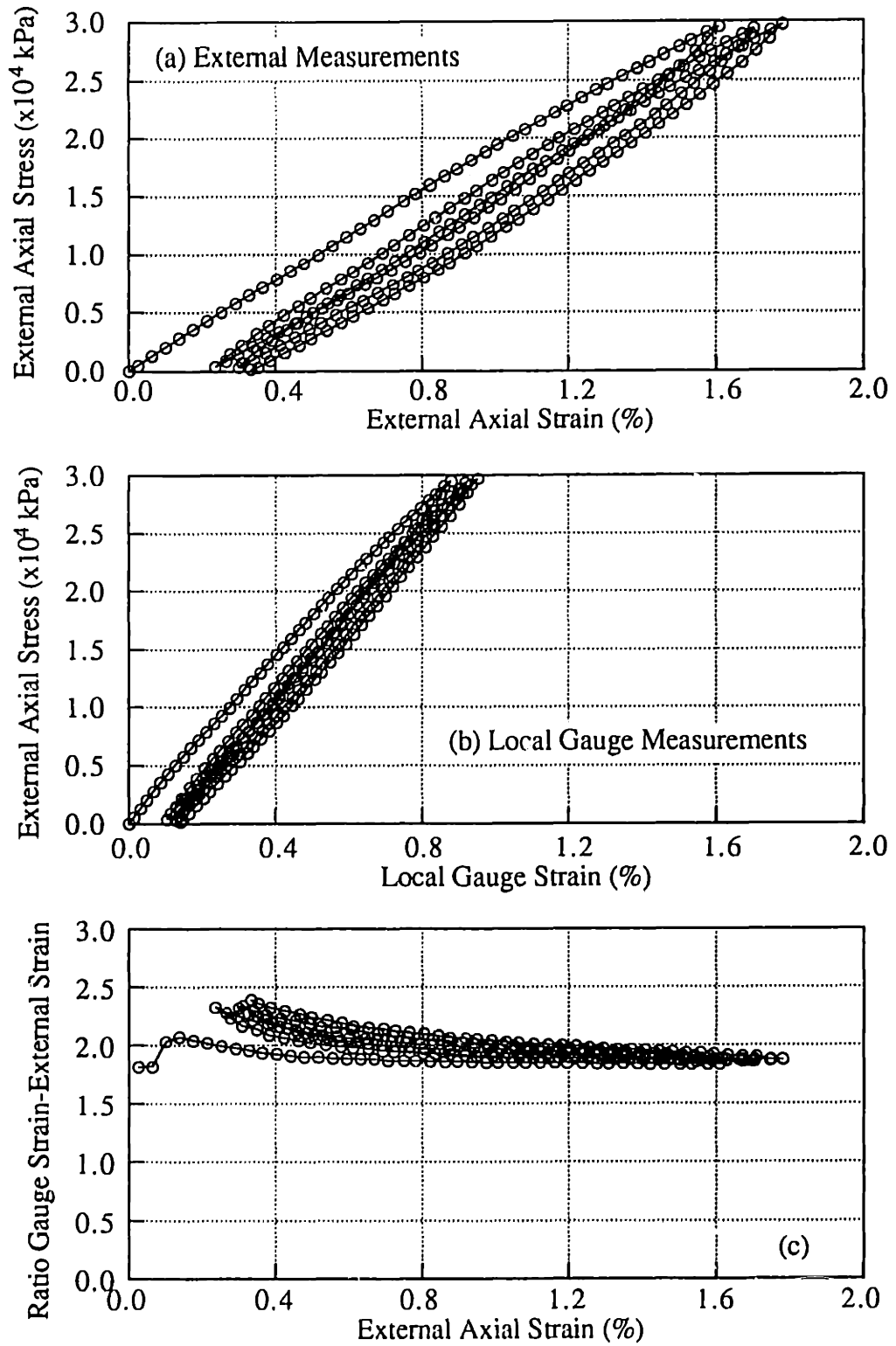
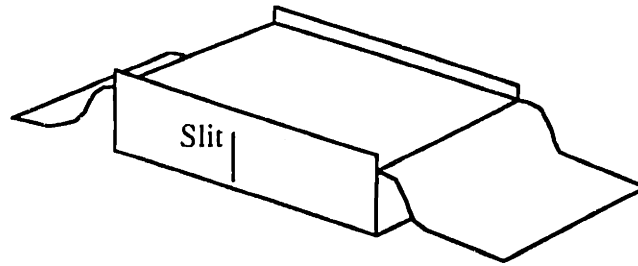
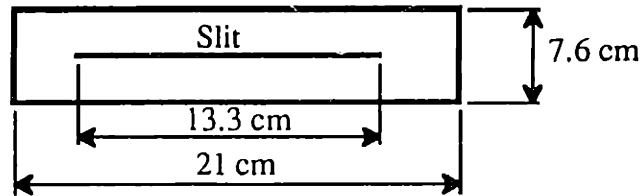


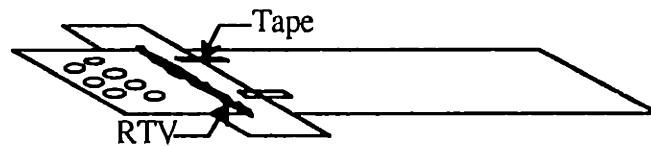
Figure 6.4: Typical Stress-Strain Results for In-Isolation Tension Tests on Nylon 6/6.



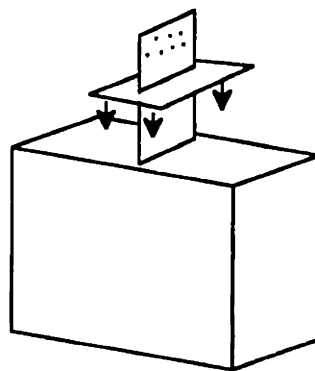
(a) Make a slit in the specimen membrane



(b) Cut a rubber collar from 0.25 mm thick dental dam



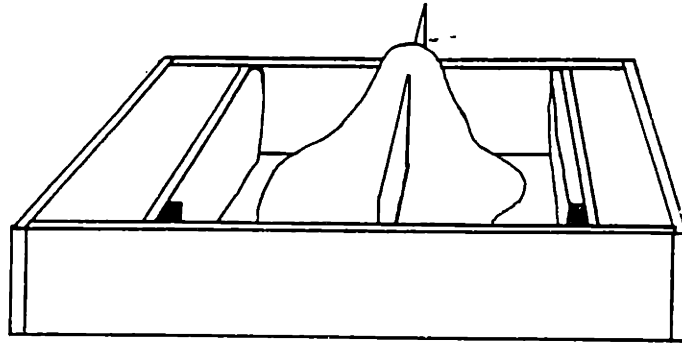
(c) Seal rubber collar to inclusion with RTV (repeat on reverse side)



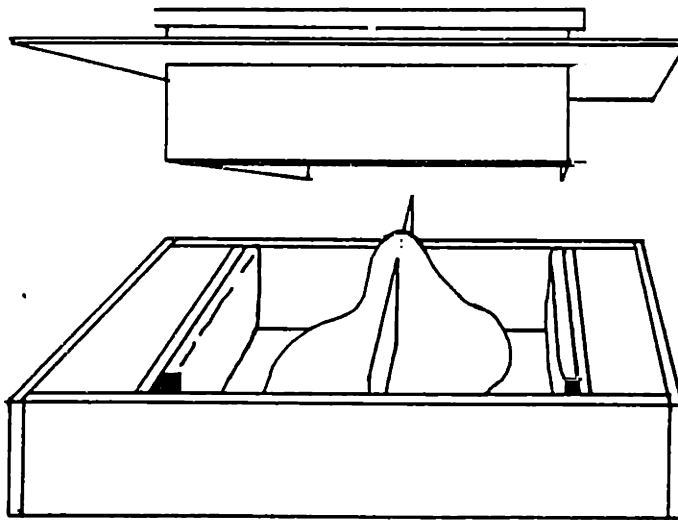
(d) Apply latex adhesive to collar and specimen membrane, and bond the two together

Figure 6.5: Specimen Membrane Preparation.

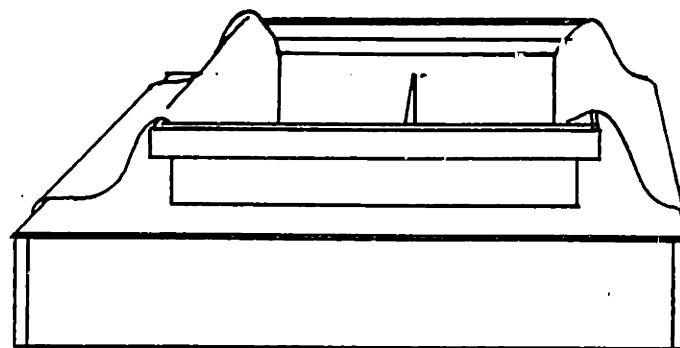
(after Larson, 1992)



(a) Membrane and inclusion inside cell



(b) Insertion of specimen mold



(c) Specimen membrane in place

Figure 6.6: APSR Specimen Membrane Installation (after Larson, 1992).

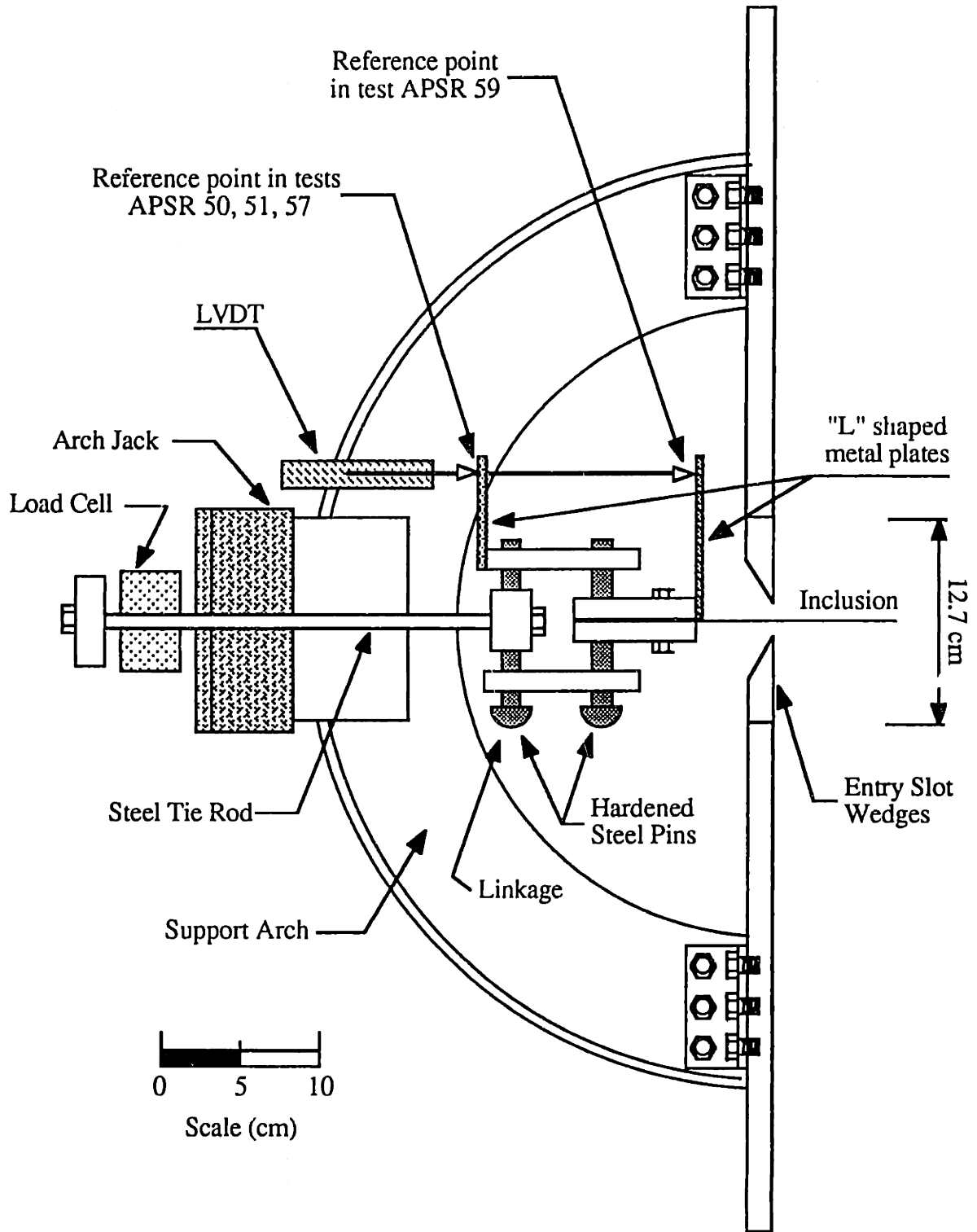
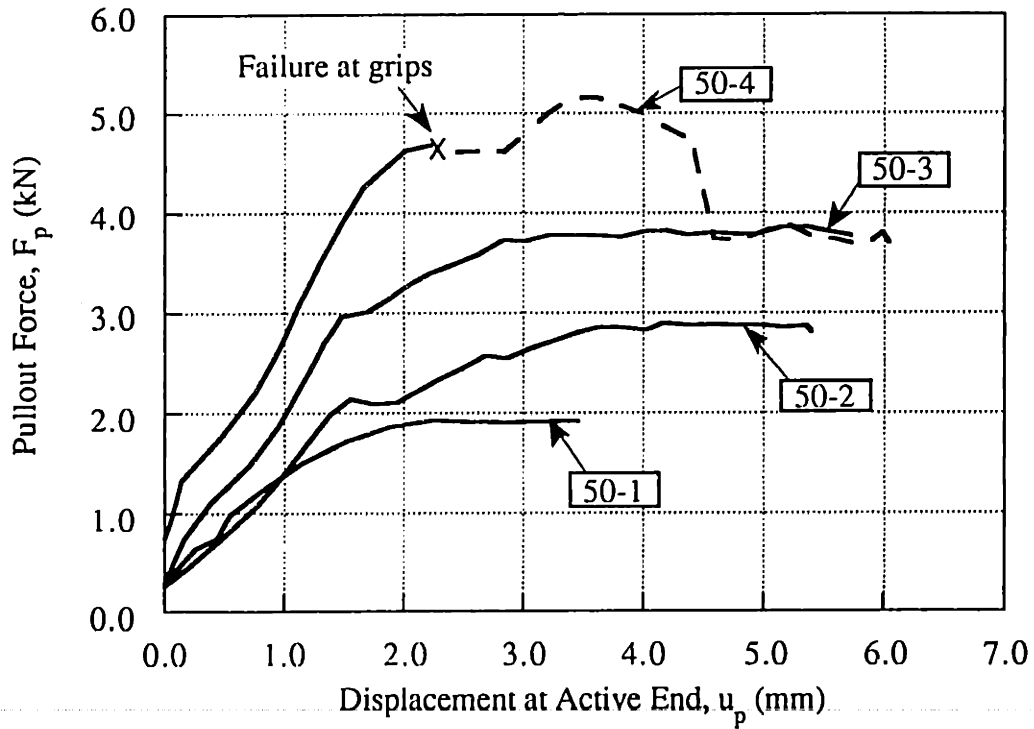


Figure 6.7: Inclusion Assembly to External Arch Piston and Monitoring Mechanism of Active End in Pullout Tests.



Steel Sheet Reinforcement		
L (cm)	f (mm)	B(mm)
36.0	0.254	133

Test	Consolidation Stresses			At Peak Pullout			
	σ_1 (kPa)	σ_3 (kPa)	$R=\sigma_1/\sigma_3$	F_p (kN) ⁽¹⁾	u_p (mm)	σ_L/σ_1 ⁽²⁾	δ ⁽³⁾
50-1	49.0	21.0	2.33	1.93	2.5-3.0	1160	22°
50-2	73.5	31.5	2.33	2.85	3.0-4.0	1150	22°
50-3	98.0	42.0	2.33	3.78	3.5-4.0	1140	22°
50-4	168.0	42.0	4	-(4)	-	-	-

- Notes: ¹ Pullout stress, $\sigma_p=F_p/Bf$
² Limit Load, $\sigma_L=(\sigma_p)_{max}$
³ From limit equilibrium, $\tan\delta=\mu=(f/2L)(\sigma_L/\sigma_1)$
⁴ Failure at grips

Figure 6.8: Measured Pullout Load-Displacement Response for Steel Sheet Reinforcements.

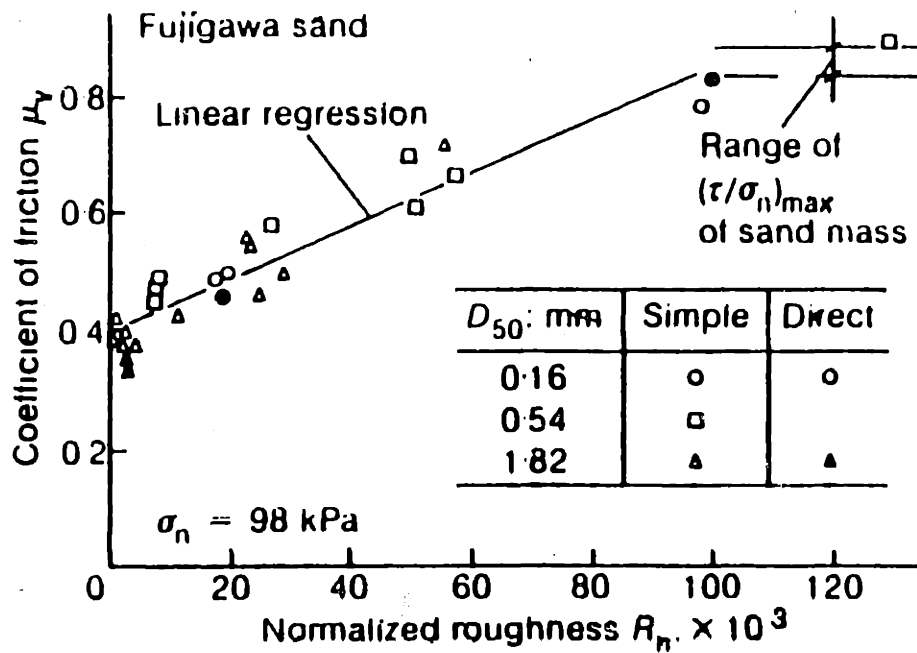
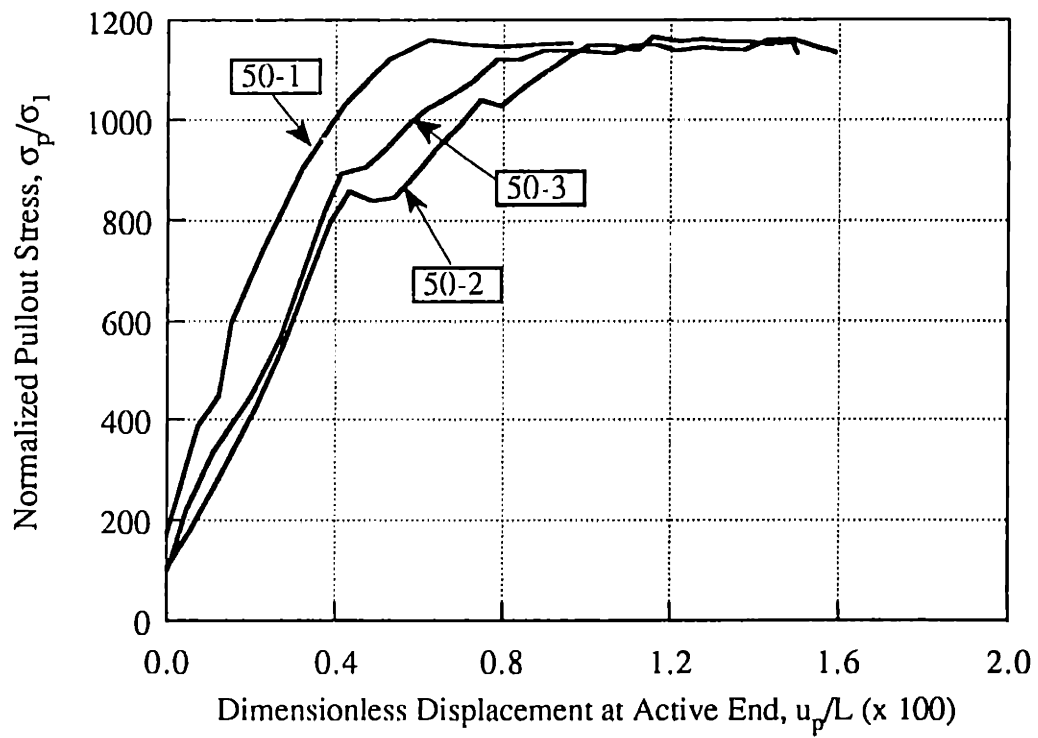


Figure 6.9: Coefficient of Interface Friction Between Steel and Sand.
(after Kishida and Uesugi, 1987)



Consolidation Stresses			
Test	σ_1 (kPa)	σ_3 (kPa)	$R=\sigma_1/\sigma_3$
50-1	49.0	21.0	2.33
50-2	73.5	31.5	2.33
50-3	98.0	42.0	2.33

Figure 6.10: Dimensionless Pullout Response for Tests on Steel Sheet Inclusions.

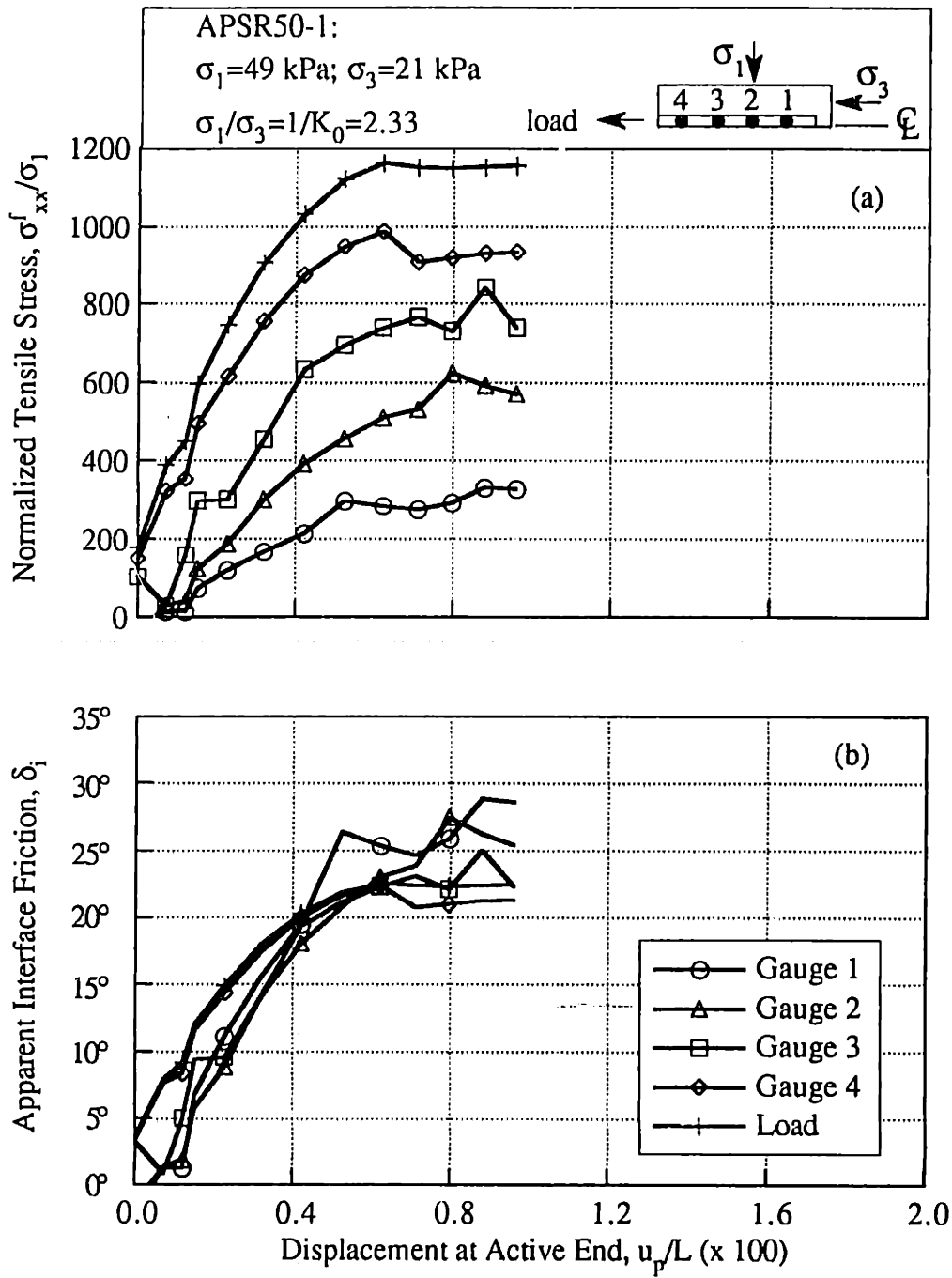


Figure 6.11: Pullout Measurements in Test APSR 50-1.

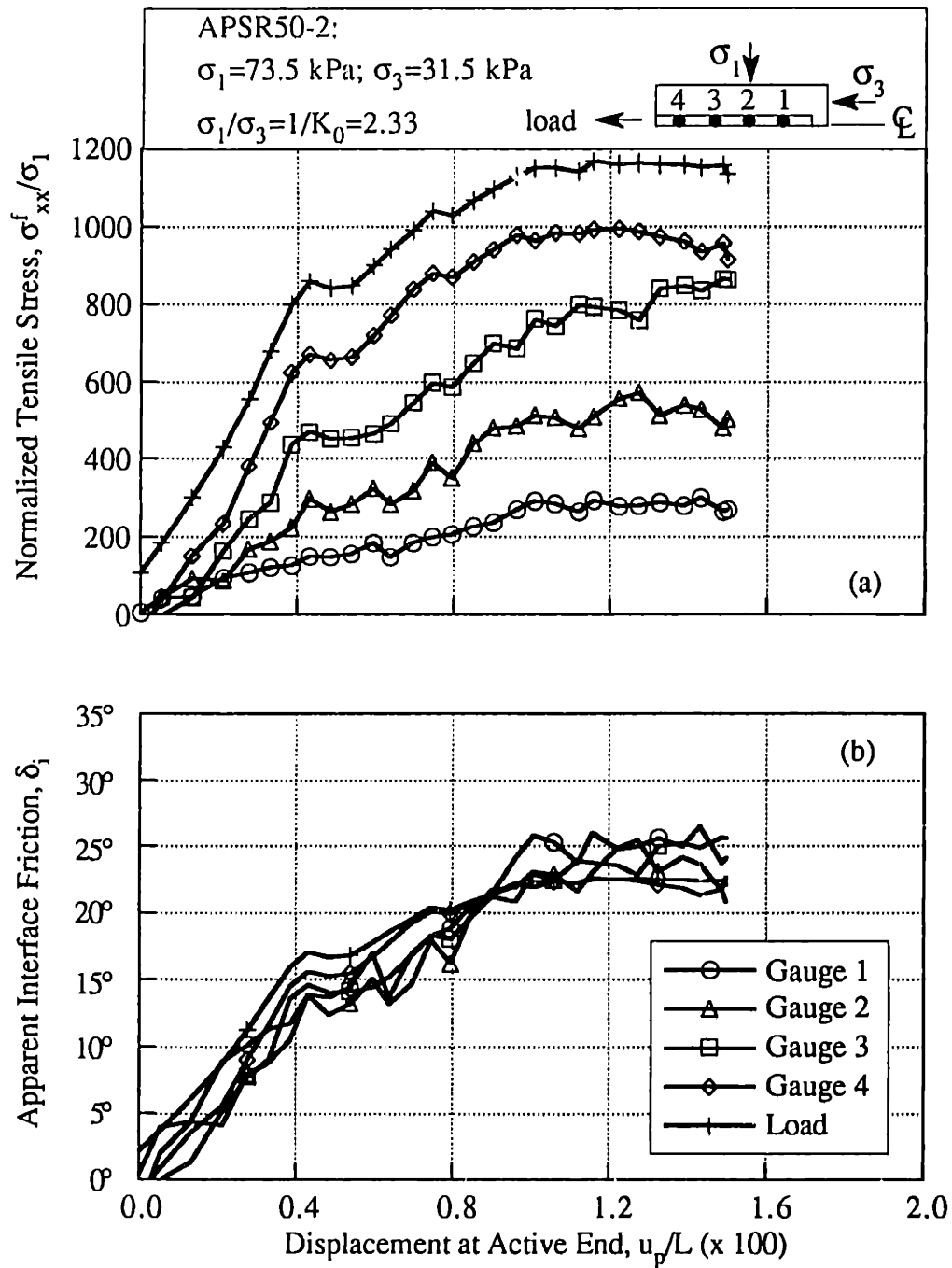


Figure 6.12: Pullout Measurements in Test APSR 50-2.

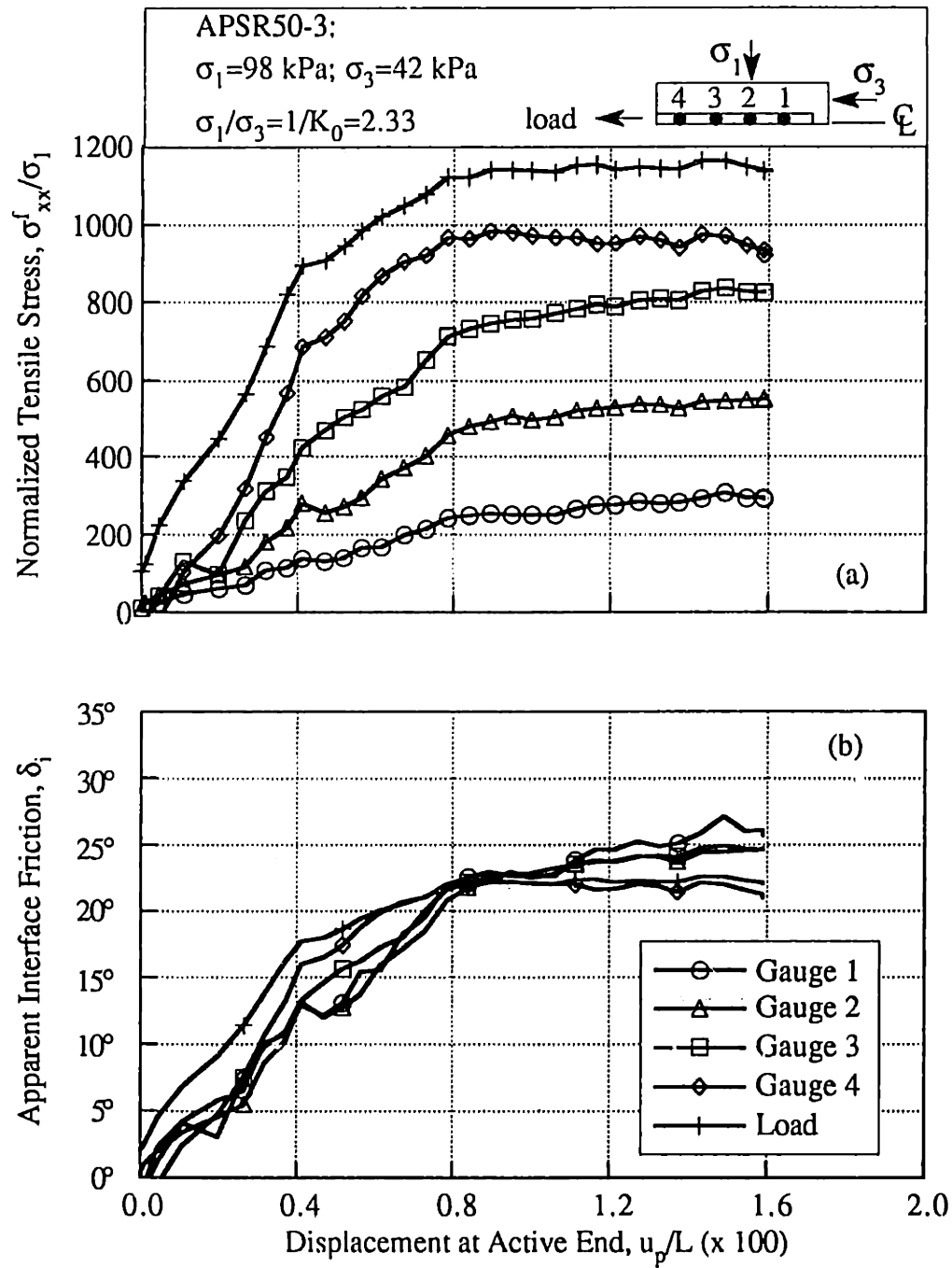


Figure 6.13: Pullout Measurements in Test APSR 50-3.

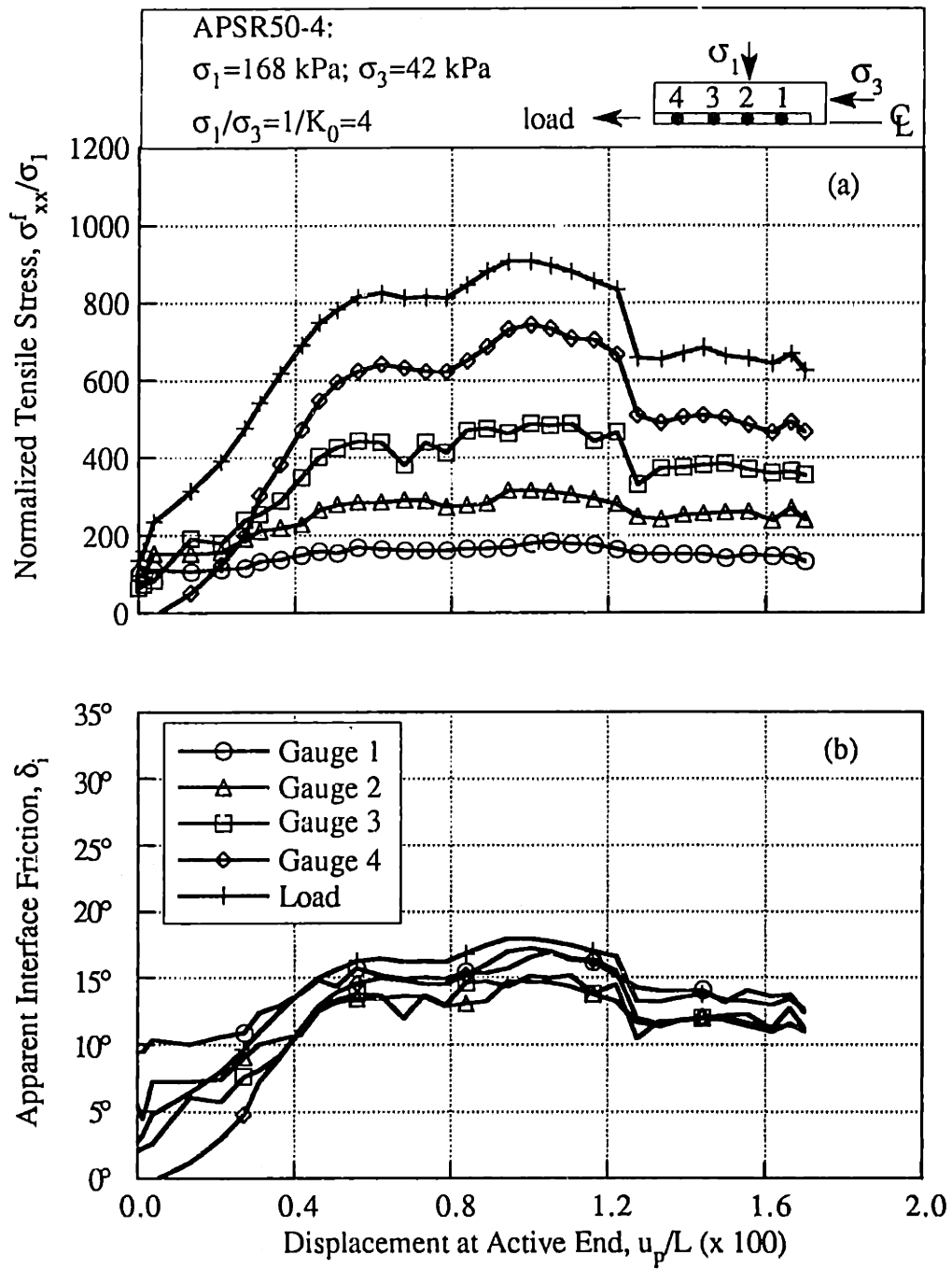


Figure 6.14: Pullout Measurements in Test APSR 50-4.

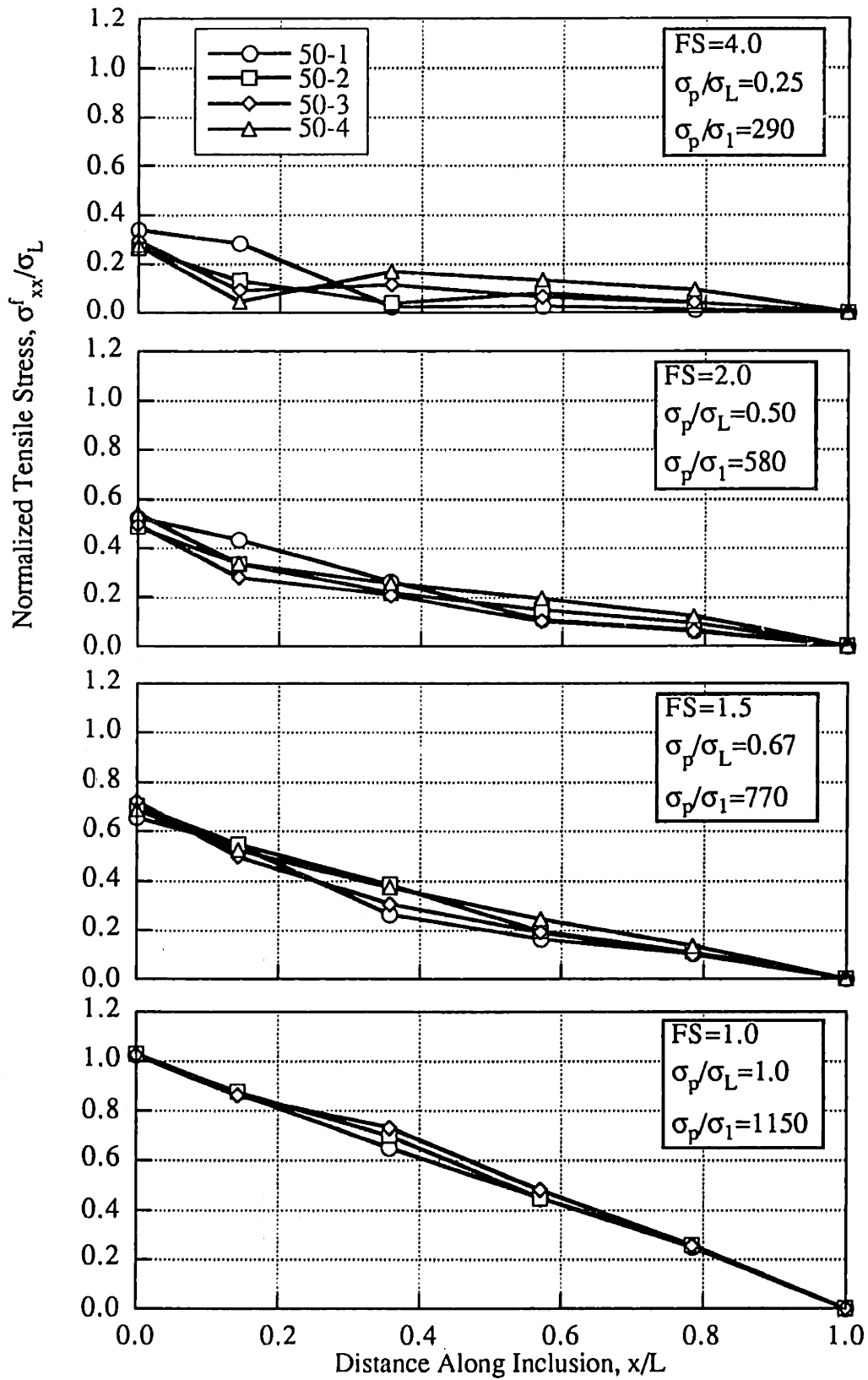


Figure 6.15: Tensile Stress Distribution in Pullout Tests on Steel Sheet Inclusion.

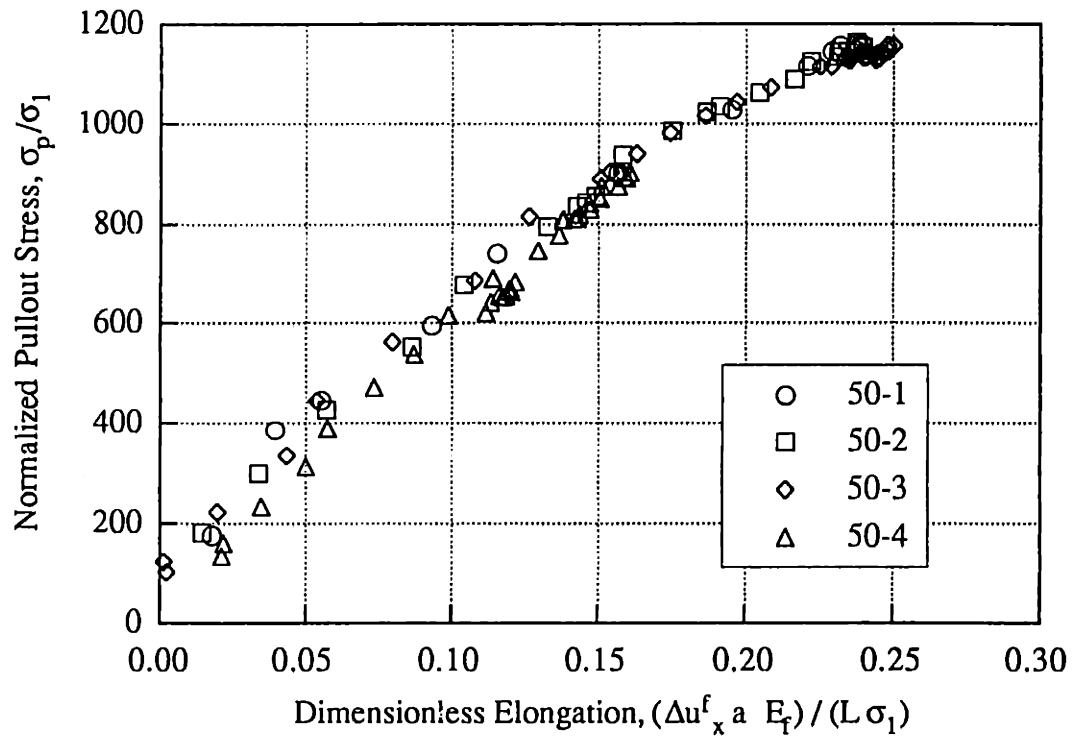


Figure 6.16: Interpreted Load-Elongation Behavior for Pullout Tests on Steel Sheet Inclusions.

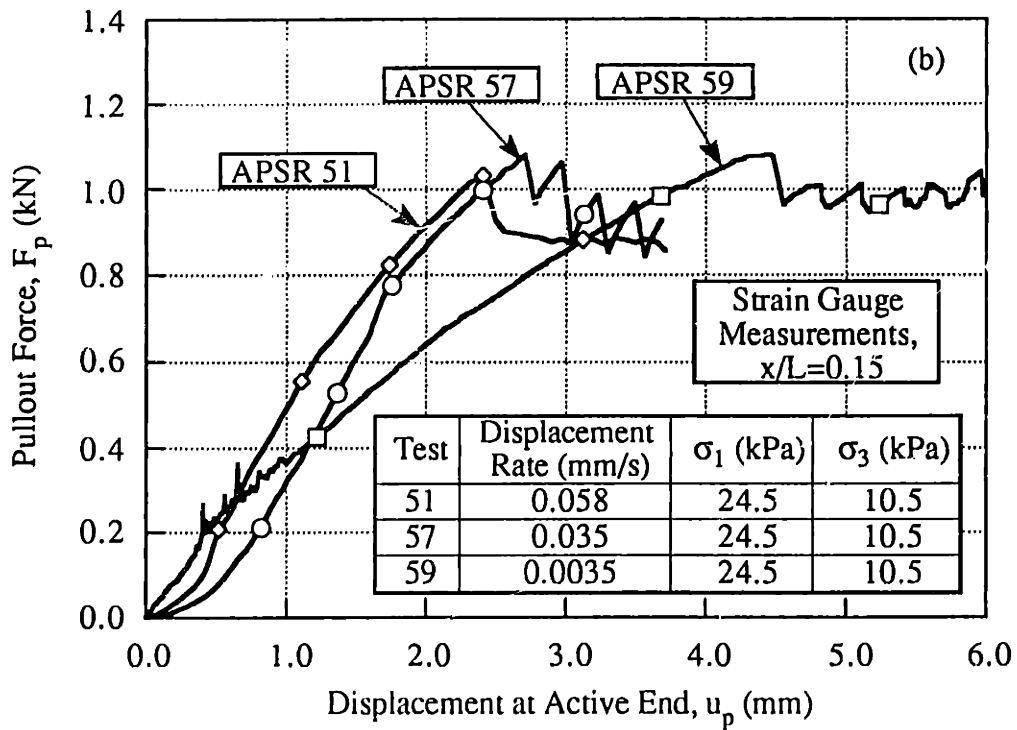
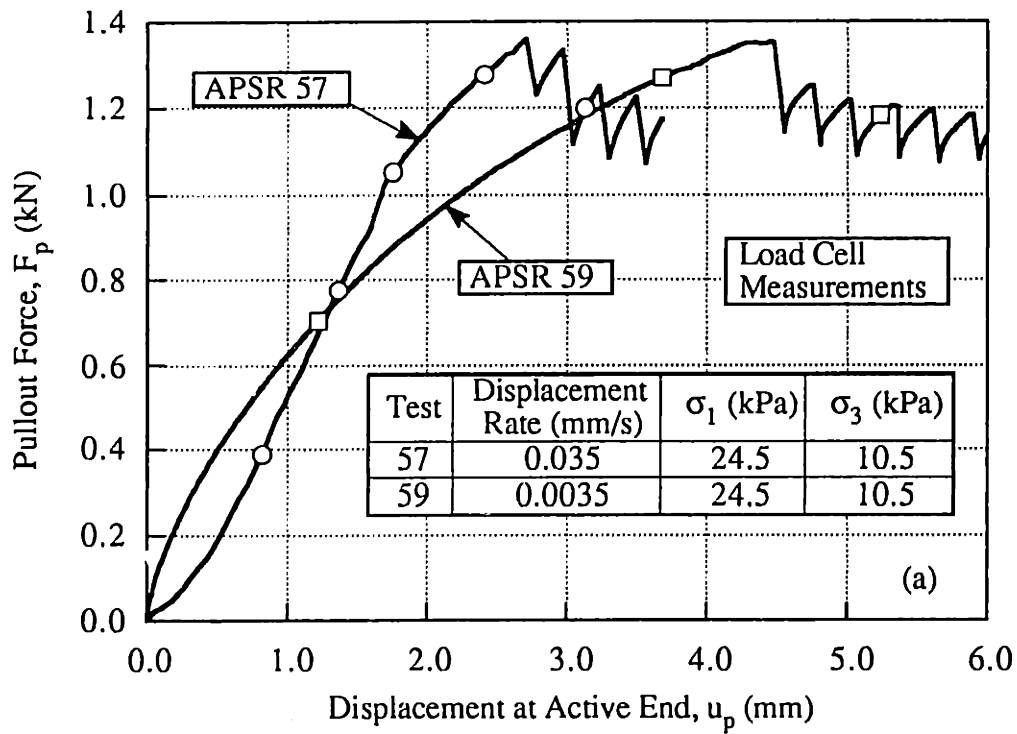


Figure 6.17: Measured Pullout Load-Displacement Response for Nylon 6/6 Reinforcements.

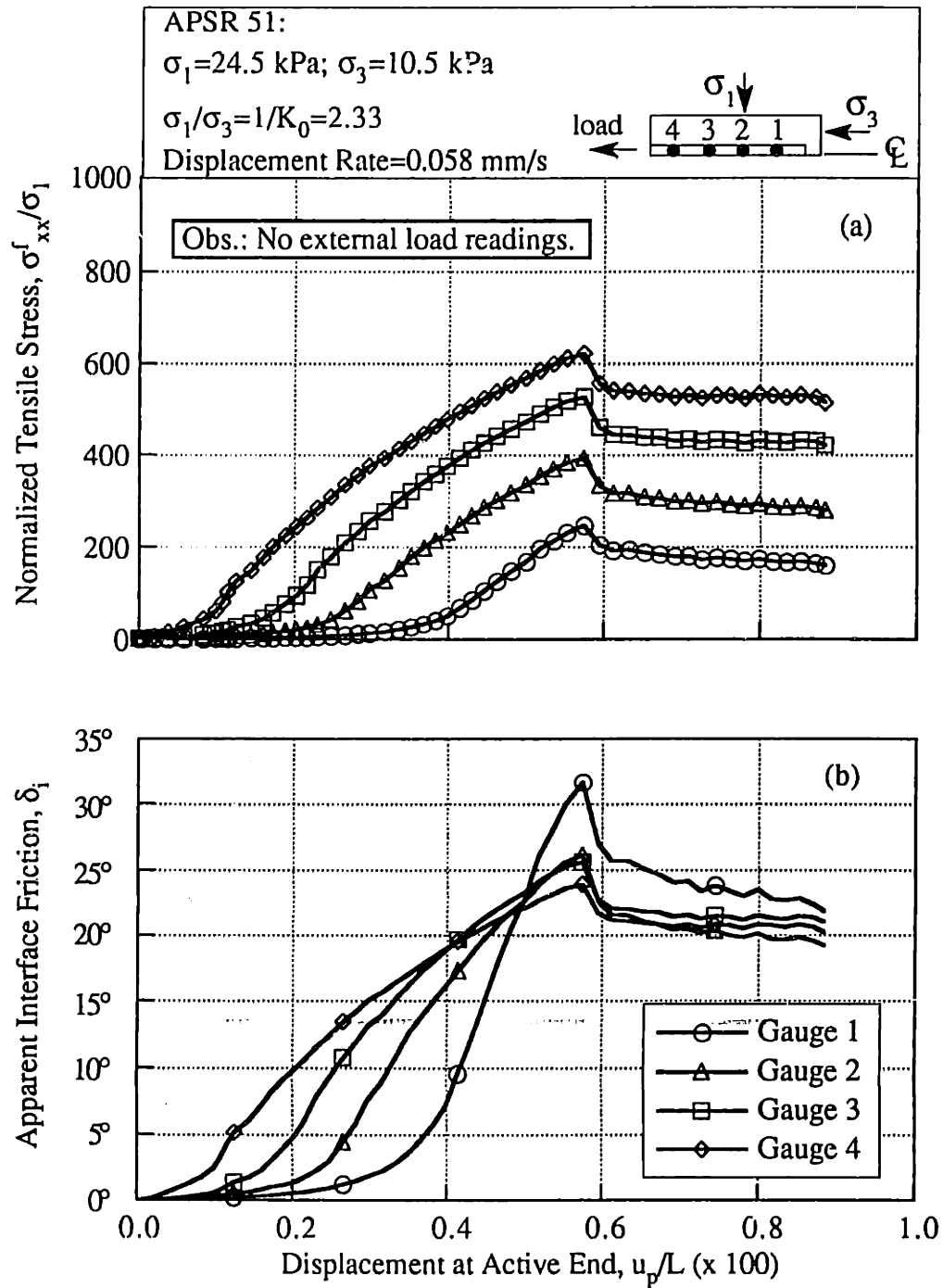


Figure 6.18: Pullout Measurements from Test APSR 51.

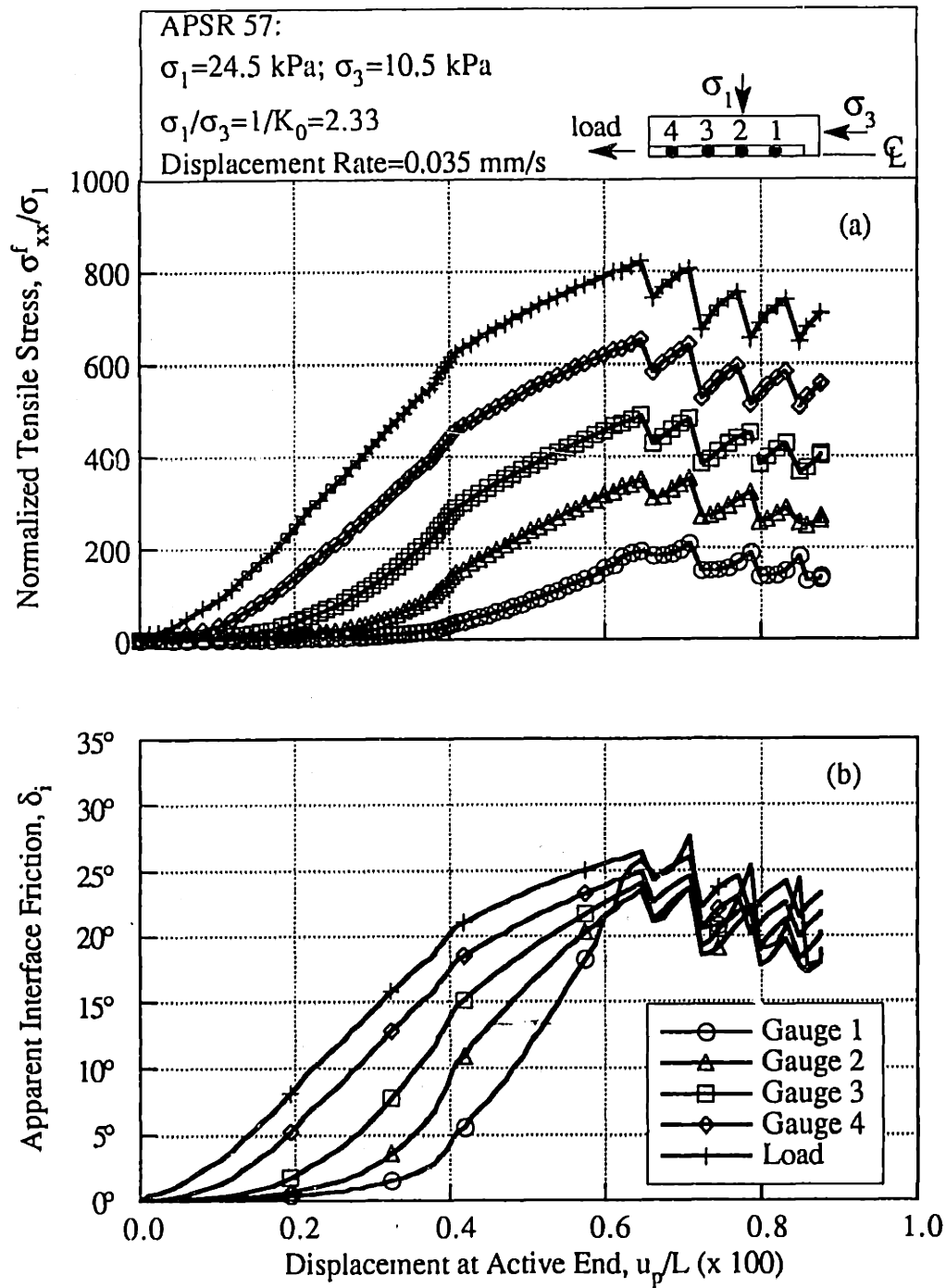


Figure 6.19: Pullout Measurements from Test APSR 57.

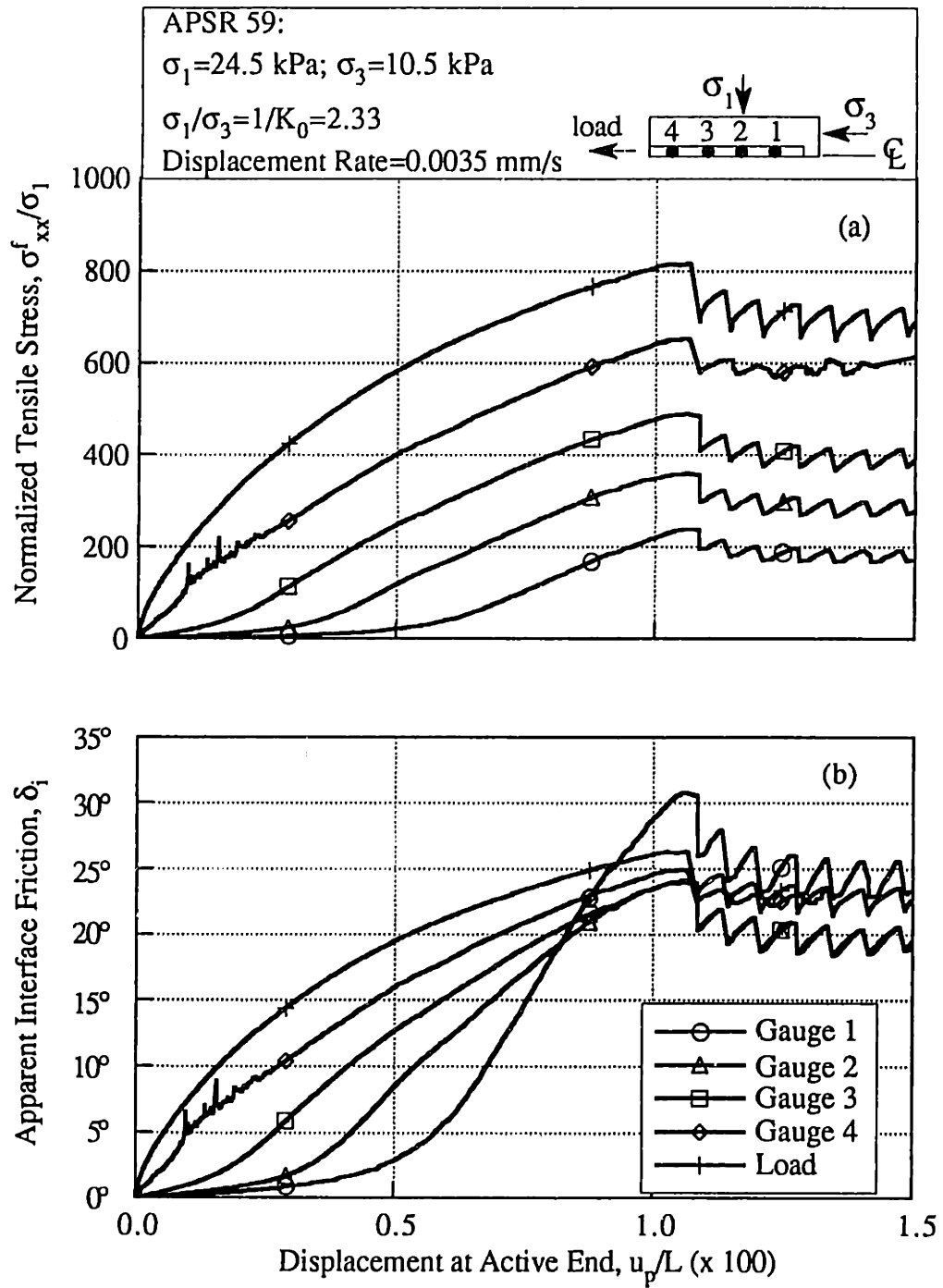


Figure 6.20: Pullout Measurements from Test APSR 59.

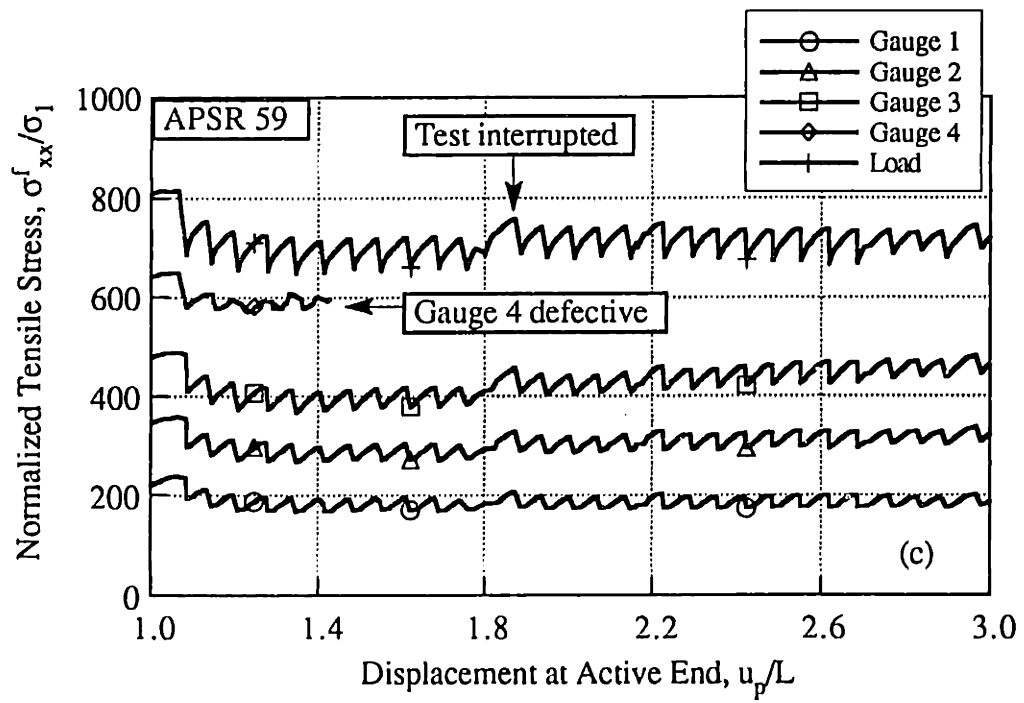


Figure 6.20 c: Stability of Residual Pullout Behavior.

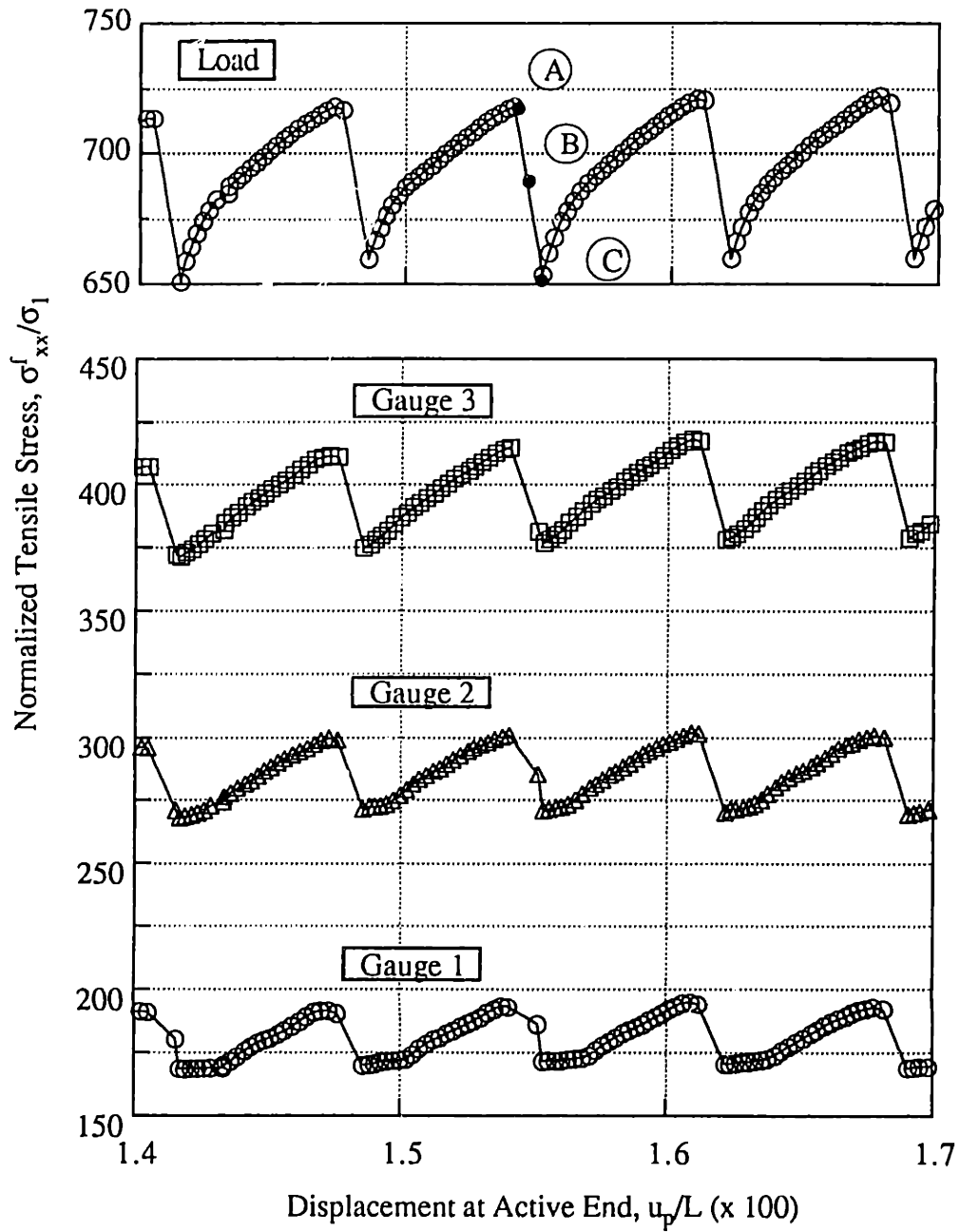
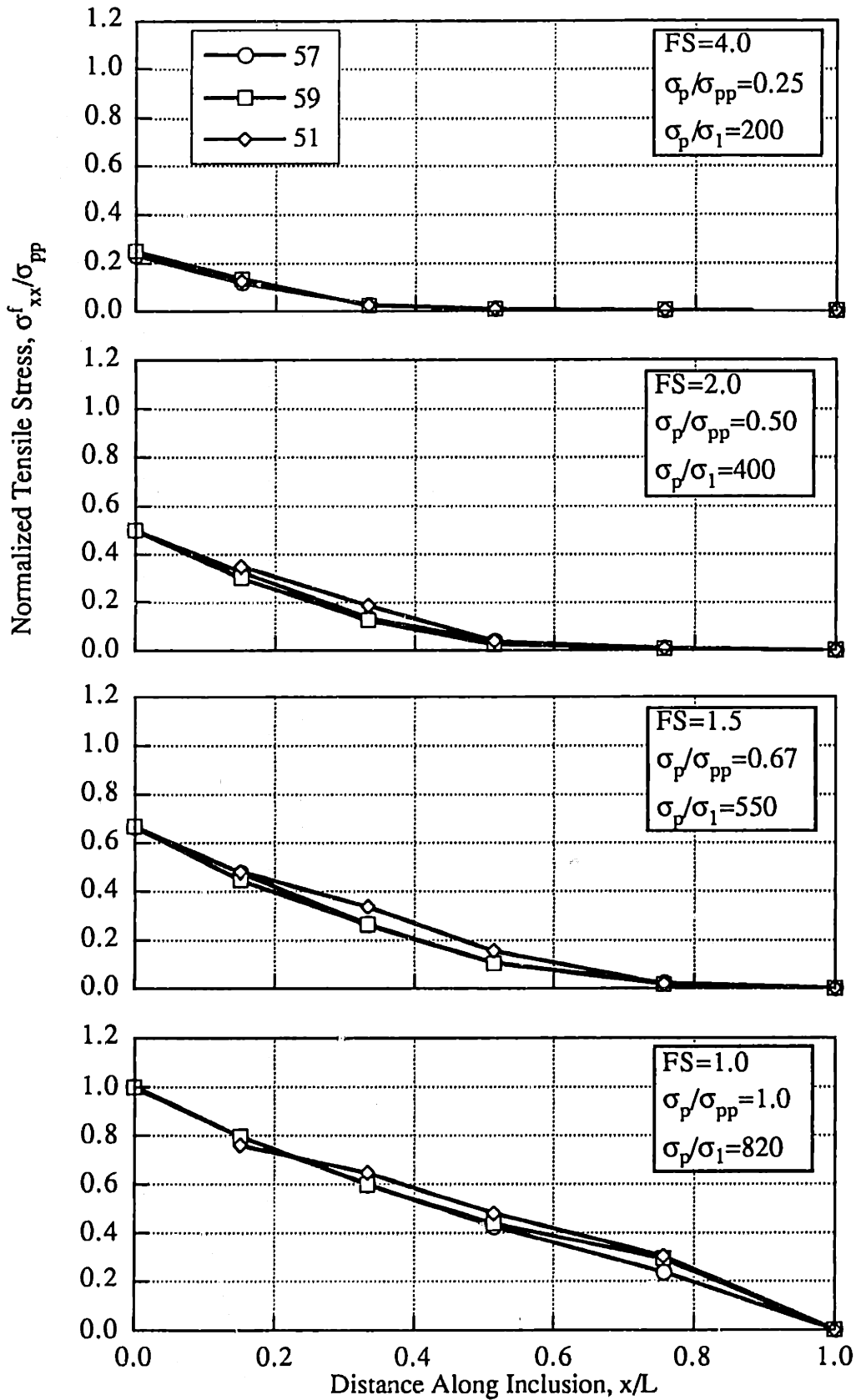


Figure 6.20 d: Detail of Stick-Slip Behavior in Pullout Test APSR 59.



Note: Figure assumes that σ_{pp} / σ_1 for APSR 51 is identical to ASPR 57, 59.

Figure 6.21: Tensile Stress Distribution in Pullout Tests on Nylon 6/6 Inclusions.

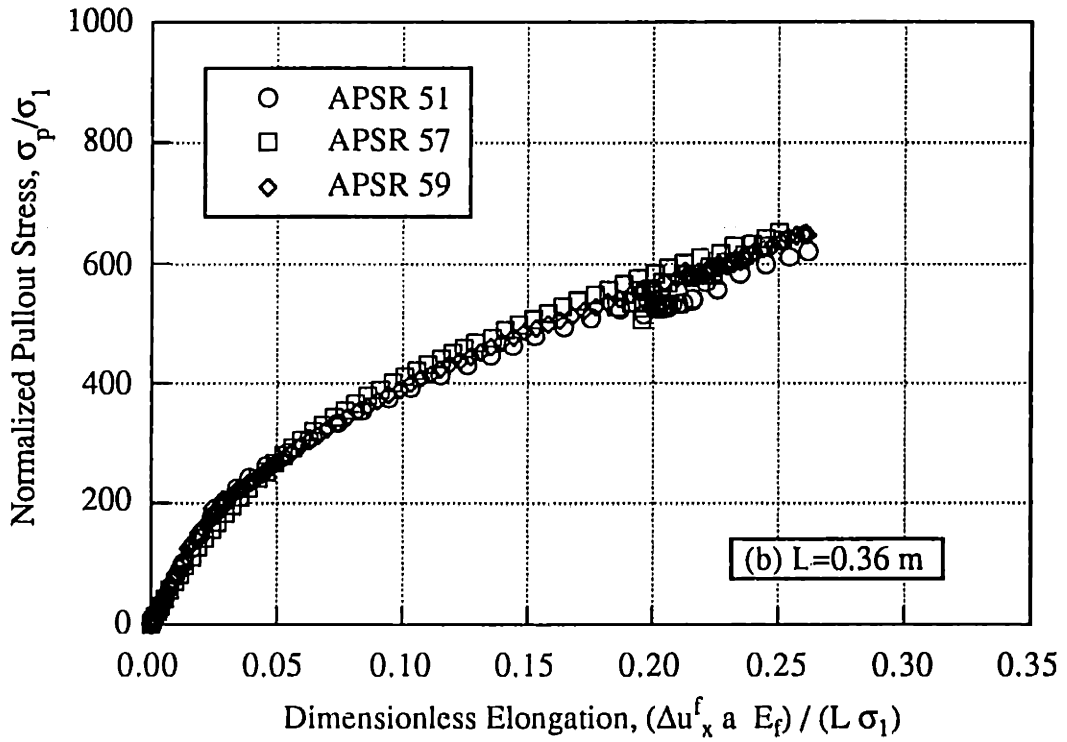
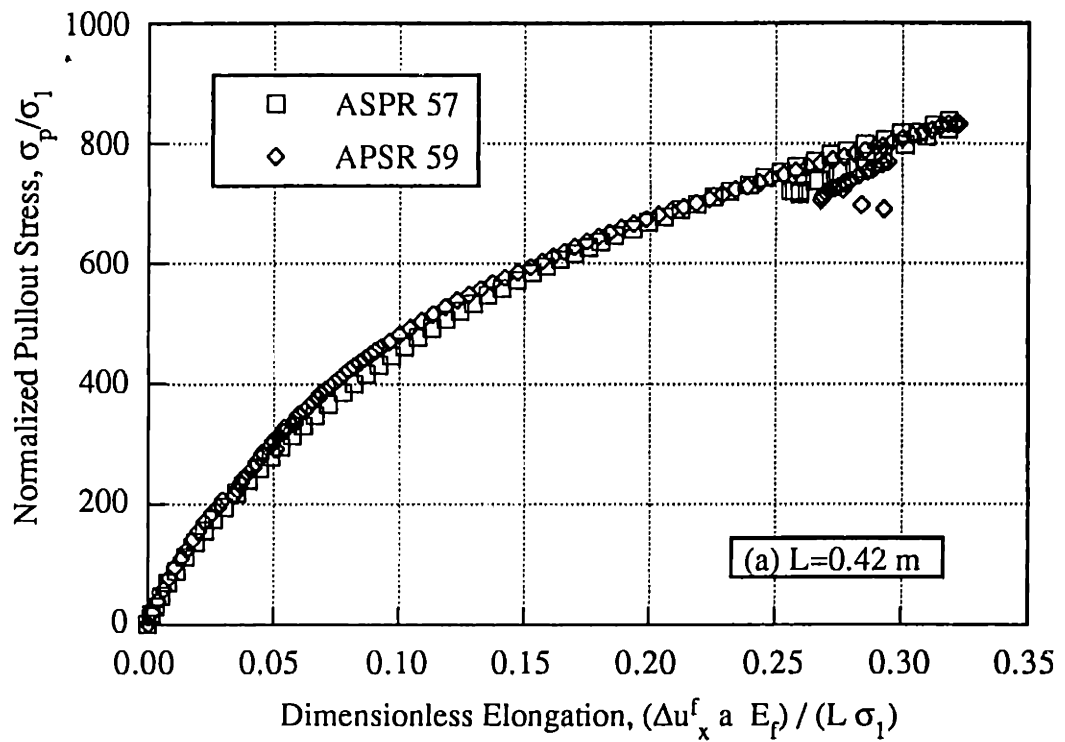
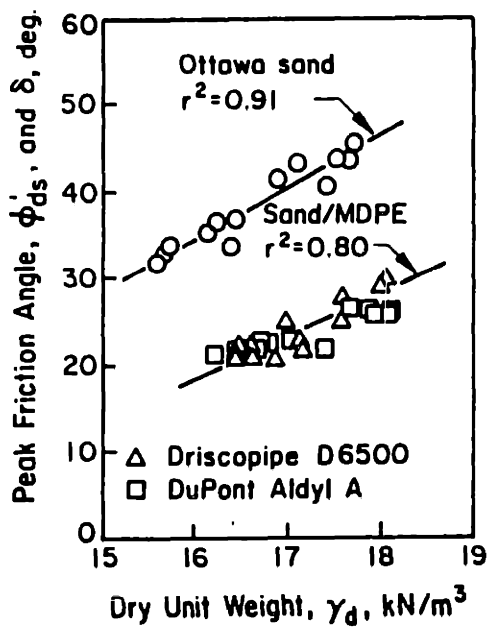
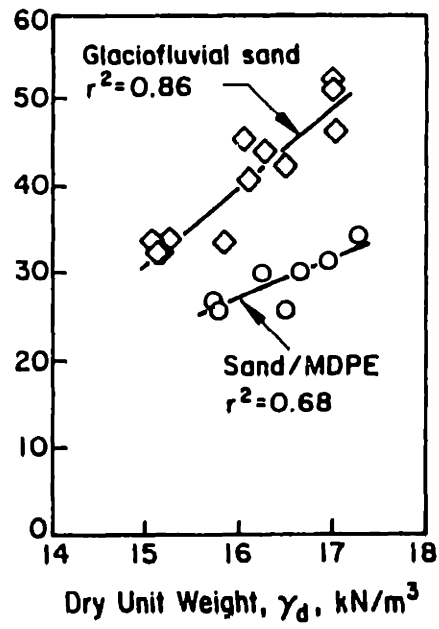


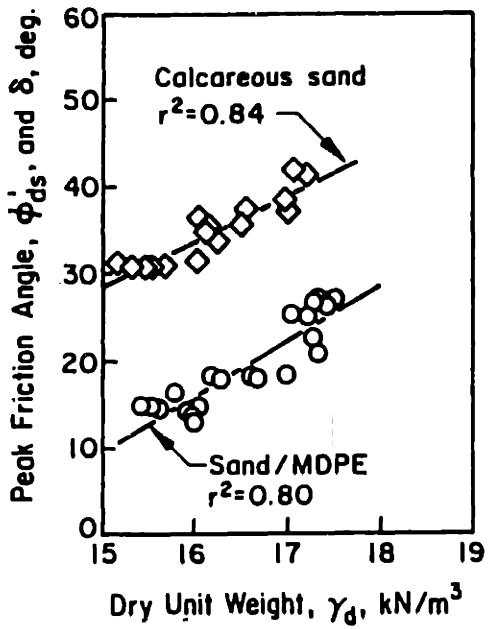
Figure 6.22: Interpreted Load-Elongation Behavior for Pullout Tests on Nylon 6/6 Inclusions.



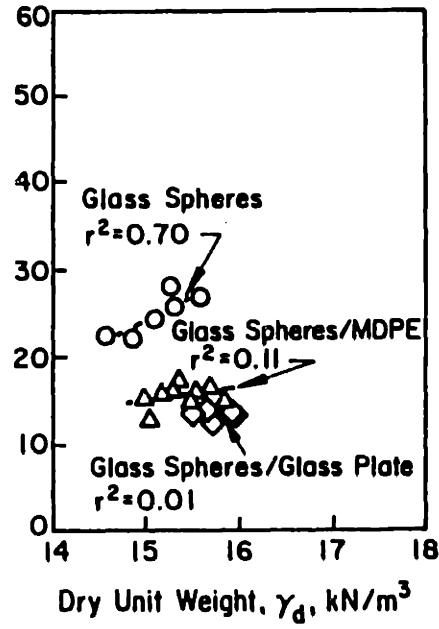
a) Ottawa Sand



b) Glaciofluvial Sand



c) Calcareous Sand



d) Glass Spheres

Figure 6.23: Measurements of Sand-MDPE Interface Friction.
(after O'Rourke et al., 1990)

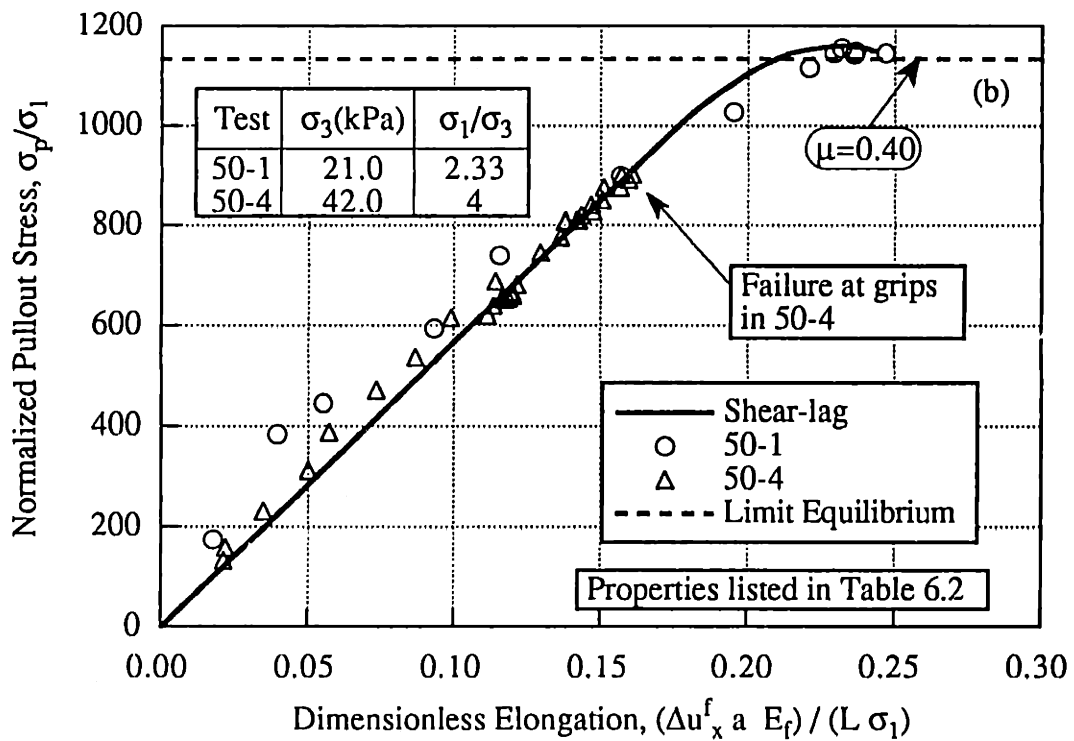
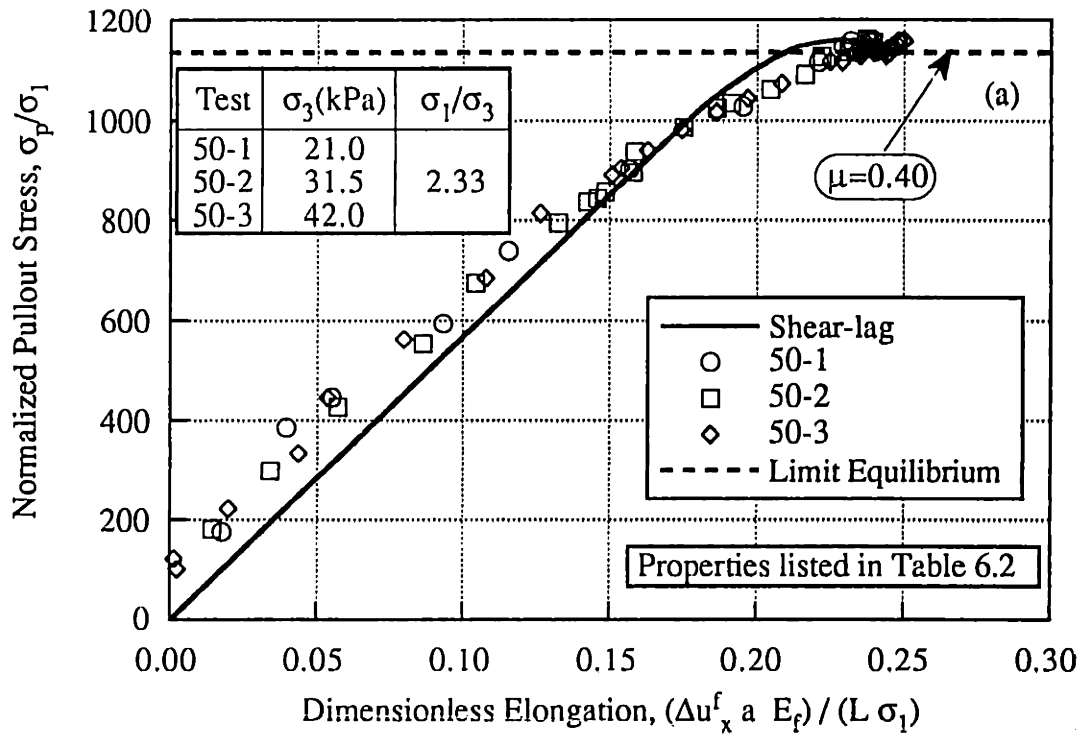


Figure 6.24: Comparison of Predicted and Measured Load-Elongation Response for Steel Sheet Inclusions.

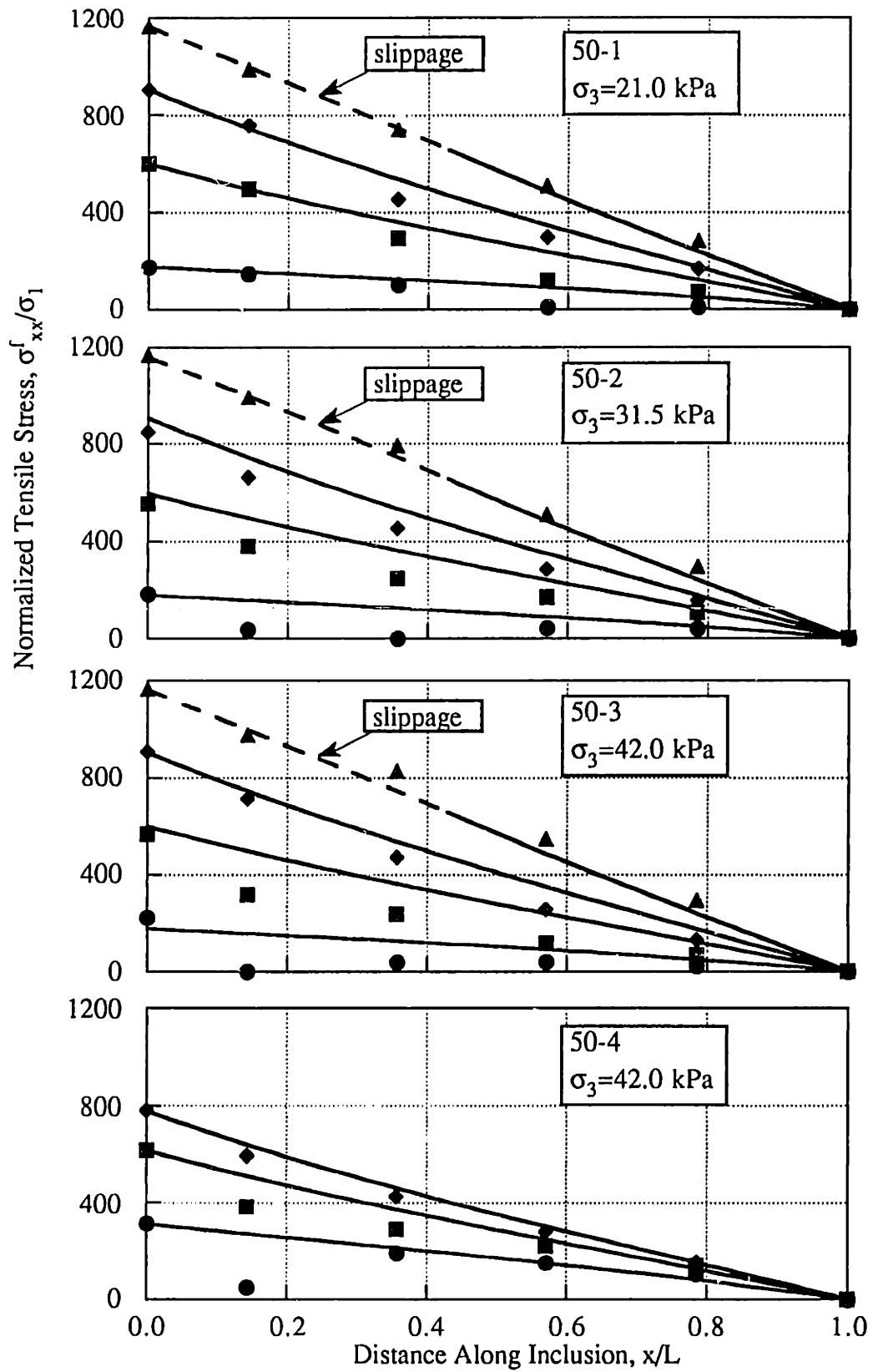


Figure 6.25: Comparison of Predicted and Measured Tensile Stress Distribution for Pullout Tests on Steel Sheet Inclusions.

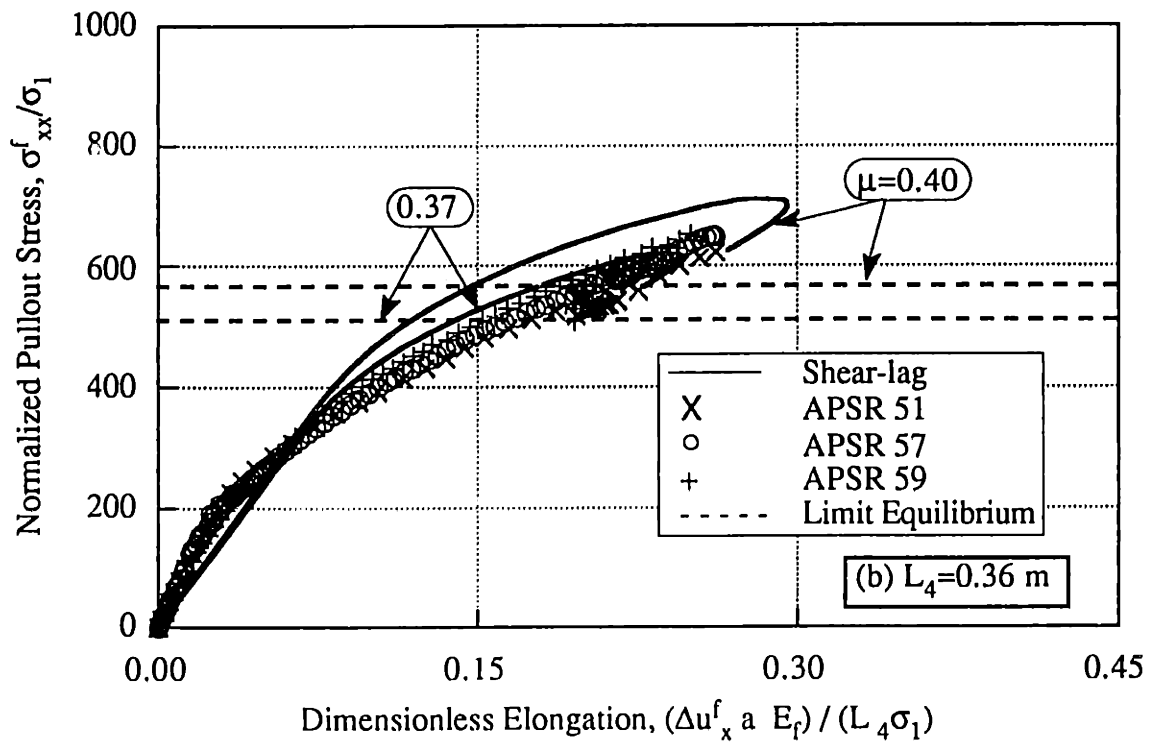
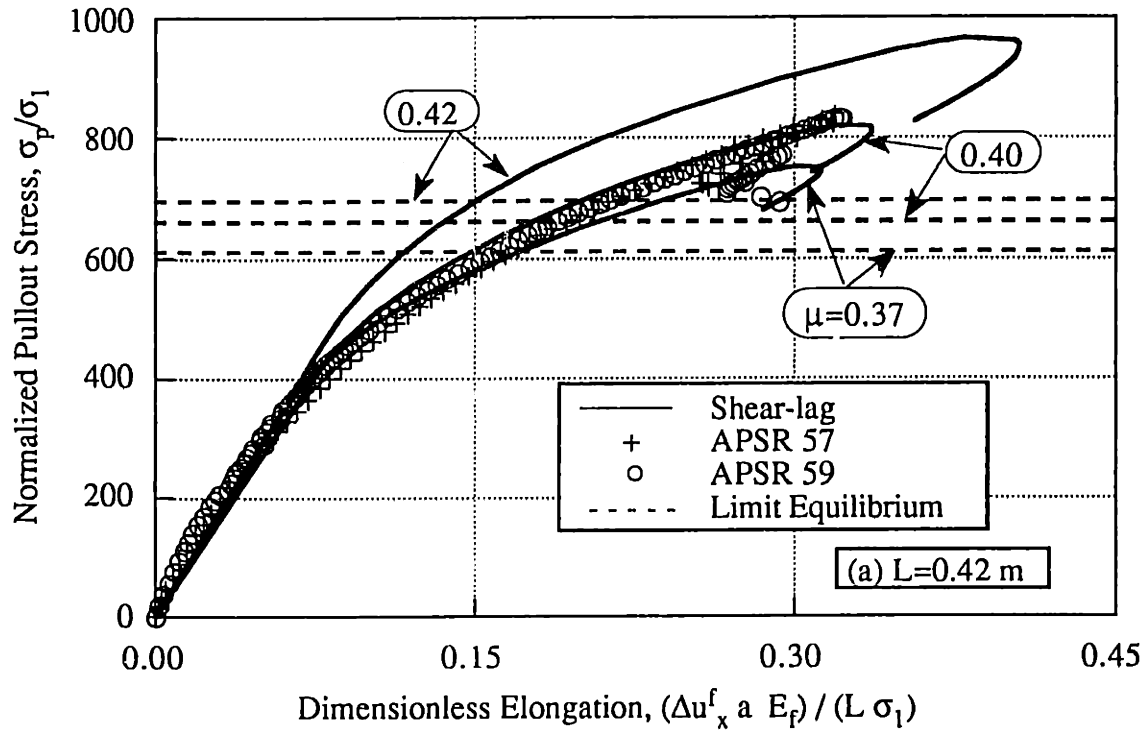


Figure 6.26: Comparison of Predicted and Measured Load-Elongation Response for Nylon 6/6 Inclusions.

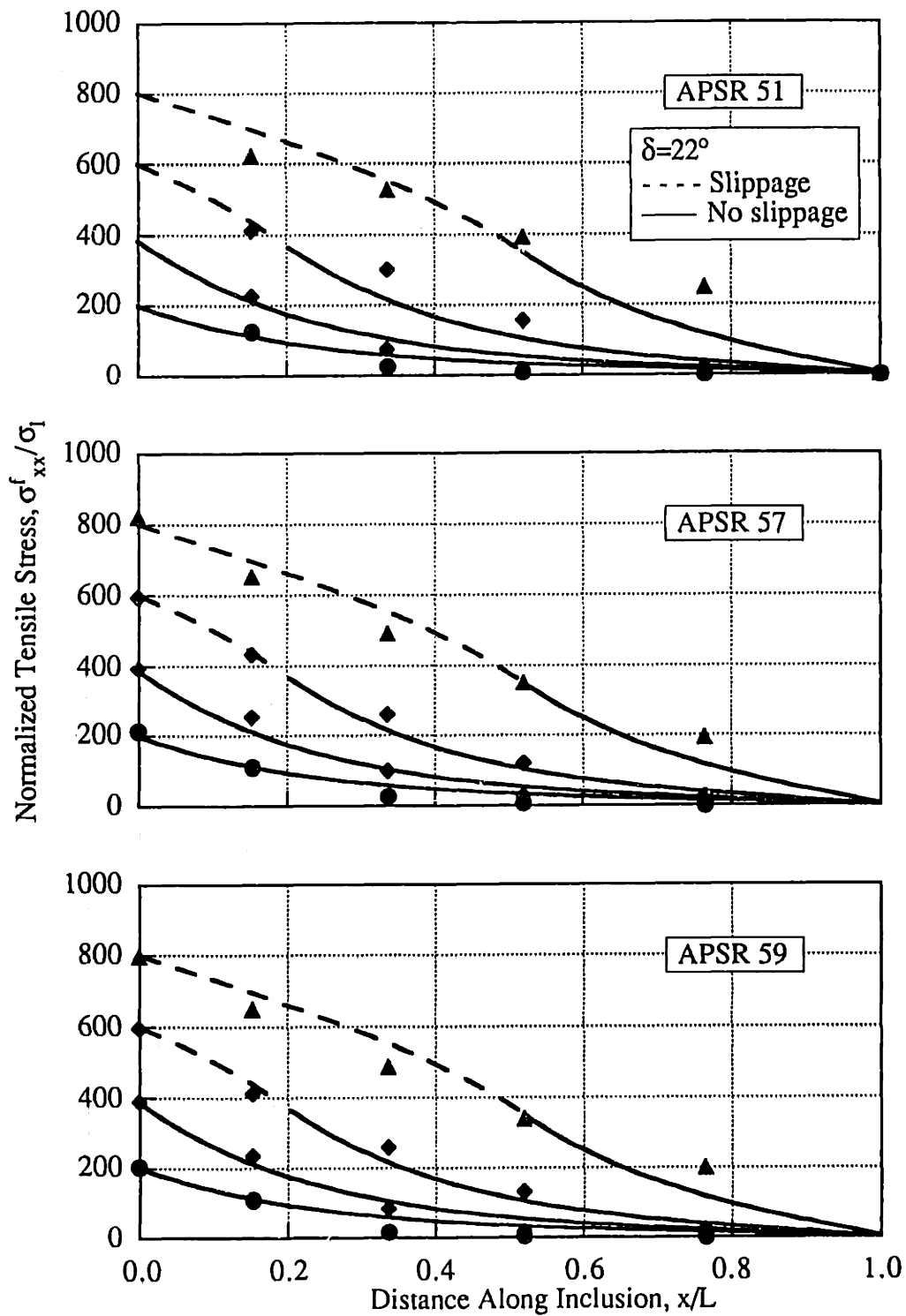


Figure 6.27: Comparison of Predicted and Measured Tensile Stress Distribution for Pullout Tests on Steel Sheet Inclusions.

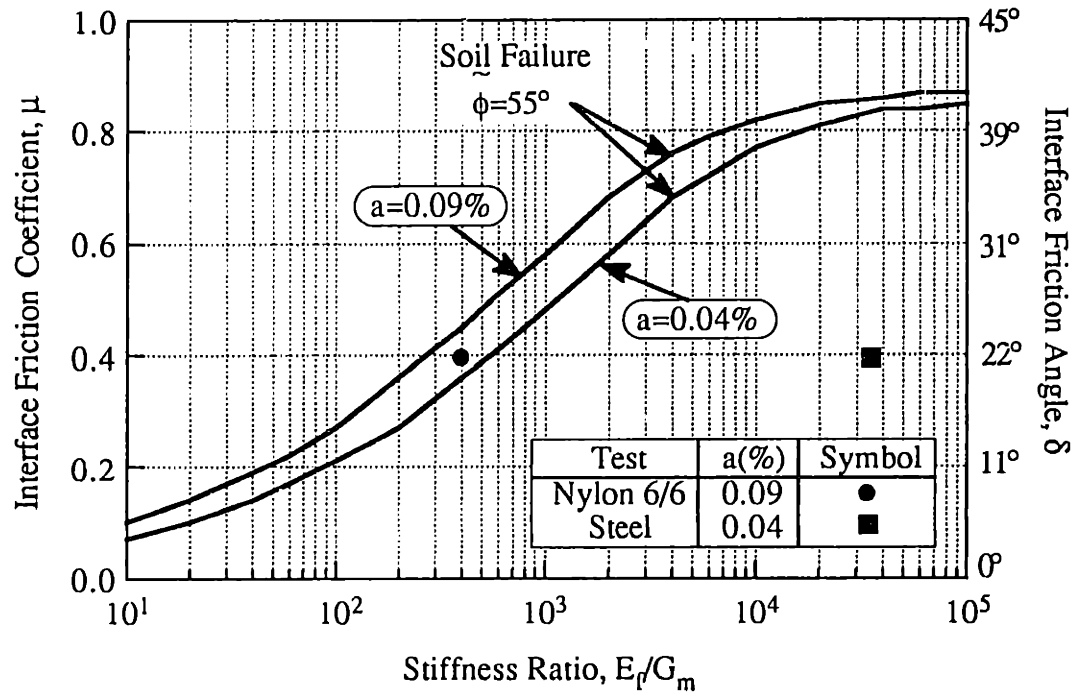


Figure 6.28: Evaluation of Soil Failure Conditions for Pullout Tests in Dense Ticino Sand.

Appendix 6.A: References

- Abramento, M. and Whittle, A. J. (1993) "Shear-Lag Analysis of a Planar Soil Reinforcement in Plane Strain Compression", *ASCE Journal of Engineering Mechanics*, 119(2), 270-291.
- Baldi, G., et al. (1985) "Laboratory Validation of In-Situ Tests", *AGI Jubilee Volume, Proc. 11th ICSMFE*, San Francisco, CA.
- Bowden, F. P. and Tabor, D. (1950) "*The Friction and Lubrication of Solids*", Oxford at the Clarendon Press, 337 pp.
- Gens, A.; Carol, I. and Alonso, E.E. (1988) "An Interface Element Formulation for the Analysis of Soil-Reinforcement Interaction", *Computers and Geotechnics*, 7, 133-151.
- Griffiths, D.V. (1985) "Numerical Modelling of Interfaces Using Conventional Finite Elements", *Proc. of the Fifth International Conference on Numerical Methods in Geomechanics*, Nagoya, 837-844.
- Guilloux, A.; Schlosser, F. and Long, N.T. (1979) "Etude du Frottement Sable-Armature en Laboratoire", *C. R. Coll. Int. Renforcement des Sols*, Paris, 35-40.
- Johnston, R. S. and Romstad, K.M. (1989) "Dilation and Boundary Effects in Large Scale Pullout Tests", *Proceedings of the XII International Conference on Soil Mechanics and Foundation Engineering*, Rio de Janeiro, 1263-1266.
- Kishida, H. and Uesugi, M (1987) "Tests of the Interface Between Sand and Steel in the Simple Shear Apparatus", *ASCE Journal of Geotechnical Engineering*, 37(1), 45-52.

- Larson, D.G. (1992) "A Laboratory Investigation of Load-Transfer in Reinforced Soil", Ph.D. Thesis, Massachusetts Institute of Technology, Cambridge, MA.
- O'Rourke, T.D.; Druschel, S.J. and Nevratali, A.N. (1990) "Shear Strength Characteristics of Sand-Polymer Interfaces", *ASCE Journal of Geotechnical Engineering*, 116(3), 451-469.
- Palmeira, E.M., and Milligan, G.W.E. (1989) "Scale and Other Factors Affecting the Results of Pullout Tests of Grids Buried in Sand", *Géotechnique*, 39(3), 511-524.
- "Plastics (2): D1601-D3099" (1988) *Annual Book of ASTM Standards*, Vol. 08.02, Philadelphia, PA.
- Schellekens, J.C.J. and DeBorst, R. (1993) "On the Numerical Integration of Interface Elements", *International Journal for Numerical Methods in Engineering*, 36, 43-66.
- Whittle, A. J.; Germaine, J. T.; Larson, D. G. and Abramento, M. (1992) "Measurement and Interpretation of Reinforcement Stresses in the APSR Cell", *Proceedings International Symposium on Earth Reinforcement Practice*, Fukuoka, Japan, November.
- Whittle, A. J.; Larson, D. G.; Germaine, J. T. and Abramento, M. (1993) "A New Device for Evaluating Load-Transfer in Geosynthetic Reinforced Soils", *Geosynthetic Soil Reinforcement Testing Procedures*, ASTM STP 1190, S. C. Jonathan Cheng, Ed., American Society for Testing and Materials, Philadelphia.

Appendix 6.B: Notation

The following symbols are used in chapter 6:

A	=	cross sectional area of inclusion
B	=	width of reinforcement
E_f	=	inclusion elastic modulus
f	=	inclusion thickness
F, F_p	=	pullout force
G_m	=	soil matrix shear modulus
K_0	=	coefficient of lateral stress at rest
L	=	inclusion length
m	=	soil matrix height
R	=	ratio σ_1/σ_3
$u_p, u_x(0)$	=	displacement at active end ($x=0$)
$\dot{u}_x(0)$	=	displacement rate at active end
\dot{u}_c	=	critical displacement rate for initiation of stick-slip
x	=	distance along inclusion
\dot{x}	=	displacement rate in uniaxial tension tests
y	=	distance along soil matrix
δ	=	interface friction angle
δ_i	=	apparent interface friction angle
Δu_x^f	=	inclusion elongation
$\Delta\mu$	=	difference static-dynamic friction coefficient: $\mu_s - \mu_k$
ν_f	=	inclusion Poisson's ratio
ν_m	=	soil matrix Poisson's ratio
μ	=	interface friction coefficient
μ_k	=	kinetic interface friction

- μ_s = static interface friction
- σ_1, σ_3 = major and minor external principal stresses
- σ_p = pullout stress
- σ_L = ideal pullout stress (for a rigid inclusion)

Chapter 7: Summary, Conclusions and Recommendations

This research describes the formulation and evaluation of approximate analytical solutions, based on techniques of shear-lag analysis, for predicting and interpreting tensile stress distributions in planar soil reinforcements. The first two parts of the thesis (Chapters 2, 3 and 4) consider the development of stresses in the reinforcement as the surrounding soil is sheared. These solutions have direct application for estimating the stresses in reinforced soil masses at working load levels and, hence, can provide a more fundamental bases for selection of reinforcing materials in design. The third part of the thesis (Chapters 5 and 6) applies the shear-lag analysis to model the pullout behavior of extensible reinforcements. This analysis provides new insights into the underlying mechanisms of soil-reinforcement interaction in pullout tests and is evaluated through a program of experimental measurements (Chapter 6).

The following sections (7.1, 7.2 and 7.3) summarize the principal findings of the research, while recommendations for future work are given in section 7.4.

7.1. Planar Soil Reinforcement in Plane Strain

Compression

The underlying mechanism of soil reinforcement, using planar inclusions, relies on the development of tensile stresses within the reinforcing material. In order to evaluate this basis hypothesis, the analysis initially focused on a composite plane strain element of reinforced soil, which is sheared in plane strain compression under the action of uniform boundary tractions. The planar reinforcement is oriented parallel to the minor external,

principal stress (i.e. in the direction of maximum tensile strain). The proposed formulation introduces shear-lag approximations, widely used in the mechanics of composites, in order to derive analytical expressions for the tensile stress in the reinforcement and interface tractions as functions of the inclusion geometry (length and thickness of reinforcement, height of soil matrix), elastic properties of the constituent materials (i.e., soil matrix and reinforcement) and interface friction. The results show that the principal factors affecting the distribution and magnitude of the tensile stress in the reinforcement are: 1) the length of the inclusion; 2) the relative stiffness of the reinforcement and soil; 3) volume changes in the soil; and 4) the magnitude of the imposed shear stress. Although frictional sliding at the soil-reinforcement interface can reduce the load transfer, these effects are insignificant for practical values of interface friction.

The proposed shear-lag analyses of maximum (centerline) reinforcement loads are evaluated through comparisons with linear, finite element calculations. These results show very good agreement (within 5%) for a wide range of practical geometric and material properties and, hence, demonstrate the accuracy of the approximate analytical solutions.

Results of the shear-lag analysis were also evaluated through comparisons with high quality experimental measurements of tensile loads in steel sheet reinforcements reported by Larson (1992). The experimental data were obtained in a new laboratory device, referred to as the Automated Plane Strain Reinforcement (APSR) cell. The APSR cell has the unique capability of measuring directly the tensile stress at the center of the reinforcing inclusion as the surrounding soil is sheared in plane strain compression. Additional instrumentation (strain gauges) is used to measure the load distributions within the inclusion. The device imposes uniform boundary tractions and, hence, models very closely the conditions assumed in the proposed shear-lag analysis. The tests of Larson (1992) were performed using steel reinforcements with half-lengths $L/2=9$ to 36cm,

embedded in dense and loose Ticino sand and sheared in the plane normal to the direction of deposition at a confining pressure $\sigma_3=31\text{kPa}$.

Input parameters for the shear-lag analysis were selected from the shear behavior of the (unreinforced) sand and (unconfined) uniaxial tension tests on the reinforcement. Detailed comparisons show excellent agreement for a base case geometry, with $L/2=36\text{cm}$. However, the analyses are sensitive to the selected Poisson's ratio of the soil matrix. The analysis and measurements show that tensile loads in the reinforcement can be described as a linear function of the external stress ratio, $R=\sigma_1/\sigma_3$, with no load transfer corresponding to K_0 -stress conditions in the soil (i.e., $R=1/K_0$). Further comparisons show that the measured centerline tensile loads for short inclusions in dense sand ($L/2<36\text{cm}$) are slightly higher than those predicted by the shear-lag analysis. There is generally better agreement between the predicted and measured load transfer for tests in loose sand.

Overall, the comparisons with APSR data provide the first basis to demonstrate that the shear-lag analysis is capable of providing reliable predictions of the tensile stresses in a planar soil reinforcement at working load levels. Using the framework of the proposed analysis, it is then possible to estimate the stresses which would develop in long reinforcements (i.e., $L>3\text{m}$) which are typical of field situations. The predictions for steel reinforcements in Ticino sand show that the tensile force measured in APSR tests (with $L=36\text{cm}$) represents approximately half the load which would be transferred in a long inclusion. Thus, the analysis can be used to provide practical guidance for the design and interpretation of small scale laboratory experiments (such as the APSR), as well as to predict stresses within reinforced soil masses at field scale.

7.2. Effects of Inclusion Orientation

The orientation of a tensile reinforcement within the soil mass is a critical parameter controlling load transfer, especially in situations where the principal stress (and strain)

directions rotate. In principle, the reinforcement develops highest tensile loads when aligned with the direction of maximum tensile strain in the soil (for a linear, isotropic soil this is directly related to principal stress directions). Chapter 4 describes the generalization of the original shear-lag analysis for a thin planar reinforcement inclined at arbitrary orientation and embedded in a soil specimen which is loaded by uniform normal and shear boundary tractions (σ_v , σ_h , τ). The formulation assumes a rough interface and neglects the bending stiffness for a thin reinforcement. Complete analytical solutions are derived for the axial stress in the reinforcement and interface tractions as functions of the specimen geometry, inclination angle (Fig. 4.4) θ , and material properties. There are two fundamental modes of interaction: 1) plane strain compression, and 2) direct shear. For inclined reinforcements in plane strain compression, the tensile stresses develop in the inclusion for $|\theta| < \theta_0$, where θ_0 is a function of the volume change characteristics of the soil (σ_v/σ_h , ν_m); the reinforcement is most effective at $\theta=0^\circ$. For the direct shear mode (τ only), tensile stresses develop for $0^\circ < \theta < 90^\circ$, with maximum load transfer at $\theta=45^\circ$. Solutions for other loading conditions of practical interest, such as simple shear tests, can be obtained by superposition of the two fundamental linear solutions.

Calculations of load transfer from linear finite element analyses show close agreement with the shear-lag analyses for inclined reinforcements using a limited range of material properties and inclusion geometries. Differences in the boundary conditions at the tips of the inclusion restricts the range of properties for comparisons of results.

Several authors have reported on the effects of inclusion orientation based on laboratory experiments in plane strain compression and direct shear box tests. Results of the shear-lag analysis are used to evaluate the composite strength of the plane strain unit cell tests reported by McGown et al. (1978), using a stress averaging technique within the soil matrix. The analyses give excellent predictions of the measured data for different types of reinforcement and initial densities of the soil. Comparisons with reinforced direct shear box

data are only possible during the initial phase of the test in which there is negligible volume change within the soil specimen. The shear-lag analysis describes accurately the effects of inclusion orientation on the measured shear resistance for the tests reported by Jewell (1980) with $\bar{x} \cong 0.5 \text{ mm}$ ($\bar{\gamma} \cong 0.3\%$). However, for $\bar{x} > 0.5 \text{ mm}$, dilation within the central shear zone of the soil provides the dominant mechanism of load transfer in these tests.

7.3. Pullout Tests on Planar Inclusions

Pullout tests simulate the action of a reinforcing inclusion as a tensile anchorage embedded in the soil mass. Although pullout data are widely used to estimate the soil-reinforcement bond capacity for limit equilibrium design calculations, the tests have several major limitations: 1) the results are significantly affected by boundary conditions; 2) deformation of extensible reinforcements introduces a progressive failure mechanism which complicates the evaluation of bond capacity; and 3) mechanisms of interactions are highly complex for grid reinforcements which are widely used in practice. Chapter 5 presents a new analysis which is capable of describing the complete load transfer behavior for pullout tests with extensible planar reinforcements. The formulation uses shear-lag approximations, together with simplified boundary conditions at the active end of the reinforcement, where pullout loads are applied.

The proposed analysis describes four successive phases in the pullout response: 1) Initial linear behavior, characterized by build up of interface tractions at the active end of the inclusion; 2) The development of a sliding front from the active end, which initiates when the local interface friction is mobilized. The results show that stress concentrations develop at the sliding front and are most significant when the reinforcement is relatively extensible; 3) The peak pullout resistance, associated with a two-way failure mechanism, where sliding fronts progress from both the active and passive ends of the inclusion; 4) The post-peak response of the inclusion, characterized by a reduction of pullout resistance and elongation (referred to as snap-through) as the sliding fronts coalesce.

The principal parameters controlling the predicted load-elongation response are the relative soil-reinforcement stiffness, inclusion length and interface friction.

The shear-lag predictions of pullout have been evaluated through comparisons with a program of experimental measurements performed in the APSR cell. Pullout tests were conducted on instrumented steel sheet and nylon 6/6 inclusions of lengths $L=0.36$ and 0.42m , respectively, embedded in dense Ticino sand. The selected inclusion materials exhibit linear, elastic and time independent stress-strain properties, have smooth surfaces with relatively low interface friction, and represent upper and lower limits of extensibility for practical soil reinforcements.

The load distribution and load-elongation response for the steel sheet inclusion were found to be approximately linear with interface friction angle $\delta=22^\circ$, well defined from repeatable measurements of the peak pullout load. In contrast, the measurements for the nylon 6/6 inclusions showed much more non-linearity in both the load distribution and load elongation response. The data show a pronounced post-peak reduction in pullout resistance, which is further complicated by stick-slip behavior in tests performed at low displacement rates. The shear-lag analysis describe accurately the measured data for an assumed interface friction angle $\delta=22^\circ$, which corresponds closely with residual conditions measured in the pullout test. The analysis shows that the peak pullout resistance is controlled by the non-linear load distribution and is significantly higher (by approximately 20%) than would be expected from a conventional limit equilibrium calculation.

7.4. Recommendations

There are three general directions for future research based on the results presented in this thesis:

1. Further evaluation of the shear-lag analyses presented in Chapters 4 and 5.

2. Extension of the analyses to incorporate more realistic modeling of the soil and reinforcing materials.
3. Applications of the analysis for practical geotechnical problems. Possible examples include predictions of the stress distributions in reinforced earth walls at working load levels and analysis of pullout tests for soil nails and piles.

7.4.1. Evaluation of Shear-Lag Analyses

The measurements of load transfer in the APSR cell provide a rational and controlled basis for evaluating the shear-lag predictions for a horizontal reinforcement (i.e., $\theta=0^\circ$) in plane strain compression. The results in Chapter 3 describe preliminary comparisons based on the first test program using steel sheet reinforcements in dry Ticino sand. Further research is currently in progress (Chauhan, 1993) to measure load transfer for different classes of geosynthetic materials. These data will provide more information to evaluate other aspects of the shear-lag predictions such as the effects of axial stiffness.

The analyses for inclined reinforcements in different modes of shear are more difficult to evaluate. Comparisons with finite element analyses have highlighted important limitations associated with load transfer at the tip of the inclusion, while comparisons with data from direct shear box tests cannot be considered reliable due to severe non-uniformities within the soil specimen. In principle, experimental simulation of the boundary conditions assumed in the analysis can be accomplished using equipment such as the Directional Shear Cell (DSC; Arthur, 1988).

The experimental evaluation of pullout tests has shown that the proposed shear-lag analysis can describe reliably the load transfer for extensible, planar reinforcements. However, there are many aspects of the proposed analysis which deserve further investigation. For example, stress concentrations at the sliding front represent a physical mechanism which has not previously been identified in the soils literature. Experimental

measurements (using miniature transducers, etc.) could be used to investigate the occurrence of such a phenomenon. Further studies should also be undertaken to compare the shear-lag analysis with numerical simulation of pullout using frictional interface elements (Schellekens and DeBorst, 1993).

7.4.2. Extension of Shear-Lag Analyses

One of the principal advantages of the proposed shear-lag analyses is that they permit closed-form derivation of the soil-reinforcement interaction. The distribution and magnitude of axial stresses in a planar soil reinforcement can be determined as a function of the geometry, boundary conditions, constituent material properties and interface traction. Thus, the shear-lag solutions provide clear physical insight into the factors controlling load-transfer in reinforced soils.

The analyses described in this thesis assume linear, isotropic and elastic property for both the soil and reinforcing material. More realistic descriptions of soil behavior should include the non-linear, inelastic and dilative behavior observed in shear tests, while modeling of time dependent material response is important for certain classes of geosynthetic materials. Further studies are also needed to establish how the shear-lag analyses can be applied to describe load transfer for grid reinforcements.

Although some of these refinements in material properties are amenable to extension of the shear-lag analysis, it is most probable that numerical solutions will be required. Finite element analyses will definitely be required for solving problems of non-linear and path dependent (inelastic) material behavior. The first requirement of these models will be to simulate realistically the boundary conditions at the tips of the inclusion (through interface and/or gap elements).

7.4.3. Other Applications

The proposed shear-lag analyses have many possible applications in two particular classes of practical geotechnical problems: 1) predictions of stresses in reinforced soil masses at working load levels; and 2) prediction and interpretation of pullout tests for inclusions ranging from soil nails to tension piles. This section discusses the analysis of reinforced soil walls and tension pile tests in more detail.

7.4.3.1. Stresses in a Reinforced Earth Wall

In current practice, the design of reinforced earth walls is based on limit equilibrium calculations (e.g. Jewell, 1990). Design stresses in the reinforcements are then estimated from local equilibrium and compatibility of strains in the soil and reinforcements. Detailed comparisons between predicted and measured stresses from instrumented walls (e.g. Jarret and McGown et al., 1987) shows that these methods are generally unreliable. More realistic assessments of stress distributions at working stress levels can be achieved by finite element methods (e.g. Al-Hussaini and Johnson, 1978; Ogisako et al, 1988). However, it is then difficult to assess the importance of the many variables affecting the load transfer.

An alternative approach, using the shear-lag analysis, is to develop models which relate the reinforcement stresses to the wall movement. Hence, the selection of reinforcing materials can be related to the control of wall deformations during construction and in subsequent loading. This type of approach has been investigated by Murray et al. (1990) using a simple one-dimensional analysis. One possible solution strategy would involve the following steps (Fig. 7.1):

1. The reinforced earth mass should be subdivided into a series of discrete composite layers (and wall segments) based on the vertical spacing of reinforcements and characterized by

an average confining pressure due to the weight of overburden. Initial lateral stresses σ_{h0} in the unreinforced soil are related to the compaction of the backfill (Duncan et al., 1991).

2. If the reinforcement is not physically connected to the wall, then lateral displacement of the wall segment can be related to average lateral stresses in the soil, σ_{hw} (through Rankine type analysis). When the reinforcement is connected to the wall, then the lateral displacement is controlled by the pullout response of the reinforcement.
3. Wall construction can be simulated using the weight of each of the composite elements and assuming a deformed mode shape for the wall (e.g., Handy, 1985; Murray et al, 1990). This is the most difficult step for design calculations. However, given the measurements of wall deformations, the analysis should be able to predict the stresses within the reinforcements.

It should be noted that substantial rotation of principal stresses may occur towards the wall toe, especially for rough and flexible walls over a soft base (e.g. Handy, 1985). The direction of principal stresses in this case may be determined with the aid of numerical simulations of the unreinforced soil mass. As a first approximation, it may be assumed that the direction of the (unreinforced) principal stresses is not affected by the presence of the inclusions, even though its magnitude is substantially reduced (Chalaturnyk et al, 1989)

7.4.3.2. Tension Tests for Piles

Tension (pullout) tests are widely used to estimate the shaft friction of piles and soil nails. In principle, these problems can be analyzed through modifications of the shear-lag analysis which include: 1) axisymmetric geometry; and 2) stress gradients due to the self-weight of the soil (i.e., boundary tractions are functions of depth). Other factors influencing the pullout response are more difficult to evaluate, including: 1) effects of pile/nail installation on the stresses and properties of the surrounding soil (and residual

stresses in the pile); and 2) time dependent response associated with movement of pore water (e.g. suction pressures mobilized at the base of the piles).

The existing analyses of pile deformations at working loads are based on linear elastic solutions using simplified analysis by finite element and boundary element methods (e.g. Poulos and Davis, 1980). The shear-lag analysis is similar in concept to the existing load transfer models but can also include the effects of progressive failure for long, slender piles, where interface sliding is an important factor at working loads.

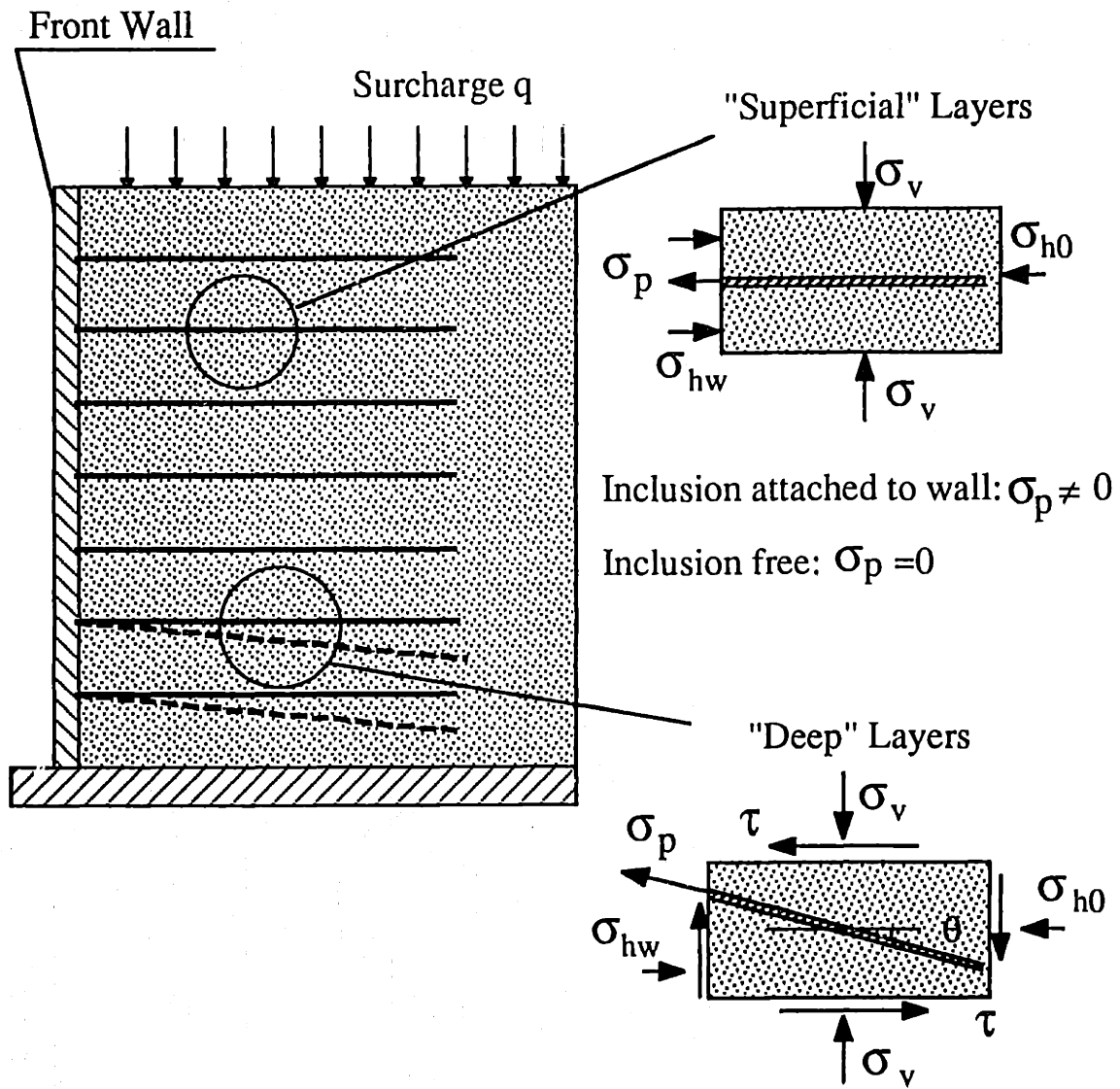


Figure 7.1: Approach for the Solution of Reinforced Wall Using the Shear-Lag Analysis.

Appendix 7.A: References

- Al-Hussaini, M.M. and Johnson, L.D.(1978) "Numerical Analysis of a Reinforced Earth Wall", *Proceedings of the Symposium on Earth Reinforcement*, ASCE, Pittsburg, 98-126.
- Arthur, J.R.F. (1988) "Cubical Devices: Versatility and Constraints", *Advanced Triaxial Testing of Soil and Rock*, ASTM STP 977, R.T. Donaghe, R.C. Chaney, and M.L. Silver, Eds., American Society for Testing and Materials, Philadelphia, 743-765.
- Chalaturnyk, R.J.; Scott, J.D.; Chan, D.H.K. and Richards, E.A.(1989) "Stresses and Deformations in a Reinforced Soil Slope", *Canadian Geotechnical Journal*, 27, 224-232.
- Chauhan, S. (1993) PhD Thesis in progress, MIT.
- Duncan, J.M.; Williams, G.W.; Sehn, A.L. and Seed, R.B. (1991) "Estimation Earth Pressures due to Compaction", *ASCE Journal of Geotechnical Engineering*, 117(12), 1833-1847.
- Handy, R.L. (1985) "The Arch in Soil Arching", *ASCE Journal of Geotechnical Engineering*, 111(3), 302-318.
- Murray, R.T., Andrawes, K.Z. and McGown, A. (1990) "Design, Construction and Performance of Reinforced Soil Walls", *Proceedings of the International Conference on Geotextiles, Geomembranes and Related Products*, The Hage, 1003-1007.
- McGown, A.; Andrawes, K.Z., and Al-Hasani, M.M. (1978) "Effect of Inclusion Properties on the Behaviour of Sand", *Géotechnique*, 28(3), 327-346.

- Jarrett, P. M. and McGown, A. , eds. (1987) *The Application of Polymeric Reinforcement in Soil Retaining Structures*, Kingston, Ontario. NATO ASI Series, Series E: Applied Sciences, 147, Kluwer Academic Publishers, Boston.
- Jewell, R.A. (1980) "*Some Effects of Reinforcement on the Mechanical Behaviour of Soils*", Ph.D. Thesis, University of Cambridge.
- Jewell, R.A. (1990) "Strength and Deformation in Reinforced Soil Design", *Proceedings of the International Conference on Geotextiles, Geomembranes and Related Products*, The Hage, 79pp.
- Larson, D. G. (1992) " A Laboratory Investigation of Load Transfer in Reinforced Soil", PhD Thesis, MIT, Cambridge, MA.
- Ogisako, E.; Ochiai, H; Hayashi, S. and Sakai, A (1988) "FEM Analysis of Polymer Grid Reinforced-Soil Retaining Walls and its Application to the Design Method", *International Geotechnical Symposium on Theory and Practice of Earth Reinforcement*, Fukuoka, Japan, 559-564.
- Poulos, H.G. and Davis, E.H. (1980) "*Pile Foundation Analysis and Design*", Series in Geotechnical Engineering, John Wiley & Sons, New York, NY.
- Schellekens, J.C.J. and DeBorst, R. (1993) "On the Numerical Integration of Interface Elements", *International Journal for Numerical Methods in Engineering*, 36, 43-66.